UNIVERSITÄT POTSDAM

From Phantom Blocks to Denudational Noise - Downwearing of the Himalaya-Tibet Orogen from a Multi-Scale Perspective

by

Henry Munack

Kumulative Dissertation
zur Erlangung des akademischen Grades
Doktor der Naturwissenschaften (Dr. rer. nat.)
in der Wissenschaftsdisziplin Geomorphologie

in the
Faculty of Science
Institute of Earth and Environmental Science

September 1, 2014

Declaration of Authorship

I, Henry Munack, declare that this thesis titled, "From Phantom Blocks to Denudational Noise - Downwearing of the Himalaya-Tibet Orogen from a Multi-Scale Perspective" and the work presented in it are my own. I confirm that:

- This work was done wholly while in candidature for a research degree at Potsdam University.
- Where any part of this thesis has previously been submitted for a degree or any other qualification at this University or any other institution, this has been clearly stated.
- Where I have consulted the published work of others, this is always clearly attributed.
- Where I have quoted from the work of others, the source is always given. With the exception of such quotations, this thesis is entirely my own work.
- I have acknowledged all main sources of help.
- Where the thesis is based on work done by myself jointly with others, I have made clear exactly what was done by others and what I have contributed myself.

Signed: ________________________________

Date: ________________________________

“It always seems impossible until it’s done.”

Nelson Mandela
(*18.06.1918, †05.12.2013)

Abstract

Knowing the rates and mechanisms of geomorphic process that shape the Earth's surface is crucial to understand landscape evolution and its implications, such as the redistribution of nutrients, the production and loss of soil, and the threat of sedimentary hazards. Modern methods for estimating denudation rates enable us to quantitatively express and compare processes of landscape downwearing that can be traced through time and space—from the seemingly intact, though intensely shattered, phantom blocks of the catastrophically fragmented basal facies of giant rockslides up to denudational noise in orogen-wide data sets averaging over several millennia. This great variety of spatio-temporal scales of denudation rates is both boon and bane of geomorphic process rates. Indeed, processes of landscape downwearing can be traced far back in time, helping us to understand the Earth's evolution. Yet, this benefit may turn into a drawback due to scaling issues if these rates are to be compared across different observation timescales.

This thesis investigates the mechanisms, patterns and rates of landscape downwearing across the Himalaya-Tibet orogen, a study area that covers a broad range of tectonic, climatic and topographic factors that all influence denudation.

Accounting for the spatiotemporal variability of denudation processes, this thesis addresses landscape downwearing on three distinctly different spatial scales, starting off at the local scale of individual hillslopes where considerable amounts of debris are generated from rock instantaneously: Rocksliding in active mountains is a major impetus of landscape downwearing. Study I provides a systematic overview of the internal sedimentology of giant rockslide deposits and thus meets the challenge of distinguishing them from macroscopically and microscopically similar glacial deposits, tectonic fault-zone breccias, and impact breccias. This distinction is important to avoid erroneous or misleading deduction of paleoclimatic or tectonic implications. ▸ Grain size analysis shows that rockslide-derived micro-breccia closely resemble those from meteorite impact or tectonic faults. ▸ From the inspection of an $n = 19$ data set we find that frictionite may occur more frequently that previously assumed. ▸ Mössbauer-spectroscopy derived results indicate basal rock melting in the absence of water, involving short-term temperatures of $>1500\,^{\circ}$C. These new findings necessitate the reevaluation of certain moraine chronologies, and of the role of monsoon precipitation as a major trigger of giant slope failure.

Zooming out, Study II tracks the fate of these sediments, using the example of the upper Indus River, NW India. There we use river sand samples from the Indus and several dozen tributaries to estimate basin-averaged rates of landscape denudation along a 320-km reach across the Tibetan Plateau margin, to determine patterns of sediment routing

and to answer the question whether incision into the western Tibetan Plateau margin is currently active or not. ▸ We find an about one-order-of-magnitude upstream decay—from 110 mm kyr^{-1} to 10 mm kyr^{-1}—of cosmogenic ^{10}Be-derived basin-wide denudation rates across the morphological knickpoint that marks the transition from the Transhimalayan ranges to the Tibetan Plateau. This trend is corroborated by independent bulk petrographic and heavy mineral analysis of the same samples. ▸ From the observation that tributary-derived basin-wide denudation rates do not increase markedly until ∼150–200 km downstream of the topographic plateau margin we conclude that incision into the Tibetan Plateau is inactive. ▸ Comparing our postglacial ^{10}Be-derived denudation rates to long-term ($>10^6$ yr) estimates from low-temperature thermochronometry, ranging from 100 mm kyr^{-1} to 750 mm kyr^{-1}, points to an order-of-magnitude decay of rates of landscape downwearing towards present. We infer that denudation rates must have been higher in the Quaternary, probably promoted by the interplay of glacial and interglacial stages.

Our investigation of regional denudation patterns in the upper Indus finally is an integral part of Study III that synthesizes denudation of the Himalaya-Tibet orogen. In order to identify general and time-invariant predictors for ^{10}Be-derived denudation rates we analyze tectonic, climatic and topographic metrics from an inventory of 297 drainage basins from various parts of the orogen. Aiming to get insight to the full response distributions of denudation rate to tectonic, climatic and topographic candidate predictors, we apply quantile regression instead of ordinary least squares regression, which has been standard analysis tool in previous studies that looked for denudation rate predictors. ▸ We use principal component analysis to reduce our set of $n = 26$ candidate predictors, ending up with just three out of these: Aridity Index, topographic steepness index, and precipitation of the coldest quarter of the year. ▸ Out of these three, topographic steepness index proves to perform best during additive quantile regression, by showing evenly spaced regression quantiles with statistical indistinguishable slopes. Our consequent prediction of denudation rates on the basin scale involves prediction errors that remain between 5 mm kyr^{-1} and 10 mm kyr^{-1}. ▸ Summarizing our findings we conclude that while topographic metrics such as river-channel steepness and slope gradient—being representative on timescales that our cosmogenic ^{10}Be-derived denudation rates integrate over—generally appear to be more suited as predictors than climatic and tectonic metrics based on decadal records.

Zusammenfassung

Die Kenntnis von Raten und Mechanismen geomorphologischer Prozesse, die die Erdoberfläche gestalten, ist entscheidend für das Verständnis von quartärer Landschaftsgeschichte und ihren Begleiterscheinungen, wie z.B. der Umlagerung von Nährstoffen, der Bodenbildung und -degradation oder der Bedrohung durch sedimentäre Naturgefahren. Denudationsraten sind dabei das Mittel zur Quantifizierung und zum Vergleich von Oberflächenabtrag; hinweg über zeitliche und räumliche Größenordnungen – von den optisch unversehrten, jedoch durchgehend zerrütteten “Phantom Blocks” der basalen Fazies katastrophaler Bergstürze bis hin zum “Denudational Noise”, dem durchaus informativen Rauschen in Datensätzen, die über ganze Orogene und tausende Jahre von Landschaftsgeschichte integrieren. Diese große räumlich-zeitliche Variabilität von Denudationsprozessen ist Chance und Herausforderung zugleich. Zum einen können Denudationsprozesse weit in der Zeit zurückverfolgt werden, was hilft, Landschaftsgeschichte nachzuvollziehen. Andererseits hat es sich gezeigt, dass geomorphologische Prozessraten mit dem Zeitraum ihrer Beobachtung skalieren, was einen Vergleich über zeitliche Größenordnungen hinweg erschwert.

Diese Dissertation untersucht in drei Studien die Mechanismen, Muster und Raten von Denudation im Himalaja-Tibet Orogen, einem Naturraum, der durch eine außerordentliche Spannweite von tektonischen, klimatischen und topographischen Einflussfaktoren auf Denudationsraten besticht.

Der räumlichen (und zeitlichen) Variabilität von Denudationsprozessen folgend beginnt diese Arbeit dort, wo bedeutende Mengen von Festgestein schlagartig in erodierbaren Schutt umgewandelt werden: Bergstürze sind ein Hauptantrieb der Abtragung von aktiven Gebirgen. Studie I systematisiert die interne Sedimentologie gigantischer Bergsturzablagerungen. Sie adressiert damit Herausforderungen durch die makro- und mikroskopische Ähnlichkeit von Bergsturzablagerungen mit glazialen Ablagerungen, tektonischen Störungsbrekkzien und Impaktbrekkzien. Ziel einer solchen Systematisierung ist die Vermeidung fehlerhafter paläoklimatischer oder -tektonischer Interpretationen. ▸ Die mikroskopische Analyse und der Vergleich von Korngrößenverteilungen zeigen, dass Bergsturzbrekkzien auf dieser Ebene nicht von tektonischen oder Impaktbrekkzien unterscheidbar sind. ▸ Friktionit, d.h. partiell geschmolzenes Gestein an der Basis großer Bergstürze, könnte weit häufiger vorkommen, als bisher angenommen. ▸ Ergebnisse von Mössbauer-Spektroskopie deuten auf Temperaturen von mindestens 1500 $^{\circ}$C sowie die Abwesenheit von Wasser als Schmiermittel hin. Diese neuen Erkenntnisse geben Anlass, Moränenchronologien sowie auch die grundsätzliche Rolle von monsunalem Starkregen als Trigger für Bergstürze im Himalaya zu überdenken.

Auf der mesoskaligen Ebene von Einzugsgebieten verfolgt Studie II, am Beispiel des oberen Indus in NW Indien den Weg dieser Sedimente, denn sie geben Auskunft über beckenweite Denudationsraten, sowie Pfade und Muster des Sedimenttransports am westlichen Tibetplateaurand. Diese Informationen sollen helfen, die Mechanismen der Einschneidung großer Flüsse, wie z.B. des Indus, in das Tibetplateau, sowie den gegenwärtigen erosionalen Status des Plateaurandes zu verstehen. ▸ Die beckenweiten Denudationsraten in den Tributären des Indus nehmen stromabwärts – und damit über den morphologischen Tibetplateaurand hinweg – von 10 mm kyr^{-1} auf 110 mm kyr^{-1} zu. Dieser Trend wird durch unabhängige Petrographie- und Schwermineralanalysen aus denselben Proben nachgezeichnet. ▸ Es zeigt sich allerdings, dass der morphologische Plateaurand und der hierfür erwartbare Anstieg der beckenweiten Denudationsraten um ∼150–200 km versetzt sind. Hieraus schließen wir, dass der westliche Rand des Tibetischen Plateaus rezent nicht maßgeblich erodiert wird. ▸ Ein Vergleich unserer postglazialen beckenweiten Denudationsraten von kosmogenen Nukliden mit Langzeit-($>10^6$ yr)-Thermochronometriedaten von 100 mm kyr^{-1} bis 750 mm kyr^{-1} deutet auf einen spätquartären Rückgang von Denudationsraten im Transhimalaya hin. Folglich muss es früher während des Quartärs, eventuell bedingt durch das Wechselspiel von Glazialen und Interglazialen, Zeiten höherer erosionaler Effizienz gegeben haben.

Studie III fokussiert schließlich, in einer Analyse beckenweiter Denudationsraten von kosmogenen Nukliden, auf Denudationsmuster und -mechanismen für das gesamte Himalaja-Tibet Orogen. Auf der Suche nach zeit-invarianten tektonischen, klimatischen oder topographischen Prädiktoren für Denudationsraten wird ein Datensatz von 297 orogenweit verteilten Einzugsgebieten untersucht. Um Einblicke in die gesamte Response-Verteilung zwischen Denudationsrate und Prädiktor zu erhalten nutzen wir – anstelle der in diesem Zusammenhang vielbenutzten Methode der kleinsten Quadrate – Quantilregression. ▸ Zuerst aber reduzieren wir einen Satz von $n = 26$ möglichen Prädiktoren, unter Nutzung der Hauptkomponentenanalyse, auf drei Prädiktoren: Ariditätsindex, topographischer Steilheitsindex und Niederschlag des kältesten Quartals. ▸ Die additive Quantil-Regression dieser drei Prädiktoren zeigt, durch gleichabständige Quantil-Modelle mit statistisch nicht unterscheidbaren Anstiegen, dass der Steilheitsindex die besten Ergebnisse im Sinne einer zeit-invarianten Beziehung zwischen Denudationsrate und Prädiktoren liefert. ▸ Zusammenfassend zeigt sich, dass topographisch basierte Prädiktoren, wie z.B. Steilheitsindex oder Hangneigung, geeigneter für die Vorhersage von kosmogenen beckenweiten Denudationsraten sind als klimatische oder tektonische Prädiktoren. Wir erklären dieses Resultat mit den jeweils über Jahrtausende integrierenden Maßzahlen für Topographie und kosmogenen Denudationsraten, und der daraus folgenden Inkompatibilität der kosmogenen Denudationsraten mit den tektonischen und klimatischen Prädiktoren, die lediglich auf Jahrzehnten von Messungen beruhen.

Acknowledgements

During the time of my PhD at the Institute of Earth- and Environmental Science, Potsdam University, I experienced a lot of friendliness and support from colleagues and students. This is why I will keep these years in good memory. Being grateful for that and hoping to further work with some of you in the future I'd like to acknowledge here:

- Oliver Korup, my supervisor and mentor, for steady support, scientific guidance, sharing knowledge, ideas and time, for preferring to promote strengths despite searching for weaknesses, and for always being constructive and fair.
- Jan Blöthe, who was my office, lab, teaching and field mate, a perpetual source of expert knowledge and ideas, a patient proofreader, and who became a friend.
- Colleagues who taught me a lot, generously sharing their expert knowledge, and who greatly helped me gaining ground in academia, namely Tibi Codilean, Dirk Scherler, Wolfgang Schwanghart, Annegret Thieken, and Hella Wittmann-Oelze.
- My office mates Nele Meyer and Swenja Rosenwinkel, and of course all other members of our precious *Geohazard Research Group* for discussing, sharing ideas, proofreading, and sharing valuable leisure time.
- All coauthors of the three studies that are part of this thesis, for sharing their knowledge and for giving the opportunity to work together.
- Colleagues, students and friends who greatly supported me during field and lab work, in sample preparation, in preparing lessons, and in managing my project, namely Piero Catarraso, Lutz Ehlert, Birgit Fabian, Christine Fischer, Katharina Horst, Tanja Klaka-Tauscher, Heide Kraudelt, Johanna Meyer, Steffen Mischke, René Muschkorgel, Antje Musiol, Ines Münch, Heiko Pingel, Bettina Richter, Tsering Samphel, Tinles Nubuu, Franziska Scheffler, Alexander Schmidt, Ed Sobel, Blanka Sperner, Anja Städtke, Amelie Stolle, Martin Struck, Judith Thäle, Daniel Vollmer, Hans Weidinger, Robert Weißbach, and Steffi Zarnack.
- The R Project, MacTeX, and Sunil Patel for sharing his LaTeX thesis template.
- The German Research Foundation (KO3937/1, 2), the Potsdam Research Cluster for Georisk Analysis, Environmental Change and Sustainability (PROGRESS), and the Potsdam University Graduate School (PoGS) for funding this research.
- Manfred Strecker, who initially gave me the opportunity and funding to carry out my research at Potsdam University. Thank you so much, Manfred!
- My family, for being there!

Contents

List of Figures

List of Tables

Abbreviations

AFTA	**A**patite **F**ission **T**rack **A**nalysis
AI	**A**ridity **I**ndex
AMS	**A**ccelerator **M**ass **S**pectrometer
a.s.l.	**a**bove **s**ea **l**evel
BP	**B**ulk **P**etrography
CN	**C**osmogenic **N**uclide
DEM	**D**igital **E**levation **M**odel
GIS	**G**eographic **I**nformation **S**ystem
GPS	**G**lobal **P**ositioning **S**ystem
HEP	**H**illslope **E**rosion **P**otential
HM	**H**eavy **M**ineral
ICP-OES	**I**nductively **C**oupled **P**lasma - **O**ptical **E**mission **S**pectrometer
ITCZ	**I**nner**T**ropical **C**onvergence **Z**one
ITSZ	**I**ndus-**T**sangpo **S**uture **Z**one
LGM	**L**ast-**G**lacial **M**aximum
LWAV	**L**ong-**W**ave **T**opography
OLS	**O**rdinary **L**east **S**quares (regression)
PC	**P**rincipal **C**omponent
PCA	**P**rincipal **C**omponent **A**nalysis
PGA	**P**eak **G**round **A**cceleration
QReg	**Q**uantile **Reg**ression
SD	**S**tandard **D**eviation
SLHL	**S**ea **L**evel **H**igh **L**atitude
SRTM DEM	**S**huttle **R**adar **T**opography **M**ission **D**igital **E**levation **M**odel
XRD	**X**-**R**ay **D**iffraction

Physical Constants

^{10}Be half-life	$t_{\frac{1}{2}}\,^{10}Be$	=	1.387±0.012 Ma
Silicate rock absorption depth	z^*	=	600 mm
Silicate rock absorption mean free path	Λ	=	150 g cm^{-2}
Silicate rock mean density	ρ	=	2.6 g cm^{-3}

Symbols

^{10}Be	Beryllium-10	
$\bar{C}$	Average nuclide concentration	atoms g^{-1}
D	Fractal dimension	
$\dot{E}$	Denudation rate	mm kyr^{-1}
k	n of data set partitions for clustering	
k_S	Steepness index	m$^{2\theta}$
M	Magnitude	
M_W	Moment magnitude scale	
$\bar{P}$	Average nuclide production rate	atoms g^{-1} yr^{-1}
t$_i$	Averaging timescale	z* $\times$ $\dot{\mathrm{E}}^{-1}$
$\bar{\epsilon}$	Basin-averaged erosion rate	mm kyr^{-1}
Θ	Reference concavity	
λ	Decay constant	s^{-1}
ρ	(Rock) Density	g cm^{-3}
$\bar{\rho}$	Mean (rock) density	g cm^{-3}
σ	Standard deviation	

Für Helge, Nele und Annett

Chapter 1

Introduction

1.1 Motivation

Physical and chemical denudation rates determine the pace of removal and redistribution of mass from Earth's surface. Thus, they serve to quantitatively express and compare the efficacy of landscape downwearing through space and time. Insight to the fundamentals of denudation is of great importance for environmental management, and has implications starting from a general understanding of the system Earth, over the mitigation of natural hazards to practical applications such as the calculation of water reservoir lifespans. Insight to processes and patterns of denudation may be attained by studying recent or by reconstructing past environments, both offering a great variety of information sources. The data that may be derived from such investigations can help to better understand Earth's past evolution, and also may be used to predict (future) trends, and to fuel numerical models and simulations.

Studies of denudation processes have been carried out with various intentions, sometimes producing enthralling findings. A recent study examining the contribution of seismic events to regional landscape downwearing fueled the exciting notion that during (exceptionally large) earthquake events more topography may be destroyed by coseismic landsliding than is generated by concomitant uplift (Parker et al. (2011); Fig. 1.1A,B); a notion that may even hold when considering the long recurrence interval of 2–4 ka of such earthquakes. Recurrence intervals are also in the focus of studies that look into the probability of the occurrence and impact of (sedimentary) natural hazards (e.g. Korup, 2012) - another application of research looking into denudation rates and processes. Studies that investigate trends in formation, accumulation and loss of soil (e.g. Heimsath et al., 2000, 1997; Small et al., 1999) may serve here as a third example of the variety of research that investigates denudation across spatial and temporal scales.

Also the impact of human activities on Earth's critical zone (Fig. 1.1C,D), i.e. the highly heterogeneous, inhabited, and vulnerable boundary layer at the intersection of the atmosphere and the lithosphere, has been in the focus of research, dealing, among others, with the growing pressure on soil resources by e.g. cultivation of land, mining, flooding or wildfires (e.g. Roering and Gerber, 2005; Tomkins et al., 2007; Vanacker et al., 2007a).

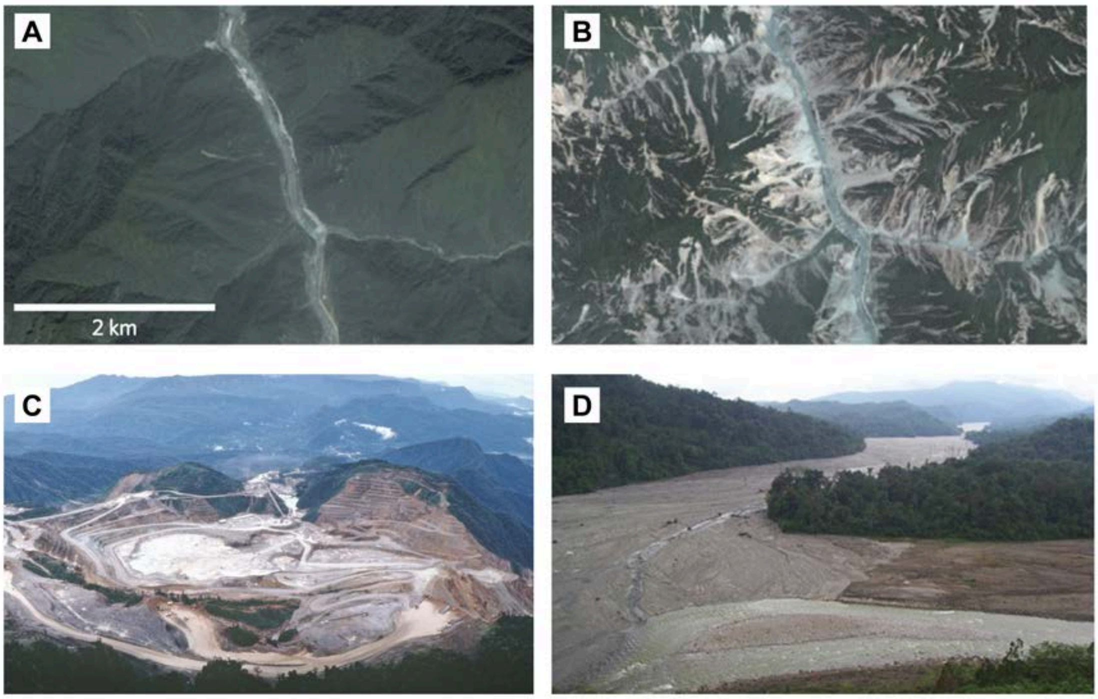

Figure 1.1: Modes of natural and anthropogenic landscape-scale denudation. A) and B) Pair of satellite images shows landscape before (A) and after (B) M_W 7.9 2008 Wenchuan earthquake in Sichuan, China, in some 24 km from the epicenter. While the mode of denudation in A) may be characterized by gradual fluvial denudation the denudational mode in B) is pulsed and catastrophic. Density of coseismic landslides amounts to >60% per unit area. Total volume of material eroded by ~195,000 landslides (Xu et al., 2014) has been estimated to ~5–15 km^3, which is greater than the net volume of 2.6 ± 1.2 km^3 added to the orogen by coseismic uplift (Ouimet (2011); Parker et al. (2011); Images: A) before (9 September 2005), and B) after earthquake (3 June 2008)). C) Manmade large-scale denudation at Ok Tedi Mine causing D) severe aggradation in the Ok Tedi River (Papua New Guinea), where mining spoils are dumped. These tailings increased sediment load of the Ok Tedi by one order to ~45 Mt yr^{-1} for the 1985–2000 gauging period (Pickup and Marshall, 2009), which is approx. the twofold value observed for the upper Indus River that drains large parts of the Transhimalaya and High Himalayas, NW India. (Image sources (C) http://research.berkeley.edu/, (D) http://derianga.wordpress.com/mining-ok-tedi/).

1.1.1 Feedbacks between tectonics, climate, erosion (and topography)

In tectonically active mountains, landscapes can be interpreted as the expression of competing endo- and exogenic forces, namely tectonics, climate, and erosion (e.g. Beaumont et al., 2000; Hodges et al., 2004; Koons, 1989; Roe et al., 2008; Zeitler, 1985). The feedbacks between these major players are manifold, though, despite decades of intensive research, partly not well constrained yet (Molnar, 2003). In this regard, the perception of tectonics setting the pace for uplift and therefore influencing climate and the rates of landscape downwearing are integral part to the debate (Burbank et al., 2003; Lamb and Davis, 2003; Molnar and England, 1990). Erosion acts as the major opponent of tectonically driven uplift by removing material, i.e. by stripping the thickened orogenic crust. Erosional feedbacks to tectonics and climate cover a wide range of physical and chemical processes involving (a) controls on the structural evolution of parts of mountain belts (Norris and Cooper, 1997; Pavlis et al., 1997), (b) controls on the topographic evolution of entire collisional orogens (Koons (1989); Willett (1999); Fig. 1.2), or (c) influences on Earth's climate due to removal of CO_2 from the atmosphere on geologic timescales (Raymo and Ruddiman, 1992; Willenbring and von Blanckenburg, 2010).

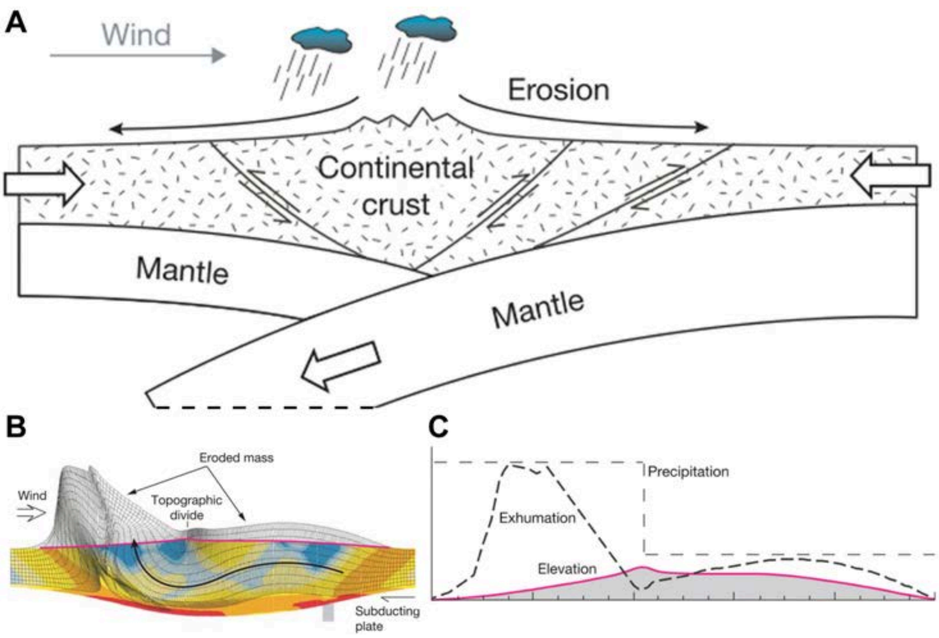

Figure 1.2: Links and feedbacks between tectonics, climate, erosion and topography in settings of convergent plate tectonism. A) Hypothetical cross section showing convergent plate boundary, with plate from the right subducting left plate, where open arrows indicate syn-compressive tectonism. Moisture-laden winds from the left promote fluvial (or glacial) erosion on wind-facing slopes. B) Numerical-modeling derived distribution of strain rates for scenario shown in panel (A), with red areas indicating high strain and blue areas low strain, respectively. Model based on the assumption of pronounced asymmetry in rainfall, entailing forced river incision and landscape downwearing to the left of the drainage divide, which leads to migration of the range divide (magenta line is surface topography) towards rainward side. This causes asymmetry in exhumation (denoted by grayish mesh), which conditions paths of bedrock (black arrow). C) Diagram reducing panel (B) to the characteristics of exhumation, elevation and precipitation (modified after Dietrich and Perron (2006), therein panel B) modified after Willett (1999)).

Figure 1.2 illustrates how climate may influence the evolution of active mountain belts. By governing fluvial, glacial and aeolian erosion—and therefore erosional efficacy and vigorousness—climate exerts first-order control on tectonic uplift, on erosion, and on topography (Lamb and Davis, 2003; Whipple, 2009). Yet studies examining the influence of climate on long-term erosion rates in tectonically active mountains have come up with strikingly conflicting results. While numerous studies support the idea of a first-order control of rainfall on denudation of active orogens (Reiners et al., 2003; Wobus et al., 2003), other studies cannot support this notion (Burbank et al., 2003), or find topography as the main factor governing denudation rates (Montgomery and Brandon, 2002). Unglaciated topography in tectonically active mountain ranges may be seen as mainly the result of competing bedrock uplift and river erosion (Burbank et al., 1996; Howard et al., 1994). Within this conceptual framework slope failure—via bedrock landsliding—is the mechanism that adjusts hillslopes to river incision (Larsen and Montgomery, 2012). Topographic relief in turn is suggested to be a function of landscape-scale material strength and drainage density, with wide river spacing promoting high topography (Burbank et al., 1996; Schmidt and Montgomery, 1995).

1.1.2 Denudation rates and the timescale problem

Though this short summary highlighted the ongoing debate regarding the influence of climate and tectonics on denudation, other factors, such as biota (Dietrich and Perron, 2006; Reinhardt et al., 2010) and lithology (Palumbo et al., 2010b), are thought to exert controls on landscape downwearing, too. Their interaction with tectonics and climate oftentimes are not straightforward, such as supposed feedbacks between weathering of silicate rocks and atmospheric CO_2 concentration (Raymo and Ruddiman, 1992; Willenbring and von Blanckenburg, 2010). Whatever the final aim of research, either disentangling the global picture or contributing jigsaw pieces to it, understanding the controls on Earth surface's denudation is of vital importance. Therefore, rates of landscape downwearing have been subject to intensive research (e.g. Montgomery et al., 2001; Pinet and Souriau, 1988) and have been quantified across orders of spatial (and temporal) scales amongst other methods using

- (historic) sediment and solute load data from river gauging (e.g. Saunders and Young, 1983; Summerfield and Hulton, 1994),
- the (cumulative) volume of landslides contributing to landscape downwearing (e.g. Barnard et al., 2001; Hovius et al., 1997),
- sediment volumes trapped in natural basins or artificial reservoirs (e.g. Garzanti et al., 2005; Reneau et al., 1989),

- dated surfaces to infer loss (and gain) of mass (e.g. Blöthe et al., 2014; Ruxton and McDougall, 1967),
- in situ produced (basin-averaged) concentrations of cosmogenic-nuclides (e.g. Bierman and Steig, 1996; Brown et al., 1995; Granger et al., 1996),
- thermal-history derived exhumation estimates from low-temperature thermochronometry (e.g. Thiede and Ehlers, 2013; Wobus et al., 2003), or
- empirical and numerical models, that predict denudation rate, e.g. as a function of driving and resisting forces (e.g. Ali and de Boer, 2010).

These different approaches by design yield results that cover a wide range of (a) temporal and (b) spatial scales; often spanning orders of magnitude. However, many studies have been pointing to the problem that time-related geomorphic process rates, such as denudation rates, scale with observation time (Gardner et al., 1987; Sadler, 1981; Sadler and Jerolmack, 2014; Schumer and Jerolmack, 2009; Willenbring and von Blanckenburg, 2010). Looking into this phenomenon, opposing trends have been found: while landscape-scale denudation rates from the tectonically idle Idaho batholith are biased towards low rates on short-term (Kirchner et al., 2001), rates of river bedrock incision from a global inventory are biased towards higher estimates for shorter averaging timescales (Finnegan et al. (2014); Fig. 1.3). To explain the bias in landscape-scale denudation rates, Kirchner et al. (2001) invoked infrequent sampling of low-frequency (but large-magnitude) events, i.e. undersampling of large denudation events (Fig. 1.1A) during the time of (short-term) river gauging. Finnegan et al. (2014) in turn propose hiatuses in bedrock incision to be the cause for the bias in their incision-rate data set. Such hiatuses could be result of bedrock shielding by hillslope material that may have been deposited in channels with infrequent large events (e.g. Fig. 1.1A) causing longer hiatuses by protracted phases of inhibited bedrock incision. Clearly, a potential time-dependency of (geomorphic) process rate estimates hinders straightforward analysis, interpretation and comparison of these data across variable timescales by (a) concealing the mechanisms behind, and (b) complicating the deduction of functional relationships between processes and their controls that are valid independent of observation timescale.

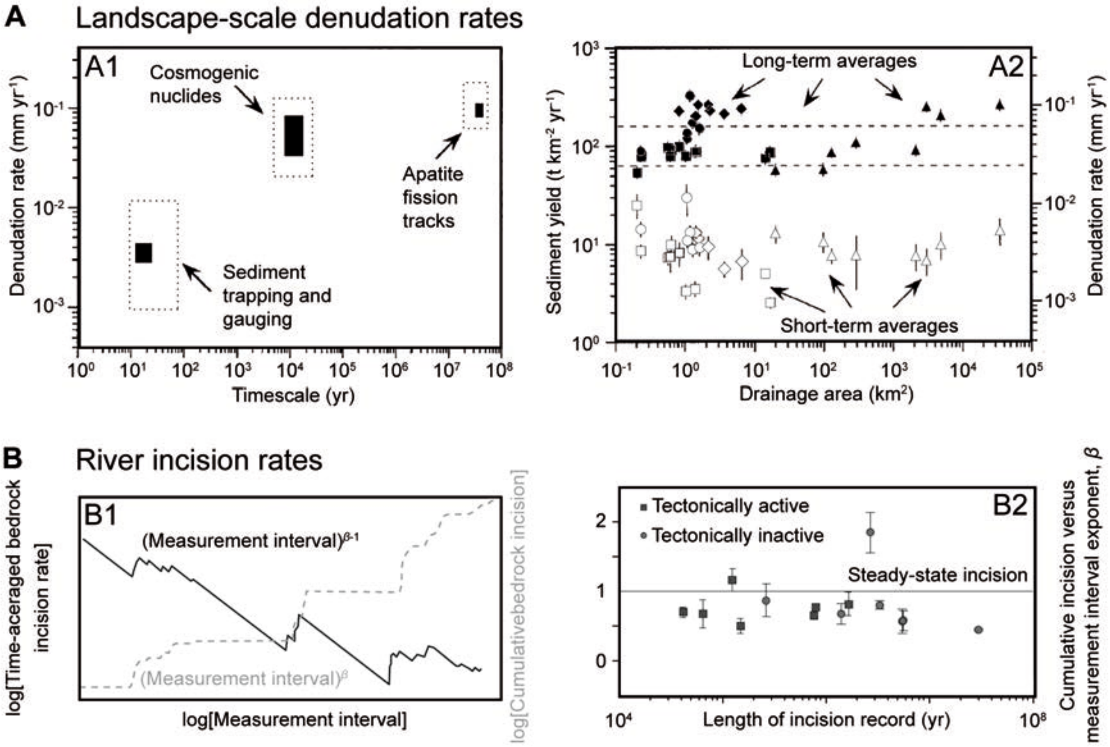

Figure 1.3: Synopsis of denudation and incision rate estimates across various timescales. A) Compilation of landscape-scale denudation rates (from tectonically idle Idaho batholith) from river gauging (resp. sediment trapping), basin-averaged cosmogenic ^{10}Beryllium (^{10}Be) analysis, and from apatite fission track analysis (AFTA) (after Kirchner et al. (2001)). A1) Denudation rates vs. averaging timescale. Dashed rectangles mark limits of respective measurement range, filled rectangles represent middle 50%, respectively. A2) Denudation rates (resp. sediment yield) vs. drainage area, with open symbols for short-term (decadal) denudation rates from river gauging / sediment trapping, and filled symbols for millennial cosmogenic-nuclide derived denudation rate estimates. B) River incision rates from N = 155 measurements compiled from 14 sites. B1) Plot of the log cumulative incision (dashed line) and log time-averaged incision rate vs. log measurement interval (calculated synthetically). B2) Cumulative bedrock incision versus measurement interval exponent β as a function of incision record length. Data points are mean exponents with 1σ error bars. Horizontal line is steady-state incision where $\beta = 1$. Data points above steady-state incision line, i.e. exponents > 1 reflect incision rates that are biased towards higher rates on long term. Note that 11 out of 14 data points are below the steady-state line, therefore reflecting a bias towards lower incision raters on long term (after Finnegan et al. (2014)).

1.2 Aims and structure of this thesis

This thesis investigates spatiotemporal variations in denudation by tracing landscape downwearing in the Himalaya-Tibet orogen from the point source of giant rockslides, across the local scale of small to medium-sized (<300 km^2) drainage basins in the upper Indus valley, to the mountain-range-scale examination of denudation rates across the entire Himalaya-Tibet orogen. The rationale behind this structured approach is to zoom from the puzzle piece of one of the processes responsible for generating large amounts of sediment from bedrock, to the fate of sediment in forms of fluvially transported grains along the upper Indus, and ultimately looking at the big picture of downwearing of Earth's largest orogenic complex, which the Indus is dissecting, in order to trace and to link up landscape downwearing across these very different scales.

The aims of this thesis derive from the challenges and gaps in understanding of landscape downwearing that have been identified in this brief review. This thesis therefore acknowledges

- the need of a better knowledge about triggers and preparatory factors of the past that promoted landsliding, a major denudational process in active mountain belts,
- the necessity to further develop methods for quantifying landscape downwearing,
- the need of testing the validity of geomorphic concepts that have been mainly derived from humid mountains in topographically comparable but arid settings, and
- the methodical challenge from denudation rates that probably scale with observation timescale, and the need to identify robust (timescale-invariant) predictors for landscape-scale denudation rates.

Addressing these points, this thesis aims to contribute to current research by exploring new sources of information and alternative approaches of denudation-data analysis, and better constraining the functional relationships between environmental metrics—so-called predictors—and denudation rates. The three-part structure of this thesis follows that of scale (Fig. 1.4):

- ▶ On the local scale starting off at hillslope locations where large amounts of bedrock are converted to ready-to-transport debris instantaneously via catastrophic and large-scale landsliding (Fig. 1.4 *Rockslides*). Deposits of giant rockslides are potentially long-lived natural archives that allow us to investigate the geomorphic legacy of large rock-slope failures, which are thought to be substantial contributors to downwearing of mountain belts in response to rock uplift, river incision, and glacial scour.
- ▶ On the scale of catchments then tracing thus liberated sediment in the form of sand grains transported by tributaries in the upper Indus River catchment (Fig. 1.4 *Catchments*). The ^{10}Be concentration in these river sands allows inferring drainage basin-wide denudation rates averaged over several millennia. Additionally, these sands hold valuable information on their provenance and routing pathways.

- Finally, bringing together the current knowledge of such ^{10}Be derived denudation-rate estimates and their potential controls on the scale of the entire Himalaya-Tibet orogen (Fig. 1.4 *Orogen*).

1.2.1 Rockslides: Efficient rock-to-debris converters

Slope instability and concomitant landsliding are pervasive phenomena in mountain areas. In combination with fluvial and glacial erosion they can be held responsible for the lion's share of denudational work in active high mountains like the Himalaya-Tibet orogen (e.g. Korup et al., 2007; Shroder, 1998). Depending on observation timescale, the landslide contribution to total denudation may be subdivided into a periodic (quasi continuous) and an episodic component (Korup et al., 2004). Within such categorization, periodic, i.e. frequent, "background"-landsliding would mainly depend on seasonality (e.g. snowmelt or monsoonal precipitation). In contrast, episodic, exceptionally large landslides (in this thesis simplistically referred to as "rockslides") would be driven by high-magnitude/low-frequency events such as high-magnitude rainstorms, earthquakes, or the gradual deterioration of rock-mass strength due to weathering, fluvial and glacial undercutting, and perhaps alpine permafrost degradation; given that frequency and magnitude of landslides are inversely and nonlinearly correlated (Malamud et al., 2004).

The mechanisms behind mass wasting processes in the Himalaya-Tibet orogen in general as well as of giant rockslides in particular have intensively been examined (Heuberger et al., 1984; Hewitt, 1988; Masch and Preuss, 1977; Weidinger, 2006; Weidinger and Korup, 2009). These studies on the one hand pushed research towards a better systematization of the sedimentological features of rockslide deposits. On the other hand they fostered the notion of (partial) rock melting during the runout process, thus doing away with speculations about volcanic, meteoritic or tectonic origin of deposits hosting suchlike rocks. Looking into the mechanisms of giant rocksliding geoscientists opted for a variety of possible triggers and preparatory factors such as copious monsoonal precipitation (e.g. Bookhagen et al., 2005b; Dortch et al., 2011b), seismic shaking in the vicinity of Earth's most prominent continent-continent collision (e.g. Dortch et al., 2011b; Mitchell et al., 2007) probably facilitated by topographic amplification of ground acceleration (Davis and West, 1973; Keefer, 2002), rock-mass weakening due to preparatory (neo)tectonism (e.g. Weidinger et al., 1996), general rock type properties, lithological variances (e.g. Korup and Weidinger, 2011), or glacial debuttressing (e.g. Hewitt, 2002).

However, studying the deposits of terrestrial landslides can be challenging, if not simply for the reason that most focus in landslide research is dedicated to a hazard perspective

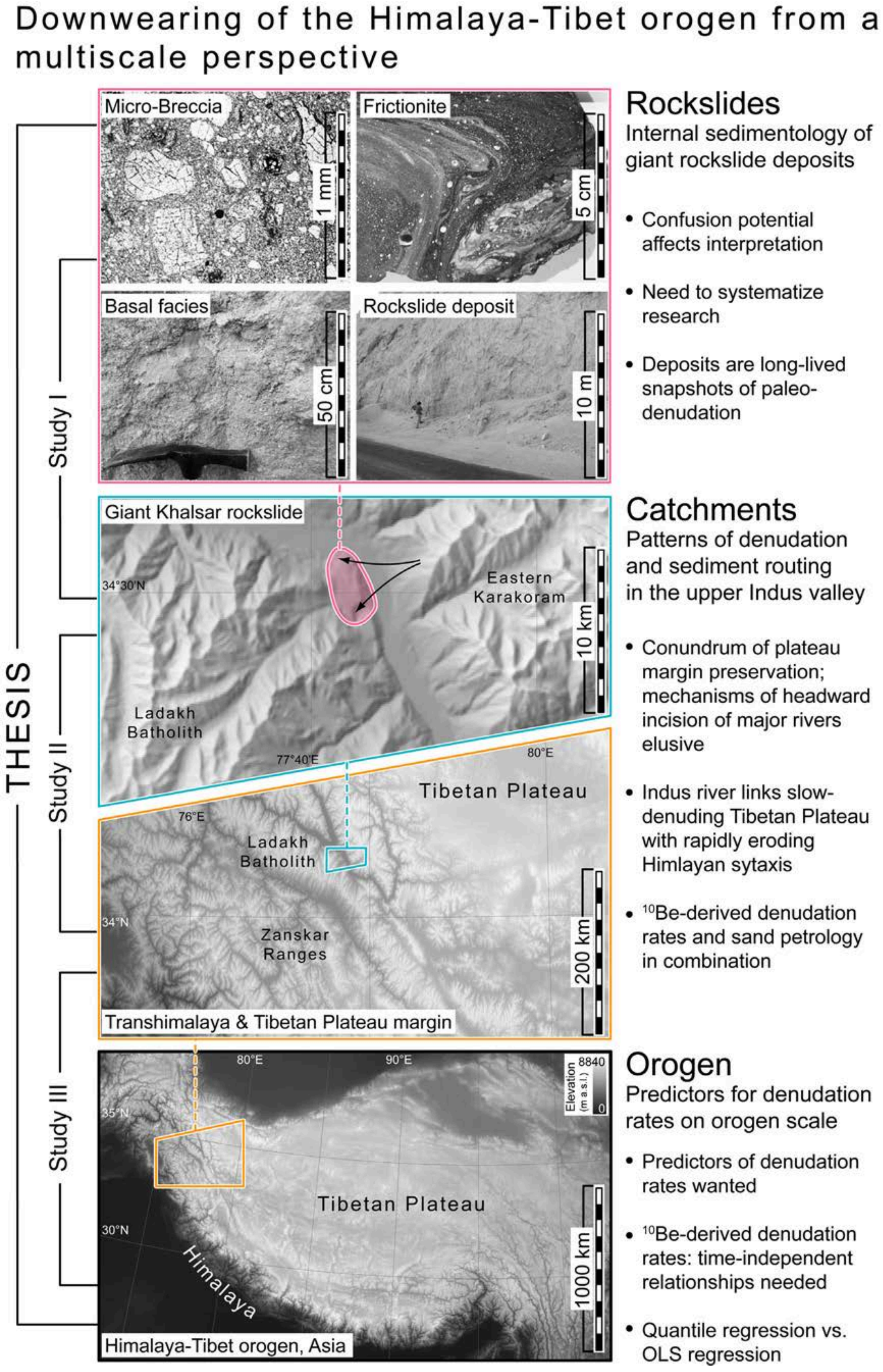

FIGURE 1.4: Advance organizer showing topic and multiscale perspective of the thesis, with spatial scale decreasing from top to bottom.

rather than one that investigates aspects of sedimentology. On the one hand comparatively small and frequent events tend to be overlooked in work grounded on remotely sensed data (Brardinoni et al., 2003) while in the field they may be obliterated by slope derived sediments or eroded fast, consequentially not being not fully detectable. On the contrary deposits of large (>10^6 m^3) events of slope failure, though being characterized by longer recurrence intervals than smaller ones, tend to be preserved much longer (Korup and Clague, 2009). This is why giant rockslide deposits in principle are well suited as long-lived records of preparatory factors and triggers, which have been controlled by past environmental conditions in turn.

Nonetheless, the study of giant rockslide deposits has been largely underexplored, although there are several good reasons to do so: Chaotic deposits from giant rockslides have been subject to misinterpretation, and often confused with glacial moraines (Hewitt, 1999; Hewitt et al., 2011) which consequentially led to incorrect or erroneous reconstruction of local or regional glacial chronologies (Deline, 2009; Santamaria Tovar et al., 2008). For example, the giant Khalsar rockslide deposit in the Shyok valley, NW India (Scherler et al., 2014; Weidinger et al., 2014), has been (mis-)interpreted as glacial moraine before (Dortch et al., 2010). Confusing giant mass wasting deposits with glacial moraines may, however, have implications beyond drawing erroneous conclusions regarding paleoclimatic conditions or the underestimation of rockslide hazards. Owing to the mechanics during runout and emplacement, landslide debris may be highly brecciated or even comminuted. Intense fragmentation of rock promotes entrainment by erosion. This in turn states a strong argument for the denudational efficacy of large bedrock landslides compared to other suppliers of sediment to the fluvial network such as hillslope slumping and soil creep. Even in their final, degraded and dissected stage, landslide deposits constitute valuable natural archives that, like many other sediments, may carry hitherto unrecognized environmental signals, such as e.g. the water content of the material during runout. However, the interior of giant rockslide deposits has not been systemized stratigraphically, which has somehow confounded comparison of field evidence, recognition of typical facies and correct interpretation of origin an effects. This need for systematization is addressed in Chapter 2 of this thesis.

1.2.2 Catchments: Manageable units of averaged denudation

Research on denudation rates at the catchment scale inevitably will have to inspect the study area for land- or even rockslide contribution because slope failure events may significantly and prolongedly distort sediment flux, and therefore patterns and rates of (cosmogenic-nuclide derived) denudation rates. Studies that attempted to quantify this influence of landslides on the pattern of cosmogenic-nuclide derived basin-averaged denudation rates came up with the notion that bedrock (or deep-seated) landsliding can have significant diluting effects (on nuclide abundances) that, however, generally should decrease with increasing catchment size (Niemi et al., 2005; Yanites et al., 2009).

Regional inventories of basin-averaged denudation rates have been put together in the last ~20 years, attempting to unravel denudational patterns of landscapes and their relationships to the variety of potentially underlying mechanisms, e.g. rock uplift (Scherler et al., 2013; Wittmann et al., 2007); differences in lithology (Chapter 3; Palumbo et al. (2010b)); climate variations (Moon et al., 2011; Riebe et al., 2001), which may be mimicked by vegetation (Torres Acosta et al., 2014); characteristics of topography (Montgomery and Brandon, 2002; Ouimet et al., 2009; Willenbring et al., 2013); or any combination of these factors (Bierman et al., 2005; Godard et al., 2014). Interestingly, most of these studies—and therefore also the geomorphic concepts that are based on these—come mainly from humid mountain belts. Hence, this study is strongly motivated by the need to transfer these concepts to arid environments of which the Transhimalaya is outstanding in both topographic steepness and aridity.

The pronounced change in topography between the highly elevated, and gently sloping landscapes of the Tibetan Plateau and its steep, rugged and mainly dissected Himalayan fringe is what strikes one's eye first when looking at an digital elevation model of High Asia (Fielding et al., 1994). The Tibetan Plateau has an average elevation of more than >4.5 km above sea level (a.s.l.) and its surface may have maintained this elevation since at least Eocene times (Decelles et al., 2007; Rowley and Currie, 2006; van der Beek et al., 2009; Wang et al., 2008). Consequentially scientists have been riveted by the circumstance that Earth's greatest orographic plateau managed to withstand dissection and considerable headward incision by Asia's major rivers, e.g. by the Indus, which may be draining the plateau margin since early to mid-Miocene times (Clift, 2002; Sinclair and Jaffey, 2001). Proposed mechanisms of plateau margin preservation have invoked tectonically forced formation of internal drainage (Sobel, 2003), glacial stabilization due to abundant blocking of the drainage network by large glacier dams (Korup and Montgomery, 2008), repeated channel damming, and concomitantly paused river incision, by large mass wasting events (Korup, 2006; Korup et al., 2006; Ouimet et al., 2007) or rock uplift locally compensating for pace of erosion (e.g. Bendick and Bilham, 2001; Lavé and Avouac, 2001). Zeitler et al. (2001) consequentially called for assessing *"the diverse ramifications of synorogenic erosion and to design field studies to determine its significance in collisional orogenesis"*.

1.2.3 Orogen: The big picture of denudation

In order to understand and quantitatively predict denudation from environmental metrics, denudation rate's covariance with various topographic, tectonic, and climatic predictors has been the focus of many an investigation (Aalto et al., 2006; Montgomery and Brandon, 2002; Ouimet et al., 2009; Summerfield and Hulton, 1994) though with varying and partly inconsistent success. The ongoing debate about the contribution of specific landscape units to Earth's denudation has led to controversial results recently (Larsen et al., 2014; Warrick et al., 2013; Willenbring et al., 2013). While Willenbring et al. (2013) postulate that roughly half of denudation's variance in their global data set can be explained using topography with only mean slopes of ~200 m km^{-1}, Larsen et al. (2014) oppose that more than half of total global denudation occurs on topography's steepest ~10%.

These contrasting views are emblematic of our unsatisfactory understanding of the rates and spatial patterns of landscape downwearing driven by the interplay of tectonics, climate and erosion, that together shape Earth's surface. Consequentially the search is still on for reliable and robust environmental predictors of denudation rates.

1.2.4 Research Questions

The three different spatial scales that have been reviewed briefly above link to three overarching research questions that address recent gaps in our understanding of denudational processes in the Himalaya-Tibet orogen:

1. *Valuable snapshots: What can the internal sedimentology of giant rockslides reveal about their runout processes and triggering mechanisms?*
2. *Active or inactive: Can basin-averaged denudation rates unveil the erosional state of the western Tibetan Plateau margin?*
3. *Tectonics, climate or topography: Do functional relationships between denudation rate and predictors exist that are independent of observation timescale?*

Addressing **Research Question 1** in Chapter 2 we investigate the internal sedimentology of chaotic deposits from giant (>10^6 m^3) rockslides, offering a comprehensive overview on the occurrence of rock fragmentation and frictional melt at eight Himalayan and eleven non-Himalayan sites. Landslides have—if sufficiently large when compared to the drainage area that is affected by their occurrence— the potential to distort local patterns of denudation (e.g. Korup et al., 2004), to significantly modulate cosmogenic-nuclide derived basin-averaged denudation rate estimates (e.g. Kober et al., 2012; West et al., 2014), to force fluvial networks to respond by aggradation and/or incision (e.g. Korup et al., 2006), and to bias magnitude-frequency relationships in landslide-related data inventories (e.g. Hovius et al., 1997). Our study aims to broaden our knowledge on triggers, occurrence, and appearance of past giant-rockslide events. To achieve this, we systematically review previous research on sedimentary aspects of giant rockslides deposits, and summarize our findings in an idealized stratigraphic column. We review sedimental assemblages from large rock-slope failures on marco- and microscopic scale, compare the grain-size distribution of giant-rockslide derived samples to those from impact breccia and fault gouge, and carry out Mössbauer spectroscopy on rockslide-derived frictionite samples with a view towards promoting a systematic knowledge basis on the sedimentology of terrestrial mass-wasting deposits.

Tackling **Research Question 2**, Chapter 3 provides some of the first quantitative constraints on the denudational pattern in the Transhimalayan high-altitude desert of Zanskar and Ladakh, NW India, which lies on the margin of the western Tibetan Plateau. Such data are direly needed to understand and explain the way that major rivers, like the Indus, incise into this part of the Tibetan Plateau. In the upper Indus valley along a ~320-long river stretch we test the hypothesis whether the most prominent knickpoint that marks the edge of the western Tibetan Plateau, is also a location of aggressive fluvial incision, and hence high denudation rates. For this purpose we set up a new inventory of 33 basin-averaged cosmogenic-nuclide derived denudation rates from Indus tributary river sediments, based on the assumption that trunk river incision sets the pace for drainage-basin wide denudation rates in its tributaries. We also use the sediment samples for petrographic analysis and evaluate their heavy-mineral assemblages for deriving short-term denudation-rate estimates, which are based on sediment yields from river gauging. We compare these modern estimates to the millennial denudation rates inferred from the concentration of cosmogenic ^{10}Be in these sediment samples, and to reported long-term exhumation rates from thermochronometers to embed our results into the geological longer-term context.

Referring to **Research Question 3**, Chapter 4 looks into the problem whether cosmogenic-nuclide (CN) derived basin-averaged denudation rates covering large parts of the Himalaya-Tibet orogen can be meaningfully predicted from a range of climatic, tectonic or topographic candidate metrics. For this purpose we compiled an inventory of 297 basin-wide ^{10}Be concentrations from the Himalaya-Tibet orogen, which we harmonized and translated to denudation rates. Emphasizing the well-documented problem of process rates that scale with observation timescale we hypothesize that any meaningful correlation between cosmogenic-derived ^{10}Be denudation rate and predictor should be timescale-independent, i.e. unaffected by any systematic bias. Against this background we test the suitability of 26 candidate predictors by (a) using the most prominent environmental metrics identified by principal component analysis, and (b) looking at denudation rate's full response distribution to these, using quantile regression analysis. Finally, we discuss ways of predicting denudation rates on the basin scale using topographic predictors such as averaged catchment channel steepness, which emerged as the most promising predictors from our analysis.

1.3 Study area

Broadly speaking, the Himalaya-Tibet orogen consists of the vast and on average >4.5 km elevated Tibetan Plateau, and its mountainous surroundings, of which the Himalaya is the most prominent (Fig. 1.5). Taken together these orogens constitute not only the lion's share of High Asia, but also >80% of Earth's topography above 4 km a.s.l. (Fielding et al. (1994); Fig. 1.5). The Himalaya arches for >2,500 km from the western Himalayan syntaxis at Nanga Parbat to the eastern Himalayan syntaxis of the Namche Barwa Region, and fringes the Tibetan Plateau to the south.

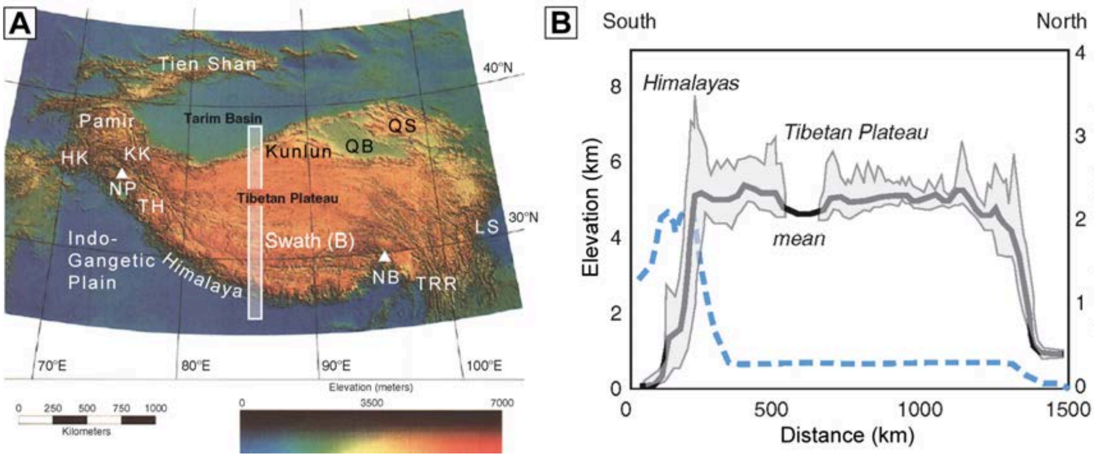

FIGURE 1.5: A) Topography of High Asia from 90-m SRTM data (LS = Longmen Shan; TRR = Three Rivers Region; NB = Namche Barwa, eastern Himalayan syntaxis; TH = Transhimalaya; NP = Nanga Parbat, western Himalayan syntaxis; KK = Karakoram; HK = Hindu Kush; QB = Qaidam Basin; QS = Quilian Shan). White-framed rectangle depicts location of B) 100 km wide N–S swath profile across the Tibetan Plateau. Solid black line is mean topography, grayish envelope is bound by max and min topography, respectively. Note table-shape of the Tibetan Plateau with striking edges and prominent increase in relief and elevation towards the (southern) plateau margin(s). Dashed line is mean annual precipitation amount that decays markedly at the orographic barrier of the Himalayan flanks (Anderson and Anderson, 2010), and after (Fielding et al., 1994)).

Geology

The Himalaya-Tibet orogen—Earth's greatest mega-landform—witnesses the ongoing Indo-Asian continent-continent collision and is often taken as a prime example for this type of tectonic plate convergence. The emergence of the Himalaya-Tibet orogen and its elevated situation since at least Eocene times (Decelles et al., 2007; Rowley and Currie, 2006; Wang et al., 2008) are closely linked to the closure of the Tethyan ocean by the northward drifting Indian continental plate. As a result, Tethyan sediments today form large parts of the Transhimalayan ranges, which are bounded by High Himalayan high-grade metamorphic rocks to the south and by the Indus-Tsangpo Suture Zone (ITSZ), followed by the Kohistan-Ladakh Arc complex to the north (DiPietro and Pogue, 2004; Yin, 2006). The regional geology of the Transhimalayan Zanskar and Ladakh ranges (e.g. Brookfield, 1983; Henderson et al., 2010; Kirstein, 2011; Searle et al., 1990) is described in detail in Section 3.2. Heading southward from the >6-km high High Himalaya, and crossing the tectonic boundary of the Main Central Thrust, low-grade metamorphic rocks of the Lesser Himalaya succeed building up a topography of up to 3 km elevation. Even farther towards the south, and crossing the Main Boundary Thrust the up to 1.5-km high Sub-Himalayan molassic hills represent the deformed and uplifted debris from older phases of the orogeny. These hills in turn are divided from the southward following Indo-Gangetic plain by the Main Frontal Thrust, where the bulk of contemporary deformation is being measured (DiPietro and Pogue, 2004; Yin, 2006).

Climate

The Himalaya-Tibet orogen constitutes an effective orographic barrier due to its considerable elevation and topographic relief (Barry (2008); Fig. 1.5). The dominant air masses are brought to the region by mainly two atmospheric circulation systems, the Westerlies of the temperate zone, and the Asian monsoon(s). Large parts of the Himalaya-Tibet orogen—especially the E, S- and central regions—are not or just slightly affected by the Westerlies, which are shifted (sub)parallel to the longitudinally migrating Innertropical Convergence Zone (ITCZ). Shifts towards the south during winter are driven by a large and stable high-pressure area situated solidly above large continental reaches of Asia, and shifts towards the north during northern-hemisphere summer are featured by a distinct low-pressure area that spatially coincides with the Tibetan Plateau (Barry and Chorley, 2003; Clift and Plumb, 2008). This spatial coincidence is a result of the high elevation vast heating surface of mainly the Tibetan Plateau causing unstable atmospheric layering, which is attracting other air masses to migrate to this region (Barry and Chorley, 2003). The most important atmospheric circulations in this regard are the

Asian monsoons, bringing moisture and heat from the Indian Ocean—mainly the Bay of Bengal—along the southern Himalayan front. These moisture-laden air masses, when forced against the Himalayan mountain front, have to ascend under moist-adiabatic conditions. As a result, mean annual rainfall amounts of 2–4 m occur, typically reaching maximum values at elevations < 3–4 km (Bookhagen and Burbank, 2010; Putkonen, 2004), leading to much lower mean annual precipitation in the Transhimalayan ranges in the rain shadow of the High Himalaya.

FIGURE 1.6: Post-flood field pictures from Indus tributaries draining the Ladakh batholith document the geomorphic impacts of the abnormal rain storm clusters that hit parts of the Indus valley in summer 2010. A) Car-sized bolder has been moved and rotated by debris flow or hyper-concentrated flow. B) This $\sim 6 \times 6$-m channel has been incised during peak discharge of the flood event in the Tharu catchment (Fig. 3.1). Residents reported massive debris flows that were followed by a clear-water flood. C) Cleared post-flood channel bed of the adjacent Nimu catchment is indicator of a clear water flood succeeding the debris flows. Note that channel walls and adjacent reaches (D) are covered with jetcrete-like flood deposits (Pictures by courtesy of Jan Blöthe).

However, during abnormal monsoon years (Bookhagen et al., 2005a), the arid to semi-arid Transhimalayan high mountain deserts may receive rainfall amounts equalling up to the half of the annual amount of ~ 90 mm in just an hour (Hobley et al., 2012; Spate et al., 1967). In summer 2010 such an extraordinary event (Fig. 1.6), with an estimated return period >100 yr, caused devastating debris flows and flash floods with peak discharge estimates on the order of >100 times the bankfull discharge (Hobley et al., 2012;

Juyal, 2010; Thayyen et al., 2012). Besides reports from such extraordinary events, meteorologic data from the Transhimalayan Zanskar and Ladakh ranges are very sparse. Mean annual precipitation generally tends to be lowest near valley bottoms, with ~40% of annual precipitation during summer, and some 30% during winter months as snowfall (Burbank and Fort, 1985; Flohn, 1958; Müller et al., 1996; Spate et al., 1967). The regional climate is characterized by moderate amplitudes in diurnal temperatures, but ~40-K amplitudes between monthly averaged extreme values of a year (for values see BIO02 and BIO07 in Table C.6). The prevailing regional aridity is reflected in the barren land where most vegetation growth is possible in irrigated oases only. As a result, the landscape is widely covered with clasts from weathering of the sedimentary Zanskar Ranges and with grit curtains from granitic disaggregation of the Ladakh Batholith, largely lacking any soil cover in a pedologic sense.

Late Quaternary glaciations

The geomorphology of Zanskar and Ladakh has been described in a general manner repeatedly (Cunningham, 1854; Fort, 1983; Osmaston, 1994), though often focussing on the conspicuous differences between the sedimentary Zanskar Ranges and the Ladakh Batholith (Dortch et al., 2011c; Hobley et al., 2010; Jamieson et al., 2004), which flank the upper Indus River for several hundred kilometers. Some studies examined deposits of Quaternary ages aiming to evaluate their paleoclimatic significance (Blöthe et al., 2014; Pant et al., 2005). Others looked into the geomorphic legacy of past glaciations (Burbank and Fort, 1985; Drew, 1873; Osmaston, 1994), partly aiming to set up a regional glacial chronology (Achenbach, 2010; Damm, 2006). Radiometric dating helped to constrain ages of glacial deposits in the upper Indus valley, including some of the oldest dated glacial successions in the Himalaya-Tibet orogen, partially yielding ages of >430 kyr (Owen et al., 2006). From these data Owen et al. (2006) derived five glacial stages (Fig. 1.7) that may have promoted glaciers of seemingly restricted extent; advancing just about ~15 km from their present extent during the last ~430 ka. Further evidence for rather restricted glaciation, limited to small regional ice bodies, comes from the Zanskar Ranges (Hedrick et al., 2011; Taylor, 2000). Currently, still ~6% of the upper Indus catchment are covered by (predominantly small cirque) glaciers.

The spatio-temporal pattern of past glaciations gets much more complex (and debated) with decreasing scale. No general scientific consensus exists concerning the timing, extent and climatic forcing of past glaciations in the Himalaya-Tibet orogen (Gillespie and Molnar, 1995; Owen et al., 2008), though workers largely agree in the point that the LGM in the Himalaya-Tibet orogen predated the maximum extents of the northern-hemisphere ice sheets (Benn and Owen, 1998; Gillespie and Molnar, 1995; Owen et al., 2008, 2005).

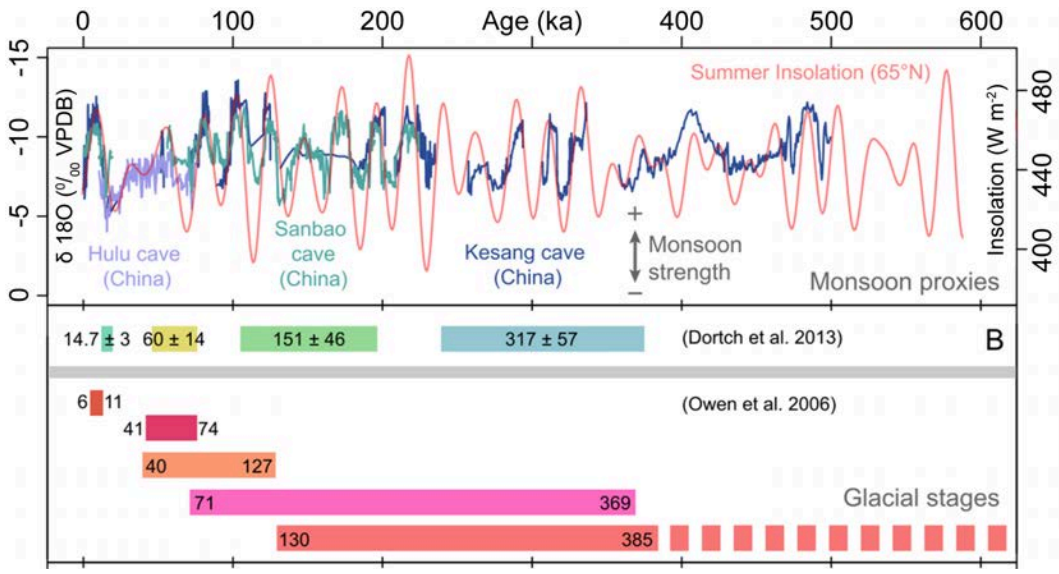

FIGURE 1.7: Synopsis of monsoon proxies and Transhimalayan glacial stages (from Blöthe et al. (2014) and references therein). A) Compilation of δ^{18}O data from various cave records (China) (after Cheng et al. (2012); Wang et al. (2008); Wang (2001)); alternating solid red line is mean summer insolation at 65 ° N (after Berger and Loutre (1991)). B) Simplified glacial chronology for the Ladakh range (after Dortch et al. (2013); Owen et al. (2006).

Monsoonal influences, generally decreasing towards the Tibetan interior, are thought to correlate with Himalayan glaciations, with strengthening monsoon coinciding with periods of deglaciations (Overpeck et al., 1996).

However, recent research has suggested that repeated phases of 10^1–10^2-m sediment aggradation and evacuation on ~10^4-yr scales in the Transhimalayan ranges may not exclusively correlate with monsoon proxies (Blöthe et al., 2014). Instead, Pleistocene glacial cycles could be reasons for—at least two—episodes of massive valley infilling and incision, with highest densities of landform ages at before ~200 ka and at ~50 to ~20 ka. Comparatively old sedimentary features testify to a high landscape preservation potential in the rain shadow of the High Himalaya, where vast fill-terrace bodies have been dated to 10^5-yr ages (Blöthe et al., 2014; Scherler et al., 2014). Also, the preservation of the oldest so-far dated glacial deposits of the Himalaya-Tibet orogen, yielding ages of up to ~430 ka (Owen et al., 2006), may be a result of the prevailing aridity and concomitant low denudation rates (Chapter 3, Table 3.3) (Dortch et al., 2011c; Garzanti et al., 2005). Both, the regional pattern of basin-averaged denudation rates from the upper Indus valley (Chapter 3, Fig. 3.3) as well as the Himalaya-Tibet orogen-wide pattern (Chapter 4) point to distinct denudational gradients across the Tibetan plateau margin, where rates generally decrease towards the plateau interior, ranging between 8 mm kyr^{-1} and 6,135 mm kyr^{-1} for the entire Himalaya-Tibet orogen (Chapter 4, Table C.4).

1.4 Some methodical remarks on cosmogenic nuclides

This thesis methodically relies to a great extent on large data sets of cosmogenic-nuclide (CN) derived basin-averaged denudation rates. Acknowledging that, this section briefly reviews cosmogenic nuclide applications, and particularly basin-averaged denudation rates. Since the advent of CN applications in geosciences (e.g. Lal, 1991; Marti and Craig, 1987; Nishiizumi et al., 1990; Phillips et al., 1986, 1990a), CN-based dating techniques fill a temporal gap between recent historical denudation estimates from sediment gauging and very long-term approaches allowing to derive estimates of landscape lowering from exhumation rates (Fig. 1.8; Dunai (2010); Summerfield (2005)). Cosmogenic nuclides are permanently produced by the interaction of cosmic rays, i.e. mostly secondary high-energy charged particles, and mineral grains of the Earth surface. Thus, nearly any geological surface that is exposed to cosmic rays can be dated by measuring the nuclide abundance that has been produced and accumulated *in situ* (Dunai, 2010). Depending on the half-life of the nuclide used, CN-based dating techniques cover the entire Quaternary, and even periods beyond.

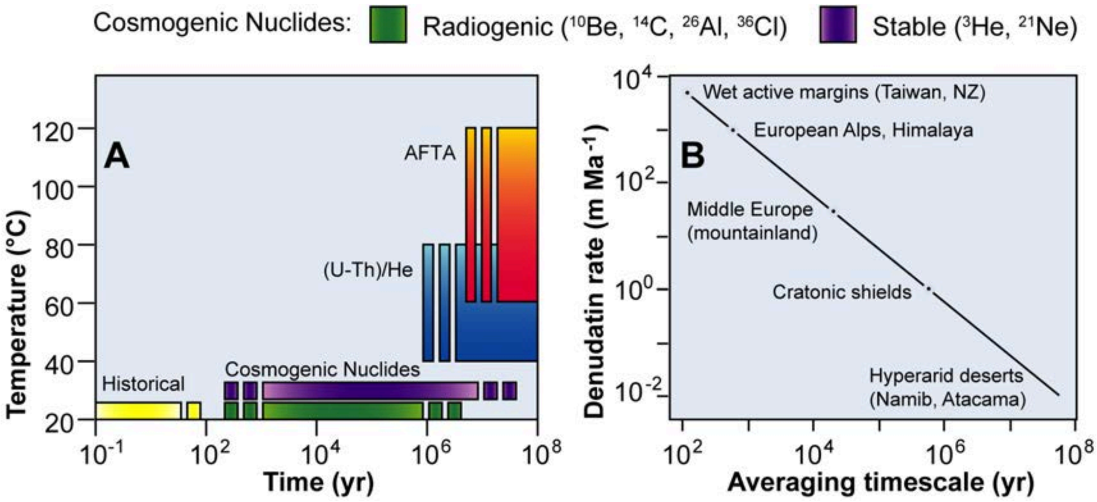

FIGURE 1.8: A) Selected methods available for the quantification of denudation rates. Cosmogenic nuclide (CN) applications fill a temporal gap between long-term thermochronometer-derived estimates of landscape downwearing and very short-term estimates from sediment gauging; covering the entire Quaternary period and even beyond (modified by courtesy of Roderick Brown, University of Glasgow), Temperatures on y-axis refer to closure temperature of AFTA and (U-Th)/He-systems; B) Cosmogenic-nuclide derived denudation rate and averaging timescale are inversely correlated by method design, with higher denudation rates causing commensurately lower averaging timescales, and vice versa (after Dunai (2010); von Blanckenburg (2005)).

From a geomorphologist's point of view the major benefits of cosmogenic nuclide applications are that they (a) capture geomorphic processes on timescales that these operate on, (b) are produced near Earth surface what makes them sensitive to changes in morphology of the surface, (c) are insensitive to short-term disturbances to some degree, i.e. that the time delay between actual change in erosion and a change in CN-derived denudation rate can be used to estimate long-term benchmark erosion rates behind the rapid changes in erosion (Hewawasam et al. (2003); Vanacker et al. (2007b); Fig. 1.9). By now cosmogenic nuclides afford a variety of robust and tested applications as for example *exposure dating*, based on continuous nuclide accumulation (e.g. Heyman et al., 2011; Stone et al., 1998); *burial dating*, based on differential decay of different CN (e.g. Fabel et al., 2002; Granger et al., 2001); the determination of *rates of uplift*, based on the known exposure history of a landform (Cyr et al., 2010; Gosse and Stone, 2006); the quantification of *soil dynamics*, like soil production, mixing, or inflation (e.g. Braucher et al., 1998; Heimsath et al., 1997); and the estimation of *erosion and denudation rates* (Cockburn and Summerfield, 2004; Dunai, 2010; von Blanckenburg, 2005; Walker, 2005). This is why during the last ∼20 years cosmogenic nuclides have become popular and multi-purpose tools for investigating the past ∼2.6 Ma, a period in Earth's evolution that has been characterized by repeated pronounced climatic fluctuations (e.g. Augustin et al., 2004; Thompson et al., 1997; Winograd et al., 1992) causing the interplay of glaciations and deglaciations (Williams et al., 1998).

These climatic fluctuations also repeatedly influenced downwearing of Earth's surface by fueling distinct erosional players, e.g. glaciers during glacial stages, while concomitantly dampening the effectiveness of others. Figure 1.9 illustrates how CN-derived denudation rates trace the ups and downs of rates of landscape downwearing. However, CN-denudation rate and averaging timescale are inversely correlated (Fig. 1.8B), with high rates implying short averaging timescales and vice versa (Dunai, 2010; von Blanckenburg, 2005). This has implications for the sensitivity of the method to changes in denudation rates. Thus alternations of forcing to landscape downwearing on 10^4 to 10^5-yr scale will cause different response characteristics of comparatively high and low CN-derived denudation rates, respectively. High denudation rates will imply timescales that may be sufficiently short to resolve these disturbances (Fig. 1.9A), while the same disturbances will be largely overlooked by low CN-derived denudation rates with concomitant longer averaging timescales (Fig. 1.9B).

Cosmogenic ^{10}Beryllium (^{10}Be) is an abundant radionuclide that enjoys great popularity in geomorphology due to the fact that the nuclide-bearing quartz mineral is nearly ubiquitous. The crucial ^{10}Be-based application for this thesis is the calculation of basin-averaged denudation rates from ^{10}Be (Bierman and Steig, 1996; Brown et al., 1995; Granger et al., 1996). This method is based on the assumption that, keeping in mind some methodical restrictions that are listed below, a single river sand sample is representative of the entire drainage area that is source of its grains. Consequently, the average

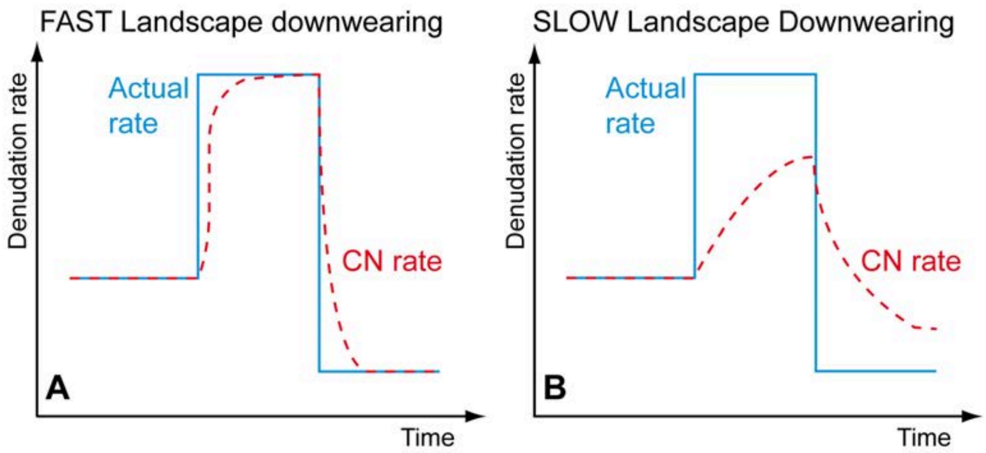

FIGURE 1.9: Influence of hypothetical disturbances to CN-derived denudation rate. Solid blue line is actual rate of landscape downwearing, which is modulated by external disturbance (i.e. fluctuation of climate), dashed red line is CN-derived denudation rate that mimics actual rates in a damped manner. A) Model for fast landscape downwearing, B) model for slow landscape downwearing (after (Bierman and Steig, 1996; Brown et al., 1998; von Blanckenburg, 2005) and modified by courtesy of Alexandru T. Codilean, University of Wollongong).

nuclide concentration $\bar{C}$ in the sample should represent a mean of the entire drainage basin—in a large statistical sample of some 10^6 to 10^8 grains—too. The average nuclide concentration $\bar{C}$ in the sediment can be expressed as

$$\bar{C} = \frac{\bar{P}}{\lambda + \bar{\rho}\bar{\epsilon}/\Lambda}$$

where $\bar{P}$ is the averaged production rate, λ is the nuclide decay constant, $\bar{\rho}$ is the mean rock density, $\bar{\epsilon}$ is the basin-averaged erosion rate, and Λ is the rock absorption mean free path. However, the calculation of basin-averaged nuclide concentrations requires the compliance of some assumptions, which have to be met to correctly to calculate denudation rates. These (abbreviated) assumptions are that:

1. Catchment erosion is constant over the averaging timescale (this is a landslide-sensitive supposition).
2. All lithologies contribute to the sample proportional to their occurrence in the catchment.
3. The target mineral (in this case quartz) has the same grain size over all lithologies.
4. Catchment denudation happens mainly at Earth's surface, and not by deep subsurficial weathering.
5. The averaging time of denudation is shorter than half-life of nuclide used, and

6. the timescale of sediment transport and storage is shorter than the timescale of erosion (Dunai, 2010).

If these preconditions are met adequately, ^{10}Be offers a methodical benefit for certain geomorphic applications since it has a comparatively long half-life of 1.387±0.012 Ma (Chmeleff et al., 2010; Korschinek et al., 2010). Additionally the analytical effort for this often used nuclide has been decreasing during the past years while measurement accuracy could be increased concomitantly (Dunai, 2010). As a methodical novelty in Study II (p. 45ff.) we combine cosmogenic ^{10}Be-derived basin-averaged denudation rates, bulk petrographic analysis and heavy minerals assemblages from the same samples for the first time.

1.5 Author contributions

The studies presented within the framework of this thesis were published in international peer-reviewed journals or are intended to being published adequately:

Study I - Giant rockslides from the inside (p. 24ff.)
This study is published as:
Weidinger, J.T., Korup, O., Munack, H., Altenberger, U., Dunning, S.A., Tippelt, G., and Lottermoser, W. (2014). Giant rockslides from the inside. Earth and Planetary Science Letters, v. 389, p. 62-73.
H.M. and J.T.W. designed the artwork. H.M. designed and conducted particle-size analysis. H.M. contributed to fieldwork, discussions, interpretations and writing the paper.

Study II - Postglacial denudation of western Tibetan Plateau margin outpaced by long-term exhumation (p. 45ff.)
This study is published as:
Munack, H., Korup, O., Resentini, A., Limonta, M., Garzanti, E., Blöthe, J.H., Scherler, D., Wittmann, H., and Kubik, P.W. (2014). Postglacial denudation of western Tibetan Plateau margin outpaced by long-term exhumation. Geological Society of America Bulletin.
All coauthors contributed to this study in advisory manner, with following exceptions: A.R. and E.G. performed bulk-petrographic analysis, M.L. and E.G. conducted heavy mineral analysis.

Study III - Denuding the Himalaya-Tibet orogen: Noise vs. Time (p. 67ff.)
This study is under review as:
Munack, H., Korup, O., Codilean, A.T., Heyman, J., Li, Y., Blöthe, J.H., Kubik, P.W., Denuding the Himalaya-Tibet orogen: Noise vs. Time, at the Geological Society of America's peer-reviewed GEOLOGY journal.
All coauthors contributed to this study in advisory manner, with following exception: A.T.C. recalculated denudation rates for the compiled ^{10}Be data. J.H. conducted ^{10}Be chemical analysis of the samples WTS13401-20.

Given that the three studies forming the core of this thesis are the result of teamwork everything in this thesis is presented from the third person's point of view, plural.

During the time of my PhD I have been contributing also to the following published studies, which are not included in this thesis:

- *Blöthe, J.H., Munack, H., Korup, O., Fülling, A., Garzanti, E., Resentini, A., Kubik, P.W. (2014). Late Quaternary valley infill and dissection in the Indus River, western Tibetan Plateau margin. Quaternary Science Reviews v. 94, p. 102-119.*

- *Sanhueza-Pino, K., Korup, O., Hetzel, R., Munack, H., Weidinger, J.T., Dunning, S.A., Ormukov, C., Kubik, P.W. (2011). Glacial advances constrained by ^{10}Be exposure dating of bedrock landslides, Kyrgyz Tien Shan. Quaternary Research v. 76, p. 295-304.*

- *Scherler, D., Munack, H., Mey, J., Eugster, P., Wittmann, H., Codilean, A.T., Kubik, P.W., Strecker, M. (2014). Ice dams, outburst floods, and glacial incision at the western margin of the Tibetan Plateau: A >100 k.y. chronology from the Shyok Valley, Karakoram. Geological Society of America Bulletin, v. 126, p. 738-758.*

Chapter 2

Study I - Giant rockslides from the inside

Abstract

The growing body of research on large-scale mass wasting events so far has only scarcely investigated the sedimentology of chaotic deposits from non-volcanic terrestrial landslides such that any overarching and systematic terminological framework remains elusive. Yet recent work has emphasized the need for better understanding the internal structure and composition of rockslide deposits as a means to characterize the mechanics during the final stages of runout and emplacement. We offer a comprehensive overview on the occurrence of rock fragmentation and frictional melt both at different geographic locations, and different sections within large ($>10^6$ m^3) rockslide masses. We argue that exposures of pervasively fragmented and interlocked jigsaw-cracked rock masses; basal mélange containing rip-up clasts and phantom blocks; micro-breccia; and thin bands of basal frictionite are indispensable clues for identifying deposits from giant rockslides that may remain morphologically inconspicuous otherwise. These sedimentary assemblages are diagnostic tools for distinguishing large rockslide debris from macro- and microscopically similar glacial deposits, tectonic fault-zone breccias, and impact breccias, and thus help avoid paleoclimatic and tectonic misinterpretations, let alone misestimates of the hazard from giant rockslides. Moreover, experimental results from Mössbauer spectroscopy of frictionite samples support visual interpretations of thin sections, and demonstrate that short-lived (<10 s) friction-induced partial melting at temperatures $>1500\,^\circ C$ in the absence of water occurred at the base of several giant moving rockslides. This finding supports previous theories of dry excess runout accompanied by comminution of rock masses down to μm-scale, and indicates that catastrophic motion of large fragmenting rock masses does not require water as a potential lubricant.

2.1 Introduction

Slope instability is a ubiquitous geological phenomenon and hazard that has attracted an widespread research attention devoted to unravelling the causes, triggers, and consequences of landslides for both society and landscape evolution (e.g. Korup et al., 2010a). The bulk of landslide research has focused on studying the abundance of historic landslide occurrences. Yet the larger and commensurately rarer rock-slope failures—generically referred to here as "rockslides"—may distort considerably the patterns of denudation and hazard of the smaller and more frequent landslides (e.g. Korup et al., 2007; Prager et al., 2007). Previous work on some of the largest ($>10^8$ m^3) rockslides in active mountain belts throughout the world has focused on documenting and characterizing causes, triggers, and the morphology of detachment areas and deposits (Hewitt, 1998). This has primarily been driven by a need to quantify the frequency of such events for hazard appraisals, their relative contribution to denudation and sediment fluxes (Korup, 2012), to back-analyze loss-inducing case studies (Dunning et al., 2007), or to support reinterpretation of glacial chronologies (Reznichenko et al., 2012; Sanhueza-Pino et al., 2011).

Such awareness of the impact of large rockslides relies upon successful detection and detailed surficial mapping (Shea and van Wyk de Vries, 2008). This, however, is complicated by the close resemblance of rockslide deposits to glacial moraines (Hewitt (1999); Fig. A.1), the geometric similarity of rockslide scars to glacial cirques (Turnbull and Davies, 2006), and high rates of erosion that may obliterate geomorphic evidence of rockslide debris in steep terrain particularly. All these factors cumulatively censor our knowledge of past events, necessitating methods that can unambiguously identify large rockslide deposits using persistent or long-lived geomorphic or sedimentological evidence. Surprisingly, the literature on catastrophic long-runout landslides in non-volcanic settings contains only few studies that systematically examine sedimentary and petrographic deposit characteristics (Dunning and Armitage, 2011; Dunning et al., 2005; Wassmer et al., 2004). Yet these may yield valuable insights into dynamics during the final stages of rockslide motion and emplacement (Crosta et al., 2007; Davies and McSaveney, 2009; Erismann and Abele, 2001; Hewitt, 1999; Morris and Herbertson, 1996; Schramm and Weidinger, 1998; Wassmer et al., 2004). Together with petrography this information may also serve as a means to uniquely distinguish large rockslide deposits from glacial or tectonic features (Weidinger and Korup, 2009).

Motivated by these studies we present a framework for these studies by summarizing an idealized stratigraphic column, based on a review of sedimentological and petrographic work augmented by new field mapping of macro- and microscopic features of deposits from giant rockslides. We hypothesize that recognizing dynamically consolidated micro-breccias and frictionite (Maddock, 1986) yields unequivocal evidence of catastrophic rock-slope failure, even where the initially more widespread and characteristic rockslide-deposit morphology has been altered beyond recognition by erosion. Our objective is to highlight means to test these field interpretations with new constraints on the duration and conditions of catastrophic rockslide motion from field and laboratory data on pervasively fragmented and partially molten rockslide debris.

2.2 Study sites and methods

We reviewed and summarized field data on the sedimentology and petrography of deposits from giant rockslides in the European Alps, the Himalaya, the Andes, the Tian Shan, Taiwan, the Rocky Mountains, and the New Zealand Southern Alps (Table 2.1). All these rockslide deposits are strongly dissected, thus allowing investigation of their interior structures (Fig. A.1). For some we mapped the degree of fragmentation and the orientation of deformation structures along basal outcrops in detail. We analyzed petrographic features macroscopically in the field, and microscopically in thin section Fig. 2.1. We further conducted X-ray diffractometry (XRD) and Mössbauer spectroscopy to quantify the conditions of frictional melting including the (a) duration of the melting process; (b) temperatures of the melt; (c) response of the involved minerals to frictional heating; and (d) evolution of frictional non-eutectic melt generation. We used microprobe and XRD to analyze the chemical and mineralogical compositions of the frictionite, i.e. highly fragmented and partially molten material, obtained from the base of two rockslide deposits (i.e. Tsergo Ri, Nepal Himalaya; and Köfels, Austrian Alps; Table 2.1), as well as their source rocks. We also measured the particle-size distribution of rockslide micro-breccias from various locations, and compared these with data from fault-zone (Billi, 2005; Billi and Storti, 2004), and impact breccia that we collected from the Nördlinger Ries area near the towns of Altenbürg and Otting, Germany.

2.2.1 Mössbauer spectroscopy

Mössbauer spectroscopy is the method of choice for the detection of small amounts of Fe in various valence states within a given material. Non-magnetic spectra are normally composed of one or more line doublets whose central position on the energy scale (mm s^{-1}) is designated as an isomer shift highly indicative of the iron valence state. Their intensity, expressed as relative absorption [%] with respect to the background, times the line width at half peak maximum, i.e. the peak area, yields the relative amount of the

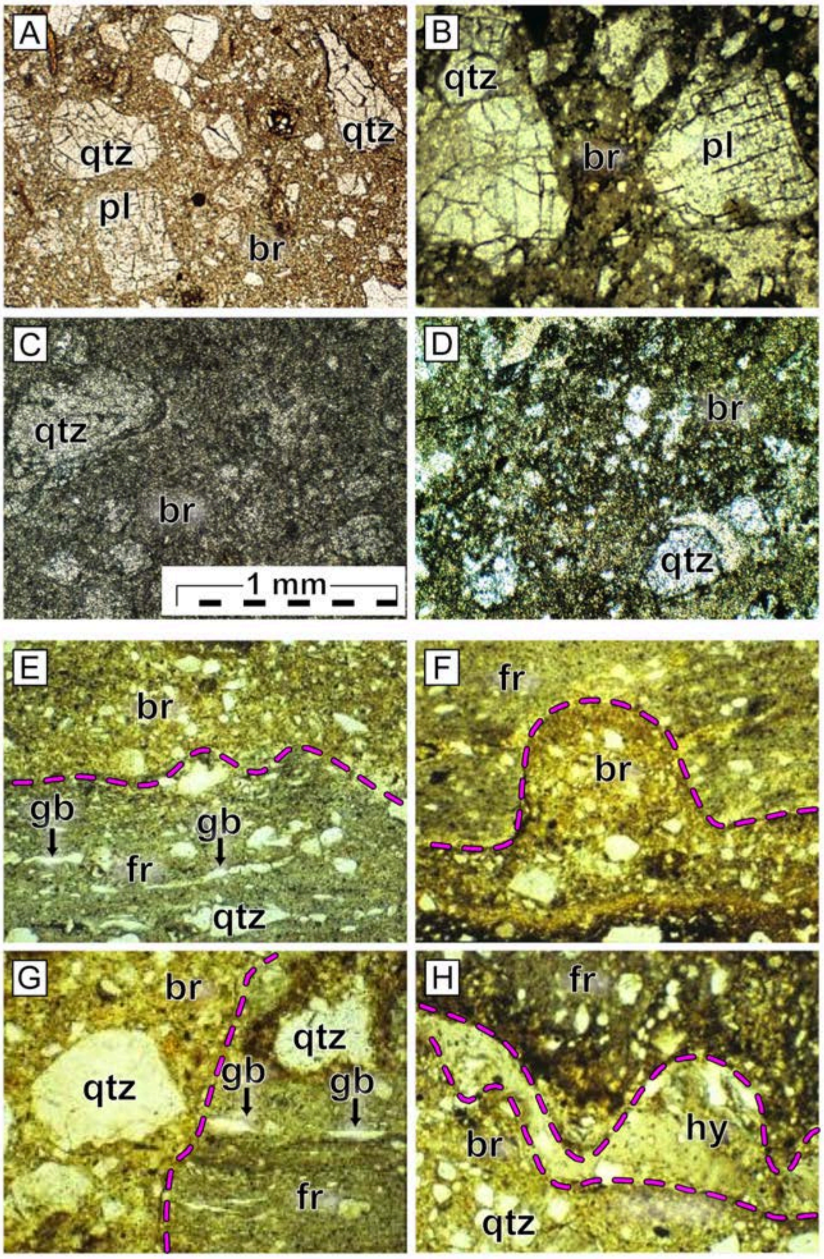

FIGURE 2.1: Thin sections of landslide micro-breccias with shattered mineral grains and jigsaw cracks: A) and B) Angular broken and shattered quartz (qtz)- and plagioclase (pl) grains in matrix of fine-grained breccia (br), Dzongri. C) and D) Rounded but almost powdered quartz grains (qtz) supported by matrix of powdered breccia (br), Lukla. E) to H) Thin sections of frictionite (fr) in contact with breccia (br) along primary shear planes, Tsergo Ri; quartz clasts (qtz) within the breccias are angular due to brittle fragmentation whereas in frictionite they are sub- or even well rounded, partly even lenticular due to fluidal and melting texture; gb = gas bubbles (mostly lenticular) in fr, hy = pure glass layer in contrast to partially melted zone with clasts. Scale bar in C) is same for all panels.

Table 2.1: Characteristics of selected rockslide deposits with documented internal sedimentology and petrography. Locations of rockslides can be explored virtually using the ∗.kml-file provided within the supplementary information of Weidinger et al. (2014).

No.	Location	LAT [°N]	LON [°E]	Dominant rock type	MB ?	F ?	Tectonic unit	Deposit volume [10^9 m^3]	References
1	Köfels, Ötztal, AT	47°06'36.00"	10°55'48.00"	Granite-Gneiss	Y	Y	Older crystalline Austro-Alpine nappes	3.3	Brückl et al. (2001)
2	Flims, Rhine, CH	46°49'12.00"	9°18'0.00"	Limestone	Y	N	Helvetic nappes	9 to 12	Wassmer et al. (2004) Pollet and Schneider (2004)
3	Tschirgant, Inn, AT	47°13'12.00"	10°50'24.00"	Limestone, Slates, Marl	N	N	N Calcareous Alps	0.2	Prager et al. (2007)
4	Hetzau, Almtal, AT	47°45'59.73"	13°58'2.99"	Limestone, Dolomite	Y	N	N Calcareous Alps	0.45	van Husen et al. (2007)
5	Val Pola, Valtellina, IT	46°22'40.99"	10°20'07.16"	Gneiss, Gabbro, Diorite	N	N	Central Italian crystalline Alps	0.041	Crosta et al. (2007)
6	Kokomeren rockslide, KG	41°55'48.00"	74°13'48.00"	Gneiss	Y	N	Late Ordovician-Silurian Struct. Complex, Tian Shan	1	Strom and Abdrakhmatov (2004b)
7	Arashan, Alamyedin, KG	42°36'34.45"	74°39'54.25"	Granite, Meta-seds.	Y	?	Cambrian-Tremadosian Struct. Complex, Tian Shan	0.015	Strom and Abdrakhmatov (2004a)
8	Braga, Marsyandi, NP	28°38'60.00"	84° 4'48.00"	Limestone, Slates, Sandstone	N	N	Tibetan Sed. Sequence	5	Weidinger (2006)
9	Latamrang, Marsyandi, NP	28°31'48.00"	84°18'36.00"	Gneiss, Quartzite	N	N	Higher Himalayan Cryst.	5.5	Weidinger (2006)
10	Tsergo Ri, Langthang, NP	28°13'54.97"	85°36'11.10"	Migmatite, Gneiss, Leucogranite	Y	Y	Higher Himalayan Cryst.	10	Weidinger et al. (2002) Takagi et al. (2007)
11	Khumjung, Dudh Kosi, NP	27°49'48.00"	86°43'12.00"	Migmatite, Gneiss	Y	Y	Higher Himalayan Cryst.	2.1	Korup and Weidinger (2011)
12	Dzongri, Ratong Chu, IN	27°28'48.00"	88°10'12.00"	Leucogranite, Gneiss	Y	Y	Higher Himalayan Cryst.	2.5	Weidinger and Korup (2009)
13	Lukla, Dudh Kosi, NP	27°41'8.97"	86°43'28.92"	Gneiss	Y	N	Lesser Himalayan Cryst.	1	(Weidinger, 2010)
14	Khalsar, Shyok, IN	34°30'24.28"	77°42'58.78"	Granite	Y	Y	Karakoram Terrane Granitoides	>2	This study
15	Pangong North, Shyok, IN	34°14'37.82"	78° 4'56.37"	Meta-seds.	N	N	Pangong migmatites and Granodiorite	0.2(?)	This study
16	Chiufener rockslide, TW	23°57' 31.09"	120°50'29.74"	Shale, Siltstone	?	Y	Western Foothills Province	0.08	Lin et al. (2001)
17	Falling Mountain, Otehake, NZ	42°53'46.57" (S)	171°41'3.92"	Greywacke, Argillite	N	N	Torlesse Terrane	0.06-0.07	Dunning and Armitage (2011)
18	Arequipa debris avalanche, PE	16°24'1.91" (S)	71°26'1.68" (W)	Complex volc. deposit	Y	Y	Arequipa Terrane	>10?	Legros et al. (2000)
19	Heart Mountain, US	44°45'41.81"	109°29'52.59" (W)	Carbonate rocks, Marble at White Mtn.	Y	Y	Wyoming Province (Madison Group)	?	Craddock et al. (2009)

MB?, F? = Micro-breccia (MB), Frictionite (F) have been described for resp. exposure (Y = yes, N = no, ? = no information) different Fe ions. The Fe(III)/Fe(II) ratios have a detection limit of ∼1 wt.%, from which we derive the oxidation properties of the sampled frictionite.

Samples were carefully crushed to powder in order to avoid contamination by Fe(III), and transformed to a Mössbauer absorber with 5 mg iron cm^{-2}. The samples were then mounted in an atmospheric pressure Mössbauer furnace and exposed to a nominal 1.8 GBq ^{57}Co/Rh source (Wissel GmbH) providing the ^{57}Fe γ-rays for the resonant absorption in the sample. The source was mounted on a driving unit with constant acceleration (Halder Elektronik GmbH, time mode arrangement). Transmitted intensities were recorded with a conventional counter tube, stored in a multichannel analyzer, and fitted with a conventional refinement routine with Lorentzian lines (Lottermoser et al., 1993). The obtained isomer shifts of the refined doublets were characteristic of the occurring Fe ion valence states. In order to evaluate the duration of partial melting during rockslide motion we exposed the unaltered source (bedrock) samples to 800 °C for various periods of time, i.e. 5 min, 1 hr, 2 hr, and 3 hr. Source rock and frictionite from both the Tsergo Ri and Köfels sites were measured at ambient conditions to compare their Fe(III)/Fe(II) ratios.

2.2.2 X-ray diffraction analysis

XRD measurements were done on the both source rock and frictionite powder samples from Köfels and Tsergo Ri (Table 2.1). We used a Philips Expert powder diffractometer with a Paar heating chamber and tube tension/current values of 40kV and 40 mA. The diffractometer has a Bragg-Brentano beam geometry with a divergence slit of 0.5 °. The patterns were recorded in a 2-θ range from 5 and 80 °, at a step width of 0.02 °, and a step time of 6 s. We obtained well-resolved powder patterns that could be attributed to the different phases with high confidence.

2.2.3 Particle-size analysis

We processed 13 micro-breccia samples of various facies (Table 2.1) for particle-size analysis. Due to post-depositional early diagenetic compaction and cementation, ten out of the 13 samples could not be suspended directly, and thus had to be fragmented in a different way. To avoid artificial particle sizes by crushing, we opted for an electrical fragmentation with Selfrag, a Lab system for selective rock fragmentation with a high voltage (`http://selfrag.com`). Only three out of the 13 micro-breccia samples could be suspended without Selfrag processing (Table A.1). Samples were prepared for Selfrag processing by breaking them up mechanically to 2–4 cm fragments. The lowest selectable voltage was chosen for Selfrag processing; the shock-wave strength was set to the lowest possible in order to avoid artificial fragmentation of polycrystalline parent-material clasts by streamlets along crystal boundaries (Table 2.1).

Post-fragmentation microscopic analysis revealed an acceptable fragmentation of macroscopic breccia components with excellent integrity of polycrystalline rock fragments of the parent material, which were cleared of any adherences at the same time. However, parts of the silt and clay fractions still remained coagulated. These nodules were disaggregated by ultrasonic treatment. We found no organic material in the samples. We considered HCl treatment unfavorable due to the potential for destroying parent material. The suspended samples were sieved wet, aiming for particle size classes from <63 μm to >4000 μm (Table A.2). After drying and weighing, two aliquots of each <63 μm fraction were re-suspended in a sodium pyrophosphate solution, and particle size distribution was measured with a Sympatec laser diffractometer. All other particle fractions were weighed (Table A.2). The weight of each particle size class was translated to numbers of equivalent spherical particles according to the procedure described by Billi and Storti (2004) in order to compare the fractal dimension (D) with results from previous studies (Fig. 2.5).

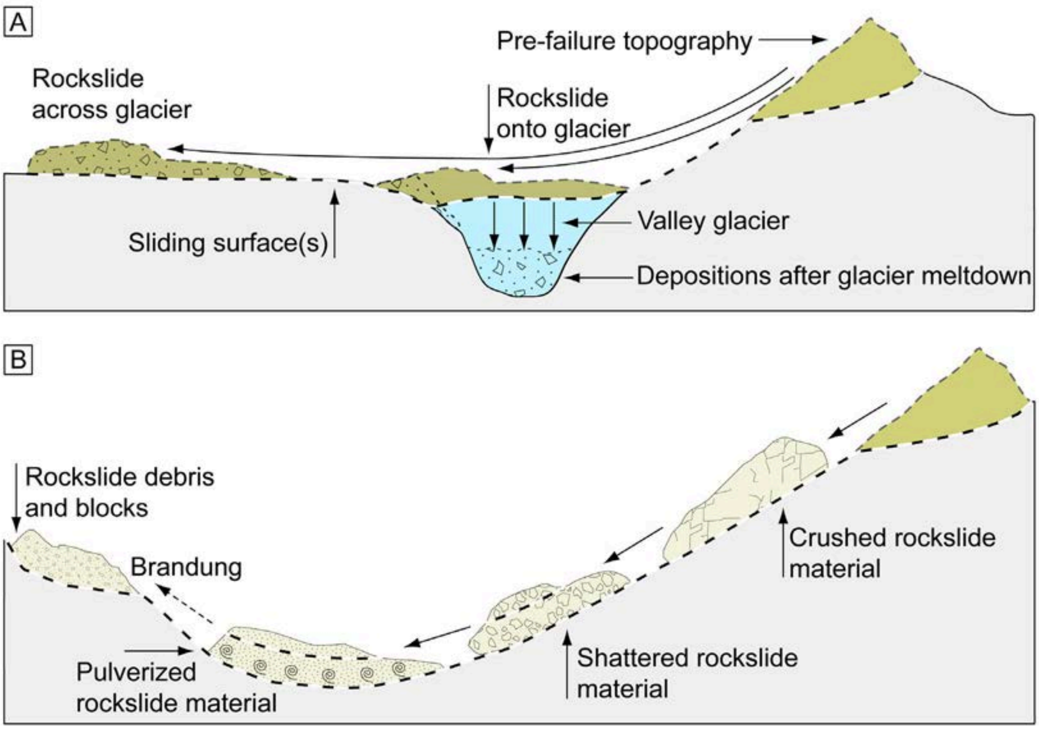

FIGURE 2.2: Mechanism of rock sliding and progressive fragmentation inferred from base facies of disrupted deposits. A) Landslide crosses valley over glacier ice forming basal features of en masse displacement (e.g. Dzongri), or falls onto valley glacier, causing deposit settling on valley bottom following ice melt-out (e.g. Braga, Almtal). B) En masse displaced rockslide mass with little disintegration develops into pervasively fragmented debris, potentially forming a run-up deposit on juxtaposed hillslope.

2.3 The sedimentology of giant rockslides

2.3.1 Main facies types

Sedimentological and petrographic profiles of large rockslide deposits reveal systematic and comparable successions of facies. Modulations of these facies are to first order consequences of (a) the topography in the runout zone; (b) pre-existing zones of weakness such as tectonic faults or fault zones in the source rock that predate the rockslide failure; (c) the generation of internal shear planes—preferentially along pre-existing faults or fault zones—characterized by further brittle deformation during runout; and (d) the generation of potentially frictionite-hosting shear planes during runout (Erismann and Abele (2001); (Fig. 2.2).

Most deposit surfaces are armoured with a 10^0-m to 10^1-m thick openwork carapace of angular boulders (Davies and McSaveney, 2011); Fig. 2.3F). This carapace typically thins with increasing runout distance, and primarily reflects passive transport and collapse along pre-existing discontinuities. The carapace covers much finer matrix-supported, angular rockslide debris (Fig. 2.3C-E) that crudely preserves original lithological boundaries, although the finest fractions may migrate over these boundaries (Hewitt, 1999). In the distal rockslide portions the basal contact of the carapace is often sharp with fragmented though coherent clasts; some crude inverse grading has been observed at some sites (Dunning and Armitage, 2011). Crushed rock characterizes initial fragmentation (Fig. 2.2), where jointed material has become degraded into separate rock fragments and mineral grains; passive collapse along pre-existing surfaces of weakness may also be possible. Shattered rock is characterized by jigsaw cracks, i.e. a fractured but not disaggregated, texture within the mineral grains, especially in quartz and feldspar (Fig. 2.1A, B). In this context, the term pulverized rock refers to fragmented mineral grains of fine sand to silt size (Strom and Abdrakhmatov (2004b); Fig. 2.1C, D). These facies of physical rock fragmentation lack any trace of dynamic compaction that may arise from impacts on opposing valley slopes, thus reducing porosity and permeability of the deposit (Masch and Preuss, 1977). However, rockslide debris may show subsequent cementation by dissolved minerals from meteoric and groundwater percolation (Prager et al., 2007).

From a large number of disrupted and fragmented rock-slope failure deposits, (Dunning and Armitage, 2011) distinguished three common units, i.e. (i) the coarse carapace; (ii) the main fragmented mass (body or en masse facies) devoid of any internal mixing of rock particles; and (iii) a mixed fragmented, occasionally diamict-like basal facies (Figs. 2.2, A.2). Wassmer et al. (2004) identified granulated, intermediary, stratified, and brecciated facies in the dissected and >400-m thick Flims rockslide deposit, the largest in the European Alps (Table 2.1). The brecciated facies cross-cuts the others, and features matrix-poor and pervasively fragmented clasts resulting from head-on collision with the juxtaposed valley flanks. Moreover, locally differing degrees of shear and interaction with substrate materials have formed intermediary facies.

2.3.2 Internal shear planes

All the deposits that we studied feature numerous thin, discrete bands of localized deformation that mark internal shear planes (Figs. 2.4, A.3, A.4). Some of these shear planes occur well above ($\leq 10^2$ m), and chiefly with both subparallel and subvertical orientations to, the rockslide base. These surfaces represent distinct stages during runout: Basal or primary shear planes form during rockslide motion. In the source area, they may be controlled by the orientation of major rock-mass discontinuities (Fig. 2.4), while topography mainly modulates the basal geometry of the lower rockslide mass. Secondary shear planes form because of transient differential motions dictated by inner shear (Fig. A.3C-F; Erismann and Abele (2001)). Schramm and Weidinger (1998) showed that such secondary shear planes have also formed within the weaker unit of the Tsergo Ri rockslide in Nepal. Hermanns et al. (2006) (re-)interpreted these secondary shear planes in between units as basal, and argued that the Köfels deposit recorded several rockslide events instead of a single one. Tertiary shear planes, first described by Schramm and Weidinger (1998) as sub-vertical internal discontinuities within the deposit of Tsergo Ri rockslide, appear to form upon collision of the moving rockslide mass with large topographic obstacles such as mountain flanks (Fig. A.4; Weidinger and Korup (2009)).

2.3.3 Basal deposits

Mechanical properties of the displaced rocks and the degree of water saturation of sediments at the rockslide base may favor diapiric intrusion of substrate sediments into the rockslide masses, indicating higher turbulence at the rockslide base than elsewhere in the deposit (Fig. 2.3, high to medium energy level). Such base-facies mélanges attest to substrate entrainment forming banded layers of pervasively fragmented though otherwise coherent clasts (Fig. 2.4). Fluvial or glacigenic boulders entrained into the basal rockslide mass, which we term phantom blocks, may retain their original shape though being internally crushed by mechanical impact during dynamic fragmentation (Davies and McSaveney, 2009) along grain-to-grain bridges (Figs. 2.3, 2.4D-G). These phantom blocks are similar to rip-up clasts that have also been reported from deposits of volcanic debris avalanches (e.g. Friele and Clague, 2004; Keigler et al., 2011), and supraglacial rockslides: The Almtal rockslide deposit, Austria, is thought to record

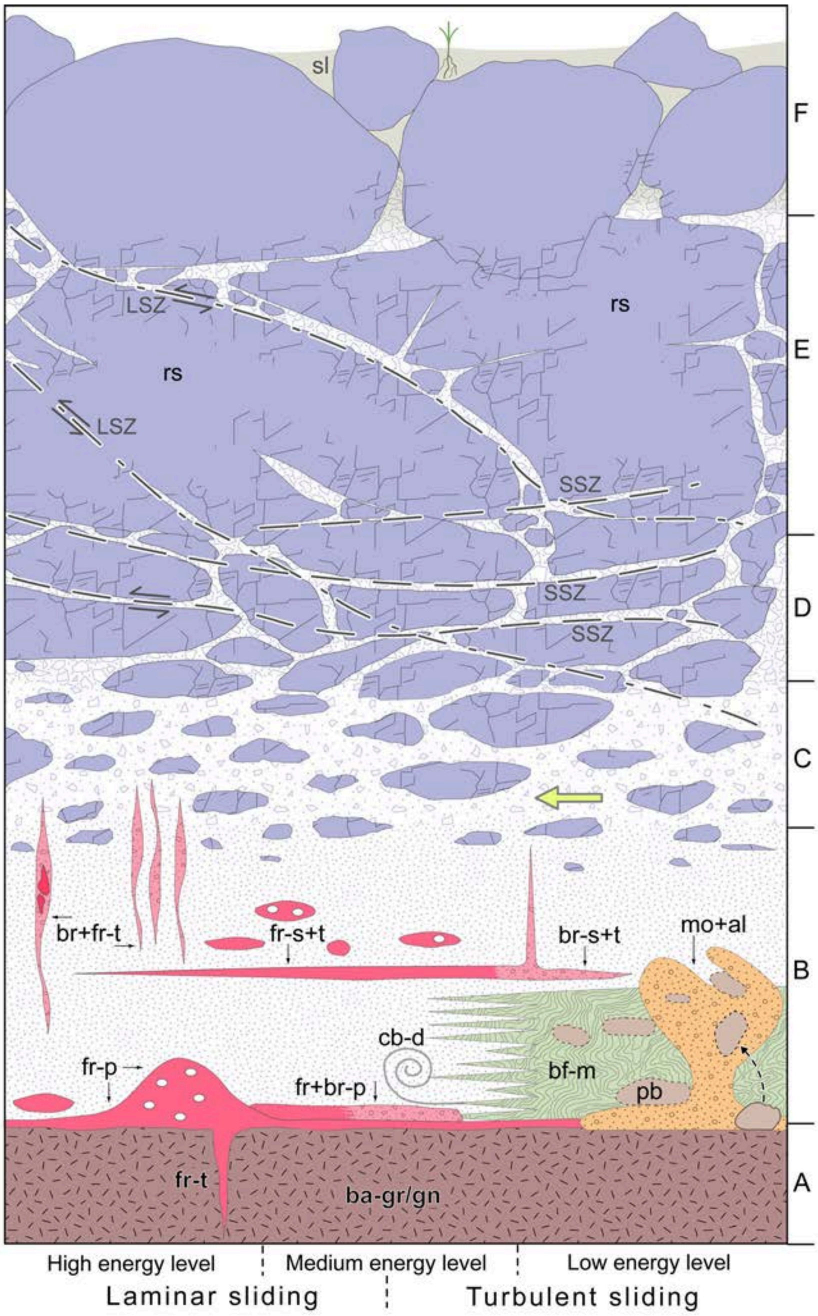

Figure 2.3: Idealized stratigraphic column of deposits from giant rockslides synthesized from field observations and petrographic investigations (different layers not to scale, bold arrow is general direction of movement): A) Nearly undisturbed basement rock (ba-gr/gn) with occasional frictionite-filled joints (fr-t). B) Shear planes in heavily shattered matrix of rockslide material: fr = frictionite with gas bubbles, br = microbreccias; suffixes -p/-s/-t = primary, secondary, tertiary shear planes, respectively; mo+al = entrained alluvial or glacigenic sediments (pb = phantom blocks, dashed arrow = direction of entrainment) at the rockslide base; bf-m = base facies mélange with underlying sediments potentially containing phantom blocks; cb-d = convoluted bands of diamictic rockslide mass. C-E) En masse rockslide deposit (rs); fragmented rock or diamict-like shattered rock blocks and boulders with downward increasing intensity of fragmentation to crushed rock, separated by shear zones: LSZ = listric shear zone (formed by partial deceleration of rockslide mass, e.g. due to impact on an obstacle), SSZ = sub-parallel shear zones (additionally to -p and s shear planes; in analogy to a sheared deck). F) Boulder carapace, optionally hosting soil (sl). Lithological patterns partly adopted from U.S. Geological Survey (2006).

detachment of a rock mass over glacier ice that created a rapid mass flow forming lenses of alluvial material floating in rockslide debris. There, rip-up clasts of coherent packages of bedded river gravel have been deemed indicative for entrainment in frozen state (van Husen et al., 2007).

2.3.4 Micro-breccias and frictionite

Most of the interiors of giant rockslides feature highly comminuted debris of varying compaction that results from dynamic fragmentation during runout. However, discrete layers of more intense fragmentation contain micro-breccias (shear planes) and traces of partial melt (frictionite along shear planes) (Schramm and Weidinger, 1998). The latter in particular formed under dominantly laminar sliding conditions that warrant sufficient heat production for rock melting (Fig. 2.3). Micro-breccias are undulating, thin, and sharply bounded bands of angular porphyroclasts supported by a fine matrix that differs from the surrounding facies in both colour and degree of hardening (Schramm and Weidinger (1998); Weidinger and Korup (2009); Fig. 2.1). Randomly sampled thin sections from 10^{-1} m-thick internal shear planes reveal that they are composed of micro-breccias without any trace of geochemical alteration (Fig. 2.1E-H), requiring highly energetic grain-to-grain contact or collision. Fractionated powdering of mineral grains along shears within the micro-breccias at the rockslide base implies highly dynamic motion with mechanical grain crushing and subsequent short-lived partial melting.

The term frictionite (or friction melt following De Blasio and Elverhøi (2008)) underlines the exogenous and purely physical origin of partly molten rock during rockslide runout. Frictionite was deemed a "self-lubricant" by Erismann et al. (1977), referring to its physical properties and dampening of brittle fragmentation during rockslide runout (Erismann and Abele, 2001; Heuberger et al., 1984). Physical experiments on generating frictionite at overburden thicknesses <1.5 km (Masch et al., 1985) are supported by field evidence by Lin et al. (2001), who found frictionite at shallow depths of $\sim$40 m, leading to glassy quenching, and a low water content ($\sim$0.4 wt.%, Masch and Preuss (1977)). Some of the best exposures of frictionite are at Tsergo Ri, Nepal Himalaya, where visual contrasts in this material reflect variable mechanical conditions and temperatures during partial melting as well as chemical compositions of the source rock (Fig. 2.8). Both the Tsergo Ri and Köfels rockslide deposits host frictionite in secondary (Fig. A.3C-F), and tertiary (Fig. A.4) shear planes also. At the Dzongri rockslide, Nepal Himalaya (Table 2.1), frictionite occurs as $<$5-mm-diameter lenses of melted biotite crystals. These are not macroscopically layered within the micro-breccias (Weidinger and Korup, 2009), indicating lower frictional energy and melt temperatures (Fig. 2.1H).

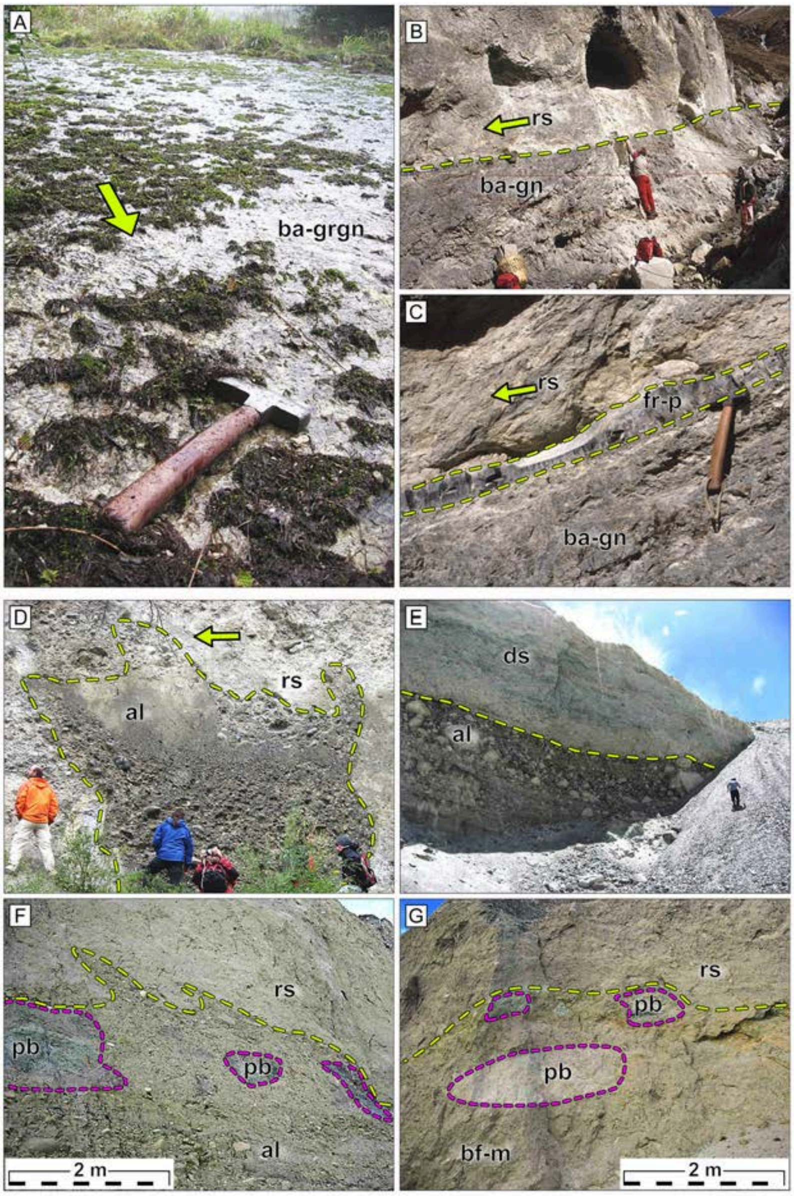

Figure 2.4: Basal rockslide portion with primary frictionite-bearing shear planes. A) Polished granite-gneiss (ba-grgn), covered by patches of organic material, forms primary shear plane of Köfels rockslide. Arrow shows runout direction in which the entire Köfels slide has passed over ba-grgn. B) Milli- to decimeter-thick band of frictionite between undisturbed gneiss basement (ba-gn) and displaced, brecciated, and fractured migmatites (rs) delineates primary shear plane of Tsergo Ri rockslide. C) Detail of B with frictionite developed at the primary shear plane (fr-p). D) to G) Partly intrusive contacts of alluvial sediments (al) into fractured rockslide (rs) or debris slide (ds) material partly with well-developed base-facies mélange at deposit base. D) Base of Tschirgant rockslide exposes entrained alluvial sediments (al); see also mo+al in Fig. 2.3A. Note that rs debris is fining upward (Patzelt, 2012). E) Pangong-North debris slide (ds) deposit with sharp contact on fluvial gravel of Shyok River. F) Alluvial deposits entrained into rockslide mass of Khalsar, India (rs); base facies mélange (G) features well-rounded boulders ("phantom blocks, pb) of coloured Khardung volcanic rocks, and white granites of Ladakh Batholith (Searle et al., 1998). Viewing direction in E), F) and G) is in direction of rs/ds movement.

2.3.5 Particle-size distribution of micro-breccias

Particle-size analyzes of en masse facies have been characterized by heavy-tailed distributions spanning from boulder to silt fractions (Dunning et al., 2006; McSaveney, 2002). Empirically estimated scaling parameters of power-law fits to particle-size data yield fractal dimensions ranging from 1.3 to 3.2, and between 2.6 and 2.7 on average. These size ranges are compatible with several theoretical models, including the plane-of-weakness model, the pillar-of-strength model, and the constrained comminution model (Crosta et al., 2007). Median particle sizes of our sampled rockslide-derived micro-breccias range from 4–25 μm for grains <100 μm, which in turn constitute 35–85 wt.%; overall median particle sizes span nearly an order of magnitude from 60–600 μm (Fig. 2.5). The resemblance with the particle-size distributions from impact breccia is striking. Moreover, parts of the rockslide-derived particle-size distributions may be approximated by power-law scaling exponents between 2.00 and 3.30, and overlap with the range of those reported from tectonic fault breccias and gouge (e.g. 2.01 to 3.04 in Billi (2005)) (Billi and Storti, 2004; Crosta et al., 2007).

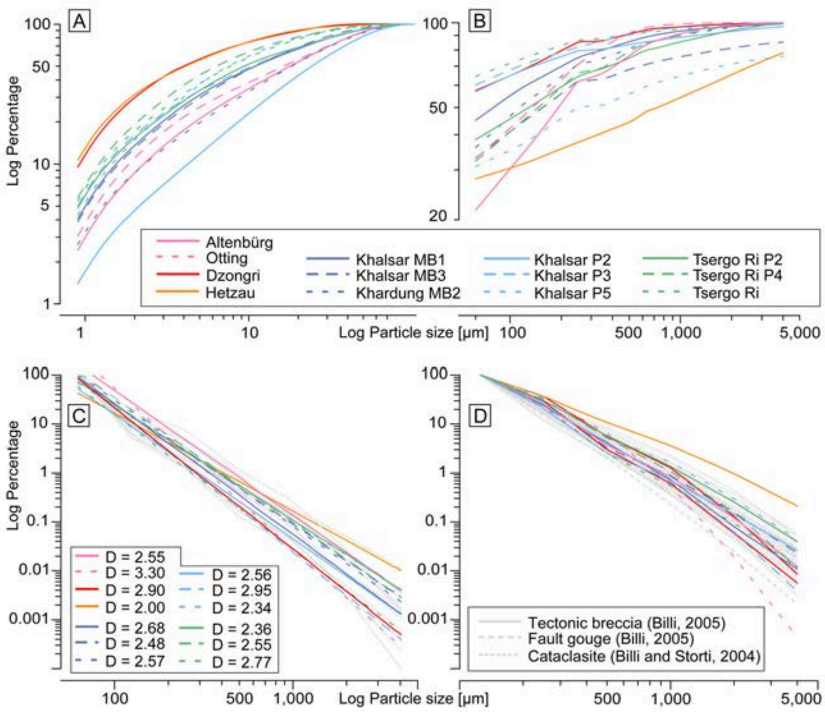

FIGURE 2.5: Particle-size distributions of micro-breccias from selected rockslide base facies close to shear planes; tectonic fault zones, and meteorite impact facies (Tables A.1, A.2). A) Particle size distributions <63 μm from laser diffractometry particle counting. B) Particle size distributions in 63–4000 μm range from sieving and weighting. C) Best fits to binned computed particle numbers (grey curves in background) using power-law functions, where the absolute value of D is the fractal dimension. D) Binned computed particle numbers from this study and previous studies (grey; Billi (2005); Billi and Storti (2004).

2.3.6 Composition and Mössbauer spectroscopy of frictionite

Our XRD and microprobe results show that the source rock at Tsergo Ri (Table 2.1) is a biotitic gneiss whereas the Tsergo Ri frictionite is mainly composed of biotite with intercalations of quartz and feldspar (Fig. A.5). These results are consistent with those of Masch and Preuss (1977). Hence, according to the microprobe results, the content of Fe(III) with respect to Fe(II) in the source sample is ∼10%, whereas we observe Fe(II) only in the frictionite. Mössbauer spectra for different heating durations are shown in Figs. 2.6 A-D. The small Fe(II) doublet of Fig. 2.6A indicates that the biotite sample was almost completely oxidized already at the lowest exposure time (5 min). However, the applied temperature of 800 °C is below that required to form melt boundaries of quartz grains, i.e. ∼1400 °C for this particular sample. Experiments with XRD show that the Fe(III) biotite is stable for temperatures of 1100 °C, whereas else it is transformed to spinel and leucite within several minutes at 1200 °C (Fig. 2.6 G, H). Direct comparison between room-temperature Mössbauer spectra of the source (Fig. 2.6E) and the frictionite sample (Fig. 2.6F) unexpectedly shows that the latter is devoid of Fe(III). Otherwise the spectrum would resemble those in Fig. 2.6A-D, and not the undisturbed source sample with mostly Fe(II) and a very small amount of Fe(III) (∼10%, Fig. 2.6E).

The source rock at Köfels (Table 2.1) is gneiss, mainly consisting of quartz, feldspar, and mica. The Mössbauer measurements yield a typical mica spectrum with rather narrow Fe(II) doublets, and an Fe(III) amount of ∼30% with respect to total iron (Fig. 2.7A). The Köfels frictionite sample resembles the one from Tsergo Ri, but has much broader doublets and a reduced Fe(III) content of 20% relative to total Fe (Fig. 2.7B). These findings agree with the XRD results. The source rock shows a well resolved diffraction pattern with a low background with good crystallinity, and the phases mentioned above consisting mainly of quartz and feldspar. The mica peaks can be found at low scattering angles (Fig. 2.7D). The XRD pattern of the Köfels frictionite has rather different properties (Fig. 2.7C): Quartz and feldspar remained stable whereas the mica peaks have largely disappeared leaving only an enhanced background hump instead. We attribute this to residual glassy components due to melted mica crystals formed at ∼650 °C (Spray, 1992) during rockslide runout. Correspondingly, the broad Mössbauer doublets and the comparably high background intensity indicate a low degree of crystallinity characterised by glass-type spectra (Fig. 2.7B).

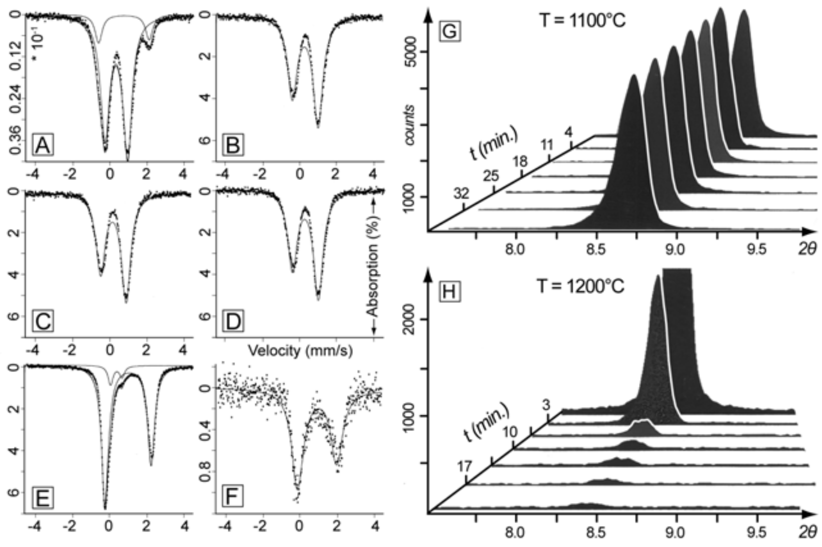

FIGURE 2.6: A-D) Mössbauer spectra of biotite from Tsergo Ri rock slide source material; the measured spectra are denoted by black squares, the calculated ones by a solid line. Different tempering time periods at T = 800 ° C: A) 5 min, B) 1 hr, C) 2 hr, and D) 3 hr. Even at the shortest time interval the biotite is nearly completely oxidized with only a small residual doublet of Fe(II) (A). E, F) Mössbauer spectra of biotite from Tsergo Ri rock slide source material (E) and frictionite (F); the measured spectra are denoted by black squares, the calculated ones by a solid line. The centres of the doublets (isomer shifts) are characteristic for Fe(II); only the source spectrum features an additional small amount of Fe(III) (10% relative to Fe(II)). The frictionite spectrum displays poor crystallinity and a high background. G, H) Time-dependent XRD powder patterns of Tsergo Ri rock slide source material. G) Characteristic biotite reflection at 1100 ° C (stable at long time periods); H) Breakdown of reflection after 10 min, annealing at 1200 ° C with subsequent generation of a spinel phase and leucite.

2.4 Discussion

2.4.1 Frictionite formation and its implications

Documented occurrences of partly molten rocks due to frictional heating during rockslide motion are rare compared to other formative processes (see Spray (2010), for a recent review on this topic). The classic exposure of pumice-like frictionite, originally dubbed hyalomylonite and thought to be of volcanic origin, is at the base of the Köfels rockslide, Austria (Heuberger et al., 1984). Further exposures were reported from the Himalayas (Schramm and Weidinger, 1998; Weidinger and Korup, 2009; Weidinger et al., 1996), the Andes (Legros et al., 2000) and Taiwan (Lin et al., 2001). Of the 19 well-exposed basal deposits of giant rockslides that we reviewed, micro-breccias and frictionite occurred in at least twelve and eight cases, respectively (Table 2.1). We infer that the formation of micro-breccias and frictionite may be more common than documented previously, partly because they can only be identified mostly from thin sections. The rockslides volumes involved were generally $>10^8$ m^3, though the smallest was 0.15×10^8 m^3 (Strom and

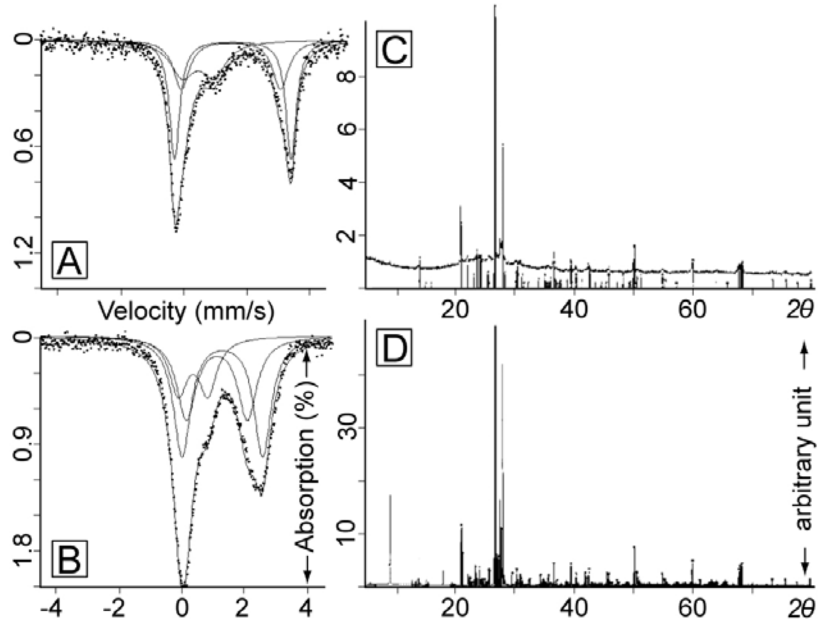

FIGURE 2.7: Mössbauer spectra of mica from Köfels rockslide source material A) and frictionite B); the measured spectra are denoted by black squares, the calculated ones by a solid line. The centre of the doublets (isomer shifts) are characteristic for Fe(II) and Fe(III) in various amounts. C, D) XRD powder patterns of Köfels rock slide source material D) and frictionite C). The mica peaks at low scattering angles D) disappear in favor of a broad hump characteristic for glassy material C).

Abdrakhmatov, 2004a). It appears that conditions necessary for generating frictionite involve crystalline or sedimentary source rocks dominated by quartz, feldspar, or mica. Giant rockslides mainly involving calcareous rocks do not show evidence of frictional melting due to the dissociation of limestone into CaO and CO_2 at confining pressures <100 MPa during runout (Erismann and Abele, 2001). Rapid motion (>10^1 m s^{-1}) is essential to warrant high slip rates and basal shear stresses without any buoyancy effects. At the same time, displacement en masse with high overburden stresses helps concentrate most of the shear in thin layers (De Blasio and Elverhøi, 2008; Erismann and Abele, 2001), converting large fractions of the rockslide kinetic energy into frictional heat focused along <10^{-1} m-thick shear planes.

Microprobe and Mössbauer spectroscopy show that the Fe(II) observed in the frictionite of Tsergo Ri had not formed because of reducing conditions or re-crystallization, given that the spinel is stable above the non-reversible phase transition. The reaction must have taken place under low oxygen fugacity, i.e. complete air exclusion (O'Hara and Huggins, 2004). Hence the partial rock melting during rockslide runout would have occurred within a very short time period. The Mössbauer spectrum of Fig. 2.6A confirms previous estimates of a very short duration of partial melting, i.e. <10 s (Erismann and Abele, 2001). For the Köfels frictionite the reduced Fe(III) contents with respect to the source rock may be explained by a reducing atmosphere during frictionite formation. The water contained in mica samples was expelled due to the high friction temperatures where the mica structure was destroyed. This is in agreement with the morphology of Köfels frictionite rock samples, which contain vesicles resembling volcanic pumice where the water appears to have been boiled out, leaving the system by diffusion and micro-cracks.

The observation that biotite as well as quartz started melting during the rockslide motion can be used for a rough calculation of the temperature conditions of the melting process. Rapid melting of rock minerals does not represent equilibrium melting, as known from crustal or mantle melting processes. In contrast, the melting point, or breaking point after Spray (1992) in particular, for (OH)-bearing minerals is significantly lower in frictional melts than in statically formed melts (Spray, 1992). Studies on tectonically formed melts (pseudotachylytes) yielded ~650 °C for biotite breakdown (Spray, 1992). Melted quartz grains indicate significantly higher temperatures, however. Although the melting point of quartz is 1705 °C (Kennedy et al., 1962), rapid melting reduces the melting point down to ~1515 °C (Petzold and Hinz, 1976). Therefore, the studied frictionites point to ephemeral temperatures of >1500 °C at the base of some giant rockslides.

2.4.2 Confusion potential

One of the most heavily debated confusion potentials for giant rockslide deposits is rooted in their macroscopic resemblance to glacial deposits, which has been documented and reviewed in detail elsewhere (Hewitt, 1999). Casual field interpretation of rounded and polymictic rip-up clasts and phantom blocks consisting of pervasively fragmented valley-fill sediments incorporated into the rockslide base may lead to potential misinterpretation under poor outcrop conditions (Fig. 2.4F, G). Such misinterpretation may substantially compromise the consistency of existing glacial chronologies (Santamaria Tovar et al., 2008).

But the confusion potential is not limited to the type of debris-generating process: The occurrence of several distinct shear planes within heavily fragmented rockslide debris from a single event may be (mis-)interpreted as the multiple emplacement of a series of successive rock-slope failures from a given source area (Hermanns et al., 2006). This may yield conflicting assessments of the frequency and magnitude of giant rockslides, and thus distort hazard assessments concerning the probability of occurrence of such rare events.

Our results also show that further confusion potential may prevail on microscopic scale (Fig. 2.5). While the presence of abundant and pervasively fragmented angular particles in scanning electron microscope micrographs may help distinguish rockslide material from glacigenic deposits (Reznichenko et al., 2012) due to the contrasting processes and environment of clast fragmentation, we find that other geological processes of formation cannot be excluded that easily. Samples from a given rockslide deposit show a substantial range in particle-size distribution that makes it problematic to distinguish rockslide-derived micro-breccias from those derived by tectonic faulting or meteorite impacts (Fig. 2.5): Differing types of process responsible for fragmentation lead to nearly indistinguishable particle-size distributions. Particle-size analysis of cataclastic rocks and its interpretation remain challenging due to the impact of methodical variations on the measured particle-size distribution, and results are often prone to ambiguous interpretation with regard to their fractal characteristics (Storti and Balsamo, 2010). The same applies to powdered rockslide debris that has a grain-size distribution that may at least partly be described as fractal (Fig. 2.5; Crosta et al. (2007)). Moreover, we infer that localized formation of micro-breccia along internal shear planes is an initial stage for generating frictionite. Such cataclasis followed by frictional melting is a well-known process from tectonically induced frictional melts. Grain-size reduction increases the active grain surface and enhances melt generation (Altenberger et al., 2011; Hetzel et al., 1996).

Yet the potential for confusing frictionites with pseudotachylyte remains (e.g. Takagi et al., 2007). Pseudotachylyte refers mainly to earthquake-generated, fine-grained, and often glassy deformation fabric that may reach lengths of several metres and 10^{-1} m thickness at the most (Sibson, 1975). They are thus smaller in lateral extent than the 10^3-m scale basal failure planes characteristic of giant rockslides (Weidinger et al., 1996). Frictionites may be confused with pseudotachylytes such that distinguishing a fault zone from shear planes belonging to a giant rockslide deposit may be difficult in the absence of further evidence. We argue that the occurrence of both micro-breccias and frictionite within pervasively fragmented deposits topped by angular boulder carapace rules out any tectonic origin. Several other macro- and microscopic characteristics help discern these tectonically generated pseudotachylytes from rockslide micro-breccia and frictionite in a given crystalline rockslide deposit (Table 2.2, Fig. 2.2). In essence, reliable and unequivocal reconstruction of the mechanism that fractures rocks within geologically instantaneous time depends on field geomorphic, stratigraphic, sedimentological, and petrographic context.

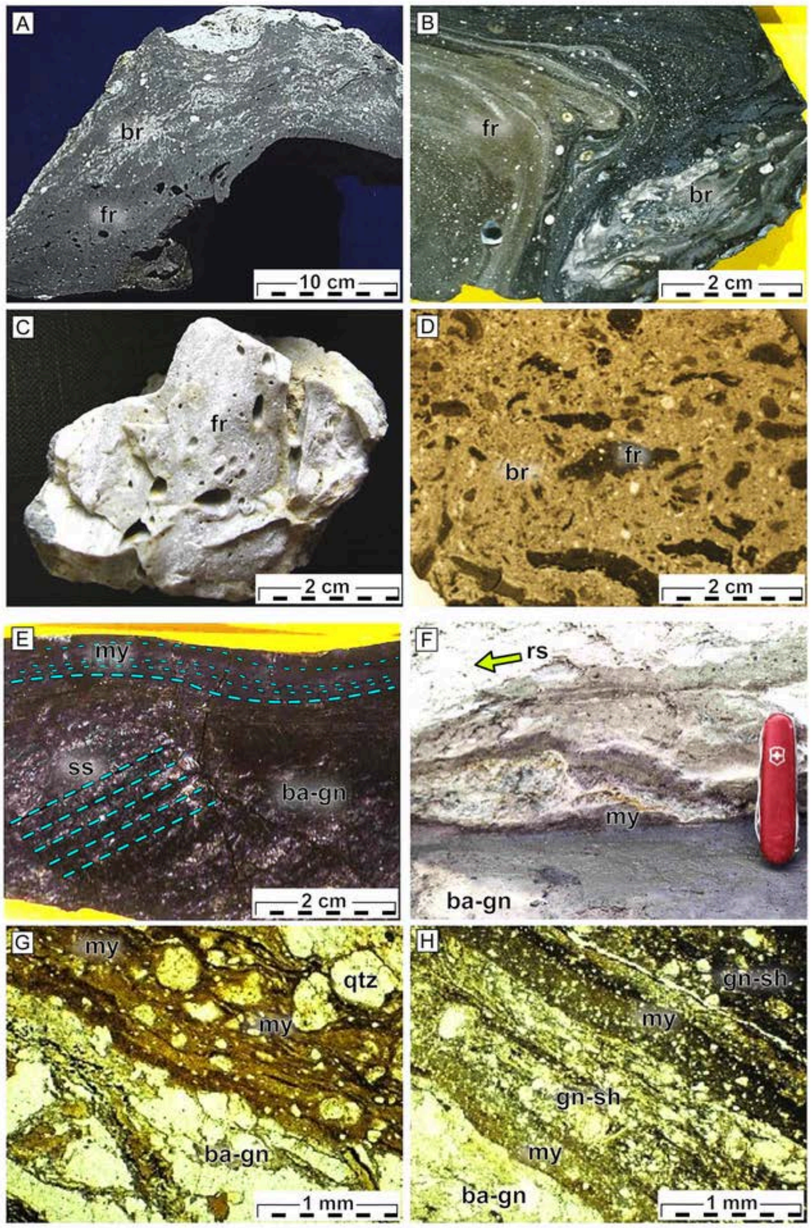

FIGURE 2.8: Frictionite from primary shear planes, Tsergo Ri. Basement rock is gneiss, dislocated rock is either migmatite or leucogranite: A) Frictionite (fr) with schlieren-like micro-breccias (br) and clasts. B) Frictionite (fr) and breccias (br) in schlieren with different chemical composition (different colors). C) White frictionite generated from leucogranite. D) Mixture of frictionite (fr) and breccias (br) from an area of lower friction energy. E)-H) (Ultra-)mylonites close to primary shear plane of Tsergo Ri landslide. E) Polished sample of gneiss (ba-gn) with schistosity (ss), and discordant (ultra-)mylonitic layer (my) defining pre-existing zone of weakness. F) Tectonically generated but rockslide-reworked (ultra-)mylonite (my) forming contact between gneiss (ba-gn) and schlieren-like rockslide material (rs); (ultra-)mylonites at least partly formed along primary shear plane(s), Tsergo Ri rockslide (arrow shows runout direction). G) Thin section of tectonic mylonites (my) in gneissic bedrock (ba-gn). H) Thin section of tectonic mylonites (my) adjacent to undisturbed (ba-gn), and sheared gneissic bedrock (gn-sh) close to primary shear plane. Note ductile deformation of quartz grains (qtz) in mylonites.

TABLE 2.2: Rocks with deformational fabric that may occur in rockslide deposits involving tectonically deformed, crystalline rocks; compiled from Altenberger et al. (2013, 2011); Lin (2008); Masch and Preuss (1977); Masch et al. (1985); Passchier and Trouw (2005); Spray (1992).

	FRICTIONITES from landslides (=hyalomylonite)	**PSEUDOTACHYLYTES from tectonic zones or impacts**	**(MICRO-)BRECCIAS from landslides, tectonic and impact areas**	**(ULTRA-)MYLONITES from tectonic zones and impact areas**
Estimated field quantity	Very rare, even in giant rockslides	Frequent in areas of paleo-seismic activity and meteoric impacts	Generally frequent, frequent in giant rockslides	Integral parts of tectonic faults
Extension and shape	Layers (1-3 × 10^{-2} m thick) or lenticular bodies, exceptionally even thicker	Fault-parallel layers, injection veins, irregular fillings of rock caverns (10^{-2} - 10^{0} m thick)	Layers or lenticular bodies (max. 10^{-1} thick)	Layers (10^{-6} - >10^{2}m thick)
General rock colour	Dark grey, brown, white (depending on source rock and chemistry)	Black with a light brown, cryptocrystalline (glass-like) matrix	Light brown, to light grey (depending on source rock and chemistry)	Black with macro-scopically visible, angular or lensoid clasts
Generation	Exogenous deformation; e.g. landslides	Endo- and exogenous deformation, e.g. seismic or reaction-enhanced events, meteoric impacts	Endogeneous (tectonic) or exogenous deformation (landslides, impacts)	Endogenous deformation; e.g. tectonic movements
Mechanism of formation	Brittle break, melting, quenching	Cataclastic deformation with subsequent melting	Cataclastic deformation locally forming thin melt films on grain boundaries	Plastic and ductile, deformation and re-crystallization
Minimum temperature [$^{\circ}$C]	1520 - <1700	≥650	<1000	250 - 300
Overburden thickness [km]	<1.5	>0 - ≥60	>0 - ≥ 60	8-10 (Sibson, 1975)
Overburden pressure [kbar]	0.1- 0.2	>0 - ≥20	>0 - ≥20	2.5
Rock porosity	Yes, partly pumice-like	In the upper crust partly porous, in deeper parts frequently	Small, due to dynamic compaction	Extremely small
Scale of runout [m]	~10^{3}	10^{-2} - 10^{-1}	10^{-6} - 10^{3}	10^{-6} - 10^{3}
Runout velocity	50 m s^{-1} (Erismann et al., 1977)	> 10 cm s^{-1}	50 m s^{-1}	cm yr^{-1}
Orientation (strike/dip)	(Sub-) Parallel or (sub-) vertical to dip of landslide movement	Often preferred orientation of newly grown minerals and clasts	(Sub-) Parallel or (sub-) vertical to dip of landslide, parallel to tectonic movement, voluminous in impact craters	In tectonic zones often (sub-) parallel to rock shistosity
Optical characterics and micro-structures	Isotropic; mainly, but depending on the mixture with micro-breccias and fine grained clasts	Quenched (new) minerals and re-crystallization of glass, flow-folds	Dynamically compressed, secondary cemented with hydrothermal minerals	Plastic deformed quartz with undulating extinction, oriented and lengthened crystals
Porphyroclasts, mineral fragments	Sub-angular to rounded	Mostly rounded, quartz mostly angular	Angular, partly with mosaic-like cracks	Round-oval (lenticular) or sharp edged

2.5 Conclusions

Petrographic evidence of rock fragmentation, internal shear planes, and frictional melt together allow constraining the dynamics and emplacement mechanisms of even highly dissected deposits of giant rockslides. Sedimentary assemblages of pervasively fragmented and interlocked jigsaw-cracked rock masses; basal mélange containing phantom blocks; micro-breccia; and thin bands of basal frictionite are, together with geomorphic and stratigraphic field evidence, indispensable clues for identifying giant rockslides and distinguishing them from Quaternary glacial deposits, tectonic fault zones, or impact breccias. Significant potential for confusion may arise at the microscopic scale, given that particle-size distributions of rockslide-induced micro-breccia have a partially fractal character, and appear indistinguishable from fault-zone and meteorite impact breccia. Without decisive field geomorphic, sedimentologic, and petrographic context, distinct shear planes within heavily fragmented rockslide debris may further be misinterpreted as the multiple emplacement of a series of successive events from a given source area. This has important implications on the detection potential and consequent hazard assessments in regions prone to large-scale rock-slope failures. From a process perspective, the occurrence of micro-breccias together with frictionite in and at the base of thick and highly fragmented angular debris indicates that short-lived ($<10^1$ s) partial melting at temperatures of $>1500\,^\circ$C may occur in the absence of water during catastrophic motion of large rockslides on bedrock substrates. This important finding supports mechanistic models of excess landslide runout without the need for invoking water as a lubricant. Given that we found such petrographic evidence in several well-exposed deposits, frictionite may not be as rare as previously thought.

Acknowledgements

This study was funded in parts by the European Commission (Contracts 026363 NATASHA, and 018412 IRASMOS), the German Research Foundation (DFG Heisenberg Program, and DFG grant KO3937/2), and PROGRESS, the Potsdam Research Cluster for Georisk Analysis, Environmental Change and Sustainability. We thank Blanka Sperner and the TU Freiberg Tectonophysics Group for providing advice and instruments for sample treatment, and Heide Kraudelt, Winfried Waldhör, Martin Struck, and Jan Blöthe for lab and fieldwork assistance. We appreciate the helpful comments by Peter Shearer and an anonymous referee.

Appendix A. Supplementary material

Supplementary material related to this study can be found in Appendix A.

Chapter 3

Study II - Postglacial denudation of western Tibetan Plateau margin outpaced by long-term exhumation

Abstract

The Indus River, one of Asia's premier rivers, drains the western Tibetan Plateau and the Nanga Parbat syntaxis. These two areas juxtapose some of the lowest and highest topographic relief and commensurate denudation rates in the Himalaya-Tibet orogen, respectively. Yet the spatial pattern of denudation rates upstream of the syntaxis remains largely unclear, let alone how major rivers drive headward incision into the Tibetan plateau. We report a new inventory of ^{10}Be-based basin-wide denudation rates from 33 tributaries flanking the Indus River along a 320-km reach across the western Tibetan Plateau margin. We find that denudation rates of up to 110 mm kyr^{-1} in the Ladakh and Zanskar Ranges systematically decrease eastward to 10 mm kyr^{-1} towards the Tibetan Plateau. Independent results from bulk petrographic and heavy mineral analyses support this denudation gradient. Assuming that incision along the Indus exerts the base-level control on tributary denudation rates, our data show a systematic eastward decrease of landscape downwearing, reaching its minimum on the Tibetan Plateau. In contrast, denudation rates increase rapidly 150–200 km downstream of a distinct knickpoint that marks the Tibetan Plateau margin in the Indus River longitudinal profile. We infer that any vigorous headward incision and any accompanying erosional waves into the interior of the plateau mostly concerned reaches well below this plateau margin. Moreover, reported long-term (>10^6-yr) exhumation rates from low-temperature

chronometry of 0.1 to 0.75 mm yr^{-1} consistently exceed our ^{10}Be-derived denudation rates. With averaging timescales of 10^3–10^4 yr for our denudation data, we report post-glacial rates of downwearing in a tectonically idle landscape. To counterbalance this apparent mismatch, denudation rates must have been higher in the Quaternary during glacial-interglacial intervals.

3.1 Introduction

The Tibetan plateau is Earth's largest and most impressive orogenic plateau with an average elevation of >4000 m a.s.l. A number of studies have demonstrated that the plateau has maintained its elevation for tens of millions of years in concert with the ongoing Indo-Asian continent-continent collision (Decelles et al., 2007; Rowley and Currie, 2006; van der Beek et al., 2009; Wang et al., 2008), and various studies have proposed mechanisms that delay the destructive action of fluvial and glacial incision into the plateau margins (Korup and Montgomery, 2008; Sobel, 2003). In the western Himalayan syntaxis, the Indus River is the main hydrological and sedimentary artery that links the low-relief western margin of the Tibetan Plateau to the steep and rugged Transhimalayan ranges flanking the Indus-Tsangpo suture zone (ITSZ) (Figs. 3.1, 3.2, 3.3). Yet, rapid exhumation and bedrock river incision in the syntaxis around Nanga Parbat (Burbank et al., 1996; Garzanti et al., 2005; Zeitler et al., 2001) are in stark contrast to slow denudation in the arid mountain deserts of the upper Indus River (Ali and de Boer, 2010; Dortch et al., 2011c; Garzanti et al., 2005; van der Beek et al., 2009). Pronounced aridity, among other controls, has helped to preserve some of the oldest glacial deposits in the Himalayas (Owen et al., 2006). However, the spatial pattern of denudation between the western Himalayan syntaxis and the plateau margin remains largely unresolved.

We hypothesize that regional denudation rates decrease eastward along a gradient from upstream of the Nanga Parbat area to the western Tibetan Plateau margin. More specifically, if fluvial headward incision into the plateau margin is active, then we would expect to see a pronounced difference between erosion rates upstream and downstream of a master knickpoint. To test our hypothesis, we combine *in-situ* produced cosmogenic ^{10}Be inventories with bulk petrography and heavy mineral assemblage analysis to quantify rates and sources of denudation along a 320-km reach along the upper Indus where it cuts through the western Tibetan Plateau margin. We focus on tributaries flanking the Indus on the assumption that incision along the trunk river controls base levels in the tributaries, and thus catchment erosional response. Our data document for the first time systematic regional-scale changes in topography, channel steepness, denudation rates, and fluvial sand petrology.

Table 3.1: Glossary of frequently used abbreviations

Abbreviation	Full term
ITSZ	Indus-Tsangpo Suture Zone
BP	Bulk Petrographic analysis
HM	Heavy Minerals
HMC	Volume percent of total Heavy Minerals
tHM	Transparent Heavy Minerals
tHMC	Volume percent of transparent Heavy Minerals
HCI	Hornblende Colour Index[a]
MI	Metamorphic Index[b]
MMI	Metasedimentary Minerals Index[c]
E	Median of denudation rates

[a] (Andó et al., 2013)
[b] (Garzanti et al., 2010; Garzanti and Vezzoli, 2003)
[c] (Andó et al., 2013)

3.2 Study area

The upper Indus River drains the Transhimalayan Ladakh and Zanskar Ranges of NW India. These ranges are nested between the Greater Himalaya and the Tethyan Himalaya to the SW, the Karakoram to the N and the Tibetan Plateau to the E (Fig. 3.1). Only marginally influenced by the South Asian Summer Monsoon, our area of interest is a mountainous high-altitude desert situated above 4,500 m a.s.l. on average, receiving as little as 90 mm of mean annual precipitation in Ladakh's capital of Leh (Müller et al., 1996; Spate et al., 1967). Two major litho-tectonic units dominate the study area. The pre-collisional granodioritic Ladakh Batholith is testimony to an ancient island arc accreted to the Eurasian margin (Ding et al., 2005; Fuchs, 1981; Gansser, 1964; Rowley, 1996; Weinberg and Dunlap, 2000), while the post-collisional sedimentary Indus Group comprises continental shales and conglomerates, alluvial deposits, and floodplain sandstones that largely form the Zanskar Range (Clift et al., 2001; Garzanti and van Haver, 1988; Henderson et al., 2010; Sinclair and Jaffey, 2001; Steck, 2003) (inset on Fig. 3.1). The Indus River separates these units by descending from the western Tibetan Plateau margin to the Shyok River confluence NE of the Deosai plateau. Locally, the Indus cuts through patches of crustal granites, gabbros, ophiolites, arc volcanics, and volcaniclastic turbidites (inset on Fig. 3.1). This simplified regional geology features structurally complex rock suites in some areas, such as around the Tso Morari dome, which hosts a core of ultra-high-pressures rocks, and along its northeastern border, high-grade migmatitic schist, large bodies of serpentinite (separate from the ophiolite sequence), blueschists, various greenschist facies slates, carbonate blocks in shale, mélange units of an accretionary prism, and an ophiolitic suite dominated by peridotite (de Sigoyer et al., 2004; Fuchs and Linner, 1996). For simplicity, we lump these rock-type assemblages into labels such as Tso Morari dome (inset on Fig. 3.1).

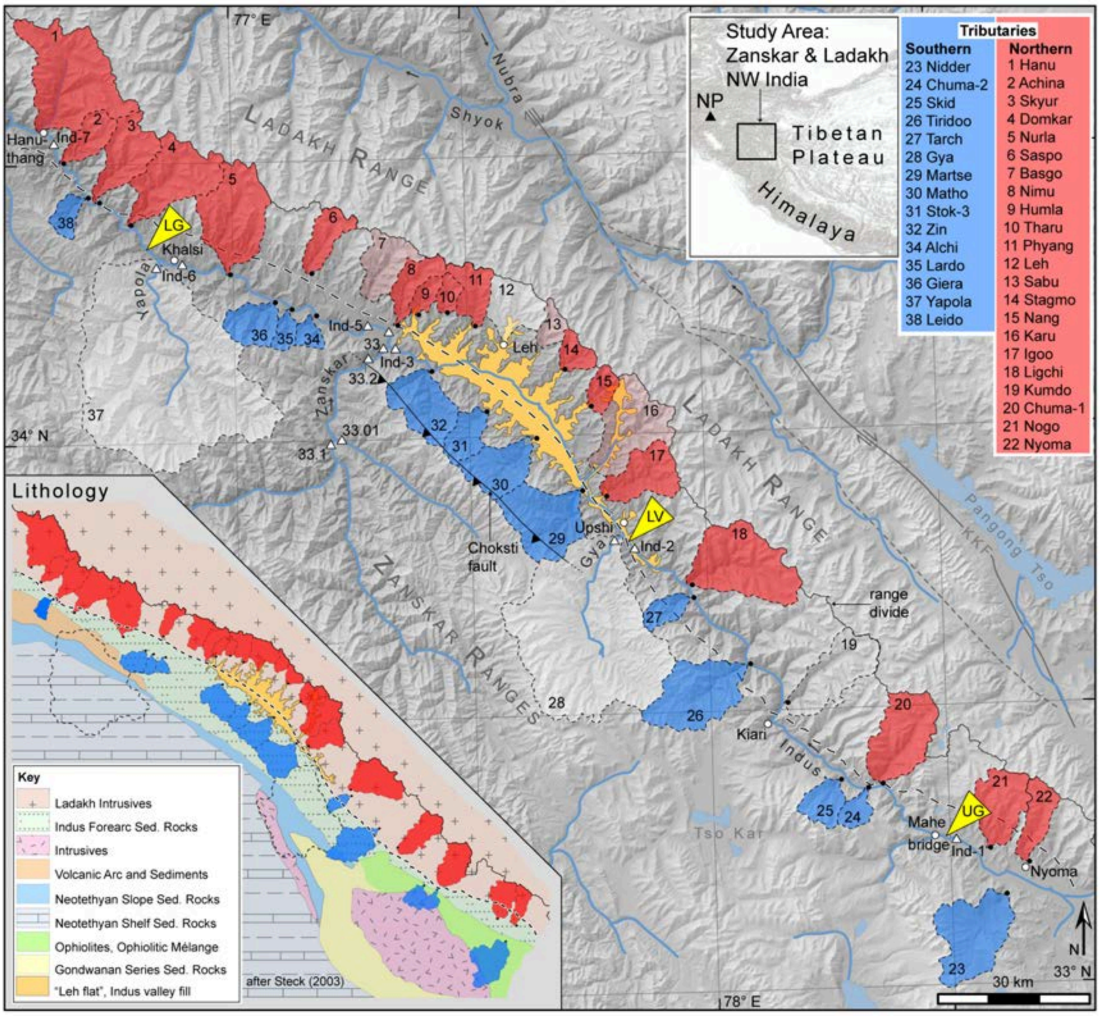

Figure 3.1: Shaded 90-m SRTM DEM derived relief of the Zanskar and Ladakh Ranges flanking the upper Indus River, NW India, and tributary catchments sampled (red = dominantly Ladakh Batholith; blue = dominantly Indus Group and structurally complex rocks of the Tso Morari Dome). UG, LG = Upper, Lower Indus bedrock gorge, respectively; LV = Leh Valley area with low-gradient valley fill (orange). Dashed black line is boundary between Ladakh Batholith and Indus Group. Small triangles are Gya, Zanskar, Yapola, and Indus River sample locations. Fault in centre is Choksti Fault (after Sinclair and Jaffey (2001)). KKF = Karakoram fault after Searle et al. (1998). Basin-wide denudation rates for catchments 7, 13, and 16 after Dortch et al. (2011c), Table B.3. Catchment No. 19 obviously affected by large landslide, ^{10}Be concentration therefore not used for analysis. Upper inset map shows location of study area, NP = western Himalayan syntaxis with Nanga Parbat. Lower inset shows major lithotectonic domains Steck (2003).

The mean elevations of tributary catchments to the upper Indus River decrease NNW-ward from >5400 m to 4000 m a.s.l., whereas topographic relief increases concomitantly

(Fig. 3.3C). The current equilibrium line altitude (or permanent snowline) is between ∼5200 and 5400 m a.s.l. (Burbank and Fort, 1985), and mostly small cirque glaciers presently cover 6% of the upper Indus catchment. The easternmost reaches of our study area are at the Tibetan Plateau margin, where high-elevation and low-relief catchments with gentle soil- and debris-mantled hillslopes border a broad, low-gradient floodplain (Fig. 3.2A). We posit the plateau margin near the village of Mahe, where the Indus River has its most pronounced knickpoint above a narrow (<100 m) bedrock gorge that zigzags through the Ladakh Batholith and the Indus Group sedimentary rocks (Figs. 3.1, 3.2B, 3.3 "UG"; also see Fig. 3A in Korup et al. (2010b)). Near the village of Upshi this upper gorge gives way to a ∼50-km long alluviated reach in the Leh area (Figs. 3.1, 3.3 "LV"), where the anastomosing Indus River occupies an up to 3-km wide valley floor beset with the largest tributary fans along its course (Fig. 3.2C). This massive >30-km long apron of coalescing fans debouching from the highest parts of the Zanskar Range documents sustained sediment input that has diverted the Indus towards the Ladakh Batholith (Jamieson et al., 2004). Up to 30-m high trimmed fan toes indicate sporadic contemporary input via these fans (Davies and Korup, 2007; Harvey, 2011). Extensive granodioritic grit curtains covering hillslopes and fans in the Ladakh Batholith are prone to catastrophic mobilization by rare rainstorms, such as in August 2010 (Hobley et al., 2012).

Previous work on regional exhumation emphasized the conspicuously lopsided transverse topography of the Ladakh Range in the Leh area. This asymmetry may result from Late Palaeogene tectonic block tilting and N-S differential exhumation (Kirstein, 2011), and transpression along the Karakoram fault with superimposed aspect-controlled glacial erosion (Dortch et al., 2011c). Others suggested that active northward thrusting along a fault along the Indus Valley prompted the build-up of the large fan apron, pushing aggradation far into the catchments draining the Ladakh Batholith (Brookfield, 1983; Jamieson et al., 2004; Searle et al., 1990; Sinclair and Jaffey, 2001).
Further downstream, the Indus River has cut another steep and narrow bedrock gorge into Indus Group sedimentary rocks upstream of the confluence with the Zanskar River (Fig. 3.2E), the largest tributary in our study area. Below this confluence the Indus continues its course through Indus Group sedimentary rocks and remnants of high-level fill terraces without touching the northern Batholith rocks (Fig. 3.2D) as far as the village of Khalsi. There the Indus enters the steep and narrow lower bedrock gorge (Fig. 3.1 "LG") of our study area. The geomorphic and litho-tectonic makeup of this lower gorge is comparable to that of the upper gorge (Fig. 3.2B, F).

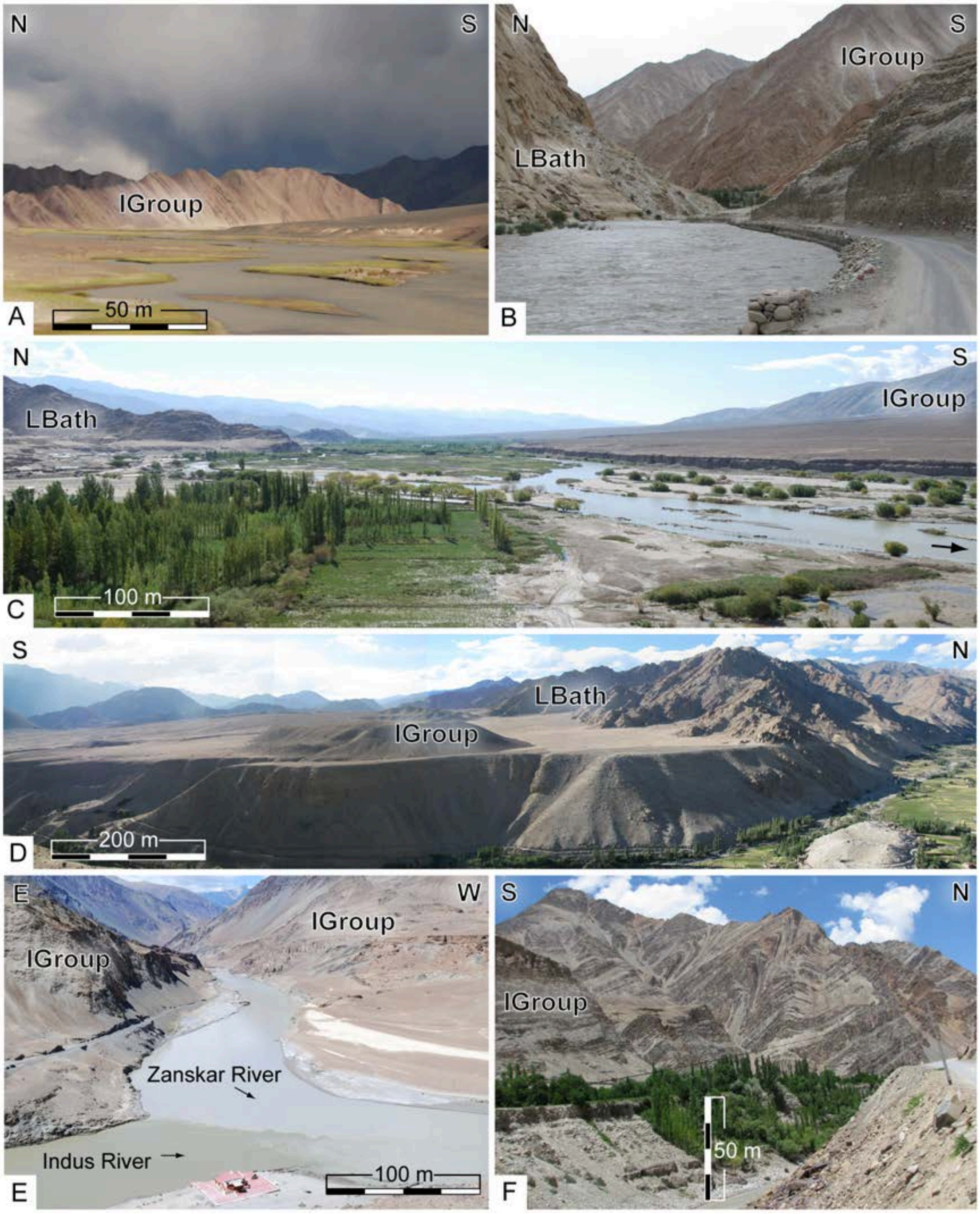

Figure 3.2: Field pictures from the upper Indus valley, Zanskar and Ladakh, NW India. A) Western Tibetan Plateau margin near Nyoma featuring low-gradient Indus River (IGroup = Indus Group sedimentary rocks). B) Upper bedrock gorge near Hymia (LBath = Ladakh Batholith). C) Alluviated Indus River near Leh; abandoned surfaces of large fan apron consisting of Indus Group clastics on right; trimmed fan toe is ∼30 m high. Bright surface on left is grit curtain from granodioritic disaggregation of Ladakh Batholith. D) Indus valley near Bazgo, ∼10 km downstream of Zanskar-Indus River confluence. Right: Spheroidally weathered Ladakh Batholith sending granodioritic sediments to S. Center: Indus Group sediments sticking out of Ladakh Batholith debris. Oasis is Bazgo valley, draining Ladakh Batholith to S. E) Zanskar–Indus River confluence near the village of Nimu, where Zanskar River discharge may exceed Indus River discharge. F) Steep and rugged topography of the lower bedrock gorge.

3.3 Methods

3.3.1 Cosmogenic nuclides

We collected 33 samples of quartz-bearing fluvial sands (1-3 kg) from Indus River tributaries between the villages of Nyoma and Hanuthang (Fig. 3.1) during the summers of 2010 and 2011. We sampled at fan heads to minimize human disturbances and potential mixing with downstream fan sediments (Figs. 3.1, Figs. 3.7C, Table 3.2). Because we collected samples in 2010 after heavy rainstorms that caused widespread flooding and debris flows throughout Ladakh (Hobley et al., 2012), we targeted submerged sand bars within channels, and avoided dried and slightly consolidated debris-flow or mass-wasting deposits that were clearly visible along several fan distributary channels. We took two replicate samples (Nimu-11; Stok-11; Tables 3.2, 3.3) in 2011 to compare with samples from the same locations collected in 2010 (Nimu and Stok-3). All samples were dried, sieved and the 125-500-μm grain size fraction was used for magnetic mineral separation. After pre-treating the samples with 19% HCl (incl. 5 centiliters of H_2O_2, for 8 hr at 90°C), they were etched with 1:1 2% HF, and 2% HNO_3 (3 times for 8 hr at 90°C in ultrasonic bath) (Kohl and Nishiizumi, 1992). Each sample was checked for natural ^{9}Be occurrence with an axial Inductively Coupled Plasma Optical Emission Spectrometer (ICP-OES). Subsequent separation of *in-situ* produced ^{10}Be was processed according to standard protocols (von Blanckenburg et al., 1996; von Blanckenburg and Kubik, 2004) in batches of 11 samples, and 1 process blank. The ^{10}Be/^{9}Be ratios were measured with the Accelerator Mass Spectrometer (AMS) of the ETH Zurich Ion Beam Physics Lab using the S2007N standard (Christl et al., 2013). All AMS-derived data were corrected with a mean lab blank (Table 3.3).

We computed production rates using the Lal/Stone time-dependent scaling scheme (Lal, 1991; Nishiizumi et al., 1989; Stone, 2000), denoted by "Lm" in the CRONUS online calculator (Balco et al., 2008)(http://hess.ess.washington.edu/). We calculated production rates for each pixel in our 90-m resolution Shuttle Radar Topography Mission digital elevation model (SRTM DEM, http://srtm.csi.cgiar.org/) based on reference production rates used by the CRONUS online calculator (Balco et al., 2008), and derived a catchment-averaged production rate vector for calculating denudation rates using the Matlab function from the CRONUS online calculator (Balco et al., 2008) for the revised ^{10}Be half-life of 1.387±0.012 Ma (Chmeleff et al., 2010; Korschinek et al., 2010). For comparison we also report denudation rates according to other scaling schemes available in the CRONUS online calculator ("De", "Du", "Li", "St"; Table B.3) (Desilets et al., 2006; Dunai, 2001; Lifton et al., 2005; Stone, 2000). Production rates were corrected for topographic shielding and glacier cover using the DEM and the present-day ice cover,

Table 3.2: Sampling sites and associated topographic parameters

No.	**Sample ID**	**Location**[a] latitude [°N]	longitude [°S]	**Area**[b] [km^2]	**Elevation** range [m asl]	mean [m asl]	**Slope** range [°]	mean [°]	**Relief**[c] range [m]	mean [m]
Northern Indus River tributaries (= Ladakh Batholith)										
1	Hanu	34.559891	76.587856	306	2788 - 5662	4631	59	26	1460	1259
2	Achina	34.504855	76.630450	65	2849 - 5529	4450	52	27	1210	1306
3	Skyur	34.433267	76.707002	119	2917 - 5728	4673	56	27	1080	1229
4	Domkar	34.391780	76.774006	181	3014 - 5712	4799	55	25	1484	1187
5	Nurla	34.301333	76.985222	209	3015 - 5779	4722	57	25	1180	1203
6	Saspo	34.300090	77.160750	69	3573 - 5751	4900	50	24	934	1118
7	Bazgo	34.253900	77.288900	97	3464 - 5798	4709	49	26	916	1228
8	Nimu	34.203889	77.342750	66	3219 - 5725	4609	47	27	897	1228
8.1	Nimu-11*	34.203342	77.341979	71	3209 - 5725	4539	47	26	897	1214
9	Humla	34.222056	77.389417	29	3724 - 5428	4507	39	26	653	1201
10	Tharu	34.225000	77.450306	28	3909 - 5608	4792	44	27	693	1279
11	Phyang	34.200306	77.508611	71	3692 - 5731	4857	42	24	938	1132
12	Leh	34.164370	77.570460	99	3471 - 5740	4644	44	24	1138	1177
13	Sabu	34.158700	77.663100	34	3906 - 5762	4954	44	25	1041	1246
14	Stagmo	34.118080	77.700260	40	3805 - 5733	4830	42	28	942	1390
15	Nang	34.051910	77.754620	41	3722 - 5638	4643	40	27	746	1332
16	Karu	33.940400	77.767600	184	3464 - 5798	4589	48	23	960	1109
17	Igoo	33.890880	77.781160	117	3476 - 5927	4597	44	24	865	1181
18	Ligchi	33.728170	77.959450	238	3586 - 6099	5184	51	26	1161	1201
19	Kumdo	33.512730	78.156090	162	3882 - 6181	5427	53	25	1425	1119
20	Chuma-1	33.364100	78.353300	173	4077 - 6459	5461	51	24	1453	1174
21	Nogo	33.242175	78.576428	122	4253 - 6143	5428	42	22	1071	951
22	Nyoma	33.216200	78.658673	73	4291 - 6146	5451	42	22	1012	994
Southern Indus River tributaries										
23	Nidder	33.159551	78.607569	196	4208 - 6445	5114	45	18	1173	1019
24	Chuma-2	33.356160	78.328650	34	4025 - 5986	5184	45	18	944	1103
25	Skid	33.372670	78.264860	59	4178 - 6359	5384	45	21	853	1166
26	Tiridoo	33.584050	78.079060	196	3717 - 5917	5107	52	22	1359	987
27	Tarch	33.704570	77.961800	42	3597 - 5983	4920	49	27	992	1389
28	Gya	33.817400	77.822550	800	3403 - 6163	4913	52	22	1075	1001
29	Martse	33.901067	77.730617	177	3392 - 5877	4595	50	26	916	1226
30	Matho	33.996900	77.634350	110	3486 - 5928	4695	49	24	1158	1194
31	Stok-3	34.046717	77.530117	64	3679 - 6038	4796	49	25	878	1229
31.1	Stok-11*	34.04148	77.527287	60	3717 - 6038	4838	49	25	878	1235
32	Zin	34.120483	77.414100	131	3216 - 6070	4490	48	27	956	1348
33	Zanskar									
34	Alchi	34.222990	77.170140	25	3141 - 5417	4367	50	30	1275	1719
35	Lardo	34.237132	77.117195	27	3099 - 5619	4544	51	29	932	1605
36	Giera	34.249573	77.080765	75	3078 - 5755	4428	58	31	935	1598
37	Yapola	34.330918	76.837504	1089	2942 - 6057	4540	66	27	1294	1340
38	Leido	34.441612	76.682392	36	2917 - 5460	4009	52	28	1054	1464

[a] GPS-recorded coordinates. Drainage points (Tab. 3), used for calculation,
may vary due to differences between measured location and DEM.
[b] Area, Elevation and Slope derived with ArcMap10 Zonal Statistics from 90 m SRTM data (WGS 84, UTM 43 N).
[c] 5-km radius, derived with ArcMap10 Zonal Statistics.
* Nimu-11 and Stok-11 are replicate samples from 2011 field season.

respectively. Although the glaciers in our study area may have been larger during the last glacial cycle, their extent appears to have been restricted. Owen et al. (2006) dated moraines in the Leh tributary catchment that are ∼5 km from the present-day ice margins to ∼96±6 kyr, and 57±3.5 kyr. Owing to the general aridity we did not correct for vegetation or snow, but we stress that any snow cover would reduce the *in-situ* production of cosmogenic nuclides (Schildgen et al., 2005), and therefore potentially lower our basin-wide denudation rate estimates slightly.

3.3.2 Sand petrology and heavy minerals

Petrographic analysis of detrital sediments composed of minerals and polycrystalline grains from various lithologies and tectonic units, allows identifying the sediment provenance, pathways, and quantifying how various source regions are contributing to the sediment load as end members. From the ^{10}Be samples we chose 20 for bulk petrographic

(BP; see Table 3.1 for abbreviations) analysis that we augmented by an additional 22 river-sand samples from tributaries and the Indus River (Fig. 3.4, Tables 3.2, B.1). We counted 400 points in each sample using the Gazzi-Dickinson method (Ingersoll et al., 1984). We classified metamorphic rock fragments according to composition and metamorphic rank that we mainly inferred from the degree of recrystallization of mica flakes. Greenschist-facies micas are commonly small muscovite flakes, upper amphibolite-facies micas are larger biotite flakes, and muscovite becomes unstable at high metamorphic grade (Garzanti and Vezzoli, 2003). We express the average rank for each sample by the Metamorphic Index (MI) that varies from 0 in detritus from sedimentary and volcanic cover rocks to 500 in detritus from high-grade basement rocks (Garzanti et al., 2010; Garzanti and Vezzoli, 2003).

For heavy-mineral (HM) analysis we selected 24 samples (Tables 3.2, B.2), including six from tributaries draining the Ladakh Batholith, three from the Indus Group, and seven samples from Indus River sands (Fig. 3.5, Tables 3.2, B.2). We focused on the 32–355-μm-particle size range that we obtained from dry sieving. Heavy minerals were separated by centrifuging in sodium polytungstate ($\rho \sim 2.9$ g cm^{-3}), and recovered by partial freezing with liquid nitrogen. On grain mounts, 200 to 250 transparent heavy-mineral grains were either counted by area or point methods at suitable regular spacing under the petrographic microscope in order to obtain volumetric fractions (Galehouse, 1971). We used the Hornblende Color Index (HCI) and the Metasedimentary Minerals Index (MMI) (Andó et al., 2013) to estimate the average metamorphic grade of metaigneous and metasedimentary source rocks, respectively. Both indices vary from 0 (detritus from greenschist-facies to lowermost amphibolite-facies rocks yielding exclusively blue/green amphibole and chloritoid) to 100 (detritus from granulite-facies rocks yielding exclusively brown hornblende and sillimanite). We also used the Sillimanite Index that is defined as the ratio between prismatic sillimanite and total (prismatic + fibrolitic) sillimanite grains. This index varies from 0 in detritus from upper amphibolite-facies metasediments to 100 in detritus from granulite-facies metasediments. Heavy-mineral concentration (Table B.2) was calculated as the volume percentage of total (HMC; for HMC classes see Fig. B.2 caption) and transparent (tHMC) heavy minerals (Garzanti and Andó, 2007).

3.3.3 Relative sediment budget and erosion rates from petrographic analysis

Downstream variations in the composition of river sediments reflect both upstream and tributary input. We determined sand compositions up- and downstream of confluences to quantify the relative contribution of tributary basins. For a known total sediment flux [t yr^{-1}] such petrography-based estimates, the so-called relative sediment budget, can be used to partition the total flux among all contributing tributary basins. To this end we used a forward sediment mixing model and sediment-budget calculation (Garzanti et al., 2012). We divided the study area into eight reaches for gaining a more detailed insight into sediment provenance (Figs. 3.4, B.1). Sediment unmixing rests on the assumption of known end-member compositional signatures of detritus (Draper and Smith, 1981; Weltje, 1997). For the Indus River at Hanuthang (Fig. 3.1, "Hanu") we estimated a total specific sediment yield of 360 t km^2 yr^{-1}, and a load equal to 5-10% of the 250±50 Mt yr^{-1} recorded upstream of Tarbela Dam (for details on the method see Garzanti et al. (2005)), i.e. 20 Mt yr^{-1}. This estimate is in good agreement with the 1983-1998 average of 23.9 Mt yr^{-1} at Kharmong gauging station ∼60 km downstream of Hanuthang (Ali and de Boer, 2007). We performed independent backward modeling on the base of sediment flux estimates from ^{10}Be derived basin-wide denudation rates to quantify the mismatch between gauged Indus River sediment load (Ali and de Boer, 2007), and the sediment load that, mathematically, would best fit our ^{10}Be derived denudation rates.

3.3.4 Morphometric analysis

We used a hydrologically corrected 90-m SRTM DEM for computing catchment topographic relief, expressed as the maximum elevation difference in a 5-km radius. We derived the average local slope gradient by fitting a polynomial to nine neighboring DEM grid cells (Horn, 1981). We calculated the steepness index k_S = SA^θ; where A is upstream drainage basin area [m^2]; S is local channel slope [m m^{-1}]; and $\theta = 0.45$ is an arbitrarily fixed reference concavity (Flint, 1974; Whipple and Tucker, 1999) for the rivers we sampled for ^{10}Be analysis, including the Indus River, to test whether differences in river channel steepness reflect those in basin-wide denudation rates (Fig. 3.3).

3.4 Results

3.4.1 Cosmogenic nuclides

Our ^{10}Be-derived basin-wide denudation rates of Indus River tributaries draining the Ladakh and Zanskar Ranges range from 10 mm kyr^{-1} to 110 mm kyr^{-1}, with averaging timescales (Granger et al., 1996), i.e. apparent exposure ages, of 65 kyr to 5 kyr, respectively (Table 3.3). Cosmogenic ^{10}Be concentrations of the 2011 replicate samples are consistent within 2-σ uncertainty with those of the 2010 samples (Fig. 3.3, Table 3.3). The sample from the northern Kumdo tributary (19 on Fig. 3.1) has a much lower ^{10}Be concentration compared to the neighboring samples; a prominent ∼1-km^2 river-blocking landslide deposit at ∼4950 m a.s.l. is a likely candidate for lowering the ^{10}Be concentration. Thus we excluded this sample from our discussion.

We find that the median of denudation rates E in the southern tributaries (E = 69.8 mm kyr^{-1}) is ∼2.5 times higher than that in the northern ones (E = 29 mm kyr^{-1}), while rates decrease towards the SE along both the Ladakh and Zanskar Ranges (Figs. 3.1, 3.3). In the southern Indus River tributaries this decrease may be modeled by a linear trend with rates decreasing at ∼50 mm kyr^{-1} per degree longitude E, i.e. twice as high as in the northern tributaries (Fig. 3.6B). Bootstrapped regression indicates that these trends are robust irrespective of individual sample locations (Fig. 3.6B). While the eastward decrease in denudation rates in northern tributaries appears to be more curved, denudation rates are lowest on the Tibetan Plateau regardless of lithology (Fig. 3.3, E <20 mm kyr^{-1}). In the northern tributaries rates remain at a median of 26 mm kyr^{-1} along the upper Indus River bedrock gorge, the Leh area, and the Zanskar confluence. In the lower Indus bedrock gorge northern tributary denudation rates increase threefold within a distance of <50 km (Fig. 3.3). We cannot detect this pronounced kink in denudation rates in the southern tributaries, which have distinctly higher denudation rates near Leh and further downstream.

3.4.2 Sand petrology and heavy minerals

The mineralogical composition of our river-sand samples allows a clear distinction of sediment sources along the Indus River. Detrital modes of Indus sands upstream of Gya River near Upshi are of mixed provenance, with contributions from the Tibetan Plateau, Transhimalayan batholiths, ophiolitic suture zone, and Tso Morari Dome (Figs. 3.1, 3.4, Table B.1). Near Leh, detritus from the ophiolitic suture (largely serpentinite and subordinate volcanic and chert grains) and Tso Morari dome (micaschist, paragneiss, and metagranitoid rock fragments, and muscovite) is diluted by the prevalent input from southern tributaries draining the sedimentary Indus Group, indicated by a sharp increase in shale/slate rock fragments (Lithics; Fig. 3.4). The composition of Indus River sands then changes abruptly downstream of the Zanskar confluence with a sharp increase in carbonate grains from the Tethys Himalaya, together with sillimanite-bearing schist and paragneiss from the Greater Himalaya. Detrital input from the Zanskar River (Fig. 3.4, Table B.1) is gradually diluted downstream by local contributions mainly from southern tributaries draining the Indus Group sediments and Khalsi limestone. At the downstream end of our study area, Indus sands receive notable additional contributions from southern tributaries draining the Dras-Nindam oceanic arc complex (serpentinite, metabasite, and slate rock fragments) (Robertson and Degnan, 1994), and the Ladakh

TABLE 3.3: Cosmogenic ^{10}Be nuclide concentrations from AMS measurement, parameters necessary for basin-wide denudation rates calculation, basin-wide denudation rates and apparent ages.

No.	Sample ID	Drainage point[a] LAT	LON	Effect. elev.[b]	Topo. shield. factor	Ice shield. factor	Total shield. factor	Production rate spallation	muogenic	^{10}Be nuclide conc.[d]	^{10}Be nuclide conc. error (int., 1σ)	Denudation rate Lm[e]	Uncertainty dLm (ext., 1σ)	App. age[f]
		[°N]	[°S]					[at g^{-1} a^{-1}]	[at g^{-1} a^{-1}]	[at g^{-1} × 10^{6}]	[at g^{-1} × 10^{6}]	[mm kyr^{-1}]	[mm kyr^{-1}]	[ka]
Northern Indus River tributaries (= Ladakh Batholith)														
1	Hanu	34.560090	76.588358	4681	0.976	0.985	0.9611	86.6	0.7	0.48	0.02	99.48	8.81	6.0
2	Achina	34.504367	76.630310	4512	0.976	1	0.9760	81.3	0.7	0.72	0.02	62.91	5.45	9.5
3	Skyur	34.433418	76.706394	4730	0.974	0.976	0.9500	87.1	0.7	0.53	0.03	90.86	8.53	6.6
4	Domkar	34.391780	76.774006	4846	0.976	0.935	0.9126	87.4	0.7	0.70	0.03	69.61	6.14	8.6
5	Nurla	34.301333	76.985222	4790	0.978	0.923	0.9028	83.1	0.7	1.36	0.04	35.18	3.06	17.1
6	Saspo	34.300151	77.160333	4939	0.979	0.934	0.9142	90.9	0.8	1.26	0.04	41.17	3.59	14.6
7	Bazgo													
8	Nimu	34.203806	77.342462	4667	0.977	0.987	0.9633	85.2	0.7	1.47	0.05	33.31	2.94	18.0
8.1	Nimu-11	34.203342	77.341979	4667	0.977	0.987	0.9649			1.54	0.06	31.16	2.80	19.3
9	Humla	34.222457	77.388803	4533	0.979	1	0.9792	81.6	0.7	2.49	0.08	19.26	1.70	31.1
10	Tharu	34.225000	77.450306	4817	0.978	1	0.9782	93.4	0.7	2.45	0.08	22.18	1.95	27.1
11	Phyang	34.199863	77.509273	4893	0.981	0.969	0.9507	93.0	0.8	2.12	0.07	25.41	2.23	23.6
12	Leh													
13	Sabu													
14	Stagmo	34.118570	77.700080	4868	0.976	0.997	0.9727	94.7	0.7	3.13	0.10	17.72	1.57	33.9
15	Nang	34.051662	77.753542	4681	0.977	1	0.9770	87.0	0.7	1.95	0.06	25.91	2.27	23.2
16	Karu													
17	Igoo	33.890431	77.781363	4651	0.982	0.991	0.9735	84.9	0.7	2.06	0.07	24.02	2.11	25.0
18	Ligchi	33.728048	77.959687	5220	0.976	0.953	0.9292	104.5	0.8	2.07	0.07	28.97	2.54	20.7
19	Kumdo	33.513190	78.155688	5449	0.978	0.916	0.8949	110.4	0.9	0.71	0.02	84.82	7.38	7.1
20	Chuma-1	33.364100	78.353300	5489	0.979	0.905	0.8858	110.3	0.9	2.31	0.07	27.46	2.41	21.8
21	Nogo	33.242864	78.576438	5454	0.986	1	0.9858	122.8	0.9	5.79	0.18	12.47	1.12	48.1
22	Nyoma	33.216204	78.658504	5476	0.985	1	0.9846	123.7	0.9	4.97	0.16	14.56	1.30	41.2
Southern Indus River tributaries														
23	Nidder	33.159951	78.607863	5156	0.989	0.999	0.9873	107.2	0.8	2.04	0.06	30.10	2.64	19.9
24	Chuma-2	33.356976	78.322111	5206	0.990	0.992	0.9818	109.5	0.8	7.02	0.22	9.26	0.84	64.8
25	Skid	33.372670	78.264860	5418	0.988	0.855	0.8454	99.7	0.9	1.93	0.06	29.62	2.59	20.3
26	Tiridoo	33.583965	78.078812	5128	0.986	0.987	0.9729	105.3	0.8	2.20	0.07	27.46	2.41	21.9
27	Tarch	33.704482	77.961643	4970	0.974	0.958	0.9328	93.2	0.8	1.52	0.05	35.12	3.06	17.1
28	Gya													
29	Martse	33.901094	77.731125	4638	0.979	0.992	0.9708	84.3	0.7	0.51	0.02	90.67	8.42	6.6
30	Matho	33.996645	77.634861	4742	0.982	0.957	0.9395	84.4	0.7	0.66	0.02	70.76	6.15	8.5
31	Stok-3	34.046717	77.530117	4839	0.981	0.950	0.9319	87.7	0.7	0.70	0.02	69.38	6.04	8.6
31.1	Stok-11	34.041480	77.527287	4839	0.981	0.947	0.9294	86.8	0.8	0.61	0.02	80.63	6.96	7.4
32	Zin	34.120441	77.414372	4533	0.975	0.988	0.9630	79.6	0.7	0.63	0.02	70.11	6.20	8.6
33	Zanskar													
34	Alchi	34.224065	77.169148	4415	0.968	1	0.9677	76.3	0.7	0.67	0.02	63.43	5.51	9.5
35	Lardo	34.237221	77.116699	4599	0.972	0.994	0.9658	83.1	0.7	0.59	0.02	77.99	6.92	7.7
36	Giera	34.249573	77.080765	4487	0.963	0.994	0.9567	77.9	0.7	0.37	0.02	113.85	10.81	5.3
37	Yapola													
38	Leido	34.441865	76.683016	4060	0.975	1	0.9748	64.5	0.6	0.33	0.02	107.26	10.59	5.6

[a] Coordinate of DEM pixel in channel, nearest to sampling point in the field (for GPS coordinate see Table 3.2.

[b] Hypsometerically-weighted elevation.

[c] Corrected for mean lab blank (09-2010 to 02-2012) with $^{10}Be/^{9}Be$ ratio = 9.38756E-15; and using Be_2SiO_2 carrier from Phenakite mineral; conc. 372.5 ± 3.5 ppm.

[d] Lal/Stone time-dependent

[e] Assuming an absorption depth of 60 cm (Granger et al., 1996; von Blanckenburg, 2005).

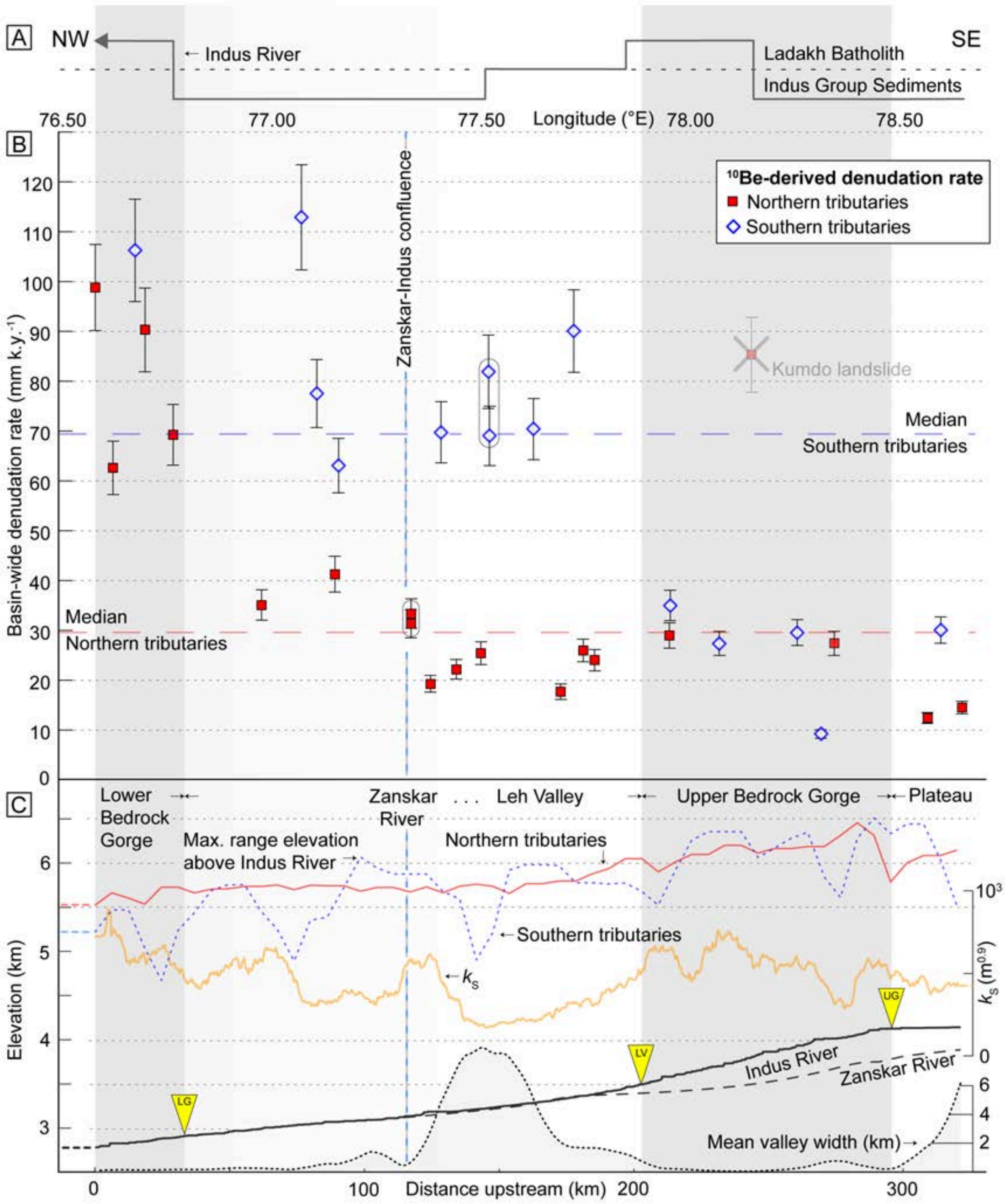

Figure 3.3: Cosmogenic ^{10}Be-derived denudation rates along the upper Indus River and key elevation profiles. Grey background panels delimit the upper (UG) and lower (LG) bedrock gorges and frame the Leh Valley (LV). A) Schematic path of the Indus River flowing over the Ladakh batholith or Indus Group sediments. B) Denudation rates of tributary basins flowing from the north (filled squares) and south (open diamonds) into the Indus River; long dashed lines are median values. Pairs of encircled points are 2010 and 2011 replicate samples. Landslide-affected Kumdo data point is anomalous and is not included in calculation of median. C) Mean elevations of tributary catchments north and south of the Indus River, elevation profiles of the Indus and Zanskar Rivers, and steepness index k_S of the Indus River smoothed with a 12-km moving average; also shown is the mean width of the Indus River valley. A pronounced knickpoint along the Indus River profile marks the boundary between the Tibetan Plateau and the upper bedrock gorge and a transition zone from the Zanskar confluence to the lower gorge is marked by sharply increasing k_S.

Batholith to the north (granitoid, plagioclase, and biotite grains). Contributions from southern tributaries draining the Himalayas, the ITSZ, and the Indus Group exceed contributions from the northern tributaries draining the Ladakh Batholith.

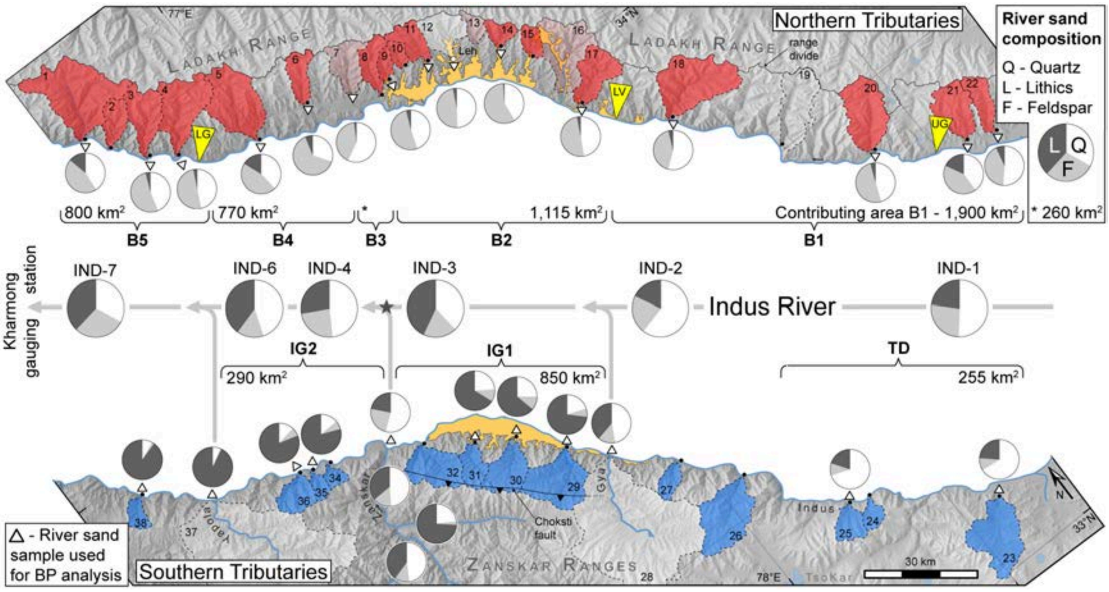

Figure 3.4: Sand petrography in the upper Indus River catchment. Northern tributaries (draining the Ladakh Batholith) shed quartzo-feldspathic to feldspatho-quartzose detritus. Instead, southern tributaries (draining Indus Group siliciclastics and different tectonic units exposed along the ophiolitic suture and in the Zanskar Range to the south) shed abundant sedimentary, metasedimentary and locally metavolcanic, metabasite and ultramafite rock fragments. Provenance reaches denoted by brackets are homogeneous units that were used to calculate relative sediment budgets (B1-5: Ladakh Batholith; TD: Tso Morari Dome, IG1-2: Indus Group). Main southern tributaries (Gya, Zanskar, and Yapola Rivers) represent distinct provenance reaches. Note stepwise increase in lithics (L) in Indus River sands downstream of the Gya confluence (IND-3) and of the Zanskar confluence (IND-6), due to prevailing IG1 and IG2 contribution. The opposite trend, observed locally at the Zanskar confluence (⋆), reflects prominent supply from the Zanskar Range (IND-4). Southern tributaries: catchments 23–25 mainly draining Tso Morari Dome; Gya (28), catchments 29–32 and 36 largely draining sedimentary Indus Group; Zanskar catchment largely draining sedimentary Tethys Himalaya Zone (THZ) and High Himalayan Crystalline Zone; Yapola (37) catchment largely draining THZ and Dras volcanics; and catchment (38) draining Dras volcanics. We show an alternative figure in the data repository (Fig. B.1).

The mineral compositions of the fluvial sands allow tracing sediment coming from both the northern and southern Indus tributaries. Very heavy-mineral rich (HMC 15±7, tHMC 11±4) and hornblende-dominated (Amp 80±7% tHM; HCI 10±5) heavy-mineral assemblages clearly identify input from the northern tributaries draining the Ladakh Batholith (Fig. 3.5, Table B.2). Other minerals include epidote, clinopyroxene, and hypersthene derived from locally exposed volcanic-arc rocks, titanite, apatite, zircon and tourmaline. In contrast, heavy-mineral assemblages of sands from the Indus Group to the south are moderately poor in heavy minerals (HMC 3±1, tHMC 1.4±0), and dominated by epidote (Ep 69±6% tHM) with subordinate amphibole, garnet, and minor zircon, and apatite. This assemblage is mainly recycled from pre-collisional forearc and post-collisional intermontane clastic wedges originally shed from the Ladakh Batholith. These markedly differing heavy-mineral suites largely result from diagenetic processes affecting Indus Group strata, such as dissolution of labile amphibole and pyroxene, and anchimetamorphic epidote growth (Garzanti and van Haver, 1988; Henderson et al., 2010). Heavy-mineral assemblages from the high-pressure metamorphic rocks of the Tso Morari Dome (Berthelsen, 1953; de Sigoyer et al., 2004; Guillot et al., 1997; Schlup et al., 2003) are rich (HMC 7±3, tHMC 5±3) (Fig. 3.5, Table B.2), and consist of garnet, blue sodic amphiboles including glaucophane (Grt 34±2% tHM; Amp 25±5% tHM); contents of epidote, apatite, clinopyroxene, zircon, tourmaline, and rutile remain minor. The Zanskar River has its headwaters in upper amphibolite-facies metamorphic rocks of the Greater Himalaya (Pognante and Lombardo, 1989), and crosses the whole Tethys Himalayan Zone (Gaetani and Garzanti, 1991). Its main tributaries include the Markha River, incised into the Triassic Lamayuru mudrocks (Fuchs, 1986; Steck et al., 1993). The heavy-mineral rich Zanskar assemblage (HMC 6±4, tHMC 5±3) (Fig. 3.5, Table B.2) includes blue-green to brown hornblende and largely fibrolitic sillimanite (Amp 29±17%t HM, HCI 24±2; Sil 26±8%t HM, MMI 98±2, Sillimanite Index <14), associated with garnet and minor tourmaline, epidote, clinopyroxene, and zircon. The very poor Markha assemblage (tHMC 0.7) includes epidote, tremolite-actinolite amphiboles, tourmaline, zircon, apatite, clinopyroxene, and garnet.

Overall, we detect some major changes in the Indus River sand petrology and heavy-mineral composition. The moderately heavy-mineral rich plateau-derived assemblage of the Indus River at Nyoma includes hornblende, sodic amphiboles, garnet, clinopyroxene, minor apatite, titanite, zircon, tourmaline, and rare olivine, rutile, enstatite, and chloritoid. Between Nyoma and the Zanskar confluence, heavy-mineral concentration tends to decrease (HMC from 4 to 2, tHMC from 2.7 to 1.5); amphiboles increase from 36 to 56% tHM (HCI decreasing from 15 to 2% tHM) and epidote increases up to 29% tHM at the expense of garnet and pyroxene. The prominent influence of Zanskar sediments from the south is highlighted by the increase in heavy-mineral concentration downstream of the confluence (HMC 7±2, tHMC 5±1) (Fig. 3.5, Table B.2), the appearance of common fibrolitic and subordinately prismatic sillimanite (Sil 19±9% tHM, MMI 99±2, Sillimanite Index 30±20), and the increase in garnet and staurolite at the expense of epidote and amphibole. Farther downstream, heavy-mineral assemblages remain rich and characterized by hornblende, sillimanite and garnet. Greater Himalaya-derived garnet progressively decreases, staurolite becomes negligible, and the decreasing HCI reflects additional supply from northern and southern tributaries between Nimu and Khalsi. At the downstream end of our study area, Indus sands are rich in heavy minerals (HMC 7, tHMC 5) and dominated by blue-green amphiboles (Amp 69% tHM, HCI 7) (Figs. 3.5, B.2, Tables B.2), indicating additional local supply from the Ladakh Batholith in the north and blueschist-facies rocks of the Sapi-Shergol mélange in the south (Mahéo et al., 2006). Pyroxenes locally derived from Dras volcanic rocks to the south or possibly from volcanic covers of the northward Ladakh Batholith also increase, whereas garnet and sillimanite derived from the Greater Himalaya via the Zanskar River decrease further.

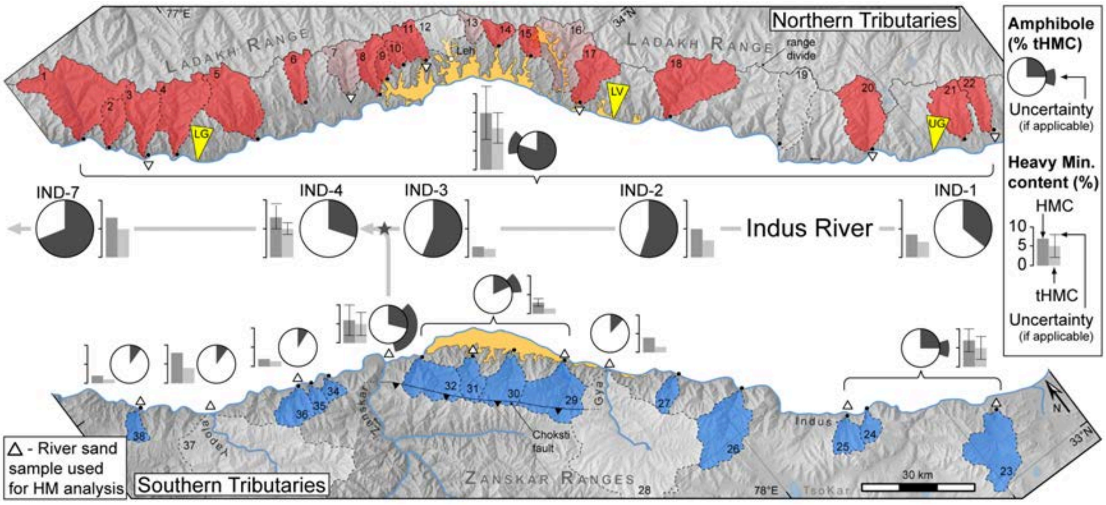

FIGURE 3.5: Heavy-minerals in the upper Indus River catchment. Pie charts indicate amphibole percentage of transparent Heavy Minerals (tHM). Bar diagrams indicate volume concentration of total (HMC, left bar) and transparent heavy minerals (tHMC, right bar) of bulk sediment (Garzanti and Andó, 2007). Uncertainties are given where applicable. Note dilution of amphibole and HMC increase in Indus sands just after the Zanskar confluence (⋆). Provenance reaches as in Fig. 3.4. We show an alternative figure in the data repository (Fig. B.2).

3.4.3 Relative sediment budget and erosion rates from petrographic analysis

Our modeling of erosion rates from the petrographic data, assuming a sediment load of 20 Mt yr^{-1}, yielded an erosion rate of 130 mm kyr^{-1} for the Indus upstream of Hanuthang (∼57.000 km^2). Approximately 25.000 km^2 of this area belongs to the upper Indus catchment between Nyoma and Hanuthang. Our ^{10}Be-derived denudation rate estimates cover 14% of this area, and these are roughly an order of magnitude lower than the BP erosion rate estimates over individual litho-tectonical reaches (Table 3.3). We computed that rate estimates from the two methods agree best for a sediment load of 3 Mt yr^{-1} in the Indus River (Fig. 3.8A). However, this would depress the overall BP-derived denudation rate of the Indus from 130 to 20 mm kyr^{-1}, assuming negligible intermittent sediment storage.

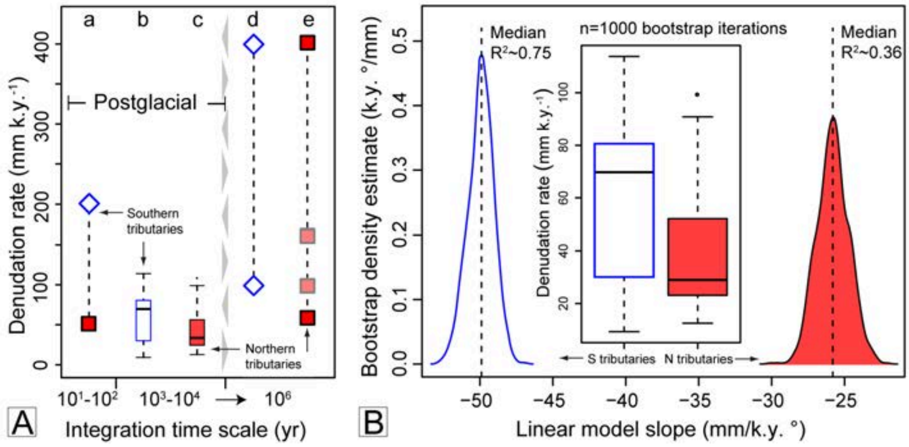

FIGURE 3.6: A) Comparison of denudation-rate estimates for the study area on various time scales; Filled squares = Ladakh Batholith, blank diamonds = Indus Molasse; a) historical estimate from sediment budget (Garzanti et al., 2005); b, c) cosmogenic ^{10}Be data (this study); d, e) long-term estimates from thermochronometry data (Clift, 2002; Kirstein, 2011; Kumar et al., 2007; Sinclair and Jaffey, 2001). B) Bootstrap estimates of linear model slopes of ^{10}Be denudation rates versus longitude [° E]. Box-and-whisker plots show range of inferred rates.

3.4.4 Morphometric analysis

Topographic relief, catchment steepness, and median channel steepness generally decrease towards the Tibetan Plateau in all tributaries (Figs. 3.3, 3.7A, B). Yet this decrease is more pronounced in the southern tributaries, thus mimicking the trend observed in ^{10}Be-derived denudation rates (Fig. 3.3, Table 3.2). The longitudinal profile of the Indus River has major knickpoints where the river is leaving the Tibetan Plateau at Mahe (Figs. 3.1, 3.3), and upstream of the confluence with the Zanskar River (Fig. 3.7C). Below the Zanskar confluence, the bed profile of the Indus is notably steeper (Fig. 3.3C). Similarly, northern tributaries draining the Ladakh Batholith are steepest below the Zanskar confluence and in the lower Indus bedrock gorge, and distinctly oversteepened in the lowermost reaches (Fig. 3.7C).

3.5 Discussion

3.5.1 Comparing denudation rate estimates between methods

Our ^{10}Be-derived denudation rates illustrate a striking order-of-magnitude decrease of landscape lowering towards the plateau margin. The rates near the Zanskar confluence are consistent with previously reported rates covering this part of our study area (Dortch et al., 2011c), and comparable to estimates based on sand petrology (Garzanti et al.

(2005); Fig. 3.6A). In the following we discuss how our data on the compositional changes of river sands and the BP-derived erosion rates consolidate the picture of a general NW increase of catchment-wide denudation rates along the Indus River (Ali and de Boer, 2010; Garzanti et al., 2005; van der Beek et al., 2009; Zeitler, 1985). Our BP-derived erosion estimate of 130 mm kyr^{-1} for the upper Indus River assumes an annual load of 20 Mt (Fig. 3.8), and approaches the highest basin-wide ^{10}Be derived denudation rates that we obtained for tributaries to the lower bedrock gorge (Fig. 3.3, Table 3.3). The BP-derived erosion estimates for various litho-tectonic reaches increase by an order of magnitude downstream of the Tibetan Plateau margin, similar to the data in our cosmogenic ^{10}Be inventory (Fig. 3.8). Given this consistent regional trend, we treat the sample of the central Batholith reach (B3 in Fig. 3.8), opposite the Zanskar confluence, as an outlier. Other local mismatches of BP- and cosmogenic ^{10}Be-derived erosion rates are prominent. We attribute these to sediment storage effects that may distort patterns of sediment provenance (Blöthe and Korup, 2013; Clift and Giosan, 2013), and the differing timescales underlying the two methods: The BP-derived erosion estimates rely on a 15-year time series of sediment load estimated from a sediment rating curve based on at least monthly measurements (Ali and de Boer, 2007). In contrast, the cosmogenic ^{10}Be derived rates smooth out short-term fluctuations (von Blanckenburg, 2005) by integrating over millennial time scales. The spatially more resolved ^{10}Be data refine estimates of erosion rates based on sand petrology, which assume uniform denudation pattern and rates proportional to the area of outcropping source areas. Moreover, our inventory of denudation rates does not fully cover the Indus drainage basin. Hence, sediment point sources such as actively undercut and landslide-prone valley walls flanking the Indus, or steep debris flow-prone low order catchments feeding directly into it are not included in our assessment.

Also, bulk petrographic and heavy-mineral analyses independently confirm our finding from the ^{10}Be inventory that tributary denudation rates in the Ladakh Batholith and the Indus Group differ along the alluvial reach around Leh and the Zanskar confluence, despite spanning a similar range of 10–110 mm kyr^{-1}. From petrographic analysis we infer higher erosion rates of the tectonic units exposed south of the Indus valley, which is consistent with the massive fan apron in this part of the Indus valley (Figs. 3.1, 3.2C). The prevailing sediment input from the Indus Group near Leh and upstream of the Zanskar confluence is confirmed by abundant shale and slate rock fragments (Figs. 3.4, B.1), decreasing HMC (Figs. 3.5, B.2), and increasing epidote in the Indus River sands (Table B.2). Zanskar-borne carbonate rock fragments and heavy minerals, derived from the Tethys and Greater Himalayas, respectively, further corroborate this sedimentary fingerprint of the southern Indus River tributaries. An unknown fraction of carbonates leaves the Zanskar as dissolved load, though this portion should be negligible due to prevailing aridity (e.g. Russell, 1937).

3.5.2 Regional denudation gradient

Previous work attributed the high sediment delivery from the Indus Group to partial northward thrusting along the Choksti Fault (Fig. 3.1), where topography was generated by pushing pre-collisional sediments over the post-collisional Nurla formation of the Indus Group (Searle et al., 1990; Sinclair and Jaffey, 2001). Our data could support such a scenario. Basin-wide denudation rates upstream of the Leh Valley and downstream of Khalsi, i.e. beyond the influence of the Choksti Fault, are indistinguishable on both Indus valley flanks. However, evidence for neotectonic activity remains elusive (Burbank and Fort, 1985), and recent GPS measurement data show no statistically significant deformation between the nearest stations of Leh and Hanle (Jade et al., 2010). Although neotectonics cannot be discarded fully as a possible control (Searle et al., 1990; Sinclair and Jaffey, 2001), any evidence to support the regional denudational asymmetry between the upper and the lower bedrock gorges on at least post-glacial timescales remains to be found by fieldwork, satellite imagery analysis or morphometric DEM analysis. Likewise the view of a simple lithological control on basin-wide denudation rates conflicts with the nearly indistinguishable denudation rates across all rock types upstream of Leh (Fig. 3.3).

At first glance, our data reveal a distinct gradient in denudation rates, consistent with a transient headward migrating erosional wave into the western Tibetan Plateau margin. This view hinges on the assumption that incision along the Indus River is communicated as a base-level signal to the tributaries, thus forcing local adjustment via downcutting. The (smoothed) variance in channel steepness of the Indus River could reflect alternations between bedrock gorges and broad alluviated reaches equally well as localized sediment input. However, if the distinct knickpoint near Mahe is the key location of driving incision into the western Tibetan Plateau margin, then the concomitant denudation rates are strikingly low (Fig. 3.3). Instead, denudation rates notably increase only as far as 150 to 200 km downstream of this master knickpoint in the northern and southern Indus tributaries, respectively. The focus of highest fluvial incision in our study reach towards the downstream end is consistent with oversteepening of the lowermost reaches in tributary catchments (Fig. (Fig. 3.7)C). We interpret these steepened river toes as adjusting to an elevated incision signal from the trunk river; this signal is now propagating upstream into the tributaries. The northern tributary profiles downstream of the Zanskar-Indus River confluence are composite, a likely result of delayed response to base-level fall (Wohl, 2000). Thus, while the regional decrease of denudation rates

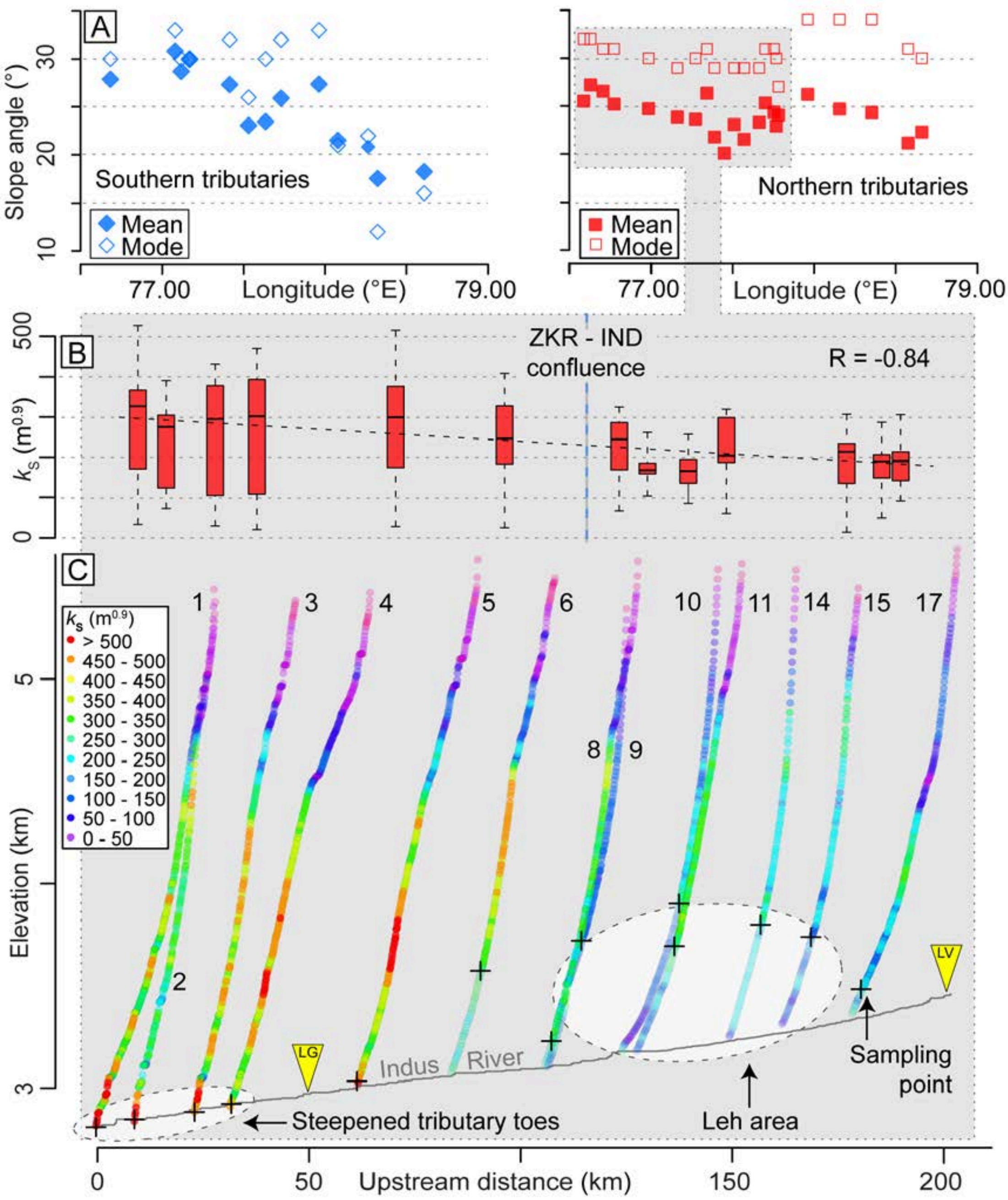

FIGURE 3.7: Morphometry of upper Indus valley flanks. A) Longitudinal distribution of slope angles of catchments under investigation in southern (left) and northern upper Indus River tributaries. Tharu catchment (Fig. 3.1, No. 10) mode (value = 3) not plotted because out of Y-axis range. B) Box- and Whisker plots of k_S index values from tributary ^{10}Be measured catchments 1–17, whiskers extend to extreme values. Note higher (interquartile) ranges for catchments 1–6, downstream the Zanskar-Indus confluence. C) k_S index values for channels of ^{10}Be measured catchments 1–17 (numbered), draining the Ladakh Batholith, derived from 90-m SRTM DEM within moving five-cell (= 450 m) segments down the respective channel. Crosses mark sampling points; "LV" triangle marks beginning alluviated Leh Valley, "LG" triangle marks beginning lower Indus bedrock gorge, coinciding with steepened tributary toes, "ZKR-IND" is Zanskar-Indus confluence (marked by vertical dashed line). Note major knickpoint between Leh Valley and Zanskar-Indus confluence.

across the western Tibetan Plateau margin is intuitive and expected to us, it is the spatial pattern of this decrease that is not.

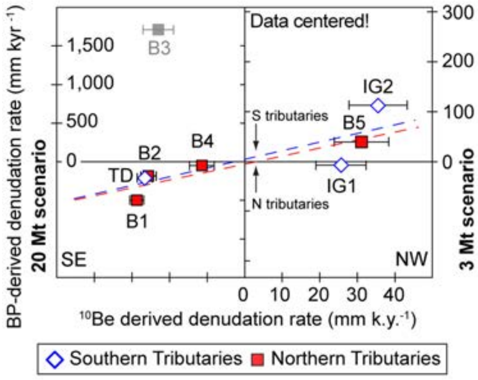

BP-derived denudation rate estimates

	20 Mt *scenario* (mm k.y.$^{-1}$)	**3 Mt** scenario (mm k.y.$^{-1}$)
Northern reaches		
B1	31	5
B2	342	52
B3	2232	340
B4	478	73
B5	786	120
Southern reaches		
TD	317	48
IG1	482	73
IG2	1261	192
IND-7	133	20

FIGURE 3.8: Comparison of cosmogenic ^{10}Be- and BP-derived erosion estimates, using centered data and linear regression with zero intercept; left and right y-axes show 20 Mt and 3 Mt scenarios, respectively. Abbreviations refer to Fig. 3.4; B3 value is not included to regression. Right panel: Erosion rate estimates from petrology and heavy minerals analyses; 20 Mt scenario from forward linear modeling (Garzanti et al., 2005); 3 Mt scenario from backward linear modeling, using ^{10}Be derived denudation rates as seed. For reaches and QFP-petrology see Fig. 3.4.

3.5.3 Postglacial denudation outweighed by long-term exhumation

Our study expands the geographic scope of previous work on landscape lowering in the Transhimalayan ranges. We emphasize that our late Quaternary denudation rates are systematically below long-term (>10^6 yr) exhumation rates of 0.1–0.4 mm yr^{-1} constrained by thermochronological data (Clift, 2002; Kirstein, 2011; Kumar et al., 2007; Sinclair and Jaffey, 2001; van der Beek et al., 2009) (Fig. 3.6A). With averaging timescales of 5–65 kyr (Table 3.3), we consider our denudation rate estimates to span postglacial periods, judging from the regional glacial chronology that rests on the Himalayas oldest dated moraines. Nonetheless, glaciers may have carved the upper Indus Valley only slightly during the late Pleistocene (Owen et al., 2006). Thus, denudation rates along both sides of the Indus valley must have been much higher before postglacial times in order to explain the observed crustal cooling patterns through denudational response. Such a postglacial slow-down of denudation necessitates that oscillating erosion rates during glacial-interglacial cycles play a key role in shaping the decay of this part of the western Tibetan Plateau margin. Denudation rates in this arid bedrock landscape are also strikingly low given the topographic relief and hillslope steepness. But which mechanisms slow down postglacial landscape downwearing at the western Tibetan Plateau margin? If accepting aridity as an obvious first-order cause of limiting rates of denudation, then glacial periods in Transhimalayan Ranges must have been either wetter, more erosive, or both. Indeed, changes to the erosional efficacy over glacial-interglacial cycles may be central to governing the erosional decay of this part of the western Tibetan Plateau margin, and perhaps aided by less vigorous erosion following the cessation of tectonic activity after tilting of the Ladakh Range (Dortch et al., 2011c).

3.6 Conclusions

We highlight a regional order-of-magnitude decrease of ^{10}Be-derived denudation rates from 110 mm kyr^{-1} to 10 mm kyr^{-1} towards the western Tibetan Plateau margin. The sedimentary signature of river sands from the Indus and its tributaries support this erosional gradient. Petrology and heavy-mineral analyses of fluvial sand allow decomposing the Indus sediment load, provenance, and erosion rates, and independently point at dominant sediment input from the central Zanskar Range along the only major (>30-km long) alluvial reach, where a massive tributary fan apron constrains the upper Indus. Moreover, the spatially better resolved denudation-rate pattern from cosmogenic nuclide inventories refines the erosion rate estimates from sand petrology. Still, the overall erosional gradient across the western Tibetan Plateau margin is inconsistent with the location of the major knickpoint that defines this margin. The highest increases in denudation rates occur 150–200 km downstream of this knickpoint. A transient wave of erosion in the lower study reaches of the Indus River is the simplest possible interpretation that can explain this pattern without additional lithological or climatic controls. The observation that our millennial-scale denudation rate estimates are outpaced by long-term crustal exhumation requires that denudation rates must have been higher beyond the averaging, that is postglacial, timescales of our ^{10}Be method in order to explain the cooling pattern via denudation.

Acknowledgements

Funded by the German Research Foundation (DFG KO3937/1, 2), and PROGRESS, the Potsdam Research Cluster for Georisk Analysis, Environmental Change and Sustainability. We thank Johanna Meyer, Martin Struck, Piero Catarraso, Robert Weibach, Judith Thäle, Franziska Scheffler, Bettina Richter, Anja Städtke and Antje Musiol for assisting with sample preparation. We are grateful for field assistance by Tsering Lonpo, Tsering Samphel and Tinles Nubuu. Helpful comments by Sarah Penniston-Dorland, Craig Dietsch, and an anonymous reviewer are well appreciated, and we thank Christian Köberl for handling the manuscript.

Appendix B. Supplementary material

Supplementary material related to this study can be found in Appendix B.

Chapter 4

Study III - Denuding the Himalaya-Tibet orogen: Noise vs. Time

Abstract

Concentrations of cosmogenic ^{10}Be in river sands allow estimates of basin-averaged denudation rates that often vary by orders of magnitude in comparable environmental settings. This variance has confounded the detection of tectonic, climatic, or topographic predictors of denudation rates. Systematically analyzing ^{10}Be inventories with ordinary least-squares (OLS) regression for identifying the more useful of such predictors has had mixed and inconsistent success, partly because of noisy data and the inherent dependence of denudation rate on the timescales that samples average over. We hypothesize that correlation between denudation rate and any tectonic, climatic, or topographic candidate predictor(s) should be independent of averaging timescale. We test this hypothesis by analyzing 297 cosmogenic ^{10}Be-derived basin-averaged denudation rates from the Himalaya-Tibet orogen. These rates span nearly three orders of magnitude (8 mm kyr^{-1} to 6,135 mm kyr^{-1}), creating significant noise that compromises meaningful OLS regression. We demonstrate that quantile regression instead deciphers, and corrects for, a timescale-dependent signal in basin-wide denudation rates. Principal component analysis reveals that four out of 26 candidate tectonic, climatic, and topographic predictors explain ~80% of the total variance. We predict denudation rates at the basin scale using the normalized channel steepness (or equally mean basin slope), and find that the largest prediction errors remain between 5 mm kyr^{-1} and 10 mm kyr^{-1}, depending on how quickly basins denude. Our results support a functional relationship between denudation rates and topographic steepness in our study area, whereas decadal

climate and tectonic metrics step back as potential predictors. We conclude that quantile regression consistently reconciles the apparent noise and timescale dependence in the data, while permitting robust predictions of denudation rates in the Himalaya-Tibet orogen.

4.1 Motivation

Meaningfully comparing estimates of denudation rates in mountainous terrain remains a challenge for geoscientists given the broad choice of archives and dating techniques that cover differing timescales of interest. The varying lengths of these temporal observation windows complicate estimates of denudation rates by blending highly erosive events with more protracted, quiescent periods within a given measurement interval (Finnegan et al., 2014; Kirchner et al., 2001). Basin-averaged denudation rates from cosmogenic ^{10}Be concentrations in river sands (Granger et al., 1996) routinely yield estimates varying over several orders of magnitude in similar environmental settings (Portenga and Bierman (2011); Willenbring et al. (2013); Fig. 4.1). This variance has compromised the search for straightforward tectonic, climatic, or topographic predictors of denudation rates, let alone the data-driven validation of models that relate denudation rates to hillslope steepness or topographic relief (Montgomery and Brandon, 2002; Roering et al., 2007).

Nonetheless, efforts have been made to unravel spatial patterns in ^{10}Be-derived denudation rates by analyzing their covariance with various topographic, tectonic, and climatic predictors, including mean basin slope gradient (Willenbring et al., 2013), river-channel steepness (Ouimet et al., 2009), rock uplift rate (Godard et al., 2014), topographic relief (Montgomery and Brandon, 2002), or precipitation-driven runoff (Godard et al., 2014). Studies taking advantage of both regional and global compilations of ^{10}Be-derived denudation rates (Portenga and Bierman, 2011; Willenbring et al., 2013) have tried to pick tell-tale trends from the broad scatter of data, though with mixed and partly inconsistent success.

Ordinary Least Squares (OLS) regression has been the commonly used prediction tool in these studies. This method returns the average expected trend of a response (variable) distribution—in this case denudation rate—for changes in one or several purported predictor variables. Using this approach, however, one overlooks that ^{10}Be-derived denudation rate estimates scale with the timescale that the samples average over in a reciprocal manner (Lal, 1991). Both measures derive from nuclide concentration, and higher denudation rates imply commensurately shorter averaging timescales (Granger et al. (1996); Fig. 4.2A). This effect may introduce substantial noise to OLS regression plots, thus compromising fit statistics and any resulting interpretations.

We hypothesize that any physically (or chemically) grounded correlation between cosmogenic ^{10}Be-derived denudation rates and tectonic, climatic, or topographic candidate predictor(s) is independent of such noise, and hence, of duration of averaging timescale. We test this hypothesis for the Himalaya-Tibet orogen (Figs. 4.1, C.1), a geographic region for which we obtained sufficient spatial data covering for both predictor and response variable(s). We carry out standard OLS regression on these data and test whether quantile regression can circumvent the seeming dilemma of meaningfully comparing denudation rates across differing timescales. Quantile regression, a statistically robust alternative to OLS regression, affords insights to the full sample distribution of a response variable (Koenker, 2005), and allows identifying potentially limiting predictors that may not be included in the analysis (Cade and Noon, 2003). Our aim is to explore whether quantile regression can be used to (a) decipher a timescale-dependent signal in basin-wide denudation rate estimates; (b) determine which tectonic, climatic, and topographic predictors are most promising; and (c) predict basin-wide denudation rates across the Himalaya-Tibet orogen.

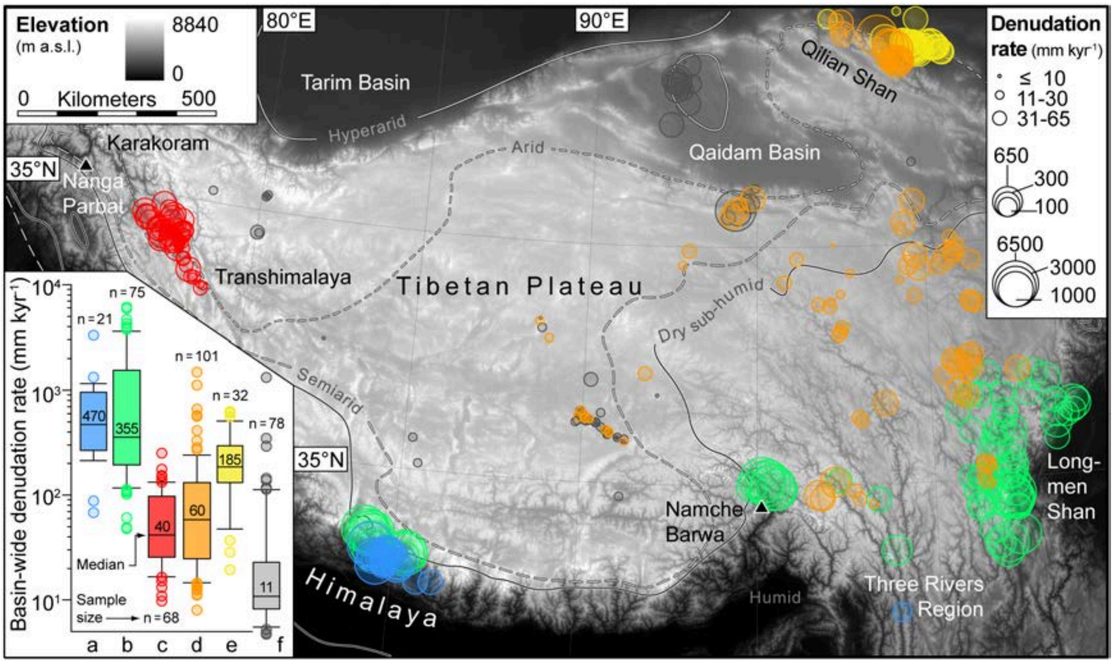

FIGURE 4.1: Shaded relief of the Himalaya-Tibet orogen (90-m SRTM DEM) with bubbles scaled to basin-wide denudation rates from ^{10}Be inventories. Circle and boxplot colors show cluster membership from k-means clustering; grey circles are denudation rates from bedrock samples. Contour lines show spatial pattern of AI (Zomer et al., 2006). Boxplot whiskers encompass 10th and 90th percentiles; circles are outliers: a) lower Himalayan front; b) High Himalayas, eastern Himalayan syntaxis, and Longmen Shan; c) Transhimalayan ranges; d) Tibetan Plateau; e) Qilian Shan; f) bedrock exposure-derived samples.

4.2 Data and Methods

We build upon and extend a worldwide compilation on basin-wide denudation rates from ^{10}Be concentrations in river sands (Willenbring et al., 2013), focusing on a geographic subset for our test site, the Himalaya-Tibet orogen (Figs. 4.1, C.1). We select 271 published and recalculated basin-wide denudation rates from 16 studies covering parts of the Himalayas, the eastern Himalayan syntaxis, the southeastern Tibetan Plateau, the Qilian Shan, and adjacent mountain ranges of northeastern Tibet (Fig. C.1). We augment this compilation by 26 new samples from the Tibetan Plateau interior, and the Transhimalayan ranges (Table C.1). We focus on drainage basins with areas $<10^3$ km^2, and exclude larger ones for reasons of statistical comparability. We complement our inventory by a set of 78 published and recalculated ^{10}Be-derived denudation rates from bedrock outcrops largely located on the Tibetan Plateau (Fig. 4.1).

For each sampled drainage basin, we computed the area-weighted means and standard deviations of 26 tectonic, climatic, and topographic candidate predictors, using data from the World Strain Map (Kreemer et al., 2003); a range of bioclimatic—BIOCLIM—parameters from the WorldClim database (Hijmans et al., 2005); a global Aridity Index (Zomer et al., 2006); the Global Seismic Hazard Assessment Program (Giardini et al., 1999), and various topographic derivatives from hydrologically corrected 90-m SRTM data (Shuttle Radar Topography Mission) (Tables C.2, C.3, C.4-C.7). We ran a k-means cluster analysis to group drainage basins with similar tectonic, climatic, and topographic characteristics using all predictors except of elevation, drainage basin area, geographic coordinates, and any ^{10}Be-concentration derived measure (Figs. 4.1, C.2). We used a dendrogram from Ward hierarchical clustering to arbitrarily limit the number of clusters (Fig. C.3). Principal component analysis (PCA) with a Varimax data transformation consolidated our predictor set, and helped identify those containing most of the overall variance of our data (Fig. C.4).

Our application of (bootstrapped; see DR C.5.3) quantile regression is motivated by its ability to fit models to any number of conditional quantiles of the sampled denudation data instead of obtaining a single OLS model fit that solely expresses the response variables average central tendency. We $\log_{10}$-transform our denudation rate estimates (Fig. 4.2A), and fit bootstrapped linear models of the form $\log_{10}\dot{\mathrm{E}} = \mathrm{x0}_i + \beta_i \mathrm{x}$, where β_i is the slope, and $\mathrm{x0}_i$ is the intercept for the i^{th} quantile model, respectively, using the most important predictors identified from PCA (Figs. C.2, C.4). For timescale-independent relationships between denudation rates and these predictors, we expect that values of β_i are statistically indistinguishable, while the intercepts $\mathrm{x0}_i$ should increase linearly with increasing denudation rates (Fig. 4.2 A1). Thus, the regression models should be shifted parallel along the y-axis, reflecting comparable trends irrespective of averaging timescale. In any other case, the quantile regression should return either invariant intercepts with varying slopes, or any other mixture of quantile models (Fig. 4.2 A2, A3).

4.3 Results

Recalculated ^{10}Be-derived basin-wide denudation rates in the Tibet-Himalaya orogen span nearly three orders of magnitude, ranging from 8 mm kyr^{-1} to 6,135 mm kyr^{-1} (Fig. 4.1, Tables C.1, C.4); the corresponding averaging timescales (see Table C.1) range from 75 kyr to 0.1 kyr, respectively. The median denudation rate is 120 mm kyr^{-1}, and bedrock-derived denudation rates are consistently lower at a median rate of 11 mm kyr^{-1}. The basins sampled at the southern and eastern margins of the Tibetan Plateau denude the most rapidly, whereas basins at the western and northeastern margins, and the plateau interior denude at rates roughly an order of magnitude lower. A hierarchical cluster analysis with five groups replicates this distinct spatial pattern (Figs. 4.1, C.3).

From PCA we find that the 26 candidate predictors may be collapsed to four principal components (PCs) that explain ~80% of the total variance (Figs. C.2, C.4). These PCs contain very high factor loadings (>0.95) from the Aridity Index (AI), the maximum temperature of the warmest month (BIO05), the precipitation of the coldest quarter (BIO19), and channel steepness (k_S). These four PCs may be labeled effective *rainfall*, *temperature*, *steepness*, and *cold aridity* (Figs. C.2, C.4). For quantile and OLS regression we simply used those predictors loading highest onto the four highest-ranking principal components, respectively, including AI, BIO05, BIO19, and k_S (Figs. C.2, C.4).

Quantile regression returns intercepts that, for the conditional quantiles, increase linearly with quantile rank for these four predictors (Figs. 4.2, 4.3). In contrast, the slopes of the quantile models remain largely invariant. However, BIO05 returned too many insignificant model slopes so that we excluded this parameter from further analysis. Multiple regression assuming additive effects reveals opposing trends in the slopes for AI and BIO19, especially for the higher quantiles (Fig. 4.2). In contrast, the regression slopes of k_S remain remarkably invariant regardless of quantile rank (Fig. 4.3).

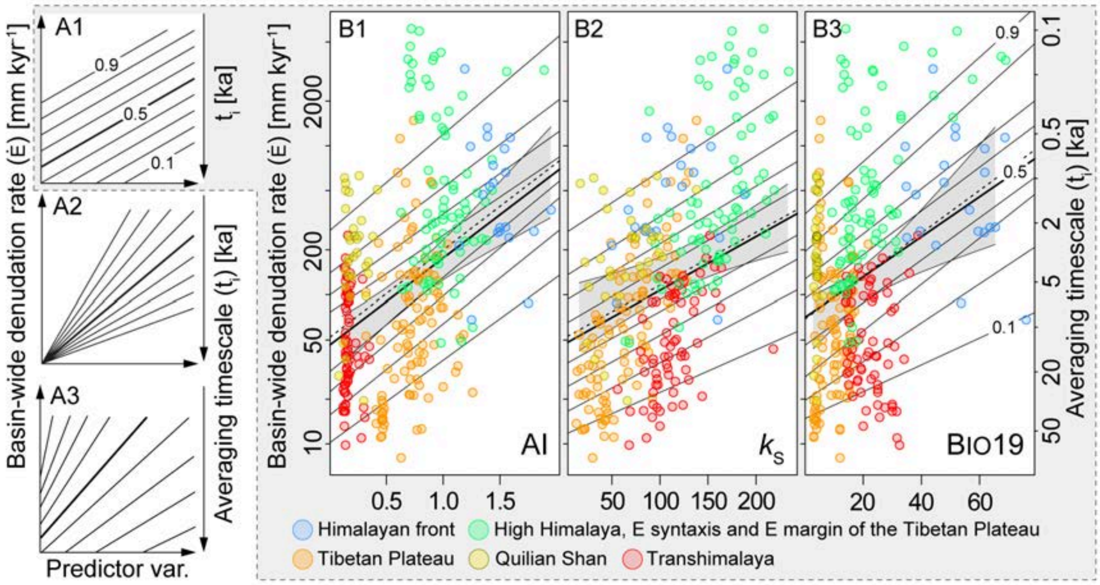

FIGURE 4.2: Schematic interpretation of quantile regression models for basin-wide denudation rates from cosmogenic ^{10}Be inventories and individual predictors. A1) Timescale-independent correlation between denudation rate and predictor(s) with comparable slopes and equally spaced intercepts, A2) varying slopes and invariant intercepts, and A3) varying slopes and intercepts indicate time-scale dependent denudation rates. Regression results with predictors B1) Aridity Index (AI), B2) Channel steepness index (k_S), and B3) Precipitation of coldest quarter (BIO19), from 1000 bootstrap simulations; for colors see Figs. C.1, C.3. Note sub-parallel and equidistant bootstrapped quantile regression models (black thin lines for 0.1- to 0.9-quantiles); dashed lines are bootstrapped robust OLS regression models with gray shaded 95% confidence intervals.

4.4 Discussion

Water availability and topographic steepness in their broadest sense feature prominently in the four PCs that explain ~80% of the variance in our 26 candidate predictors of basin-wide denudation rates in the Himalaya-Tibet orogen (Fig. C.4). The Aridity Index (AI), together with annual precipitation, has the highest loading on the first principal component (PC1), and expresses the ratio of mean precipitation and mean evapotranspiration, offering a proxy of the water available for runoff and storage. Although evapotranspiration has only minor influence on Himalayan river discharge (Bookhagen and Burbank, 2010), AI explains the highest percentage of the total variance of all candidate predictors by far. River-channel steepness k_S, and the highly covariant mean basin slope (Fig. C.6A), are the prime topographic predictors, and largely encapsulated in PC2. This result confirms theoretical considerations and vindicates the use of hillslope or channel steepness as proxies of denudation rates (Montgomery and Brandon, 2002; Roering et al., 2007). The precipitation of the coldest quarter (BIO19) is snowfall in most parts of the study area. Snow cover may modulate cosmogenic-derived denudation rates either by storing excess water released during snowmelt and by enhancing shielding from secondary cosmic rays, in combined net effect yielding higher denudation rate estimates (Schildgen et al., 2005). We cannot exclude that tectonics and seismicity may play more central roles in controlling denudation in the Himalaya-Tibet orogen (Godard et al., 2014), mainly for reasons of lacking detailed data. Clearly, a better spatio-temporal resolution tectonic deformation data, and particularly of rock uplift rates throughout the region is desirable.

Bootstrapped quantile regression using our predictors of water availability and topographic steepness returns evenly spaced intercepts and nearly indistinguishable slopes as a function of quantile rank (Figs. 4.2B, 4.3). The rates at which denudation rates increase with AI and BIO19 remain largely comparable irrespective of quantile rank. If viewing the different quantiles as fractions of different averaging timescales, then this finding supports our initial hypothesis that the rates of change in ^{10}Be denudation rates with a given predictor are comparable across different timescales (Figs. 4.2, C.8). The regression slopes simply shift their location over the conditional quantiles of the sample data, thus smearing out in parallels the linear trend for a given timescale, largely reconciling the impression of noisy data. In contrast, OLS regression offers mostly unsatisfactory models with substantial scatter; the variance in denudation rates is much better captured by regression quantiles. For example, basins with low denudation rates tend to respond slightly less to changes in basin-averaged channel steepness than do rapidly denuding basins (Fig. 4.3).

Multiple quantile regression with additive effects in the predictors, assuming that any predictor's effect on the response distribution remains the same, highlights the robustness of k_S (and similarly, mean basin slope) as a potential control on denudation rates. Channel steepness is a widely used topographic metric of bedrock-river adjustment to climate, rock type, and tectonic uplift, and turns out to be more robust than the decadal climate metrics (Figs. 3, C.8). Especially BIO19 has bootstrap intervals that overlap with zero slope for all quantiles such that the influence of the precipitation of the coldest quarter on denudation rates remains doubtful (Fig. C.8).

Finally, the remaining 25% of testing data show that our quantile models are well suited for predicting unseen denudation rates (Figs. 4.3, C.8). We use the averaged sums of absolute residuals with respect to the testing and training data for expressing the fitting and generalization errors, respectively. Using k_S as a single predictor, >95% of the largest computed prediction errors are between 5 mm kyr^{-1} and 10 mm kyr^{-1} for the 0.1- and 0.9-quantiles, respectively (Fig. 4.3C). The higher prediction error for more rapidly denuding basins is consistent with the higher analytical uncertainties involved for samples with low ^{10}Be concentrations (Figs. 3C, C.8).

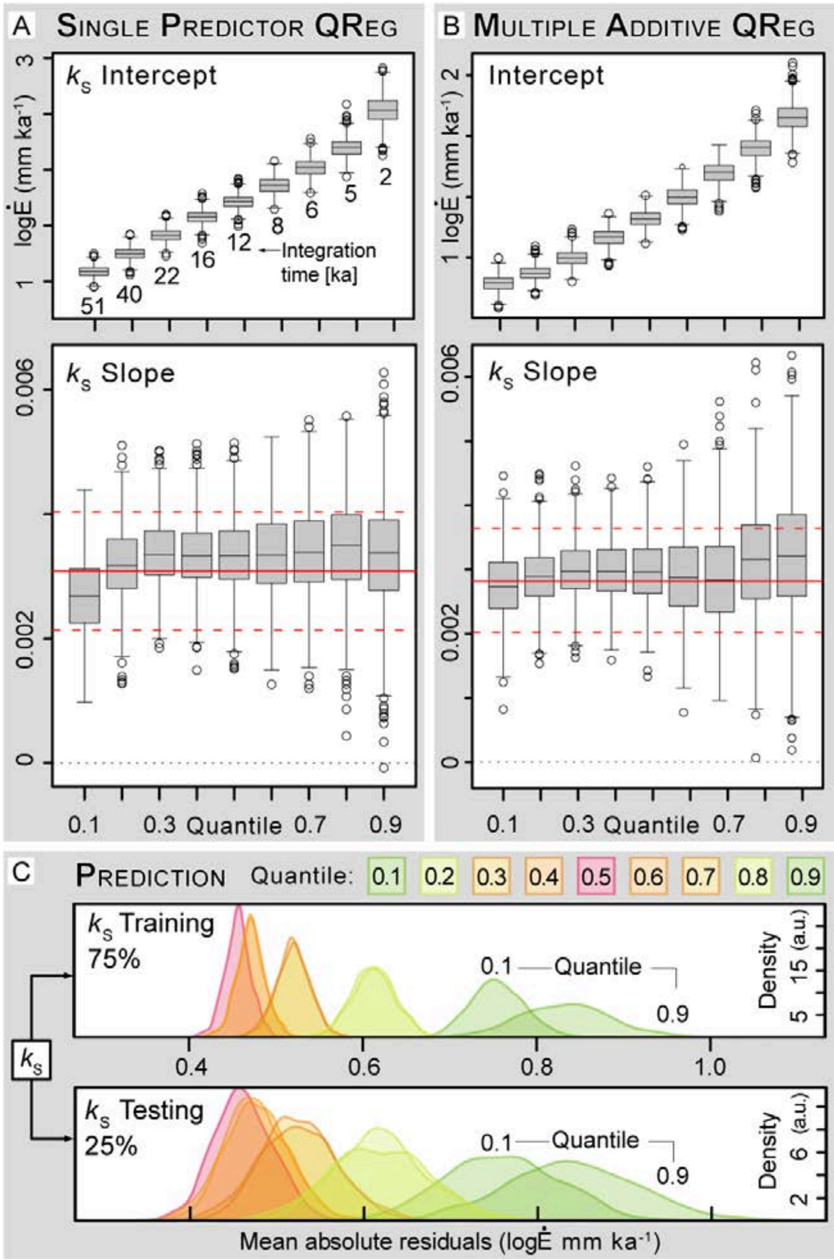

FIGURE 4.3: Quantile regression models and residuals for the 0.1- to 0.9-quantiles, using cosmogenic ^{10}Be-derived basin-wide denudation rate as the response variable and steepness index (k_S) as predictor. A) Intercepts and slopes per quantile rank from 1000 bootstrap simulations; blacked dashed lines are zero regression slopes. Boxes frame 25^{th} to 75^{th} percentiles, bold lines in box are medians; whiskers extend to 1.5 times the interquartile range; circles are outliers. Solid red lines are median slopes from 1000 bootstrap simulations of OLS (Ordinary Least Squares) regression; dashed red lines are 95% confidence bounds. (B) Results from multiple quantile regression with additive effects. C) Mean absolute residuals for training and testing data. Central quantiles (red to orange) have smaller errors than distal (greenish) quantiles; generalization errors of testing data consistently exceed the fitting errors of the training data.

4.5 Conclusions

Cosmogenic ^{10}Be-derived basin-wide denudation rates from small to moderate basins ($<10^3$ km^2) draining the Himalaya-Tibet orogen span three orders of magnitude, ranging from 8 mm kyr^{-1} to 6,135 mm kyr^{-1}, with averaging timescales of 75 to 0.1 kyr, respectively. Quantile regression offers a statistically robust way of gauging the influence of tectonic, climatic, and topographic predictors on ^{10}Be-derived denudation rates across different timescales, while resolving the seeming dilemma of noisy data that arise from relying on simple OLS regression. Our quantile regression results corroborate earlier views of functional relationships between denudation rate and topographic steepness. Multiple regression highlights how widely used metrics of channel (or hillslope) steepness offer largely timescale-invariant predictions, whereas predictors summarizing historic climate conditions such as aridity or precipitation partly yield insignificant regression slopes.

Acknowledgements This study was funded by the German Research Foundation (DFG KO3937/1, 2), and the Potsdam Research Cluster for Georisk Analysis, Environmental Change and Sustainability (PROGRESS). Hella Wittmann and the GFZ Potsdam Earth Surface Geochemistry staff generously shared their lab. We computed statistics using the R software environment (www.r-project.org).

Appendix C. Supplementary material

Supplementary material related to this study can be found in Appendix C.

Chapter 5

Discussion

The following discussion distills a number of findings that emerge from the combined results of the three previous studies. The original questions are revisited in the light of the findings that we obtained from these studies, and reflections on the overarching implications of this PhD thesis that derive as added value to the sum of the individual studies are presented. The discussion sets off at the regional scale and then gradually zooms in to conclude about the role of local (hillslope) processes of denudation in the Himalaya-Tibet orogen.

5.1 Topographic vs. climatic predictors for ^{10}Be-derived basin-averaged denudation rates in the Himalaya-Tibet orogen

Research Question 3

Tectonics, climate or topography: Do functional relationships between denudation rate and predictors exist that are independent of observation timescale?

The challenge of meaningfully comparing geomorphic process rates that scale with observation timescale has been introduced in Chapter 1 (Finnegan et al., 2014; Gardner et al., 1987; Kirchner et al., 2001; Sadler, 1981; Sadler and Jerolmack, 2014; Willenbring et al., 2013). Dealing with inventories of cosmogenic-derived denudation rates, especially when these data range over several orders of magnitude, or in other words cover a wide range of averaging timescales (Fig. 1.8B; Portenga and Bierman (2011); Willenbring et al. (2013)), is emblematic of this problem. How do we know, that the relationship between explanatory and explained variable, i.e. between predictor and denudation rate stays the same across orders of observation timescales? In order to investigate this problem we hypothesized that any meaningful correlation between cosmogenic-derived ^{10}Be denudation rate and predictor should be timescale-independent. To look into the full response distribution to candidate predictors we choose quantile regression analysis, which has not been used in this context to our knowledge so far.

In Section 4.3 we show how quantile regression can help converting the drawback of data scatter in response distributions to valuable time-related information on the relationship between predictor and predicted variable. To do so we boiled down a set of n = 26 topographic, tectonic and climatic candidate predictors to the number of just four, using principal component analysis (PCA). The subsequent application of (bootstrapped single predictor) quantile regression on these four predictors, that still represent ∼80% of data's total variance, points to the significance of just three out of the full set: Aridity Index (AI), steepness index (k_S), and precipitation of the coldest quarter (BIO19). The qualities of these distilled predictors suggest that for the n = 297 samples from our study area—the Himalaya-Tibet orogen—the availability of water as a transport agent and topographic steepness are the most decisive environmental controls on basin-averaged denudation rates. With respect to this we note that average slope gradient performs equally (good) as k_S does, and other slope-derived predictors (HEP, LWAV; Fig. C.7) also yield evenly spaced regression quantile models with similar slopes. However, due to k_S's assumed robustness referring to denudation rate analysis (e.g. Ouimet et al., 2009) we decided to not further use mean basin-slope gradient in our analysis. Further, we exclude metrics like HEP and LWAV from analysis because these variables turned out to be of low explanatory power regarding the total variance of our data set.

For the conditional regression quantiles on the response distributions of the three selected predictors we find (a) equally spaced intercepts accompanied by (b) nearly indistinguishable model slopes. The observation that regression slopes are simply shifted over the conditional quantiles firms up our hypothesis as it brings out the information that the functional relationships between denudation rate and said predictors are time-independent. However, AI, k_S, and BIO19 have been identified as the highest-loading variables of the principal components with the highest explanatory power, respectively. Thus these three predictors originate from sets of linearly uncorrelated sets of variables. Acknowledging this finding we assume additive effects of AI, k_S, and BIO19, consequentially performing additive multiple regression analysis with stable effects of individual predictors on the response distribution.

While AI and BIO19 show inconclusive trends from multiple quantile regression, partially not being statistically non-zero, k_S turns out to be the most robust predictor regarding the requirements of our hypothesis best (Fig. 4.3). Regarding this finding, and keeping in mind the similarly good performance of SLP, and additionally having tested long-wave topographic gradient (Table C.2, Fig. C.7) for its suitability as predictor it becomes apparent that out of our set of 26 tectonic, climatic and topographic candidate predictors topographic metrics are best-performing. We propose that this may be owed to the differences in observation timescales behind our topographic, tectonic and climatic predictors. While the climate and tectonics data have been derived from decadal observations, topographic metrics rather integrate over millennial scales (and hence they may be interpreted as the direct result of climate and tectonics). However, estimates of cosmogenic-derived denudation rates are—depending on pace of denudation—fairly insensible to short-term system fluctuations or disturbances (von Blanckenburg, 2005). We therefore argue that topographic predictors and cosmogenic-derived denudation rates are timescale-compatible, whereas our predictors representing climate and tectonism are not.

5.2 Spatial offset between peak denudation rates and location of the western Tibetan Plateau margin

Research Question 2

Active or inactive: Can basin-averaged denudation rates unveil the erosional state of the western Tibetan Plateau margin?

Various thinkable mechanisms behind the conspicuous resistivity of the Tibetan Plateau margin against erosive decay have been introduced on page 11ff. Regardless of the mechanism behind the seemingly slow plateau margin decay there are striking differences in topography between (a) the low-relief Tibetan Plateau and (b) its deeply dissected mountainous surroundings (Fielding et al. (1994); Fig. 1.5). The transition between (a) and (b) is reflected in the long profiles of rivers (Wohl, 2000) draining the Tibetan Plateau as more or less pronounced knickpoints (or -zones) downstream of which channel slope increases measurably (Walsh et al., 2012). Consequentially, and assuming active river incision, rates of (associated) catchment denudation should increase concomitantly, (e.g. Ahnert, 1970; Flint, 1974; Montgomery and Brandon, 2002; Ouimet et al., 2009).

Our data from Section 3.4 suggest that the topographical knickpoint of the Indus River long profile (near Mahe, Fig. 3.3) marking the transition from the western Tibetan Plateau margin to the Transhimalayan Zanskar and Ladakh ranges, and the highest basin-wide denudation rates that we determine from cosmogenic-^{10}Be derived concentrations in the sands of Indus tributaries are offset by 150 to 200 km (Fig. 3.1). Seeking after possible controls of this offset we find that the values of channel steepness in the Indus tributaries reveal focussed fluvial incision and concomitant oversteepened tributary toes in the very downstream reaches of our study area (near Hanuthang on Fig. 3.7). Together with upward trending k_S values of the Indus River we interpret this as ongoing adjustment of the downstream tributaries to intensified incision of the trunk river there (Wohl, 2000), perhaps in response to a transient headward migrating erosional wave into the Tibetan Plateau. This transient erosional wave, however, has not propagated into reaches upstream Indus-Zanskar confluence (Fig. 3.7), and fluvial incision into the plateau margin with <20 mm kyr^{-1} is close to being inactive.

The short and narrow bedrock gorge that connects the broad and alluviated sedimentary basin of the Leh valley (see orange colored area on Fig. 3.1) and the Indus-Zanskar confluence appears to be the bottleneck that this erosional wave would have to pass before tapping the sedimentary fill of the Leh basin. This idea is fueled by the observation that the fluvial network of the Indus did not manage to evacuate the presently estimated ~25 km^3 (Blöthe and Korup, 2013) of sedimentary Leh valley fill (see orange area on Fig. 3.1), that shields bedrock from erosion and buffers upstream (plateau) reaches from river incision. Accommodation space for such alluviated reaches, even though generally smaller than the in Leh valley, is provided by the alternation of narrow bedrock gorges and broadened river (confluence) reaches in all major tributaries of the upper Indus River—e.g. Shyok, Shigar, or Hunza. Our data from the upper Indus valley give reason to speculate that these alluviated reaches could play a decisive role in plateau margin preservation, by promoting intermittence of sediment flux and prolongedly storing sediments that sufficiently shield bedrock. Looking further into this theory gives rise to the question after the process(es) that provide(s) these sediments.

Given our knowledge of the regional glacial (Burbank and Fort, 1985; Dortch et al., 2013; Mitchell et al., 1999; Owen et al., 2006) and infill-and-incision history (Blöthe et al., 2014; Dortch et al., 2011a; Pant et al., 2005) that involved repeated alternations of glacial and inter-glacial stages—and concomitant phases of paraglacial transitions (Ballantyne, 2002)—it appears more than likely that the upper Indus valley has experienced arid settings comparable to the current state repeatedly during the Quaternary. Regarding this Blöthe et al. (2014) postulate that major phases of valley infilling and incision on timescales of 10^3–10^4 years do neither require evidence of tectonic or lithological controls (nor do they show obvious correlation with monsoon proxies) for the region in the vicinity of the Indus-Zanskar confluence. Instead these authors stress the concomitance of phases of terrace formation with post- and inter-glacial sediment pulses, and attribute the formation of large lakes in the region to damming by large landslides, glaciers or alluvial fans. This see-saw of sediment deposition and incision, in concert with accommodation space sufficient for km^3-sized sediment reservoirs could have served as first-order control on the preservation of the western Tibetan Plateau margin, by episodically holding off an, otherwise plateau-attacking, upstream migrating erosional wave. This explanation is not in conflict, but in fact reconcilable with theories invoking river damming and concomitant aggradation by repeated glacial advances or slope failure, with the latter being most effective in deep and narrow gorges.

The denudation rate estimates that we derived from bulk petrography (BP), and that are based on a 15-year gauging time series yielding an annual sediment load of ~20 Mt for the upper Indus (Ali and de Boer, 2007), show a downstream increase for our study area similarly to that derived from our millennial ^{10}Be-derived estimates. Nonetheless, BP-derived denudation rate estimates range approximately one order of magnitude above the CN-derived values. We attribute this disparity to various methodical limitations with the most important being uncertainties arising from (a) grain counting and other BP procedure that relies on individual decision, (b) making generalizations when delimiting homogenous erosional reaches that contain catchments of similar erodibility (Figs. 3.4, B.1), and mainly (c) the short observation time of 15 years of river gauging that is related to the millennial ^{10}Be-derived denudation rates. We therefore note that denudation rate estimates derived from the two methods appear to be limitedly comparable. Nonetheless, we stress that despite this drawback bulk petrography yielded valuable insight to the routing pathways and relative contributions of riverine sediments that CN-abundances would not have revealed.

The notion of past periods of Transhimalayan landscape evolution that have been characterized by more effective denudation is further promoted by our comparative review of studies employing thermochronometer-derived data to quantify long-term (>10^6 yr) exhumation. These rates range between 0.1 to 0.4 mm yr^{-1} (Fig. 3.6), or even 0.75 mm yr^{-1} (Clift, 2002; Kirstein, 2011; Kumar et al., 2007; Sinclair and Jaffey, 2001; van der Beek et al., 2009), depending on level of confidence. Surprisingly, our ^{10}Be-derived denudation rates, with largely postglacial averaging timescales of of 5 to 65 ka, range between 0.01 and 0.1 mm yr^{-1}, i.e. clearly below said long-term rates. The simplest explanation—including the possibility of millennial lag times in sediment routing (Blöthe and Korup, 2013) and concomitant sediment storage—for this difference in landscape downwearing would involve a postglacial relaxation of the geomorphic system (Ballantyne, 2002), i.e. denudation rates that must have been higher before the (postglacial) interpolation interval of our cosmogenic ^{10}Be denudation rates. Climatic fluctuations during the Quaternary, involving repeated glaciation and deglaciation (Owen et al., 2006, 2008), entraining considerable accumulation and evacuation of sediments (Blöthe et al., 2014), may have involved much more effective denudational processes in this arid bedrock landscape than recent ones. Since recent denudation, and evacuation of sediments, in the study area seem to be on the drip of prevailing aridity with lacking morphological effective surface runoff (Lamb and Davis, 2003), pre-postglacial periods may have been characterized by a climatic shift towards more humid conditions and concomitantly increased efficacy of denudation.

However, indications for prolongedly stable environmental conditions in the Transhimalaya exist. Some glacial moraines and fan sediments in the upper Indus valley have been dated to far beyond 300 ka, and even >400 ka (Owen et al., 2006), accounting for a high landform preservation potential. Field observations of terrace bodies situated on steep valley flanks and elevated high above river level, of glacial moraines at the edge of incised bedrock gorges and of alluvial fans seemingly inactive during postglacial times reveal partly well preservation of these unconsolidated sedimentary bodies. Taking further into account the limited extent of these (and any following) glaciations that shaped these landforms (Owen et al., 2006)—which can be interpreted as indication of lacking moisture—prolonged and prevailing aridity, interrupted by wetter phases of incision and washing off, in the rain shadow of the High Himalaya is the simplest and most conclusive explanatory mechanism for low denudation rates and long-lasting landscape preservation. This notion is supported by the conspicuous stability of the cluster formed by the Transhimalayan samples (Figs. 4.1, C.3) using k-means cluster analysis across runs with varying k.

5.3 Learning about denudation from the internal sedimentology of giant rockslides

Research Question 1

Valuable snapshots: What can the internal sedimentology of giant rockslides reveal about their runout processes and triggering mechanisms?

In active mountain ranges landsliding is a major contributor to denudation. Especially (chaotic) deposits of giant rockslides are large sediment sources whose potentially high comminution facilitates entrainment by erosion agents. Studies dealing with the unambiguous interpretation of deposits with chaotic internal sedimentology have been facing a number of interpretative uncertainties. One possible solution to that has been introduced by Reznichenko et al. (2012) who presented a diagnostic technique on microscopic scale that helps identifying rapid, high-stress comminution—a typical feature of debris from large (>10^6 m^3) catastrophic rockslides —in candidate deposits. Identifying the mechanisms that led to the emplacement of chaotic mass-wasting deposits in active mountain areas based on exclusively microscopically-diagnosis is fascinating, but also somehow unsatisfying mainly for one reason: there are processes apart from rocksliding that involve mechanisms of rock comminution too, such as meteorite impact or tectonic faulting. Exclusively relying on microscopic evidence to distinguish between said processes, again, may lead to misinterpretation. We propose that the combination of fragmented or even comminuted rock, the presence of internal shear planes, and of frictional melt altogether mantled with a carapace of angular boulders serve as distinct evidence for giant-rockslide origin of the respective deposit.

However, confusion of rockslide deposits (or their features) with other natural structures may not be exclusively caused by rock comminution. Outcrops of several shear planes may be interpreted as multi-phase landslide emplacement (Hermanns et al., 2006). Consequent over- or underestimation of large landslide contribution to overall landsliding may lead to distorted magnitude-frequency relationships (Hovius et al., 1997) causing concomitantly biased hazard assessment, which relies on information on e.g. recurrence intervals of events of a certain size. The fine-grained, and often glassy deformation fabric of rockslide-derived frictionites closely resembles that of pseudotachylites (Sibson, 1975; Takagi et al., 2007), the latter, however, being generated by earthquakes. We also stress that additional confusion potential arises when material from shear zones of rockslide deposits is compared with fault gouge of tectonic origin or impact-breccia. Referring to this we show that grain-size distribution of samples that represent these different cataclasic processes cannot help distinguishing between their different origins since the underlying mechanism of rock brecciation or comminution is nearly the same (Fig. 2.5, Table A.2). This is why the lab-based microscopic identification of brecciated or comminuted mass wasting deposits, which have been taken out of the stratigraphic context of facies, may lead to erroneous and misleading interpretation.

Regarding the contribution of large catastrophic rockslides to landscape downwearing in the Himalaya-Tibet orogen our results make clear that the correct identification of the origin of (chaotic) deposits is a clue to improve our understanding the causes, mechanisms, and patterns of mountain-belt denudation. Moraine chronologies for example are popular ways to reconstruct climatic fluctuations of the Quaternary (Abramowski et al., 2006; Heyman, 2014; Owen, 2009; Phillips et al., 1990b). The knowledge of absolute (or relative) moraine ages paired with their geographic situation enables workers to reconstruct paleoclimate, -environment, and hence mechanisms of denudation. But what if some of these moraine chronologies are based on deposits with an origin other than glacial? Previous research (e.g. Hewitt, 1999; Hewitt et al., 2011) already pointed to this problem and even reinterpreted supposed moraines as landslide(-induced) debris (e.g. Santamaria Tovar et al., 2008). Here we stress that (mis-)interpreting for example rockslide deposits as glacial moraines would result in the erroneous and misleading reconstruction of regional climatic effects such as glacial stages or glaciations (that, in the worst case, may never have happened). While the position of a moraine marks the (former) extent of glacier ice, the occurrence of a rockslide deposit may be indicator for both slope failure due to glacial undercutting (Hewitt, 1998; Korup et al., 2007) or valley flank collapse due to glacial debuttressing (Brückl et al., 2001). McColl and Davies (2012) have shown that—for reasons of differences in densities between rock and ice—glacial buttressing of hillslopes and their destabilization via glacial undercutting should be seen as rather end-members of a variety of possible influences of glaciers on failures of hillslopes.

Apart from the exclusion of any glacial origin of chaotic deposits in the Himalaya-Tibet orogen other information can be derived from deposits of giant rockslides. We present experimental results from Mössbauer spectroscopy that indicate short-lived (<10 s) partial melting of rock material at temperatures >1500 ° C. We deduce from Mössbauer-spectroscopy derived results that water has not been involved during rockslide runout as a lubricant, i.e. dry rockslide runout was based on the formation of frictionite as a “self-lubricant”. Consequentially, if water should not have been involved necessarily to formation and runout of (giant) rockslides, the role of monsoon precipitation as a potential trigger may have to be re-evaluated for these events (Bookhagen et al., 2005b; Dortch et al., 2011b). If the involvement of water during runout of large catastrophic rockslides, such as from traveling across water-saturated substrates of valley floors or intense slope infiltration causing pore-water pressure to exceed resisting forces, may be even excluded with certainty, then monsoonal triggering of slope failure appears to be highly unlikely. Since rockslides are thought to be usually triggered by (a) large earthquakes or (b) strong rainstorms (Densmore and Hovius, 2000) suchlike notion could be used to extend paleoseismic records and to revise information on recurrence intervals of high-magnitude earthquakes. Spatially adjacent Holocene large landsliding events in the NW Himalaya that indeed where dated to comparable ages by Bookhagen et al. (2005b) and Mitchell et al. (2007) but have been attributed to intensified monsoon (a) and a high-magnitude earthquake (b) as triggers, respectively, may serve as an example for that.

5.4 Evaluation of the multi-scale approach

This thesis aimed at quantifying rates and elucidating patterns of landscape downwearing in the Himalaya-Tibet orogen by tracing denudation from initial processes to the orogen-wide removal of mass from Earth’s surface. To achieve this a multi-scale approach across spatiotemporal orders of magnitude has been set up. Regarding the performance and the meaningfulness of this multi-scale approach it should be noted that

- rockslide deposits have to be included to considerations when looking at denudation processes and sediment redistribution on catchment (and even orogen) scale because they (a) are important point sources of ready-to-transport debris (and therefore major contributors to landscape downwearing in active mountains), (b) shield bedrock from erosion, (c) modulate channel morphology and therefore may contribute to sediment storage, and they (d) may significantly dilute cosmogenic nuclide abundances.
- additionally, information derived from the internal sedimentology of these giant rockslide deposits can help to better understand triggers and preparatory factors of rock-slope failure. Suchlike information can be upscaled to basin or even orogen scale. We also showed how information derived from the internal sedimentology of rockslide deposits can be used for the argumentative exclusion of certain preparatory settings, as for instance to argue against the glacial origin of these deposits, or to cause the rethinking of often drawn-on concepts as for instance the monsoonal triggering of giant rockslides.
- bulk petrography, heavy mineral analysis and cosmogenic nuclide abundances do complement one another in an consistent manner, with the latter yielding robust denudation rate estimates averaging over entire catchments, and bulk petrography and heavy mineral analysis being capable of providing information on provenance and pathways the sediments under investigation.
- however, denudation rates derived from bulk petrography and heavy mineral analysis and from cosmogenic nuclide analysis seem to be fairly incomparable, which may be owed to the different observation timescales behind these methods.

5.5 Outlook

Our study of the interior of giant rockslides suggests that it may be worth to systematically recheck known giant rockslide deposits for frictionite occurrence, considering the systematization we propose. Suchlike reassessment may lead to the revalidation or reevaluation of moraine chronologies, of outcrops with suspected multiphase rockslide emplacement, or of outcropping frictionite that has been classified as pseudotachylyte with tectonic origin. Additional data from radiometric dating of rockslide deposits could help to correlate the time of slope failure with climate proxies—which may lead to reinterpretation of moraine chronologies, again. Furthermore the standardization of analytic procedures, e.g. of sample treatment and particle sizing may lead to decreasing uncertainties and concomitantly increased comparability of different reports of rockslide deposits.

Another comparability issue appeared with the use of the same river sand samples to estimate denudation rates from (a) CN abundances and (b) bulk petrography (BP). The emerging question whether millennial cosmogenic-^{10}Be derived basin-averaged denudation rates from the western Tibetan Plateau margin can be considered as natural background denudation when compared to decadal petrography-derived denudation estimates cannot be answered in a straightforward manner therefore. The results presented in Chapter 3 suggest that—without further improvement of methodology—denudation rate estimates from BP analysis and from CN abundances may not be compared reasonably. Nonetheless, the use of the same river sands samples for BP analysis yielded the added value of information on the sands provenance complementing the CN-derived denudation rate estimates. However, the limited comparability of BP and CN-derived denudation rates illustrates the need to further develop ways of data analysis that enable us to compare denudation rate estimates—and geomorphic process rates in general—across different orders of averaging timescales. Clearly, future investigations will have to address this topic.

We showed that future research may also benefit from the use of quantile regression instead of OLS regression. Originally developed for the purpose of econometrics (Koenker and Bassett, 1978) quantile regression has become a popular tool for data analysis in very different disciplines such as ecology (Cade and Noon, 2003) or climatology (Elsner et al., 2008; Hirschi et al., 2010). However, despite the promising results from these studies and the frequent need to look into the full response distribution only few studies in geomorphology have made use of regression quantiles so far (e.g. Korup, 2012). We argue that whenever data span orders of magnitude, or involve outliers, quantile regression should be considered as an approach to learn from these data, especially when extreme values of distributions are in focus of investigation or their tails have to be modeled.

Chapter 6

Conclusions

This thesis examined landscape downwearing of the Himalaya-Tibet orogen from a multi-scale perspective, linking denudation processes from point to orogen-scale with emphasis on the climatically fluctuating Late Quaternary. To achieve this we combined conventional geologic fieldwork and stratigraphic considerations; up-to-date analytical techniques including XRD, Mössbauer spectroscopy, laser particle sizing, atomic spectroscopy, mass spectrometry, grain-size analysis, cosmogenic-nuclide applications, petrography and heavy mineral assemblages, and GIS. This thesis contributes to research by systematizing research on giant rockslides and investigating their deposits aiming to find alternative sources of information on paleoenvironment (p. 24ff.), by giving new insight into the patterns of landscape downwearing in the denudational transition zone of the upper Indus valley between the western Himalayan syntaxis and the western Tibetan Plateau margin (p. 45ff.), by identifying robust time-invariant predictors of basin-averaged denudation rates for the Himalaya-Tibet orogen, and by demonstrating resort from the seeming dilemma of meaningfully comparing basin-averaged denudation rates across differing timescales (p. 67ff.).

Beyond that, yet equally valued, this thesis tested the value and feasibility of combining so far separated or even not considered techniques as for instance: the high-voltage electrical fragmentation of micro-breccia to analyze their particle-size distribution, aiming for the comparison of rockslide-derived sample's fractal dimensions with those from impact material or fault gouge; or the combination of basin-averaged abundances of cosmogenic ^{10}Be with bulk petrography and heavy-mineral assemblages from the same parent-material, respectively.

Studying deposits from giant rockslides aims to better understand (a) preparatory factors and triggers of slope failure, (b) mechanisms of runout and emplacement, and (c) the influence of these long-lived chaotic sedimentary bodies on local and regional processes of redistribution of matter. On this knowledge, information about paleoenvironmental conditions as well as about consequential hazard assessments in regions prone to large-scale rock-slope failures can be based. The fact that features of deposits from giant rockslides—on macro- and microscopic scale—may deceptively resemble natural structures of totally different genesis and origin like glacial moraines, tectonic fault zone, or impact breccias, may lead to misleading or erroneous interpretation of these deposits.

However, the dynamics of runout and emplacement of, even highly degraded, giant rockslide deposits can be constrained from the side by side of fragmented or comminuted rock, internal shear planes and frictional melt. Systematizing previous work on these sedimentological features demonstrates that, based on geomorphic and stratigraphic field evidence, giant rockslides can be identified and distinguished from phenomena of similar phenotype by thoroughly fragmented and jigsaw-cracked rock masses; basal mélange containing phantom blocks; micro-breccia; and thin bands of basal frictionite together occurring at the same spot. Yet uncertainties in identification remain on microscopic scale since rockslide-derived micro-breccia have a particle-size distribution with partially fractal character, and cannot be distinguished from fault gouge or impact-breccia with certainty. Other potential drawback may arise from the occurrence of multiple shear planes that may be (mis-)interpreted as different events.

Novel insights from Mössbauer spectroscopy about rockslide runout could give reason to reevaluate the role of monsoonal precipitation as a major trigger of giant rockslides. The occurrence of frictionite in the basal mélange of giant rockslides indicates short-lived ($<10^1$ s) partial melting at temperatures of $>1500\,^\circ$C in the absence of water. As a consequence there is no forcing further need to argue for water as lubricant during rockslide runout. This fact together with the notion that frictionite may occur more often in the field than hitherto supposed, should give reason for rethinking triggers of giant rockslides.

In the upper Indus valley, across the knickpoint in Indus river long profile that marks the topographic transition from the western Tibetan Plateau to the high-relief Transhimalayan mountain ranges, ^{10}Be-derived denudation rates increase from 10 mm kyr^{-1} to 110 mm kyr^{-1} concomitantly to topographic relief, catchment steepness, and median channel steepness. As much as this gradient was expected, the finding that the denudational and topographic plateau margin would spatially not coincide, but rather be offset by 150–200 km, was not. Neglecting (neo)tectonic controls, and even excluding decisive lithological influences on the regional pattern of denudation rates a transient wave of erosion in the lower study reaches of the Indus River is the simplest possible interpretation for that offset.

The identified pattern of postglacial cosmogenic ^{10}Be-derived basin-averaged denudation rates is clearly backed up by results from bulk petrography and heavy mineral analysis of the same river sand samples; across-method peak signals from tributaries draining the Zanskar Range in the vicinity of the major (>30-km long) alluvial reach testify to that. However, petrography-derived rates of landscape downwearing, which are volumetrically based on 15 years of river gauging, are about one order higher than the millennial CN-derived denudation rates. We attribute this mismatch to the limited compatibility of the observation times behind the two methods. However, we do not favor a similar explanation for the observation that our millennial-scale denudation rate estimates are outpaced by long-term crustal exhumation. From the observation of a transport-limited modern erosional regime that is signed, however, by manifold morphologic evidence of massive former sediment infill and evacuation, we note that pre-postglacial denudation rates must have been higher beyond the postglacial averaging in order to explain the cooling pattern with denudation.

Data from an inventory of n = 297 ^{10}Be-derived basin-wide denudation rates from $<10^3$-km^2 catchments draining the Himalaya-Tibet orogen span about three orders of magnitude, ranging from 8 mm kyr^{-1} to 6,135 mm kyr^{-1}, with averaging timescales of 75 to 0.1 ka, respectively. Using ordinary least squares (OLS) regression to identify trends in response distributions of such data to potential predictors has been a typical approach in geosciences. However, since it has been designed to express the response variables average central tendency, especially when dealing with data that range over several orders of magnitude OLS regression fails to account for data scatter that may contain valuable information, as for example the time-dependence or -independence of the relationship between CN-derived denudation rate and candidate predictor. Quantile regression instead accounts for such demand by offering a statistically robust way of gauging the influence of tectonic, climatic, and topographic predictors on ^{10}Be-derived denudation rates across different timescales.

Topographic steepness and the availability of water—represented by Aridity Index, steepness index, and precipitation of the coldest quarter—have been identified as the variables with the highest explanatory power regarding the total variance of our data inventory. At first glance, single predictor quantile-regression derived results suggest meaningful and timescale-invariant relationships between denudation rate and said three predictors. However, additive multiple quantile regression finally reveals that only channel (or hillslope) steepness, as a representative of topographic predictors, offers largely timescale-invariant predictions, whereas relationships between denudation rate and predictors based on historic climate conditions, such as aridity or precipitation, or tectonic metrics break down.

Appendix A

Supplementary content: Study I

Giant rockslides from the inside

Johannes T. Weidinger[a,b], Oliver Korup[c], Henry Munack[c,*], Uwe Altenberger[c], Stuart A. Dunning[d], Gerold Tippelt[e], Werner Lottermoser[e]

[a]Geography and Geology, University of Salzburg, A-5020 Salzburg, Austria
[b]Erkudok© Institute, A-4810 Gmunden, Austria
[c]Earth and Environmental Sciences, University of Potsdam, 14476 Potsdam, Germany
[d]Geography and Environment Management, Northumbria University, Newcastle-Upon-Tyne NE1 8ST, United Kingdom
[e]Material Sciences and Physics, University of Salzburg, A-5020 Salzburg
[*]Corresponding author e-mail: henry.munack@geo.uni-potsdam.de

This supplementary content has been published with the following publication:
Weidinger, J.T., Korup, O., Munack, H., Altenberger, U., Dunning, S.A., Tippelt, G., and Lottermoser, W. (2014). Giant rockslides from the inside. Earth and Planetary Science Letters, v. 389, p. 62-73.

TABLE A.1: List of micro-breccia samples used for particle size analysis.

No.	Sample ID	Source	Facies	Description	Process	Selfrag process parameters: Electrode gap [mm]	n Pulses	n Effective Pulses[a]	U [kV]	f [Hz]
1	Altenbürg	Nördlinger Ries, GER	Impact	Impact-breccia, Rieskrater Suevit incl. glass	Selfrag	10	250	∼50	90	3
2	Dzongri	Dzongri	Rockslide	Micro-breccia, PSS	Selfrag	10	250	∼50	90	3
3	Hetzau	Hetzau (Almtal), AT	Rockslide	Breccia	Selfrag	10	250	∼50	90	3
4	Khalsar MB 1	Khalsar, Shyok valley, IN	Rockslide	Micro-breccia	Elutriation	-	-		-	-
5	Khalsar MB 3	Khalsar, Shyok valley, IN	Rockslide	Micro-breccia	Elutriation	-	-		-	-
6	Khalsar P2	Khalsar, Shyok valley, IN	Rockslide	Base Facies	Selfrag	10	250	∼50	90	3
7	Khalsar P3	Khalsar, Shyok valley, IN	Rockslide	Frictionite	Selfrag	10	250	∼50	90	3
8	Khalsar P5	Khalsar, Shyok valley, IN	Rockslide	Base Facies	Selfrag	10	250	∼50	90	3
9	Khardung MB 2	Khalsar, Shyok valley, IN	Rockslide	Micro-breccia	Elutriation	-	-		-	-
10	Otting	Nördlinger Ries, GER	Impact	Impact-breccia, Rieskrater Suevit incl. glass	Selfrag	10	250	∼50	90	3
11	Tsergo Ri P2	Tsergo Ri, Langthang, NP	Rockslide	Micro-breccia, PSS	Selfrag	10	250	∼50	90	3
12	Tsergo Ri P4	Tsergo Ri, Langthang, NP	Rockslide	Micro-breccia, PSS	Selfrag	10	250	∼50	90	3
13	Tsergo Ri	Tsergo Ri, Langthang, NP	Rockslide	Micro-breccia	Selfrag	10	250	∼50	90	3

[a]Effective pulses: Sample is in water when processed with Selfrag. Effective pulses affect the sample; ineffective pulses just cross water body; audible difference.
PSS - primary sliding surface; TSS - tertiary sliding surface. Organic material was not found in the samples.

TABLE A.2: Particle-size distribution from weighting (63 – >4000 μm), and counting (<63 μm).

Class limits	**Altenbürg**	**Dzongri**	**Hetzau**	**Khalsar MB 1**	**Khalsar MB 3**	**Khardung MB 3**	**Otting**	**Khalsar P2**	**Khalsar P3**	**Khalsar P5**	**Tsergo Ri P2**	**Tsergo Ri P4**	**Tsergo Ri**
sieved and weighted													
[μm]	[g]	[g]	[g]	[g]	[g]	[g]	[g]	[g]	[g]	[g]	[g]	[g]	[g]
< 63	26.15	46.42	51.58	46.88	33.02	59.00	41.19	81.75	66.83	47.43	53.14	34.37	62.38
64 - 124	16.53	9.07	6.99	15.30	12.01	26.19	18.32	16.84	13.00	10.30	14.78	14.32	10.42
125 - 249	31.69	13.41	11.13	15.89	16.52	30.40	29.30	15.25	11.46	19.03	20.65	21.66	11.07
250 - 354	5.51	0.75	5.55	5.10	1.45	6.23	13.89	1.81	4.93	1.67	6.53	3.39	1.16
355 - 499	12.02	4.11	6.68	5.64	4.82	9.71	11.90	4.26	4.54	7.22	8.08	10.30	2.87
500 - 629	8.75	2.47	7.16	3.85	3.35	6.84	5.32	3.05	2.92	5.91	7.02	5.80	1.61
630 - 709	3.11	0.58	2.38	1.34	1.07	2.59	1.35	1.12	1.01	2.15	1.52	1.76	0.63
710 - 999	6.84	1.42	8.69	3.07	3.29	6.39	2.42	3.26	2.28	5.65	6.16	4.55	1.64
1000 - 1399	4.97	0.99	9.11	2.06	2.73	5.05	1.04	3.10	1.40	4.82	5.46	4.27	1.46
1400 - 1999	2.91	0.73	11.57	1.47	2.80	4.55	0.26	3.15	1.02	5.18	6.07	3.45	1.30
2000 - 2799	1.41	0.51	11.54	1.34	2.39	2.54	0.12	3.08	0.46	4.13	4.58	1.91	0.95
2800 - 3999	0.87	0.22	11.95	0.88	1.55	1.85	0.00	2.55	0.17	3.15	3.86	0.58	0.65
> 4000	0.00	0.19	40.46	1.06	14.70	1.94	0.00	4.34	1.16	36.84	0.00	0.06	0.59
total	120.76	80.87	184.77	103.87	99.70	163.28	125.12	143.55	111.20	153.48	137.86	106.43	96.72
< 63μm fraction; counted with particle sizer; upper class limits													
[μm]	[%]	[%]	[%]	[%]	[%]	[%]	[%]	[%]	[%]	[%]	[%]	[%]	[%]
0.90	2.43	9.53	10.71	4.07	3.89	2.67	3.06	1.40	5.04	4.34	4.87	5.78	5.46
1.10	3.66	14.03	15.60	6.06	5.79	3.95	4.61	2.07	7.44	6.47	7.18	8.59	8.04
1.30	4.85	18.14	19.90	7.93	7.57	5.14	6.13	2.71	9.66	8.50	9.28	11.25	10.41
1.50	5.99	21.89	23.67	9.69	9.24	6.25	7.61	3.31	11.69	10.41	11.21	13.73	12.57
1.80	7.62	26.87	28.48	12.14	11.55	7.77	9.72	4.14	14.45	13.13	13.81	17.18	15.49
2.20	9.67	32.63	33.81	15.13	14.39	9.61	12.35	5.18	17.71	16.52	16.92	21.39	18.98
2.60	11.60	37.58	38.23	17.88	16.99	11.29	14.77	6.17	20.60	19.74	19.74	25.23	22.13
3.10	13.84	42.78	42.80	21.02	19.98	13.22	17.52	7.35	23.78	23.56	22.95	29.59	25.69
3.70	16.33	47.96	47.43	24.46	23.27	15.36	20.43	8.75	27.13	27.92	26.51	34.28	29.62
4.30	18.63	52.31	51.48	27.61	26.33	17.38	22.97	10.14	30.11	32.08	29.86	38.52	33.29
5.00	21.09	56.57	55.70	30.96	29.63	19.61	25.54	11.76	33.22	36.65	33.53	42.92	37.30
6.00	24.28	61.58	60.98	35.22	33.92	22.61	28.70	14.08	37.13	42.58	38.26	48.34	42.51
7.50	28.53	67.48	67.38	40.63	39.58	26.77	32.71	17.50	42.12	50.09	44.21	54.87	49.19
9.00	32.31	72.05	72.30	45.13	44.50	30.59	36.21	20.86	46.38	56.21	48.98	60.03	54.72
10.50	35.74	75.69	76.14	48.98	48.84	34.18	39.37	24.14	50.13	61.18	52.83	64.21	59.33
12.50	39.96	79.67	80.24	53.44	53.97	38.67	43.27	28.40	54.63	66.56	57.05	68.77	64.50
15.00	44.85	83.74	84.29	58.34	59.59	43.92	47.80	33.51	59.67	71.97	61.45	73.48	69.87
18.00	50.31	87.62	88.02	63.47	65.39	49.72	52.83	39.32	64.98	77.07	65.87	78.08	75.15
21.00	55.38	90.69	90.87	67.95	70.37	55.01	57.49	44.77	69.59	81.09	69.65	81.87	79.47
25.00	61.55	93.68	93.60	73.04	75.85	61.25	63.11	51.47	74.70	85.12	73.92	85.91	83.99
30.00	68.48	96.21	95.92	78.36	81.36	68.05	69.38	59.05	79.86	88.84	78.49	89.89	88.34
36.00	75.78	98.10	97.72	83.62	86.51	75.00	75.99	67.15	84.78	92.08	83.26	93.54	92.23
43.00	82.90	99.31	98.95	88.52	91.03	81.74	82.56	75.30	89.27	94.82	88.02	96.60	95.45
51.00	89.17	99.87	99.67	92.74	94.66	87.80	88.57	82.93	93.15	96.99	92.36	98.72	97.81
61.00	94.47	100.00	99.95	96.31	97.48	93.22	93.91	90.07	96.45	98.67	96.15	99.78	99.33
73.00	98.06	100.00	100.00	98.75	99.27	97.26	97.75	95.72	98.77	99.69	98.76	100.00	99.91
87.00	99.68	100.00	100.00	99.81	99.91	99.47	99.61	99.11	99.81	99.99	99.82	100.00	100.00
103.00	100.00	100.00	100.00	100.00	100.00	100.00	100.00	100.00	100.00	100.00	100.00	100.00	100.00

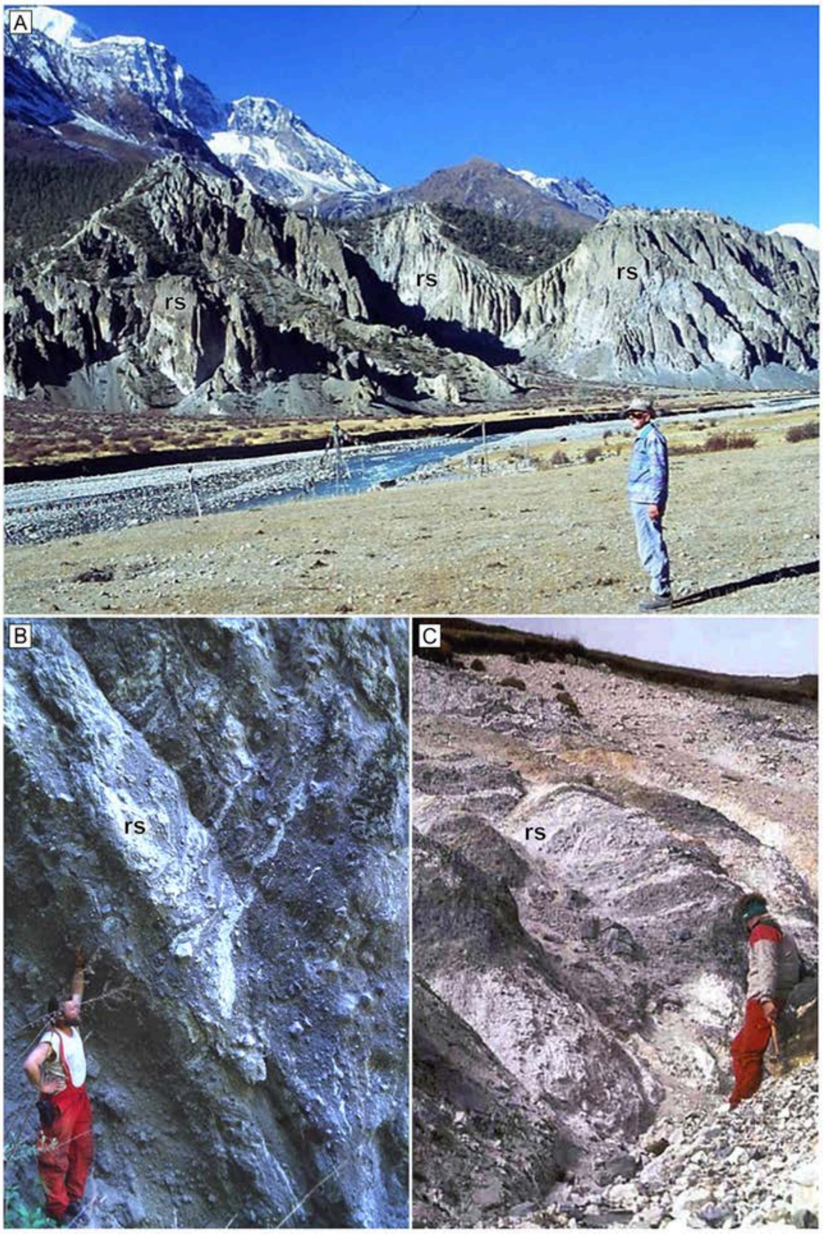

FIGURE A.1: A) Deeply dissected deposit (rs) of Braga rockslide, Manang valley, Annapurna massif, Nepal. B) and C) Fractured rocks in giant landslide deposits with en masse displacement. B) Latamrang rockslide, Nepal, with highly fragmented and convoluted diamict in turbulent flow conditions. C) Base of Tsergo Ri rockslide with highly fractured migmatites and leucogranite dikes and intact primary rock texture.

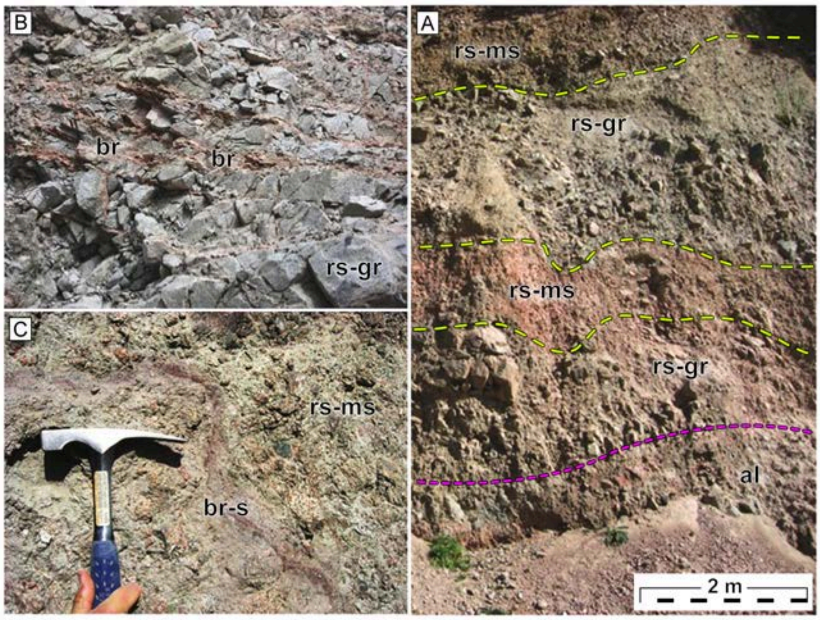

Figure A.2: Stratigraphic profile (right) of Arashan rockslide topping an alluvial gravel layer (al): A) granites (rs-gr) reacted brittle during fragmentation, and were crushed to angular blocks, whereas metasediments (rs-ms) reacted more brittle and were fragmented to much smaller grain sizes. B) Granitic angular blocks and boulders separated by swarms of micro-brecciated shear zones (br). C) Metasediments with secondary sliding planes (br-s).

FIGURE A.3: Examples of primary shear planes developed on basal sediments devoid of frictional melt at landslide base. A) Alluvial and moraine gravel (al-mo) buffering fractured rockslide material (rs) from gneissic basement (ba-gn), Latamrang. B) 101-m thick alluvial gravels (al) separate Kokomeren rockslide debris (rs) from granitic basement rock (ba-gr). C-F) Secondary shear planes of Tsergo Ri and Kfels rockslides, composed of frictionite: C) Band of mixed frictionite and breccias (fr-s) within fractured rockslide material (rs), Tsergo Ri. D) Close-up (area in brackets) of mixed frictionite and breccias (fr-br). E) Frictionite sample (fr-pu) that was originally a lenticular body within fragmented rockslide material, Tsergo Ri. F) Sample from Kfels rockslide.

FIGURE A.4: Vertical tertiary shear planes composed of breccias (br-t) within rockslide mass (rs), composed of migmatites and leucogranites, Tsergo Ri rockslide, resulting from collision of the sliding mass with obstacles. Frictionite was found in the vertical breccia horizon in B). Vertical tertiary shear planes composed of frictionite (fr-t) within rockslide material (rs) C) and gneissic basement (ba-gn) D), Tsergo Ri rockslide. Field evidence suggests that these vertical planes are shearing planes, which have opened during sliding and into which frictionite has been injected during its creation along the associated primary shear plane (in D) and secondary shear plane (in C).

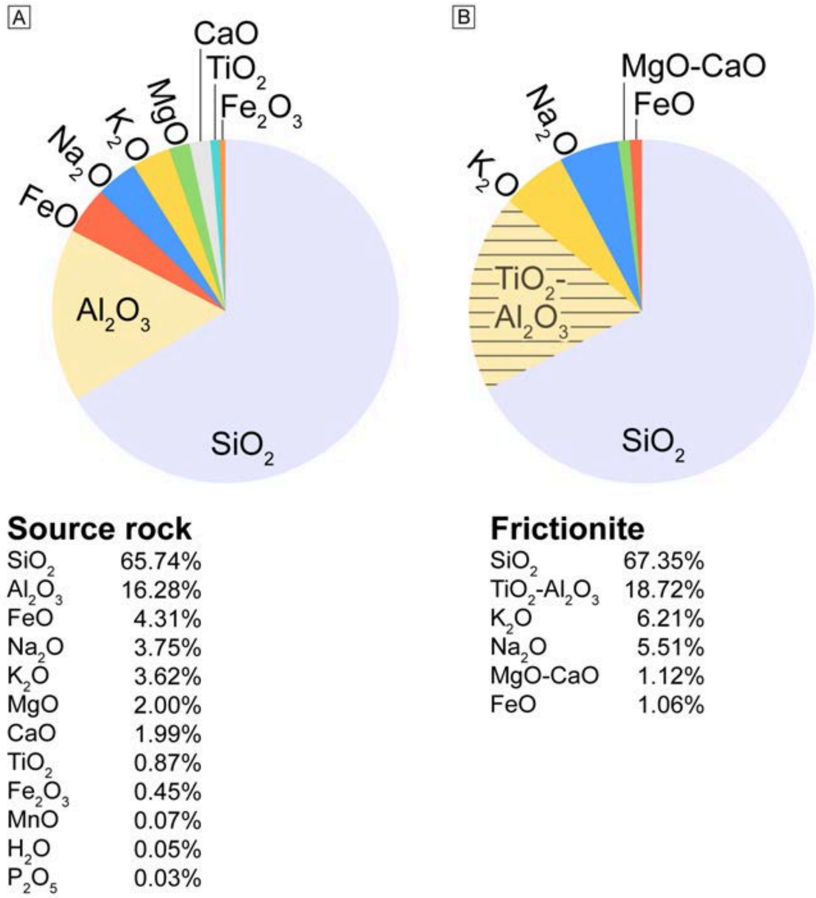

FIGURE A.5: Composition of A) Tsergo Ri source rock and B) Tsergo Ri frictionite from XRD and microprobe analysis. Note that the Fe(III)/Fe(II) ratio is 0.1 in the source rock whereas no Fe(III) was identified in the frictionite sample.

Appendix B

Supplementary content: Study II

Postglacial denudation of western Tibetan Plateau margin outpaced by long-term exhumation

Henry Munack[a,*], Oliver Korup[a], Alberto Resentini[b], Mara Limonta[b], Eduardo Garzanti[b], Jan H. Blöthe[a], Dirk Scherler[a, c], Hella Wittmann[d], Peter W. Kubik[e]

[a]Earth and Environmental Sciences, University of Potsdam, 14476 Potsdam, Germany

[*]Corresponding author e-mail: henry.munack@geo.uni-potsdam.de

[b]Department of Earth and Environmental Sciences, Università degli Studi di Milano-Bicocca, 20126 Milano

[c]Geological and Planetary Sciences, California Institute of Technology, Pasadena, CA 91125, USA

[d]GFZ Deutsches GeoForschungsZentrum, 14473 Potsdam, Germany

[e]Laboratory of Ion Beam Physics, ETH Zürich, 8093 Zürich, Switzerland

This supplementary content has been published with the following publication:
Munack, H., Korup, O., Resentini, A., Limonta, M., Garzanti, E., Blöthe, J.H., Scherler, D., Wittmann, H., and Kubik, P.W. (2014). Postglacial denudation of western Tibetan Plateau margin outpaced by long-term exhumation. Geological Society of America Bulletin.

Here we provide data and additional figures concerning the petrographic analysis and the heavy minerals assemblages behind this study. Also, for the purpose of comparison, we show basin-wide ^{10}Be-derived denudation rates from various scaling schemes.

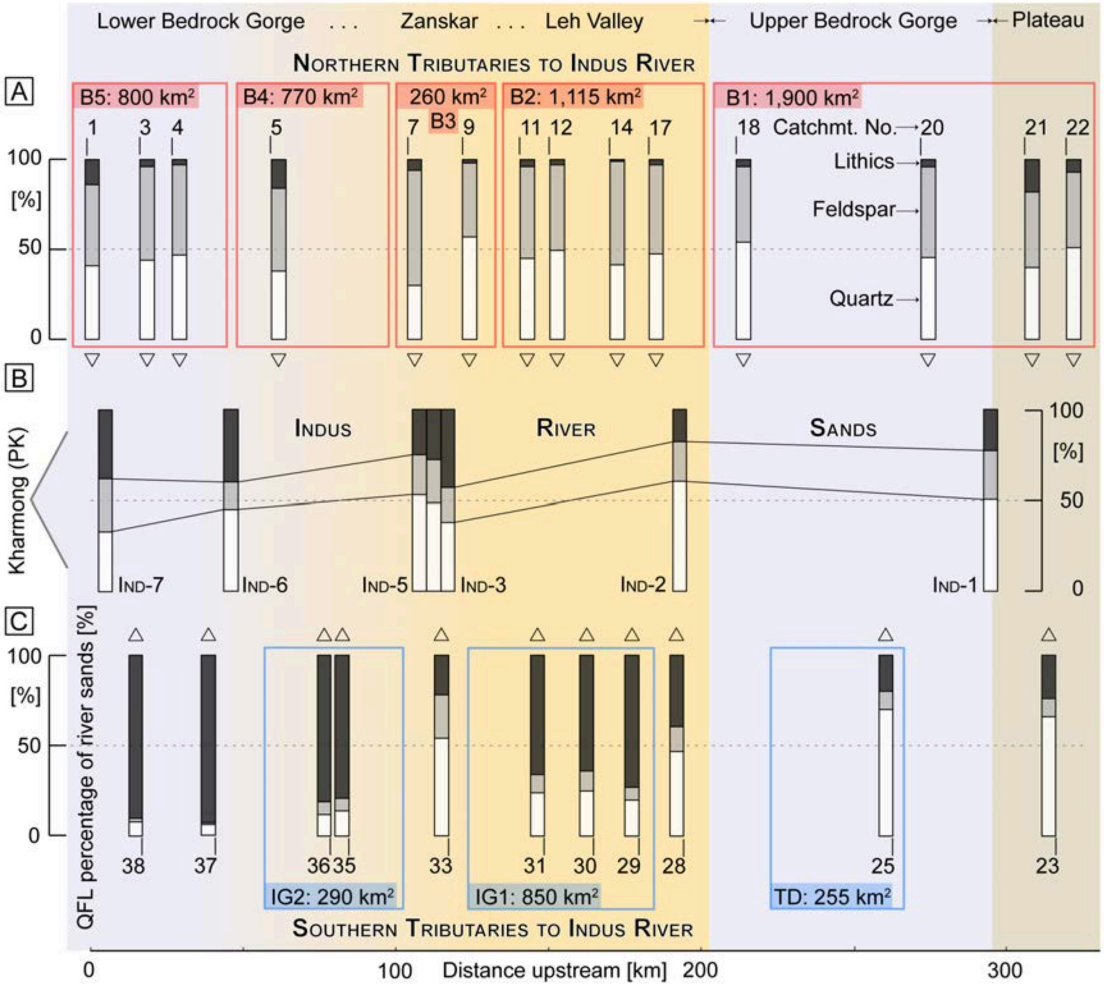

Figure B.1: Alternative to Fig. 4. Sand petrography in the upper Indus River catchment. Northern tributaries (draining the Ladakh Batholith) shed quartzo-feldspathic to feldspatho-quartzose detritus. Instead, southern tributaries (draining Indus Group siliciclastics and different tectonic units exposed along the ophiolitic suture and in the Zanskar Range to the south) shed abundant sedimentary, metasedimentary and locally metavolcanic, metabasite and ultramafite rock fragments. Provenance reaches denoted by frames are homogeneous units that were used to calculate relative sediment budgets (Red: B1–5 = Ladakh Batholith; Blue: TD = Tso Morari Dome, IG1–2 = Indus Group). Main southern tributaries (Gya (28), Zanskar (33), and Yapola (37) Rivers) represent distinct provenance reaches. Note stepwise increase in lithics (L) in Indus River sands downstream of the Gya confluence (Ind-3) and of the Zanskar confluence (Ind-6), due to prevailing IG1 and IG2 contribution. The opposite trend, observed locally at the Zanskar confluence, reflects prominent supply from the Zanskar Range (Ind-4). Southern tributaries: catchments 23–25 mainly draining Tso Morari Dome; Gya (28), catchments 29–32 and 36 largely draining sedimentary Indus Group; Zanskar catchment largely draining sedimentary Tethys Himalaya Zone (THZ) and High Himalayan Crystalline Zone; Yapola (37) catchment largely draining THZ and Dras volcanics; and catchment (38) draining Dras volcanics.

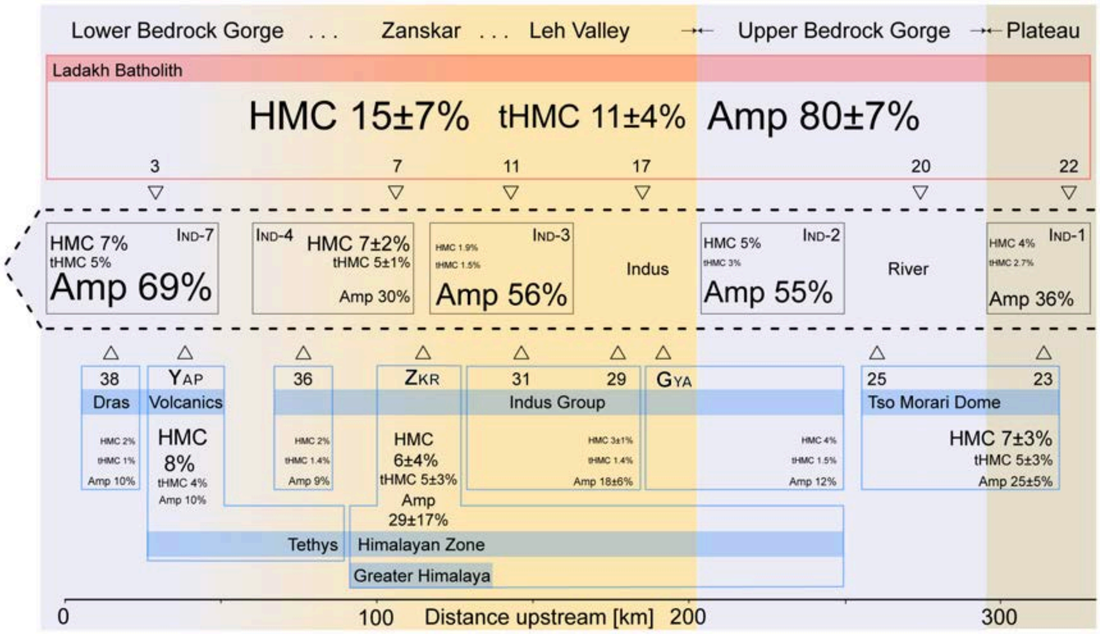

FIGURE B.2: Alternative to Fig. 5. Heavy minerals in the upper Indus River catchment. Font size is scaled proportionally to relative HM contribution to respective samples. YAP = Yapola River, ZKR = Zanskar River, GYA = Gya River; Amp = Amphibole, HMC = volume percentage of total, and tHMC = transparent heavy minerals (Garzanti and Andó, 2007). Note dilution of amphibole and HMC increase in Indus sands just after the Zanskar confluence. HMC (Heavy Mineral Concentration) classes are defined as follows: < 0.1 - extremely poor in Heavy Minerals; $0.1 \leq$ HMC < 0.5 - very poor; $0.5 \leq$ HMC < 1 - poor; $1 \leq$ HMC < 2 - moderately poor; $2 \leq$ HMC < 5 - moderately rich; $5 \leq$ HMC < 10 - rich; $10 \leq$ HMC < 20 - very rich. Provenance reaches as in Figure B.1.

TABLE B.1: Data from petrographic analysis.

No.	Sample (River)	Site	Components Q	KF	P	Lithic grains Lvm	Lch	Lcc	Lcd	Lp	Lms	Lmf	Lmb	Lu	Mu	Bi	HM	total	MI[a]	Q	F	L
Northern Indus River tributaries (= Ladakh Batholith)																						
22	Nyoma	Nyoma	48	15	24	1	0	0	0	0	1	4	0	0	0	3	3	100	363	51	42	7
20	Chuma-1	Chumathang	36	10	30	0	0	0	0	0	0	3	0	0	0	1	20	100	379	45	50	4
18	Ligchi	Ligchi	44	11	23	0	0	0	0	0	0	3	0	0	4	4	12	100	393	54	42	4
17	Igoo	Igoo	41	15	29	0	0	0	0	0	0	2	0	0	0	5	7	100	428	48	50	3
14	Stagmo	Stagmo	29	7	33	0	0	0	0	0	0	1	0	0	2	7	21	100	456	41	57	1
12	Leh	Leh	39	14	24	0	0	0	0	1	0	1	0	0	0	8	12	100	420	50	48	3
11	Phyang	Phyang	34	9	29	0	0	0	0	0	0	2	1	0	0	5	19	100	391	45	51	4
9	Humla	Humla	38	8	19	0	0	1	0	0	0	1	0	0	1	6	27	100	444	57	41	2
7	Basgo	Basgo	27	17	41	1	1	1	0	1	1	1	0	0	1	1	9	100	NA	30	64	6
4	Domkar	Domkar	40	14	29	0	0	0	0	0	0	1	0	0	0	2	13	100	374	47	50	3
3	Skyur	Skurbuchan	40	12	35	0	0	1	0	0	0	1	1	0	1	3	4	100	400	44	52	4
Ladakh Batholith (+ Indus Group component)																						
21	Nogo	Nogo	38	10	30	0	0	1	0	11	3	2	0	0	0	1	3	100	204	40	42	18
5	Nurla	Nurla	31	6	31	0	0	0	0	6	6	1	0	0	0	3	15	100	133	38	46	16
1	Hanuthang	Hanuthang	35	10	28	0	0	3	1	1	3	2	1	0	1	2	12	100	344	41	45	14
Southern Indus River tributaries																						
Tsomorari Dome																						
23	Nidder	Nidder	54	3	5	0	0	3	1	2	7	6	1	1	6	2	10	100	291	66	10	24
25	Skid	Skid	62	4	4	0	0	0	0	1	1	14	1	1	8	2	3	100	345	70	10	20
Nyimaling Granite																						
28	Gya	Upshi	44	4	9	1	0	8	1	12	11	2	1	1	0	0	6	100	114	47	14	39
Indus Group																						
29	Martse	Martselang	19	2	5	1	0	5	0	51	13	0	0	0	0	0	2	100	28	20	7	73
30	Matho	Matho	25	2	9	0	0	3	0	38	22	0	0	0	0	0	1	100	50	25	11	64
31	Stok	Stok	24	2	8	2	0	3	0	42	19	0	1	0	0	0	0	100	47	24	10	66
Zanskar catchment																						
33	Zanskar	pre Indus	48	11	11	0	0	10	3	0	1	4	1	0	3	5	3	100	NA	54	24	22
33.2	Zanskar	post Sumdah	43	5	8	1	0	22	3	0	2	2	1	0	0	1	11	100	337	49	15	36
33.1	Zanskar	pre Markha	42	3	8	0	0	24	5	0	2	3	0	0	0	1	10	100	332	48	12	40
33.01	Markha	pre Zanskar	23	1	2	0	0	44	2	6	12	5	0	3	0	0	2	100	155	23	3	74
Indus Group																						
35	Lardo	Lardo	14	1	6	4	0	2	0	28	44	0	0	0	0	0	1	100	80	14	7	79
36	Giera	Giera	12	1	6	2	0	14	0	27	35	0	0	2	0	0	1	100	70	12	7	81
Spontang Ophiolite																						
37	Yapola	Kalshi	5	0	1	1	0	46	6	14	12	0	2	10	0	0	3	100	86	6	1	93
Dras-Nidam volcanics																						
38	Leido	Leido	8	0	1	1	0	9	1	26	40	0	0	12	0	0	1	100	70	8	2	91
Trunk Indus River																						
	LAT [°N]	LON [°E]																				
Ind-1	33.26613	78.48705	46	11	13	1	1	4	2	0	5	5	0	2	2	1	6	100	236	51	27	23
Ind-2	33.80973	77.83070	56	8	12	2	0	4	1	0	3	4	0	3	3	1	5	100	250	61	22	18
Ind-3	34.16052	77.33836	36	6	12	1	0	5	2	21	8	2	1	1	1	2	3	100	NA	38	19	43
Ind-4	34.18390	77.33632	45	11	11	0	0	10	3	4	3	5	1	0	1	2	4	100	NA	49	24	28
Ind-5	34.20691	77.29174	48	8	12	0	0	15	3	1	2	2	0	0	1	4	6	100	262	53	22	25
Ind-6	34.31893	76.88656	40	4	9	1	0	22	3	4	4	2	0	0	1	3	6	100	157	45	15	40
Ind-7	34.54000	76.61967	28	10	15	0	0	14	1	7	5	3	0	2	0	5	8	100	226	33	29	38

Q - Quartz; KF - K-feldpar; P - Plagioclase; Lithic grains: Lvm - Volcanic and Metavolcanic, Lch - Chert, Lcc - Limestone, Lcd - Dolostone, Lp - Shale/Siltstone/Sandstone, Lms - Metasedimentary, Lmf - Felsic Metamorphic (med. and hi. rank), Lmb - Mafic Metamorphic (med. and hi. rank), Lu - Ultramafic (serpentinite), Mu - Muscovite, Bi - Biotite, HM - Heavy Minerals (as determined from petrographic point counting), MI - Metamorphic Index [a] (Garzanti et al., 2010; Garzanti and Vezzoli, 2003).
Samples range from upper-very-fine sand to upper-medium sand (3.5 to 1 ϕ); grain size was determined by ranking and direct measurement in thin section.

TABLE B.2: Heavy Minerals assemblages derived from river sands that were also used for *in-situ* ^{10}Be analysis and petrographic analysis.

No.	HM% VFS-FS	HM% trp	% trp	% opq	% tbd	Zrn	Tur	Rt	Ttn	Ap	Brt	Ep	Grt	St	And	Sil	Hbl	Na-Amp	Amp	Cpx	En	Hyp	Ol	Spl	HCI	MMI	SI	ZTR
Northern Indus River tributaries (= Ladakh Batholith)																												
22	4	3	80	4	16	1	1	1	2	4	0	7	1	0	0	0	72	0	3	6	0	2	1	0	15	NA	NA	3
21	16	14	82	6	12	0	1	0	3	2	0	10	1	0	0	0	76	0	1	4	0	0	0	0	5	NA	NA	1
17	5	4	88	6	6	1	0	0	7	5	0	6	0	0	0	0	79	0	0	0	0	0	0	0	4	NA	NA	2
11	22	12	57	35	8	4	1	0	6	2	0	4	0	0	0	0	65	0	4	7	0	5	0	0	14	NA	NA	5
7	20	13	63	29	8	1	0	0	2	1	0	6	1	0	0	0	82	0	0	3	0	2	0	0	16	NA	NA	1
3	14	12	82	7	11	0	0	0	6	1	0	2	0	0	0	0	88	0	1	1	0	0	0	0	10	NA	NA	0
Southern Indus River tributaries																												
Tsomorari Dome																												
23	10	7	67	2	31	1	1	2	1	6	0	13	36	0	0	0	1	21	6	8	0	1	2	0	NA	NA	NA	4
25	5	3	56	6	38	4	5	1	1	14	0	10	33	0	0	1	8	12	1	5	0	0	0	0	8	NA	NA	11
Nyimaling Granite																												
28	4	1.5	36	14	51	9	7	2	3	5	0	53	6	0	0	0	11	0	1	1	0	0	0	3	5	NA	NA	18
Indus Group																												
29	4	1.4	33	6	60	3	2	0	1	3	0	65	8	0	0	0	13	0	1	0	0	0	0	1	6	NA	NA	6
31	3	1.4	46	6	48	2	0	0	1	1	0	66	4	0	0	0	20	0	2	1	0	0	0	0	12	NA	NA	3
Zanskar catchment																												
33	4	3	95	2	3	3	9	1	2	0	0	7	10	1	0	21	39	0	2	4	0	0	0	0	22	96	2	13
33.1	9	7	82	4	14	3	2	0	2	3	0	3	31	0	0	32	16	1	0	4	0	0	0	0	26	99	14	5
33.01	4	0.7	15	9	76	8	11	0	1	8	2	31	8	0	0	0	2	0	19	8	0	0	0	0	NA	NA	NA	20
Indus Group																												
36	2	1.4	67	1	32	2	1	0	0	1	0	76	4	0	2	1	7	0	1	2	0	0	0	0	24	67	NA	4
Spontag Ophoilite																												
37	8	4	46	3	51	0	0	0	0	0	0	20	0	0	0	0	0	0	0	7	14	0	55	2	NA	NA	NA	0
Dras-Nidam Volcanics																												
38	2	0.9	48	3	49	0	1	0	0	1	0	18	1	0	0	0	8	0	2	69	1	0	0	1	7	NA	NA	1
Trunk Indus River																												
Upstream Indus-Zanskar confluence																												
IND-1	4	3	60	8	32	3	2	1	5	6	0	10	18	0	0	0	18	12	5	13	1	0	2	0	15	NA	NA	6
IND-2	5	3	57	4	39	0	3	1	2	2	0	21	10	0	0	0	32	20	3	4	0	0	0	0	5	NA	NA	5
IND-3	1.9	1.5	78	11	11	2	3	0	2	0	0	29	3	0	0	0	56	0	0	3	0	0	0	1	2	NA	NA	5
Downstream Indus-Zanskar confluence																												
IND-4	7	6	86	10	4	4	2	0	2	0	0	8	39	1	0	10	28	0	2	3	0	0	0	0	23	96	0	7
IND-5	4	4	87	5	8	1	1	0	4	2	0	2	15	0	0	27	42	0	2	1	0	0	0	0	13	100	43	3
IND-6	10	7	68	17	15	3	3	1	4	4	0	6	24	0	0	19	31	0	0	3	0	0	0	0	17	100	10	7
IND-7	7	5	74	10	16	1	3	0	2	5	0	9	4	0	0	5	55	9	5	5	0	1	0	0	7	100	56	3

HM% VFS-FS - Percentage of Heavy Minerals in the very-fine to fine sand class (63 - 250 μm); HM% transp. - Percentage of transparent Heavy Minerals, %trp (transparent) + %opq. (opaque) + %tbd (turbid) = 100%.

The following HM percentages sum up to a total of 100%:
Zrn - Zircon; Tur - Tourmaline; Rt - Rutile; TiO - Ti Oxides*; Ttn - Titanite; Ap - Apatite; Mnz - Monazite*; Brt - Barite; Ep - Epidote; Grt - Garnet;
Cld - Chloritoid (Cld (not in Table) was detected in the samples 33 and Ind-1 with 1%, respectively); St - Staurolite; And - Andalusite; Ky - Kyanite*; Sil - Sillimanite;
Hbl - Hornblende; Na-Amp - Na Amphibole; Amp - Amphibole; Cpx - Clinopyroxene; En - Enstatite; Hyp - Hypersthene; Ol - Olivine; Spl - Spinel; * HM not detected.

HCI - Hornblende Colour Index; MMI Metasedimentary Minerals Index (Andó et al., 2013); SI - Sillimanite Index;
ZTR - Percentage of chemically ultrastable mineral species (Zrn, Tur, Rt) among transparent detrital HM.

TABLE B.3: Denudation rates and uncertainties from different scaling schemes.

No.	Sample ID	**Denudation rate** - De (mm kyr^{-1})	**Uncertainty** dDe (1-σ level) (mm kyr^{-1})	**Denudation rate** - Du (mm kyr^{-1})	**Uncertainty** dDu (1-σ level) (mm kyr^{-1})	**Denudation rate** - Li (mm kyr^{-1})	**Uncertainty** dLi (1-σ level) (mm kyr^{-1})	**Denudation rate** - Lm (mm kyr^{-1})	**Uncertainty** dLm (1-σ level) (mm kyr^{-1})	**Denudation rate** - St (mm kyr^{-1})	**Uncertainty** dSt (1-σ level) (mm kyr^{-1})
Northern Indus River tributaries (= Ladakh Batholith)											
1	Hanu	103.06	12.17	99.66	11.71	105.64	10.68	99.48	8.81	99.20	9.01
2	Achina	66.11	7.73	65.07	7.57	68.15	6.78	62.91	5.45	61.24	5.44
3	Skyur	94.74	11.57	91.96	11.18	97.25	10.29	90.86	8.53	90.20	8.65
4	Domkar	73.83	8.72	72.42	8.51	76.07	7.68	69.61	6.14	68.13	6.16
5	Nurla	38.50	4.53	38.68	4.53	40.04	4.00	35.18	3.06	33.01	2.94
6	Saspo	45.02	5.31	45.02	5.29	46.74	4.69	41.17	3.59	38.99	3.49
7	Bazgo									38.53	8.00
8	Nimu	36.33	4.32	36.53	4.32	37.81	3.83	33.31	2.94	31.13	2.81
8.1	Nimu-11	34.02	4.08	34.30	4.10	35.43	3.64	31.16	2.80	28.95	2.66
9	Humla	21.24	2.53	21.62	2.57	22.24	2.25	19.26	1.70	17.43	1.57
10	Tharu	24.77	2.95	25.19	2.99	25.93	2.63	22.18	1.95	20.22	1.83
11	Phyang	28.35	3.37	28.75	3.40	29.62	2.99	25.41	2.23	23.35	2.10
12	Leh										
13	Sabu									20.09	2.80
14	Stagmo	20.03	2.40	20.50	2.45	21.02	2.14	17.72	1.57	15.93	1.45
15	Nang	28.53	3.38	28.87	3.41	29.79	3.00	25.91	2.27	23.83	2.14
16	Karu									20.08	2.80
17	Igoo	26.48	3.14	26.86	3.18	27.69	2.79	24.02	2.11	21.97	1.97
18	Ligchi	32.67	3.88	33.09	3.92	34.14	3.45	28.97	2.54	26.75	2.41
19	Kumdo	91.17	10.72	88.87	10.40	93.91	9.40	84.82	7.38	83.77	7.48
20	Chuma-1	31.39	3.74	31.91	3.78	32.87	3.33	27.46	2.41	25.23	2.27
21	Nogo	14.72	1.79	15.27	1.85	15.55	1.60	12.47	1.12	10.90	1.01
22	Nyoma	17.11	2.07	17.69	2.13	18.05	1.85	14.56	1.30	12.84	1.18
Southern Indus River tributaries											
23	Nidder	33.65	4.00	34.02	4.03	35.20	3.56	30.10	2.64	27.75	2.50
24	Chuma-2	10.85	1.33	11.28	1.37	11.48	1.19	9.26	0.84	7.94	0.74
25	Skid	33.47	3.97	33.90	4.00	35.01	3.53	29.62	2.59	27.33	2.45
26	Tiridoo	30.80	3.67	31.20	3.70	32.22	3.26	27.46	2.41	25.23	2.27
27	Tarch	38.67	4.57	38.87	4.57	40.28	4.05	35.12	3.06	32.82	2.93
28	Gya										
29	Martse	93.69	11.37	90.87	10.97	96.16	10.09	90.67	8.42	89.90	8.53
30	Matho	74.29	8.69	72.76	8.47	76.54	7.63	70.76	6.15	69.24	6.17
31	Stok-3	73.28	8.59	71.84	8.38	75.53	7.55	69.38	6.04	67.81	6.05
31.1	Stok-11	84.66	9.88	82.53	9.58	87.09	8.65	80.63	6.96	79.47	7.04
32	Zin	72.96	8.61	71.45	8.39	75.11	7.59	70.11	6.20	68.58	6.21
33	Zanskar										
34	Alchi	66.06	7.72	64.94	7.55	68.08	6.78	63.43	5.51	61.71	5.49
35	Lardo	81.22	9.60	79.26	9.32	83.52	8.46	77.99	6.92	76.77	6.97
36	Giera	115.93	14.20	111.54	13.59	118.55	12.63	113.85	10.81	114.14	11.07
37	Yapola										
38	Leido	107.15	13.39	103.38	12.85	109.47	12.01	107.26	10.59	107.28	10.80

Scaling schemes: Time-dependent - De (Desilets et al., 2006), Du (Dunai, 2001), Li (Lifton et al., 2005), Lm (Lal, 1991; Nishiizumi et al., 1989; Stone, 2000);
Time-independent - St (Lal, 1991; Stone, 2000).
Also see CRONUS online calculator for scaling schemes and reference production rates ((Balco et al., 2008); http://hess.ess.washington.edu/).
Denudation rates for Bazgo, Sabu and Karu catchments taken from Dortch et al. (2011c); there labelled BWR-5 (Sabu), BWR-6 (Karu) and BWR-14 (Bazgo).

Appendix C

Supplementary content: Study III

Denuding the Himalaya-Tibet orogen: Noise vs. Time

Henry Munack[a,*], Oliver Korup[a], Alexandru T. Codilean[b], Jakob Heyman[c], Yingkui Li[d], Jan H. Blöthe[a], Peter W. Kubik[e]

[a] Earth and Environmental Sciences, University of Potsdam, 14476 Potsdam, Germany

[*] Corresponding author e-mail: henry.munack@geo.uni-potsdam.de

[b] School of Earth and Environmental Sciences, University of Wollongong, Wollongong NSW 2522, Australia

[c] Department of Physical Geography and Quaternary Geology, Stockholm University, SE-106 91 Stockholm, Sweden

[d] Department of Geography, University of Tennessee, Knoxville, TN 37996, USA

[e]Laboratory of Ion Beam Physics, ETH Zürich, 8093 Zürich, Switzerland

Here we provide information on

- studies that we used for our inventory of basin-wide ^{10}Be-derived denudation rates;
- the set of BIOCLIM variables that we tested for their qualification as predictor variables;
- the new ^{10}Be derived basin-wide denudation rates presented in this study, the associated sample treatment, the harmonization of the basin-wide data, the calculation of ^{10}Be production rates, the computing of the basin-wide explanatory variable statistics; and
- details of the statistical analysis behind this study.

C.1 Study area and data compilation

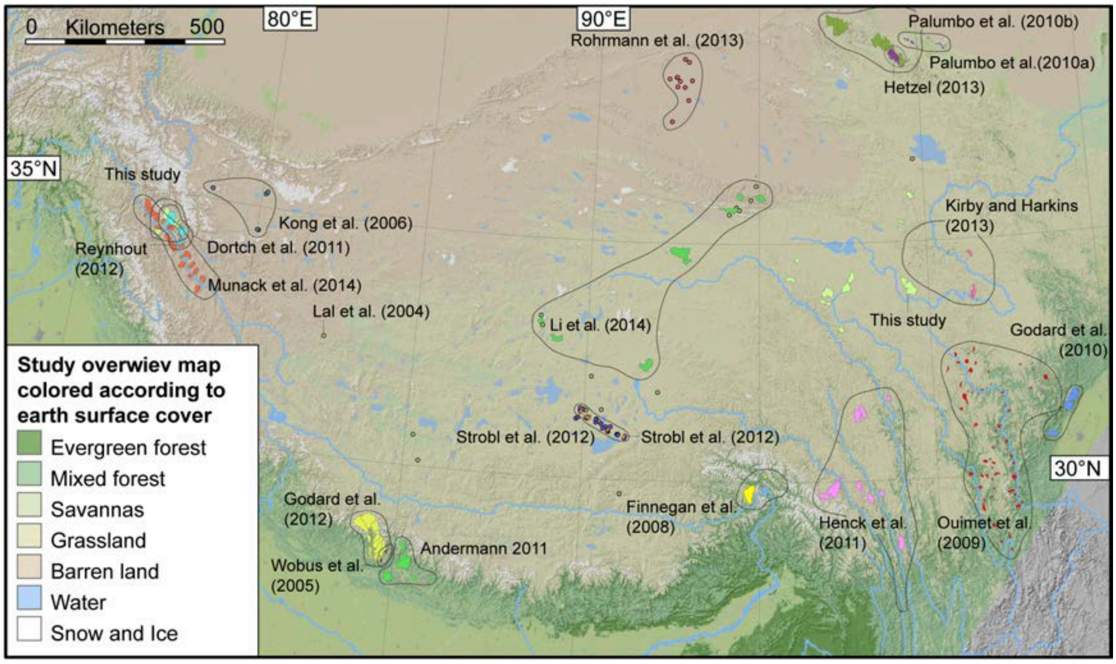

Figure C.1: Land cover map of the Himalaya-Tibet orogen (Moderate Resolution Imaging Spectroradiometer MODIS, Product MCD12Q1, http://modis.gsfc.nasa.gov/) with sites of previous ^{10}Be basin-wide denudation studies (framed), and of n = 26 new basin-wide ^{10}Be denudation rate data used for this study; only catchments $<10^3$ km^2 are shown. ^{10}Be concentrations for recalculation of basin-wide denudation rates were extracted from Andermann (2011); Dietsch et al.; Dortch et al. (2011c); Finnegan et al. (2008); Godard et al. (2012, 2010); Henck et al. (2011); Hetzel (2013); Kirby and Harkins (2013); Li et al. (2014); Munack et al. (2014); Ouimet et al. (2009); Palumbo et al. (2010a,b); Strobl et al. (2012) and (Wobus et al., 2005) (for ^{10}Be-concentration derived data and basin-averaged predictor values see Tables C.4, C.5, and C.6); bedrock-exposure derived denudation rates were recalculated using ^{10}Be concentrations from Kong et al. (2006); Lal et al. (2004); Rohrmann et al. (2013) and (Strobl et al., 2012).

TABLE C.1: List of new ^{10}Be-derived basin-wide samples presented in this study; sampling sites and associated topographic parameters, cosmogenic ^{10}Be nuclide concentrations from AMS measurement, parameters necessary for basin-wide denudation rates calculation, and basin-wide denudation rates.

Sample ID	**Drainage point**[a] LAT [°N]	LON [°E]	**Grainsize** [$\mu m * 10^2$]	**AMS**	**Standard**	**^{10}Be conc.** [at. g^{-1} $*10^6$]	1σ	**Area** [km^2]	**Mean basin elevation** [m a.s.l.]	1σ	**Mean basin slope** [m km^{-1}]	1σ	**Denudation rate** [mm kyr^{-1}]	1σ
Bayan-Har														
WTS13401	35.8883	99.6758	2.5-5	PRIME	KNSTD	0.4534	0.0204	206	4414	256	298.03	143.07	143.85	16.93
WTS13403	33.8203	97.1498	2.5-5	PRIME	KNSTD	3.0014	0.1372	617	4607	93	87.21	62.93	21.50	2.46
WTS13405	35.4234	99.3747	2.5-5	PRIME	07KNSTD	0.4126	0.0189	35	4378	151	259.05	112.79	136.05	16.01
WTS13406	35.3724	99.2595	2.5-5	PRIME	07KNSTD	2.6933	0.0690	78	4456	91	149.74	77.76	21.24	2.24
WTS13407	34.4220	97.7258	2.5-5	PRIME	07KNSTD	2.8625	0.0404	303	4670	128	119.85	129.50	21.32	2.26
WTS13408	34.2492	99.2032	2.5-5	PRIME	07KNSTD	4.1112	0.1023	244	4407	100	124.33	80.87	12.62	1.38
WTS13409	33.9030	99.6126	2.5-5	PRIME	07KNSTD	1.0925	0.0304	729	4317	145	167.63	105.09	46.39	4.99
WTS13410	33.2887	97.4663	2.5-5	PRIME	07KNSTD	1.1637	0.0706	54	4530	133	257.81	121.88	47.29	5.85
WTS13411	33.2116	97.4864	2.5-5	PRIME	07KNSTD	2.0335	0.0521	8	4566	86	212.77	87.05	27.18	2.84
WTS13412	33.1930	97.4054	2.5-5	PRIME	07KNSTD	1.2497	0.0386	20	4402	150	318.65	118.91	40.92	4.69
WTS13413	33.1431	97.3565	2.5-5	PRIME	07KNSTD	1.1541	0.0321	149	4443	214	398.15	139.31	45.39	4.94
WTS13414	33.9795	97.4346	2.5-5	PRIME	07KNSTD	5.0187	0.1046	400	4754	117	96.31	99.80	12.39	1.38
WTS13415	35.0154	97.2396	2.5-5	PRIME	07KNSTD	6.8583	0.1305	21	4478	108	140.26	65.45	8.05	0.86
WTS13417	34.7220	96.1432	2.5-5	PRIME	07KNSTD	2.0614	0.0516	115	4692	79	79.55	66.20	30.76	3.31
WTS13418	34.2421	95.7834	2.5-5	PRIME	07KNSTD	1.8350	0.0380	231	4688	153	229.93	122.94	33.96	3.64
WTS13419	33.7793	96.7679	2.5-5	PRIME	07KNSTD	1.0576	0.0266	136	4576	147	246.31	129.47	54.75	6.26
WTS13420	33.7328	97.1129	2.5-5	PRIME	07KNSTD	1.7638	0.0301	96	4654	99	159.73	107.14	33.88	3.65
Zanskar and Ladakh, Transhimalaya[b]														
WTS13201	34.3222	77.8331	1.25-5	ETH	S2007N	1.6231	0.0515	372	4872	544	442.80	192.40	43.48	4.74
WTS13202	34.7670	77.1184	1.25-5	ETH	S2007N	0.4647	0.0249	40	4780	574	604.50	214.40	151.55	18.52
WTS13203	34.0390	77.2036	1.25-5	ETH	S2007N	0.1899	0.0206	20	4176	456	572.70	230.60	250.11	37.86
WTS13204	34.5836	77.4584	1.25-5	ETH	S2007N	0.7540	0.0242	520	5076	520	484.50	215.40	104.82	11.42
WTS13205	34.4942	77.7129	1.25-5	ETH	S2007N	0.6780	0.0257	104	4863	691	489.40	216.90	107.49	11.44
WTS13206	34.3683	77.6729	1.25-5	ETH	S2007N	2.6318	0.0838	93	5117	326	431.50	176.50	29.77	3.37
WTS13207	34.3752	77.6611	1.25-5	ETH	S2007N	2.3112	0.0738	106	5157	335	451.80	201.00	34.74	3.90
WTS13209	34.6697	77.2996	1.25-5	ETH	S2007N	0.9068	0.0328	345	5114	510	506.90	229.40	88.97	9.88
WTS13210	34.1050	77.2113	1.25-5	ETH	S2007N	0.3441	0.0243	168	4576	502	559.20	182.30	175.87	22.06

[a] Coordinate of DEM pixel in channel, nearest to sampling point in the field (GPS coordinate see Tab. 1).
[b] Corrected for mean lab blank (09-2010 to 02-2012) with ^{10}Be/^{9}Be ratio = 9.38756E-15; using Be_2SiO_4 carrier from Phenakite mineral; conc. 372.5 ± 3.5 ppm.
Averaging timescales were calculated assuming an absorption depth of 60 cm (Granger et al., 1996; von Blanckenburg, 2005).

Table C.2: Candidate predictors used in this study.

Parameter (Abbreviation) [Unit]	Meaning (Reference)
Slope (SLP) [m km^{-1}]	Average local slope gradient derived by fitting a polynomial function to nine neighboring DEM grid cells (Horn, 1981)
Steepness Index (k_S) [m$^{0.9}$]	k_S = SA$^{\theta}$ (A = upstream drainage basin area [m^2], S = local channel slope [m m^{-1}], $\theta = 0.45$ (reference concavity)) (Flint, 1974)
Hillslope Erosion Potential (HEP)	Product of SLP and mean annual precipitation (Mitchell and Montgomery, 2006)
Long-Wave Topography (LWAV) [m km^{-1}]	Slope of the regional maximum elevation range in a 25-km radius (Blöthe and Korup, 2013)
Peak Ground Acceleration (PGA) [m s^{-2}]	PGA with 10% probability of exceedance in 50 yr, corresponding to a return period of 475 yr (Giardini et al., 1999); GSHAP[a]
Strain (STRAIN)	Second invariant of model strain rate tensor field (Kreemer et al., 2003); GSRMP[b]
Aridity Index (AI)	Ratio of mean annual precipitation and mean annual potential evapo-transpiration (Zomer et al., 2006); Global-Aridity[c]

[a] Global Seismic Hazard Assessment Programm, http://www.seismo.ethz.ch/static/GSHAP
[b] Global Strain Rate Map Project, http://gsrm.unavco.org/
[a] Global Aridity Database, http://www.cgiar-csi.org/data/global-aridity-and-pet-database

C.2 ^{10}Be sample treatment

The WTS13201 - 10 samples were dried, sieved and the 125-500-μm grain size fraction was used for magnetic mineral separation. After pre-treating the samples with 19% HCl (incl. 5cl of H_2O_2, for 8h at 90 $^\circ$C), they were etched with 1:1 2% HF, and 2% HNO_3 (3 times for 8 h at 90 $^\circ$C in ultrasonic bath) (Kohl and Nishiizumi, 1992). Each sample was checked for natural ^{9}Be occurrence with an axial Inductively Coupled Plasma Optical Emission Spectrometer (ICP-OES). Subsequent separation of in-situ produced ^{10}Be was processed according to standard protocols (von Blanckenburg et al., 1996; von Blanckenburg and Kubik, 2004) in batches of 11 samples, and 1 process blank (Table C.2). The ^{10}Be/^{9}Be ratios were measured with the Accelerator Mass Spectrometer (AMS) of the ETH Zurich Ion Beam Physics Lab using the S2007N standard (Christl et al., 2013). All AMS-derived data were corrected against a mean lab blank (Table C.2).

C.3 Harmonization of basin-wide data and ^{10}Be production rates calculation

All basin-wide denudation rates were harmonized by recalculating topographic parameters using 90-m Shuttle Radar Topography Mission (SRTM, http://srtm.csi.cgiar.org) data according to Willenbring et al. (2013) and by restandardization to 07KNSTD (Balco et al., 2008). The ^{10}Be production rates were re-calculated using the scaling methods of (Dunai, 2000) and (Codilean, 2006) with ^{10}Be SLHL production rates of 4.5±0.5 for neutrons, 0.097±0.007 for slow muons, and 0.085±0.012 for fast muons; re-calculated from Balco et al's calibration dataset (Balco et al., 2008), using a ^{10}Be half life of 1.387 Ma (Chmeleff et al., 2010; Korschinek et al., 2010) and Dunai's scaling scheme (Dunai, 2000), and the new primary ^{10}Be standard and T1/2 for AMS at ETH, Ion Beam Physics, ETH Zurich (Christl et al., 2013).

C.4 Computing of basin-wide explanatory variable statistics

In order to derive catchment-wide statistics for the predictor variables to test we computed for each sampled drainage basin in our data compilation of basin-wide ^{10}Be catchment-wide averages the average local slope gradient, derived by fitting a polynomial function to nine neighboring DEM grid cells (Horn, 1981); the normalized steepness index $k_S = \mathrm{SA}^{\theta}$, where A = upstream drainage basin area [m^2], S = local channel slope [m m^{-1}], and $\theta = 0.45$ (arbitrarily fixed reference concavity) (Flint, 1974); the slope of the regional maximum elevation distance in a 25-km radius (LWAV) (Blöthe and Korup, 2013); hillslope erosion potential (HEP), which is the product of SLP and mean annual precipitation (Mitchell and Montgomery, 2006); WorldClims BIOCLIM products 1-19 (BIO), representing annual trends, seasonality or extremes in temperature and precipitation (Table S2) (Hijmans et al., 2005); the ratio of mean annual precipitation and mean annual potential evapotranspiration (AI) (Zomer et al., 2006); the peak ground acceleration (PGA) with 10% probability of exceedance in 50 years, corresponding to a return period of 475 years (Giardini et al., 1999); and the second invariant of the model strain rate tensor field given in the World Strain Map (STRAIN) (Kreemer et al., 2003).

Table C.3: Summary of BIOCLIM variables that have been tested for their predictive value on ^{10}Be-derived basin-wide denudation rates response distributions

Variable[a]	**Meaning**
BIO1	Annual Mean Temperature
BIO2	Mean Diurnal Range (Mean of monthly (max temp - min temp))
BIO3	Isothermality (BIO2/BIO7) (* 100)
BIO4	Temperature Seasonality (standard deviation *100)
BIO5	Max Temperature of Warmest Month
BIO6	Min Temperature of Coldest Month
BIO7	Temperature Annual Range (BIO5-BIO6)
BIO8	Mean Temperature of Wettest Quarter
BIO9	Mean Temperature of Driest Quarter
BIO10	Mean Temperature of Warmest Quarter
BIO11	Mean Temperature of Coldest Quarter
BIO12	Annual Precipitation
BIO13	Precipitation of Wettest Month
BIO14	Precipitation of Driest Month
BIO15	Precipitation Seasonality (Coefficient of Variation)
BIO16	Precipitation of Wettest Quarter
BIO17	Precipitation of Driest Quarter
BIO18	Precipitation of Warmest Quarter
BIO19	Precipitation of Coldest Quarter

[a] The BIOCLIM variables are derived from monthly temperature and rainfall data, representing annual trends, seasonality and extreme conditions.
A quarter is 1/4 year (Hijmans et al., 2005); Source: http://www.worldclim.org/bioclim.

C.5 Statistical analysis

C.5.1 Cluster analysis

We computed clustering statistics using the R software environment (www.r-project.org) and its *hclust* {*stats*} (Ward hierarchical clustering) (Ward, 1963) and *kmeans* {*stats*} (K-Means clustering) *functions* {*resp.packages*}. A dendrogram from Ward hierarchical clustering (Fig. C.4) was decision base for k-means input value (k = 5). K-means aims to minimize the sum of squares from data points to cluster centers. By default the Hartigan and Wong (1979) algorithm is used by *kmeans* {*stats*}. Note that elevation, basin area, geographic situation and ^{10}Be concentration-derived data were not included to cluster analysis.

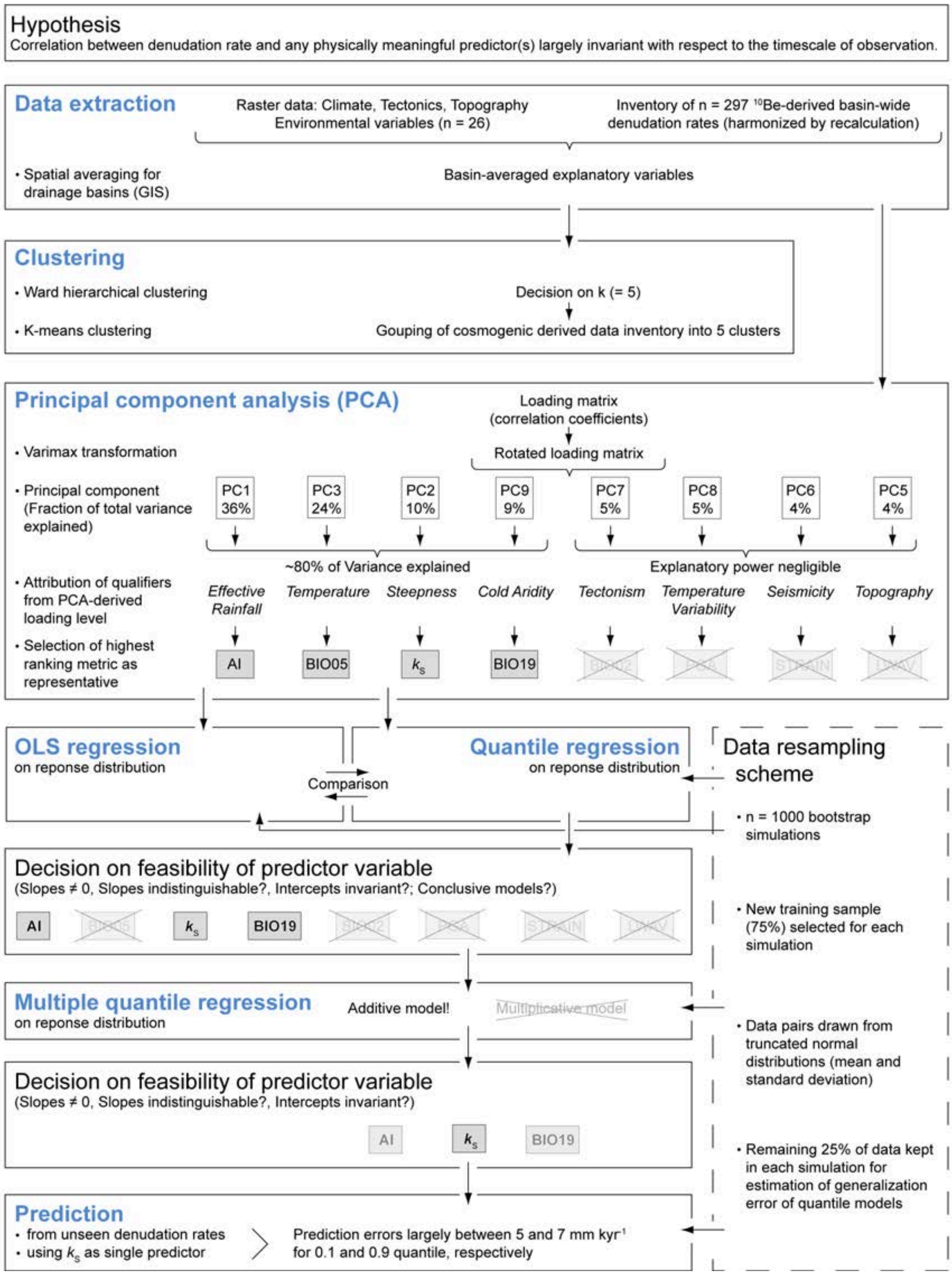

FIGURE C.2: Schematic workflow of the statistical approach behind the study

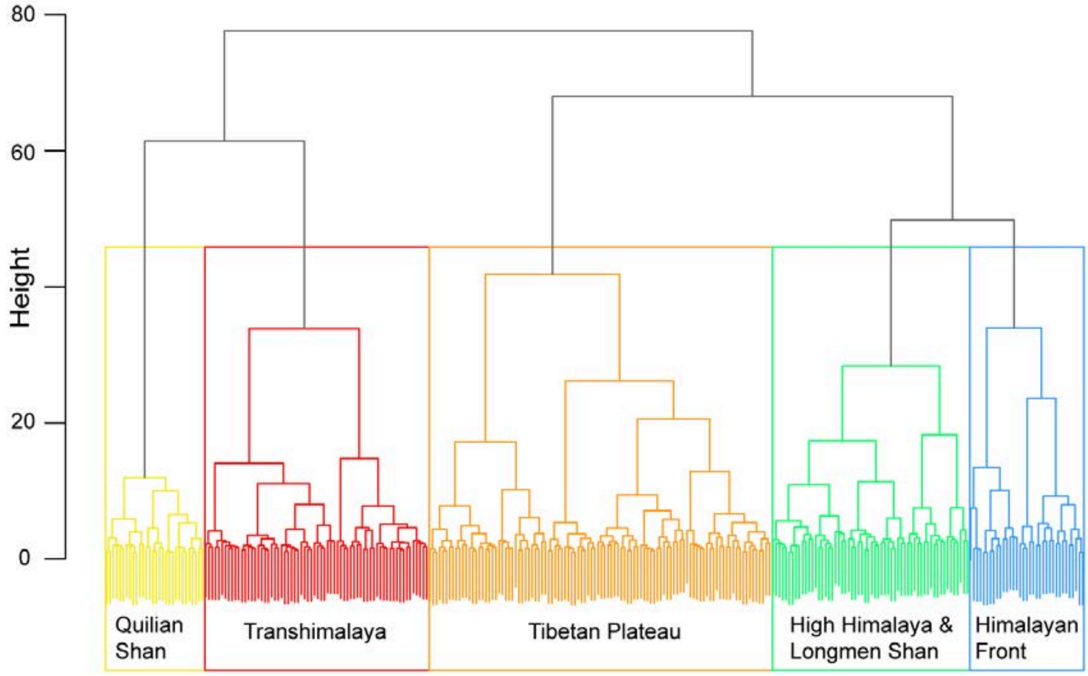

FIGURE C.3: Dendrogram showing result of Ward hierarchical clustering of n = 297 basin-averaged candidate predictor sets from ^{10}Be-measured basins from the Himalaya-Tibet orogen. Presented solution was chosen as basis for decision on number of clusters for k-means clustering (k = 5). Height on y-axis is dissimilarity level throughout the tree structure; color-coding of clusters consistent with Fig. 1.

C.5.2 Principal component analysis (PCA)

We computed PCA statistics using the R software environment (www.r-project.org) and its *principal* {*psych*} and *corrplot* {*corrplot*} *functions* {*resp.packages*}. Performing a PCA aims for decomposing a potentially correlated bulk of variables into linearly uncorrelated and orthogonally arrayed principal components, returning a loadings matrix that is built up by a correlation (or covariance) matrix. We applied *Varimax* transformation to the PCA-derived loadings matrix we used, aiming to improve its interpretability by matrix rotation (Kaiser, 1958). Finally we reordered the resulting principal components according to their explanatory power (Fig. C.3).

FACTOR LOADING

	PC 1	PC 3	PC 2	PC 9	PC 7	PC 8	PC 6	PC 5
SSL	9.4	6.2	2.6	2.3	1.2	1.2	1	1
Prop.Var.	36	24	10	9	5	5	4	4
Cum.Var.	36	60	70	79	84	88	92	96
SLP	9	8	**94**	15	10	11	12	12
STRAIN	17	16	16	24	**92**	10	5	11
PGA	-6	-17	-20	-7	-5	-6	**-95**	-7
HEP	78	41	34	16	4	10	8	13
LWAV	18	21	34	11	13	20	10	**85**
ks	16	6	**94**	9	7	13	11	14
AI	**95**	10	8	10	-8	9	3	4
BIO01	49	**84**	10	15	7	6	6	7
BIO02	-11	-16	-32	-29	-13	**-84**	-9	-22
BIO03	87	6	3	4	8	-31	-2	-2
BIO04	-91	-9	-19	-16	-10	-3	-2	-1
BIO05	3	**98**	1	11	4	2	7	5
BIO06	60	69	17	21	12	20	6	10
BIO07	-85	-10	-23	-21	-13	-26	-3	-9
BIO08	27	**93**	0	2	4	0	6	8
BIO09	51	68	20	32	22	15	6	4
BIO10	19	**97**	5	10	4	6	7	7
BIO11	66	69	14	17	9	7	6	5
BIO12	**86**	42	3	21	6	7	4	7
BIO13	**84**	42	-6	20	9	10	3	11
BIO14	57	40	14	57	10	20	8	-4
BIO15	57	8	-31	-38	-24	-15	-6	13
BIO16	**85**	42	-2	19	8	9	4	10
BIO17	54	28	20	**71**	16	17	8	9
BIO18	**89**	39	1	12	7	8	3	10
BIO19	36	24	19	**80**	26	18	6	13
QUALIFIER	Effective Rainfall	Temperature	Steepness	Cold Aridity	Tectonism	T Variability	Seismicity	Topography

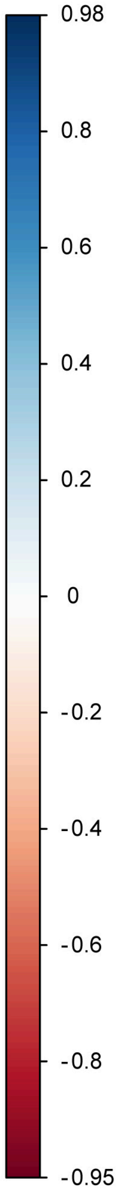

FIGURE C.4: Loading matrix from principal components analysis (PCA), including *Varimax* transformation. Principal components (PC) ordered by explanatory power regarding the variance of the data set; SSL (SS loadings) = Sum of Squared factors Loadings of particular PC column, i.e. Variance, that is explained by this PC; Prop. Var. = Proportion of Variance that is explained by this PC, i.e. SSL / nVar; Cum. Var =Cumulative proportion of explained Variance. Items given below the table represent supposed meaning, or reification, of individual PC.

C.5.3 Quantile regression

We computed quantile regression statistics using the R software environment (www.r-project.org) and its *rq* {*quantreg*} *function* {*resp.package*}. For details of the method see Koenker (2005). We ran 1000 bootstrap simulations, in which we selected for each run a random training sample of 75% of all data points. Data pairs were drawn from (truncated) normal distributions specified by the empirical means and standard deviations of the ^{10}Be laboratory reports and GIS-based zonal statistics. We kept the remaining 25% of the data in each simulation for computing the generalization error of the quantile models fitted to the training data. Various models of multiple (quantile) regression do exist. Additive models deal with the assumption that the effect of the explanatory variable on the response variable stays the same, even if the value of other included explanatory variables is varying (Friedrich, 1982).

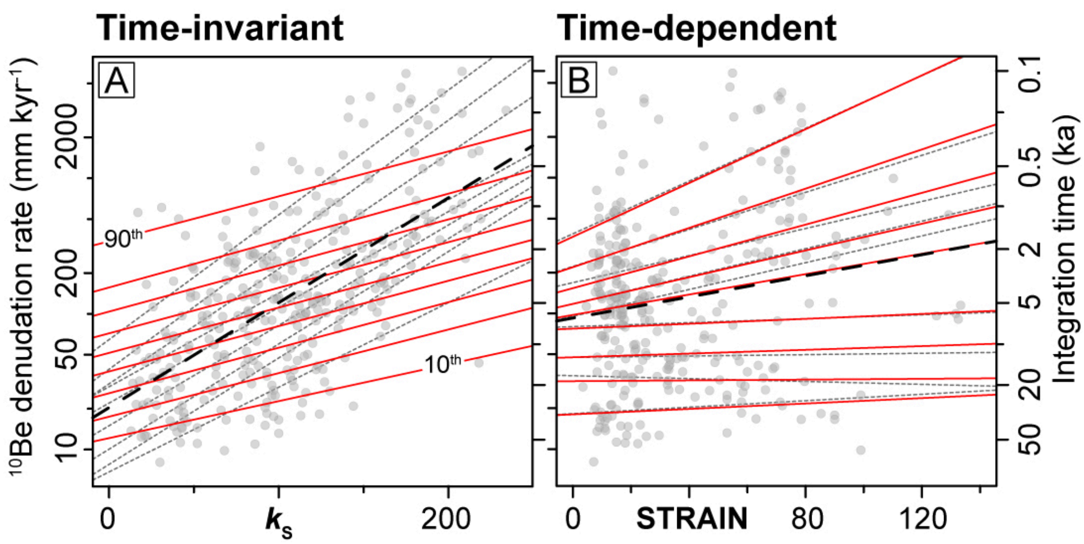

Figure C.5: Quantile regression-derived models for A) a time-invariant correlation between predictor (here k_S) and response variable and B) a timescale-dependent correlation between predictor (here STRAIN) and response variable. Grey circles are response distribution to respective predictor; solid red lines represent 0.1st to 0.9th QReg quantiles from n = 1000 resampling iterations bootstrap scheme; black dashed line is OLS regression model; thin dotted lines are 0.1st to 0.9th QReg quantile.

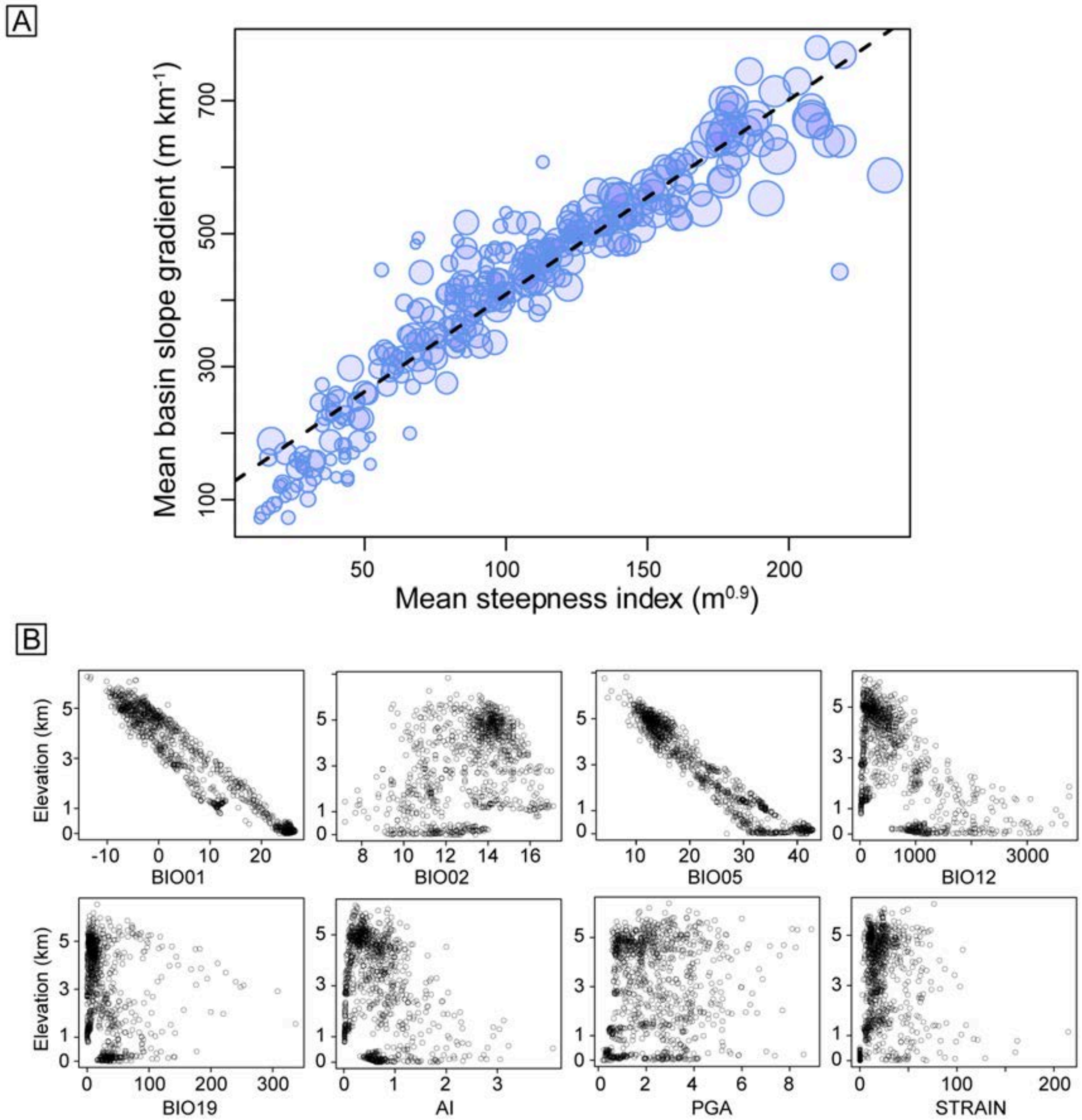

FIGURE C.6: A) Mean basin slope gradient (SLP) and mean steepness index (k_S) plot highly covariant. Bubble size is scaled to logarithmized ^{10}Be-derived basin-wide denudation rate; Dashed line is linear model from OLS regression. B) Pixel value from 90-m SRTM DEM (y) (elevation [km]) and climatic and tectonic predictor variables (x), as identified from PCA. Note the systematic correlations of $y \sim$ BIO01 and $y \sim$ BIO05. Samples (n = 1000) were drawn from equally sized ($5.7 * 10^6$-cell) raster data (resampled to 900-m resolution) using the R {*raster*} package and its *sampleRandom* function.

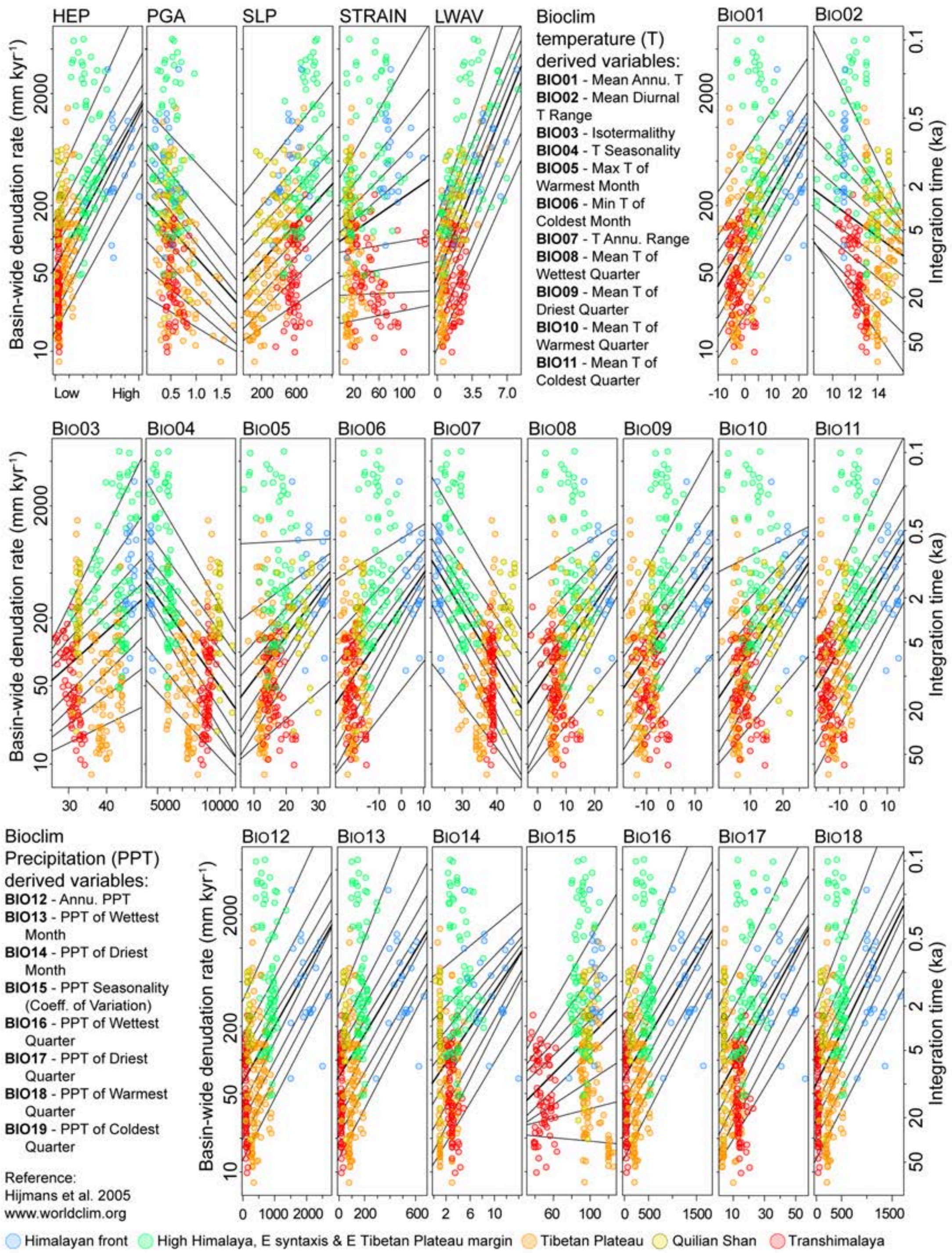

Figure C.7: Quantile regression results with 23 (out of 26) predictors, that have been discarded for reasons of low explanatory power or inconclusive model trends. Basin wide denudation rates versus HEP (Hillslope erosion potential), PGA (Peak ground acceleration), SLP (Average local slope gradient), STRAIN (Second invariant of the global model strain rate field), LWAV (Slope of the regional maximum elevation distance in a 25-km radius); BIO01–BIO11 (WorldClims Bioclim temperature derived variables), and BIO12–BIO18 (WorldClims Bioclim precipitation derived variables); color coded by result of k-means cluster analysis with n = 5 clusters. Black lines are 0.1^{st} to 0.9^{th} quantile regression lines; bold line is 0.5^{th} (median) quantile. Consistent correlations were found for HEP and SLP as well as for the BIOCLIM parameters 01, 04, 06, 07, 09, 11–14, and 16–18 (Fig. S3); the remainder of parameters had inconclusive trends.

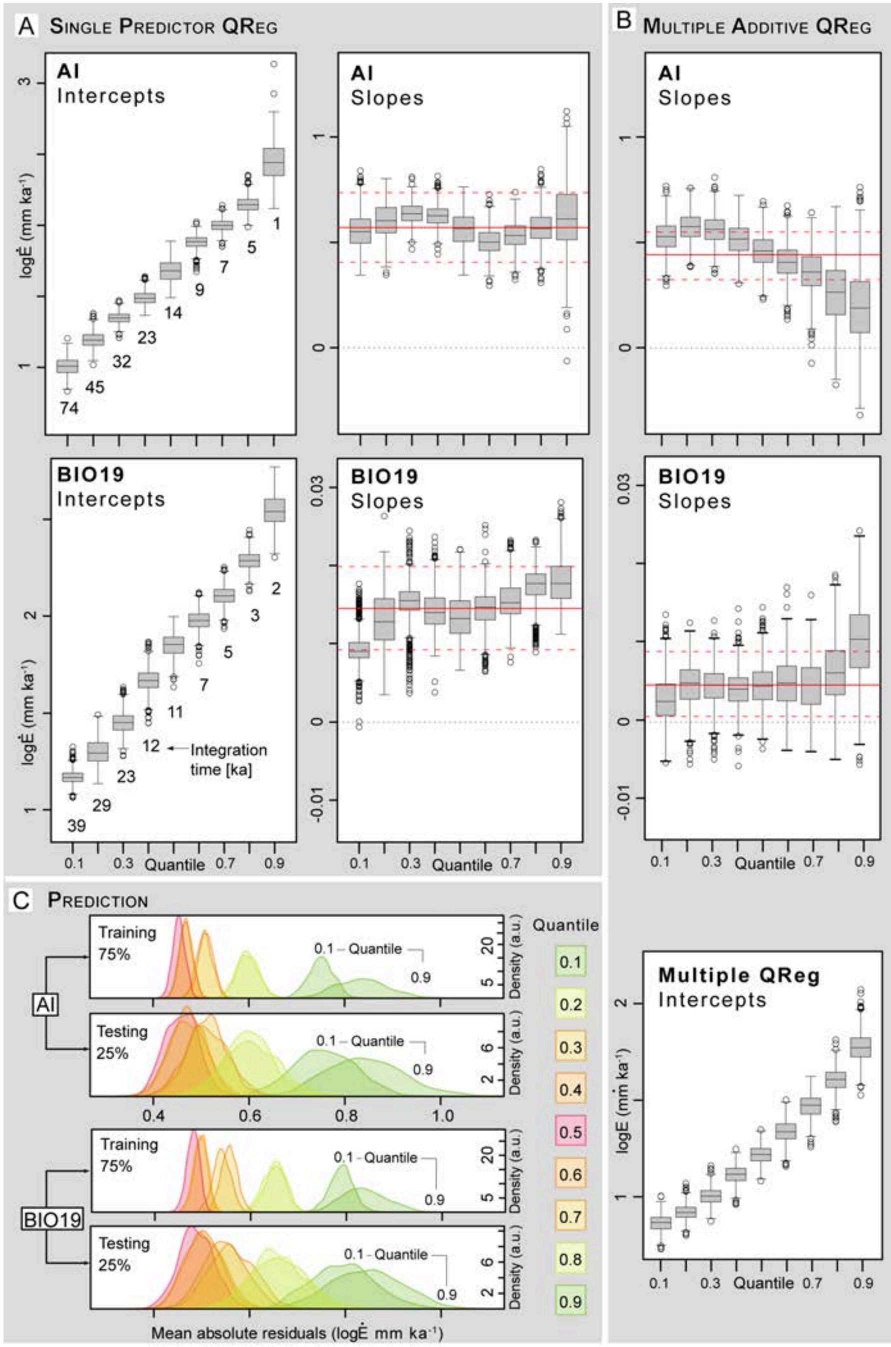

FIGURE C.8: Quantile regression models and residuals for the 0.1- to 0.9-quantiles, using cosmogenic ^{10}Be-derived basin-wide denudation rate as the response variable and Aridity index (AI) and Precipitation of the coldest quarter (BIO19) as predictors. A) Intercepts and slopes per quantile rank from 1000 bootstrap simulations; blacked dashed lines are zero regression slopes. Boxes frame 25th to 75th percentiles, bold lines in box are medians; whiskers extend to 1.5 times the interquartile range; circles are outliers. Solid red lines are median slopes from 1000 bootstrap simulations of OLS (Ordinary Least Squares) regression; dashed red lines are 95% confidence bounds. (B) Results from multiple quantile regression with additive effects. C) Mean absolute residuals for training and testing data. Central quantiles (red to orange) have smaller errors than distal (greenish) quantiles; generalization errors of testing data consistently exceed the fitting errors of the training data.

TABLE C.4: List of samples from previous studies that were included to the ^{10}Be-derived inventory used in this study; sampling sites and associated topographic parameters, cosmogenic ^{10}Be nuclide concentrations from AMS measurement, and re-calculated basin-wide denudation rates.

Sample ID	**Sample ID published[b]**	**Drainage point[a]** LAT [°N]	LON [°E]	**Grain-size** [$\mu m * 10^2$]	**AMS**	**Standard**	**^{10}Be conc. published[b]** [at. $g^{-1} * 10^6$]	1σ	**CF[c]**	**Area** [km^2]	**Mean basin elevation** [m a.s.l.]	1σ	**Mean basin slope** [m km^{-1}]	1σ	**^{10}Be conc. recalculated** [at. $g^{-1} * 10^6$]	1σ	**Denudation rate** [mm kyr^{-1}]	1σ
Nam Co, Tibetan Plateau, China (Strobl et al., 2012)																		
WTS10301	08T14	31.3327	90.1539	2.5-5	ETH	S2007N	5.180	0.160	1	42	5211	135	133.60	114.99	5.180	0.160	13.49	1.52
WTS10302	08T15	31.3169	90.1752	2.5-5	ETH	S2007N	4.050	0.120	1	13	5189	130	129.52	68.83	4.050	0.120	17.21	1.89
WTS10303	08T21	31.4889	89.9313	2.5-5	ETH	S2007N	3.156	0.095	1	53	5069	186	182.80	102.38	3.156	0.095	21.08	2.31
WTS10304	08T23	31.4015	90.0043	2.5-5	ETH	S2007N	4.450	0.130	1	9	5007	100	162.52	92.77	4.450	0.130	14.29	1.55
WTS10305	08T26	31.4527	89.8976	2.5-5	ETH	S2007N	4.020	0.120	1	3	5024	72	170.51	73.63	4.020	0.120	16.04	1.70
WTS10306	09T4	31.1056	90.6456	2.5-5	ETH	S2007N	3.268	0.098	1	3	5027	81	216.18	80.23	3.268	0.098	19.58	2.16
WTS10307	09T11	31.0385	90.7500	2.5-5	ETH	S2007N	5.460	0.160	1	2	4958	75	193.93	85.81	5.460	0.160	11.08	1.25
WTS10308	09T19	31.1049	90.6523	2.5-5	ETH	S2007N	5.510	0.170	1	4	5000	96	222.53	86.67	5.510	0.170	11.26	1.24
WTS10309	09T21	31.3540	89.8516	2.5-5	ETH	S2007N	3.720	0.110	1	19	5173	145	133.68	87.66	3.720	0.110	18.72	2.04
WTS10310	09T26	31.3212	90.0522	2.5-5	ETH	S2007N	4.370	0.130	1	33	5239	152	139.42	123.96	4.370	0.130	16.30	1.84
WTS10311	09T27	31.3480	90.0390	2.5-5	ETH	S2007N	4.760	0.140	1	43	5172	185	153.32	129.33	4.760	0.140	14.47	1.61
WTS10312	09T43	31.0636	90.7437	2.5-5	ETH	S2007N	4.410	0.130	1	14	5063	108	169.01	69.35	4.410	0.130	14.64	1.57
WTS10313	09T44	31.0619	90.7457	2.5-5	ETH	S2007N	4.440	0.130	1	34	5101	152	160.02	83.11	4.440	0.130	14.80	1.67
WTS10314	09T48	30.8813	91.1848	2.5-5	ETH	S2007N	5.040	0.150	1	53	5056	110	104.44	64.59	5.040	0.150	12.61	1.43
Ladakh Batholith, Transhimalaya, India (Dortch et al., 2011c)																		
WTS10701	BWR-1	34.0412	77.8193	2.5-10	PRIME	07KNSTD*	2.062	0.299	1	30	5107	360	432.00	176.30	2.062	0.299	37.08	6.81
WTS10702	BWR-10	34.4807	77.4344	2.5-10	PRIME	07KNSTD*	0.935	0.029	1	221	5235	333	470.00	216.70	0.935	0.029	89.93	9.97
WTS10703	BWR-12	34.5110	77.4154	2.5-10	PRIME	07KNSTD*	0.623	0.025	1	341	5185	381	471.70	216.60	0.623	0.025	132.45	15.01
WTS10704	BWR-14	34.2541	77.2886	2.5-10	PRIME	07KNSTD*	1.275	0.202	1	98	4704	538	478.10	161.60	1.275	0.202	50.34	9.84
WTS10705	BWR-15	34.2949	77.8429	2.5-10	PRIME	07KNSTD*	1.115	0.040	1	163	4933	534	478.10	185.60	1.115	0.040	65.45	7.32
WTS10706	BWR-16	34.2847	77.8276	2.5-10	PRIME	07KNSTD*	0.833	0.118	1	87	4966	439	421.60	184.80	0.833	0.118	89.15	15.63
WTS10707	BWR-17	34.5787	77.4576	2.5-10	PRIME	07KNSTD*	0.783	0.060	1	519	5078	517	484.60	215.50	0.783	0.060	100.98	13.30
WTS10708	BWR-2	34.1881	77.8557	2.5-10	PRIME	07KNSTD*	2.700	0.099	1	43	5230	281	426.60	179.30	2.700	0.099	30.50	3.43
WTS10709	BWR-3	34.3101	77.8375	2.5-10	PRIME	07KNSTD*	1.471	0.036	1	369	4881	536	442.50	192.00	1.471	0.036	48.24	5.23
WTS10710	BWR-4	34.2798	77.7624	2.5-10	PRIME	07KNSTD*	1.174	0.149	1	32	5173	273	419.30	178.00	1.174	0.149	69.15	11.19
WTS10711	BWR-5	34.1586	77.6637	2.5-10	PRIME	07KNSTD*	2.712	0.099	1	35	4938	436	470.50	159.20	2.712	0.099	26.28	2.99
WTS10712	BWR-6	33.9408	77.7675	2.5-10	PRIME	07KNSTD*	2.202	0.101	1	184	4586	605	430.10	185.30	2.202	0.101	27.29	3.20
WTS10713	BWR-7	34.3038	77.3226	2.5-10	PRIME	07KNSTD*	1.929	0.056	1	58	5014	366	460.10	156.20	1.929	0.056	38.55	4.08
WTS10714	BWR-8	34.3396	77.3531	2.5-10	PRIME	07KNSTD*	2.001	0.044	1	14	5262	220	455.20	171.80	2.001	0.044	41.89	4.48
Ladakh Batholith, Transhimalaya, India (Dietsch et al.)																		
WTS10801	CR40B	33.9647	77.7839	NA	PRIME	07KNSTD	2.450	0.075	1	1	3956	137	493.30	159.20	2.450	0.075	16.52	1.85
WTS10802	CR45B	33.9914	77.8011	NA	PRIME	07KNSTD	2.508	0.111	1	3	4180	187	473.40	142.30	2.508	0.111	18.43	2.01
WTS10803	CR50B	34.0322	77.7981	NA	PRIME	07KNSTD	2.548	0.139	1	3	4541	159	441.50	120.70	2.548	0.139	22.22	2.63
WTS10804	LH40B	34.1707	77.6041	NA	PRIME	07KNSTD	1.690	0.076	1	2	3873	119	445.60	171.80	1.690	0.076	23.25	2.68

Continued on next page

Sample ID	Sample ID published[b]	Drainage point[a] LAT [°N]	LON [°E]	Grain-size [μm*10^2]	AMS	Standard	^{10}Be conc. published[b] [at. g^{-1}*10^{6}]	1σ	CF[c]	Area [km^{2}]	Mean basin elevation [m a.s.l.]	1σ	Mean basin slope [m km^{-1}]	1σ	^{10}Be conc. recalculated [at. g^{-1}*10^{6}]	1σ	Denudation rate [mm kyr^{-1}]	1σ
WTS10805	LH45B	34.187	77.6232	NA	PRIME	07KNSTD	3.608	0.153	1	1	4238	142	477.90	112.60	3.608	0.153	13.16	1.53
WTS10806	LH50B	34.2386	77.6195	NA	PRIME	07KNSTD	2.597	0.096	1	1	4775	150	478.10	103.40	2.597	0.096	24.94	2.81
WTS10807	PH40B	34.1836	77.4586	NA	PRIME	07KNSTD	2.218	0.050	1	1	3903	181	607.80	189.80	2.218	0.050	17.77	1.92
WTS10808	PH45B	34.1876	77.4680	NA	PRIME	07KNSTD	2.500	0.107	1	2	3984	200	531.60	167.80	2.500	0.107	16.55	1.90
WTS10809	PH50B	34.2264	77.4872	NA	PRIME	07KNSTD	3.578	0.152	1	1	4642	168	489.50	141.90	3.578	0.152	16.69	1.90
WTS10810	TS40B	34.0106	77.7256	NA	PRIME	07KNSTD	3.379	0.158	1	1	3642	132	484.30	154.10	3.379	0.158	9.81	1.13
WTS10811	TS45B	34.0328	77.7622	NA	PRIME	07KNSTD	1.879	0.058	1	1	4194	170	511.50	124.70	1.879	0.058	24.97	2.71
WTS10812	TS50B	34.0361	77.7578	NA	PRIME	07KNSTD	2.772	0.077	1	2	4343	231	539.40	137.20	2.772	0.077	18.24	2.04
Zoulang Nan Shan, NE Tibetan Plateau, China (Hetzel, 2013)																		
WTS11901	QS-JG-33	38.7673	99.4099	2.5-5	ETH	S2007N	0.143	0.008	1	15	3768	446	489.10	173.20	0.143	0.008	330.07	39.82
WTS11902	QS-JG-34	38.8258	99.3128	2.5-5	ETH	S2007N	0.130	0.008	1	155	4002	375	381.10	178.30	0.130	0.008	412.15	48.81
WTS11903	QS-JG-40	38.8063	99.3065	2.5-5	ETH	S2007N	0.653	0.027	1	6	4052	271	493.60	156.20	0.653	0.027	82.02	9.22
WTS11904	QS-JG-41	38.8136	99.3179	2.5-5	ETH	S2007N	0.560	0.021	1	14	3928	378	463.30	181.70	0.560	0.021	90.12	9.93
WTS11905	QS-JG-42	38.7677	99.4498	2.5-5	ETH	S2007N	0.175	0.008	1	546	3874	453	423.50	179.50	0.175	0.008	284.22	32.67
WTS11906	QS-JG-43	38.8283	99.2734	2.5-5	ETH	S2007N	0.447	0.016	1	6	4166	276	478.10	198.30	0.447	0.016	127.78	14.22
WTS11907	QS-JG-47	38.7686	99.1633	2.5-5	ETH	S2007N	1.608	0.048	1	13	4175	206	287.40	120.50	1.608	0.048	35.55	3.77
WTS11908	QS-JG-48	38.7252	99.2865	2.5-5	ETH	S2007N	2.341	0.070	1	12	4210	186	338.20	107.80	2.341	0.070	24.74	2.73
WTS11910	QS-JG-55	38.8017	99.0929	2.5-5	ETH	S2007N	2.215	0.066	1	14	4265	208	299.30	162.30	2.215	0.066	27.10	2.98
Anyemaquen Shan, E Tibet, China (Kirby and Harkins, 2013)																		
WTS12401	KE-04-2	35.0967	100.7611	NA	PRIME	KNSTD	0.634	0.015	0.904	1	3662	61	245.69	99.44	0.573	0.013	64.02	6.99
WTS12402	KE-04-3	34.8979	100.8854	NA	PRIME	KNSTD	0.708	0.011	0.904	2	3953	72	246.51	89.70	0.640	0.010	67.28	7.19
WTS12403	KE-04-4a	34.7985	100.8118	NA	PRIME	KNSTD	0.427	0.009	0.904	1	3702	87	317.82	102.59	0.386	0.008	96.65	10.27
WTS12404	KE-05-1	34.7776	100.8130	NA	PRIME	KNSTD	0.430	0.014	0.904	2	3736	127	328.05	123.42	0.389	0.012	97.72	10.49
WTS12405	KE-05-2	34.7531	99.6945	NA	PRIME	KNSTD	0.448	0.017	0.904	8	4299	200	412.09	112.39	0.405	0.015	128.91	14.48
WTS12406	KE-05-3	34.5273	100.3941	NA	PRIME	KNSTD	0.546	0.080	0.904	4	4166	165	350.55	105.00	0.494	0.073	97.04	18.02
WTS12407	KE-05-6	33.6938	101.3882	NA	PRIME	KNSTD	0.568	0.022	0.904	4	3936	164	411.30	138.56	0.513	0.020	79.30	8.89
WTS12408	NHKCB06-1	34.5992	101.3400	NA	PRIME	KNSTD*	0.631	0.026	0.904	119	3800	157	230.72	103.50	0.571	0.023	68.77	7.72
WTS12409	NHKCB06-2	33.7654	101.2272	NA	PRIME	KNSTD*	0.517	0.017	0.904	55	4087	209	336.16	130.20	0.467	0.015	95.66	10.46
WTS12410	NHKCB06-3	33.7241	101.2720	NA	PRIME	KNSTD*	0.623	0.035	0.904	214	4154	217	315.30	141.01	0.563	0.031	82.44	10.21
WTS12411	NHKCB06-4	34.5572	99.4807	NA	PRIME	KNSTD*	0.911	0.035	0.904	4	4810	117	325.80	140.16	0.823	0.031	82.15	9.15
WTS12412	NHKCB06-5	34.4792	99.7785	NA	PRIME	KNSTD*	0.461	0.019	0.904	6	4530	179	405.78	144.56	0.417	0.017	140.06	15.40
WTS12413	NHKCB06-6	34.6891	100.6224	NA	PRIME	KNSTD*	0.154	0.007	0.904	20	3701	339	342.93	144.60	0.139	0.007	272.13	30.76
Himalaya, Nepal (Wobus et al., 2005)																		
WTS12501	01WBS5	28.2057	84.8746	NA	LLNL	KNSTD*	0.042	0.002	0.904	4	1635	337	610.30	213.21	0.038	0.002	241.44	29.34
WTS12502	01WBS6	28.1380	84.8540	NA	LLNL	KNSTD*	0.028	0.002	0.904	18	2028	529	666.77	294.20	0.025	0.001	470.09	55.72
WTS12503	01WBS7	28.0997	84.8343	NA	LLNL	KNSTD*	0.014	0.002	0.904	17	1432	433	517.88	197.10	0.013	0.002	663.33	106.95
WTS12504	03WBS1	28.0806	84.8193	NA	LLNL	KNSTD*	0.006	0.001	0.904	3	959	167	459.43	195.95	0.005	0.000	1138.24	151.08
WTS12505	03WBS2	28.0615	84.8641	NA	LLNL	KNSTD*	0.028	0.001	0.904	4	1111	161	366.60	109.02	0.025	0.001	266.38	30.57

Continued on next page

Sample ID	Sample ID published[b]	Drainage point[a] LAT [°N]	LON [°E]	Grain-size [μm*10^2]	AMS	Standard	^{10}Be conc. published[b] [at. g^{-1}*10^6]	1σ	CF[c]	Area [km^2]	Mean basin elevation [m a.s.l.]	1σ	Mean basin slope [m km^{-1}]	1σ	^{10}Be conc. recalculated [at. g^{-1}*10^6]	1σ	Denudation rate [mm kyr^{-1}]	1σ
WTS12506	01WBS3	27.9483	84.7306	NA	LLNL	KNSTD*	0.022	0.002	0.904	17	805	176	349.73	126.50	0.020	0.002	284.07	37.92
WTS12507	01WBS2	27.9281	84.7291	NA	LLNL	KNSTD*	0.023	0.002	0.904	22	900	235	354.45	114.91	0.021	0.002	281.97	36.85
WTS12508	01WBS1	27.8814	84.7436	NA	LLNL	KNSTD*	0.025	0.002	0.904	10	913	252	346.66	120.19	0.023	0.002	261.89	32.77
Marsyandi Basin, Himalaya, Nepal (Godard et al., 2012)																		
WTS12601	NEP003a	27.8932	84.5426	2.5-10	CEREGE	NIST‡	0.009	0.001	1	618	1462	1081	430.28	211.54	0.009	0.001	1155.78	143.61
WTS12603	NEP030a	27.9548	84.4203	2.5-10	CEREGE	NIST‡	0.060	0.003	1	110	731	212	296.82	156.22	0.060	0.003	88.04	10.28
WTS12605	NEP080a	28.0579	84.4840	2.5-10	CEREGE	NIST‡	0.016	0.001	1	310	1818	977	420.09	172.14	0.016	0.001	740.10	94.08
WTS12606	NEP099a	28.1121	84.4271	2.5-10	CEREGE	NIST‡	0.017	0.001	1	83	960	245	345.94	170.54	0.017	0.001	371.18	43.77
WTS12608	NEP118a	28.3196	84.4053	2.5-10	CEREGE	NIST‡	0.007	0.000	1	216	3464	1222	616.70	279.86	0.007	0.000	4255.15	548.57
WTS12610	NEP138	28.5583	84.2604	2.5-10	CEREGE	NIST‡	0.024	0.001	1	891	5185	707	552.26	292.42	0.024	0.001	2807.87	333.35
WTS12612	NEP140	28.5522	84.2555	2.5-10	CEREGE	NIST‡	0.014	0.001	1	743	4836	853	576.45	308.63	0.014	0.001	3993.00	539.09
WTS12613	NEP151	28.6197	84.1445	2.5-10	CEREGE	NIST‡	0.016	0.001	1	562	4938	767	533.39	288.81	0.016	0.001	3767.54	521.42
WTS12615	NIB-975-02a	28.2818	84.3555	2.5-10	CEREGE	NIST‡	0.006	0.001	1	136	2601	915	537.38	195.82	0.006	0.001	3293.53	791.78
WTS12620	NIB-975-10	28.5277	84.3587	2.5-10	CEREGE	NIST‡	0.009	0.001	1	383	4615	981	657.93	355.97	0.009	0.001	5912.93	755.25
WTS12623	NIB-975-21	28.5171	84.3606	2.5-10	CEREGE	NIST‡	0.038	0.003	1	130	4850	1104	698.03	346.59	0.038	0.003	1555.32	207.47
WTS12625	NIB-975-37a	27.8932	84.5426	2.5-10	CEREGE	NIST‡	0.008	0.000	1	618	1462	1081	430.28	211.54	0.008	0.000	1327.62	155.85
WTS12626	NIB-975-44a	28.1675	84.4481	2.5-10	CEREGE	NIST‡	0.012	0.001	1	353	2881	1558	578.93	233.59	0.012	0.001	2175.99	257.25
Zanskar & Ladakh, Transhimalaya, India (Munack et al., 2014)																		
WTS12701	Achina	34.5040	76.6301	1.25-5	ETH	S2007N	0.724	0.024	1	65	4449	598	512.30	181.90	0.724	0.024	77.76	8.90
WTS12702	Alchi	34.2237	77.1696	1.25-5	ETH	S2007N	0.675	0.023	1	25	4369	523	573.70	173.40	0.675	0.023	81.94	9.12
WTS12703	Chuma-1	33.3641	78.3537	1.25-5	ETH	S2007N	2.306	0.073	1	173	5460	432	456.80	195.70	2.306	0.073	38.75	4.12
WTS12704	Chuma-2	33.3570	78.3230	1.25-5	ETH	S2007N	7.024	0.223	1	34	5193	367	321.60	177.20	7.024	0.223	10.96	1.21
WTS12705	Domkar	34.3915	76.7737	1.25-5	ETH	S2007N	0.698	0.026	1	182	4797	549	476.50	207.60	0.698	0.026	98.31	10.99
WTS12706	Giera	34.2501	77.0817	1.25-5	ETH	S2007N	0.374	0.019	1	75	4429	580	597.30	202.60	0.374	0.019	153.81	17.78
WTS12707	Hanu	34.5611	76.5880	1.25-5	ETH	S2007N	0.477	0.018	1	307	4630	535	482.60	213.80	0.477	0.018	132.71	14.87
WTS12708	Humla	34.2222	77.3887	1.25-5	ETH	S2007N	2.490	0.080	1	29	4503	384	479.00	151.70	2.490	0.080	22.17	2.52
WTS12709	Igoo	33.8901	77.7811	1.25-5	ETH	S2007N	2.059	0.066	1	117	4596	559	447.40	154.20	2.059	0.066	29.09	3.33
WTS12710	Kumdo	33.5139	78.1554	1.25-5	ETH	S2007N	0.706	0.023	1	162	5428	397	467.00	209.20	0.706	0.023	127.14	14.39
WTS12711	Lardo	34.2374	77.1175	1.25-5	ETH	S2007N	0.589	0.023	1	27	4552	567	544.50	165.40	0.589	0.023	102.90	11.30
WTS12712	Leido	34.4419	76.6833	1.25-5	ETH	S2007N	0.334	0.020	1	37	4015	524	520.50	155.30	0.334	0.020	139.58	17.15
WTS12713	Ligchi	33.7283	77.9600	1.25-5	ETH	S2007N	2.071	0.066	1	238	5184	496	496.90	192.40	2.071	0.066	38.86	4.25
WTS12714	Martse	33.9017	77.7311	1.25-5	ETH	S2007N	0.510	0.024	1	177	4596	513	480.40	168.30	0.510	0.024	120.16	13.99
WTS12715	Matho	33.9965	77.6349	1.25-5	ETH	S2007N	0.662	0.023	1	106	4731	507	443.50	187.70	0.662	0.023	99.66	11.24
WTS12716	Nang	34.0516	77.7535	1.25-5	ETH	S2007N	1.950	0.062	1	40	4646	459	496.80	152.60	1.950	0.062	31.50	3.46
WTS12717	Nidder	33.1600	78.6079	1.25-5	ETH	S2007N	2.035	0.065	1	195	5117	507	333.50	175.90	2.035	0.065	37.07	4.16
WTS12718	Nimu	34.2056	77.3445	1.25-5	ETH	S2007N	1.472	0.051	1	67	4597	581	502.10	164.30	1.472	0.051	41.40	4.69
WTS12719	Nimu-11	34.2030	77.3416	1.25-5	ETH	S2007N	1.539	0.059	1	70	4552	607	495.20	169.70	1.539	0.059	39.09	4.49
WTS12720	Nogo	33.2428	78.5756	1.25-5	ETH	S2007N	5.788	0.183	1	79	5448	413	390.80	181.50	5.788	0.183	15.08	1.65

Continued on next page

Sample ID	Sample ID published[b]	Drainage point[a] LAT [°N]	LON [°E]	Grain-size [μm*10^2]	AMS	Standard	^{10}Be conc. published[b] [at. g^{-1}*10^6]	1σ	CF[c]	Area [km^2]	Mean basin elevation [m a.s.l.]	1σ	Mean basin slope [m km^{-1}]	1σ	^{10}Be conc. recalculated [at. g^{-1}*10^6]	1σ	Denudation rate [mm kyr^{-1}]	1σ
WTS12721	Nurla	34.3022	76.9865	1.25-5	ETH	S2007N	1.360	0.043	1	209	4721	633	464.60	205.10	1.360	0.043	48.83	5.35
WTS12722	Nyoma	33.2162	78.6584	1.25-5	ETH	S2007N	4.969	0.157	1	73	5449	415	411.70	167.40	4.969	0.157	17.54	1.94
WTS12723	Phyang	34.1998	77.5088	1.25-5	ETH	S2007N	2.123	0.068	1	74	4833	477	447.60	161.90	2.123	0.068	32.32	3.58
WTS12724	Saspo	34.2997	77.1606	1.25-5	ETH	S2007N	1.257	0.041	1	69	4891	496	457.90	188.90	1.257	0.041	55.73	6.16
WTS12725	Skid	33.3727	78.2655	1.25-5	ETH	S2007N	1.934	0.062	1	59	5384	470	380.50	148.00	1.934	0.062	45.23	5.03
WTS12726	Skyur	34.4338	76.7072	1.25-5	ETH	S2007N	0.527	0.026	1	119	4671	592	504.40	203.00	0.527	0.026	123.36	14.45
WTS12727	Stagmo	34.1183	77.7003	1.25-5	ETH	S2007N	3.133	0.100	1	40	4827	469	517.70	140.40	3.133	0.100	20.89	2.30
WTS12728	Stok-11	34.0413	77.5269	1.25-5	ETH	S2007N	0.608	0.020	1	60	4847	474	453.60	176.70	0.608	0.020	114.70	12.83
WTS12729	Stok-3	34.0471	77.5306	1.25-5	ETH	S2007N	0.701	0.024	1	64	4797	500	456.70	177.00	0.701	0.024	96.12	10.48
WTS12730	Tarch	33.7048	77.9617	1.25-5	ETH	S2007N	1.516	0.049	1	42	4921	554	517.40	171.00	1.516	0.049	47.57	5.28
WTS12731	Tharu	34.2249	77.4510	1.25-5	ETH	S2007N	2.453	0.079	1	27	4811	377	496.40	132.90	2.453	0.079	26.97	3.01
WTS12732	Tiridoo	33.5843	78.0794	1.25-5	ETH	S2007N	2.204	0.070	1	196	5107	346	394.30	181.80	2.204	0.070	34.28	3.81
WTS12733	Zin	34.1209	77.4146	1.25-5	ETH	S2007N	0.632	0.024	1	131	4490	494	514.40	171.80	0.632	0.024	90.70	10.19
Himalaya, Nepal (Andermann, 2011)																		
WTS13307	NP_A12s	28.1875	85.3003	2.5-10	CEREGE	NIST‡	0.010	0.001	1	226	4423	1076	641.29	270.18	0.010	0.001	4671.82	796.11
WTS13308	NP_A14s	28.1803	85.2973	2.5-10	CEREGE	NIST‡	0.008	0.001	1	42	3000	551	571.25	214.15	0.008	0.001	2537.86	356.60
WTS13309	NP_A16s-I	28.2259	85.3686	2.5-10	CEREGE	NIST‡	0.018	0.003	1	20	3527	755	638.94	227.43	0.018	0.003	1593.77	301.17
WTS13310	NP_A16s-II	28.2259	85.3686	2.5-10	CEREGE	NIST‡	0.019	0.002	1	20	3527	755	638.94	227.43	0.019	0.002	1521.70	258.93
WTS13312	NP_A1s	27.8615	85.1358	2.5-10	DREAMS	NIST‡	0.020	0.002	1	653	1656	886	458.49	208.89	0.020	0.002	533.22	81.59
WTS13314	NP_A23s	28.1008	84.8313	2.5-10	CEREGE	NIST‡	0.009	0.001	1	17	1438	430	517.34	198.25	0.009	0.001	958.16	121.70
WTS13316	NP_A3s	27.9290	85.1338	2.5-10	CEREGE	NIST‡	0.013	0.001	1	53	1257	359	442.09	167.42	0.013	0.001	567.33	70.87
WTS13318	NP_A5s	27.9759	85.1902	2.5-10	CEREGE	NIST‡	0.014	0.001	1	147	2112	865	531.76	185.27	0.014	0.001	990.55	116.09
WTS13319	NP_A9s	28.1073	85.3118	2.5-10	CEREGE	NIST‡	0.082	0.003	1	52	3541	757	523.76	211.08	0.082	0.003	350.83	37.11
WTS13323	NP080924A	27.5946	85.6738	2.5-10	CEREGE	NIST‡	0.032	0.001	1	113	1146	250	260.69	149.77	0.032	0.001	213.89	24.05
WTS13324	NP080929A	27.6173	86.0861	2.5-10	CEREGE	NIST‡	0.038	0.002	1	54	1797	386	336.50	128.30	0.038	0.002	266.55	31.63
Kunlun Shan and Central Tibet, China (Li et al., 2014)																		
WTS13501	SH-08-38	33.3022	88.5867	2.5-5	PRIME	07KNSTD	4.6468	0.1660	1	150	5262	140	120.55	100.97	4.646	0.166	16.98	1.92
WTS13502	SH-08-56	32.9604	88.8926	2.5-5	PRIME	07KNSTD	5.0840	0.1269	1	357	5059	73	72.30	68.52	5.083	0.127	13.70	1.52
WTS13503	TB-04-05	35.6301	94.2064	2.5-5	PRIME	KNSTD	0.8825	0.2023	0.904	11	5436	246	320.21	197.06	0.882	0.202	124.17	32.17
WTS13506	TB-08-02	36.0007	94.8286	2.5-5	PRIME	07KNSTD	0.5306	0.0272	1	294	4264	433	397.73	211.26	0.530	0.027	103.63	12.18
WTS13508	TB-08-04	35.8936	94.4332	2.5-5	PRIME	07KNSTD	1.1145	0.0284	1	213	4415	347	384.14	204.17	1.114	0.028	53.00	5.79
WTS13510	TB-08-07	35.7476	94.3230	2.5-5	PRIME	07KNSTD	0.3136	0.0163	1	365	4726	333	221.98	173.39	0.313	0.016	222.49	25.95
WTS13512	TB-08-09	34.8858	92.9354	2.5-5	PRIME	07KNSTD	2.1135	0.0661	1	1009	4793	137	92.86	80.93	2.113	0.066	32.02	3.48
WTS13513	TB-08-10	34.5871	92.7439	2.5-5	PRIME	07KNSTD	2.5576	0.1522	1	193	4890	107	155.31	98.18	2.557	0.152	27.49	3.40
WTS13516	TB-08-14	32.3159	91.7263	2.5-5	PRIME	07KNSTD	1.4945	0.0547	1	564	4958	101	124.55	99.39	1.494	0.055	44.44	5.02
Namche Barwa-Gyala Peri Massif, Tibet, China (Finnegan et al., 2008)																		
WTS33002	NB-13-02	29.9084	95.5144	5-8.5	LLNL	KNSTD*	0.016	0.001	0.904	20	4116	540	641.90	249.40	0.014	0.001	2696.20	296.07
WTS33003	NB-14-02	29.9469	95.4100	5-8.5	LLNL	KNSTD*	0.012	0.000	0.904	20	4262	448	654.30	264.70	0.011	0.000	3822.21	415.61

Continued on next page

Sample ID	**Sample ID published**[b]	**Drainage point**[a] LAT [°N]	LON [°E]	**Grain-size** [μm$*10^2$]	**AMS**	**Standard**	^{10}**Be conc. published**[b] [at. g$^{-1}*10^6$]	1σ	**CF**[c]	**Area** [km^2]	**Mean basin elevation** [m a.s.l.]	1σ	**Mean basin slope** [m km^{-1}]	1σ	^{10}**Be conc. recalculated** [at. g$^{-1}*10^6$]	1σ	**Denudation rate** [mm kyr^{-1}]	1σ
WTS33004	NB-23-02	30.1022	95.1121	5-8.5	LLNL	KNSTD*	0.012	0.001	0.904	29	3737	683	670.00	210.20	0.011	0.001	3015.38	403.66
WTS33007	NB-5-02	30.0660	95.1796	5-8.5	LLNL	KNSTD*	0.016	0.001	0.904	26	3888	657	674.30	213.40	0.014	0.001	2468.30	302.23
WTS33008	NB-5-04	29.9460	94.8040	2.5-5	LLNL	KNSTD*	0.128	0.005	0.904	807	4173	485	427.60	206.70	0.115	0.004	356.02	40.33
WTS33010	NB-7-02	30.0446	95.2594	5-8.5	LLNL	KNSTD*	0.007	0.000	0.904	11	4064	685	672.10	182.90	0.007	0.000	6134.12	704.07
WTS33013	P-6-02	29.9531	95.3841	5-8	LLNL	KNSTD*	0.011	0.001	0.904	2	3853	396	644.30	145.80	0.010	0.000	3584.09	404.36
E Tibet, China (Ouimet et al., 2009)																		
WTS37001	wbo302	30.2696	101.5300	2.5-5	PRIME	NIST†	1.088	0.019	1.043	36	4074	101	100.76	54.27	1.134	0.020	33.44	3.67
WTS37002	wbo305	29.8895	101.5405	2.5-5	PRIME	NIST†	1.805	0.049	1.043	21	4295	35	73.03	51.61	1.882	0.051	22.16	2.39
WTS37003	wbo316	29.4299	101.2373	2.5-5	PRIME	NIST†	0.196	0.009	1.043	33	4469	397	484.33	222.57	0.204	0.009	228.23	25.54
WTS37004	wbo424	31.3001	103.5273	2.5-5	PRIME	KNSTD	0.067	0.003	0.904	16	3004	440	664.02	190.12	0.060	0.003	371.61	44.71
WTS37005	wbo439	29.4096	101.2263	2.5-5	PRIME	KNSTD	0.124	0.005	0.904	94	4496	467	500.13	216.72	0.112	0.005	421.84	49.33
WTS37006	wbo444	29.3747	102.2429	2.5-5	PRIME	KNSTD	0.042	0.005	0.904	24	1938	345	557.66	191.93	0.038	0.004	296.32	47.66
WTS37007	wbo445	29.4986	102.1794	2.5-5	PRIME	KNSTD	0.020	0.002	0.904	10	2033	453	617.54	228.76	0.018	0.002	684.55	93.26
WTS37008	wbo448	29.9146	102.1934	2.5-5	PRIME	KNSTD	0.066	0.002	0.904	96	3381	861	636.09	218.26	0.059	0.002	483.58	55.03
WTS37009	wbo450	30.2270	102.1800	2.5-5	PRIME	KNSTD	0.084	0.004	0.904	28	3326	669	644.41	163.44	0.076	0.003	351.57	39.96
WTS37010	wbo501	31.5565	103.4814	2.5-5	PRIME	KNSTD	0.090	0.004	0.904	14	2833	574	779.53	246.70	0.081	0.003	256.50	29.21
WTS37011	wbo502	31.7522	102.7405	2.5-5	PRIME	KNSTD	0.202	0.006	0.904	26	4133	390	482.06	147.90	0.183	0.005	232.16	25.65
WTS37012	wbo505	32.2106	101.6186	2.5-5	PRIME	KNSTD	0.189	0.010	0.904	20	3699	412	528.57	161.61	0.171	0.009	201.02	24.32
WTS37013	wbo506	31.8902	100.7501	2.5-5	PRIME	KNSTD	0.274	0.007	0.904	41	4235	316	477.12	167.16	0.248	0.006	181.54	19.62
WTS37014	wbo508	32.1979	101.0199	2.5-5	PRIME	KNSTD	0.968	0.016	0.904	87	4049	209	341.35	178.68	0.876	0.015	46.39	4.94
WTS37015	wbo510	31.7152	100.9306	2.5-5	PRIME	KNSTD	1.025	0.033	0.904	169	3934	171	223.90	140.20	0.926	0.030	40.25	4.36
WTS37016	wbo511	31.7728	100.9869	2.5-5	PRIME	KNSTD	0.473	0.010	0.904	9	4213	290	462.20	177.43	0.428	0.009	102.64	10.74
WTS37017	wbo512	31.7876	101.1057	2.5-5	PRIME	KNSTD	0.370	0.008	0.904	11	4004	309	481.89	188.25	0.335	0.008	117.53	12.47
WTS37018	wbo513	31.7738	101.3658	2.5-5	PRIME	KNSTD	0.268	0.009	0.904	24	4136	407	556.23	255.42	0.242	0.008	175.59	19.70
WTS37019	wbo514	31.7504	101.9975	2.5-5	PRIME	KNSTD	0.212	0.005	0.904	23	3662	456	558.32	200.24	0.191	0.005	174.14	18.83
WTS37020	wbo515	31.4198	102.0500	2.5-5	PRIME	KNSTD	0.171	0.005	0.904	14	3227	433	522.05	151.71	0.155	0.004	167.48	18.06
WTS37021	wbo518	30.9540	101.7201	2.5-5	PRIME	KNSTD	0.127	0.005	0.904	22	3617	470	634.52	186.18	0.115	0.005	274.61	30.64
WTS37022	wbo519	31.0197	102.2791	2.5-5	PRIME	KNSTD	0.178	0.007	0.904	9	3372	361	605.18	176.88	0.161	0.006	169.67	19.24
WTS37023	wbo521	30.5415	101.6189	2.5-5	PRIME	KNSTD	0.142	0.008	0.904	28	4188	321	427.99	173.13	0.129	0.007	324.05	39.81
WTS37024	wbo522	30.6795	101.7433	2.5-5	PRIME	KNSTD	0.078	0.005	0.904	15	3880	513	691.81	226.81	0.071	0.005	506.22	61.81
WTS37025	wbo523	30.7312	102.0038	2.5-5	PRIME	KNSTD	0.028	0.002	0.904	50	3471	683	654.49	223.36	0.025	0.002	1175.39	147.16
WTS37026	wbo524	30.3751	102.1279	2.5-5	PRIME	KNSTD	0.046	0.002	0.904	34	3140	631	729.08	236.15	0.041	0.002	587.38	67.97
WTS37027	wbo529	30.1047	102.0596	2.5-5	PRIME	KNSTD	0.058	0.004	0.904	7	3823	507	689.20	190.56	0.052	0.003	651.35	81.35
WTS37028	wbo530	30.0787	102.0732	2.5-5	PRIME	KNSTD	0.074	0.004	0.904	14	3738	784	768.70	247.56	0.067	0.003	503.40	59.66
WTS37029	wbo536	30.0419	100.9835	2.5-5	PRIME	KNSTD	0.346	0.014	0.904	79	3795	393	533.53	161.79	0.313	0.013	106.73	12.44
WTS37030	wbo538	30.0402	101.2200	2.5-5	PRIME	KNSTD	0.412	0.011	0.904	43	4047	357	497.20	175.33	0.373	0.010	101.82	11.05
WTS37031	wbo544	29.9799	101.5804	2.5-5	PRIME	KNSTD	0.809	0.020	0.904	62	3963	267	396.10	174.90	0.731	0.018	48.97	5.24
WTS37032	wbo545	30.3300	101.5214	2.5-5	PRIME	KNSTD	1.582	0.046	0.904	17	3914	97	273.05	113.78	1.430	0.042	24.19	2.64
WTS37033	wbo549	29.6543	102.1102	2.5-5	PRIME	KNSTD	0.016	0.001	0.904	72	4205	1272	553.15	260.58	0.015	0.001	3232.50	413.34

Continued on next page

Sample ID	Sample ID published[b]	Drainage point[a] LAT [°N]	LON [°E]	Grain-size [μm*10²]	AMS	Standard	¹⁰Be conc. published[b] [at. g⁻¹*10⁶]	1σ	CF[c]	Area [km²]	Mean basin elevation [m a.s.l.]	1σ	Mean basin slope [m km⁻¹]	1σ	¹⁰Be conc. recalculated [at. g⁻¹*10⁶]	1σ	Denudation rate [mm kyr⁻¹]	1σ
WTS37034	wbo550	29.5401	102.1399	2.5-5	PRIME	KNSTD	0.014	0.002	0.904	27	2590	570	714.10	253.93	0.013	0.002	1323.55	212.16
WTS37035	wbo551	29.3429	102.2502	2.5-5	PRIME	KNSTD	0.097	0.009	0.904	76	2429	747	580.21	237.77	0.087	0.008	185.91	25.38
WTS37036	wbo604	32.0182	103.2734	2.5-5	PRIME	KNSTD	0.099	0.004	0.904	99	3353	537	619.93	196.36	0.089	0.004	318.88	36.90
WTS37037	wbo605	32.1298	102.8944	50-100	PRIME	KNSTD	0.112	0.004	0.904	12	3548	342	547.35	149.84	0.102	0.003	305.26	33.79
WTS37038	wbo607	32.2693	102.4950	50-100	PRIME	KNSTD	0.203	0.006	0.904	17	4005	195	373.65	127.98	0.184	0.005	218.36	23.52
WTS37039	wbo609	32.4191	100.8110	50-100	PRIME	KNSTD	0.272	0.006	0.904	42	4190	244	431.22	157.89	0.246	0.006	181.92	19.73
WTS37040	wbo610q	32.5299	100.6704	50-100	PRIME	KNSTD	0.456	0.015	0.904	47	4141	198	408.78	137.96	0.412	0.014	105.83	12.05
WTS37041	wbo610s	32.5299	100.6704	2.5-5	PRIME	KNSTD	0.360	0.012	0.904	47	4141	198	408.78	137.96	0.325	0.011	134.38	15.17
WTS37042	wbo612	32.2202	100.3879	50-100	PRIME	KNSTD	0.770	0.030	0.904	38	4242	176	290.93	103.17	0.696	0.027	65.09	7.43
WTS37043	wbo613	32.6184	101.1869	50-100	PRIME	KNSTD	0.390	0.012	0.904	36	4145	323	485.98	178.07	0.352	0.011	123.73	13.28
WTS37044	wbo614	32.5776	101.0804	50-100	PRIME	KNSTD	0.315	0.010	0.904	15	3945	246	435.90	125.56	0.285	0.009	138.81	15.46
WTS37045	wbo616	32.4324	101.0500	50-100	PRIME	KNSTD	0.228	0.009	0.904	76	3819	192	340.04	138.56	0.206	0.008	177.22	19.70
WTS37046	wbo617	32.3404	101.2212	50-100	PRIME	KNSTD	0.548	0.015	0.904	30	3937	179	347.79	129.48	0.496	0.013	77.96	8.33
WTS37047	wbo618	31.4500	100.7199	50-100	PRIME	KNSTD	0.358	0.012	0.904	44	3980	290	466.41	157.83	0.324	0.011	118.50	13.03
WTS37048	wbo619	31.0262	101.0760	50-100	PRIME	KNSTD	0.175	0.006	0.904	58	3973	406	444.24	168.41	0.158	0.006	241.62	27.09
WTS37049	wbo621	30.3198	101.3793	50-100	PRIME	KNSTD	0.914	0.030	0.904	63	4270	97	123.54	78.87	0.827	0.027	51.40	5.80
WTS37050	wbo622	30.3090	101.4211	50-100	PRIME	KNSTD	0.634	0.013	0.904	3	4253	62	160.03	73.99	0.573	0.012	73.80	7.80
WTS37051	wbo623	30.1423	101.5097	50-100	PRIME	KNSTD	0.764	0.016	0.904	12	3810	154	385.91	128.62	0.691	0.014	47.71	4.89
WTS37052	wbo624q	29.7678	101.0950	50-100	PRIME	KNSTD	0.319	0.011	0.904	54	3830	416	527.78	173.69	0.288	0.010	117.39	13.02
WTS37053	wbo624s	29.7678	101.0950	2.5-5	PRIME	KNSTD	0.233	0.007	0.904	54	3830	416	527.78	173.69	0.210	0.006	161.08	17.47
WTS37054	wbo625	30.0498	101.3067	50-100	PRIME	KNSTD	0.366	0.013	0.904	5	4261	184	400.96	155.31	0.331	0.012	128.26	13.82
WTS37055	wbo626	30.0601	101.3595	50-100	PRIME	KNSTD	0.901	0.020	0.904	5	4361	46	163.70	83.15	0.814	0.018	54.16	5.95
WTS37056	wbo633	29.5972	102.0187	2.5-5	PRIME	KNSTD	0.017	0.001	0.904	6	4451	638	587.76	164.83	0.015	0.001	3164.97	392.83
WTS37057	wbo637	28.7741	102.2507	2.5-5	PRIME	KNSTD	0.012	0.001	0.904	8	2691	277	398.20	160.67	0.010	0.001	1712.60	243.16
WTS37058	wbo638	28.3990	101.8770	2.5-5	PRIME	KNSTD	0.053	0.002	0.904	25	2936	566	661.61	178.99	0.048	0.002	430.76	49.41
WTS37059	wbo639	28.6180	101.8959	2.5-5	PRIME	KNSTD	0.018	0.001	0.904	50	2938	724	557.87	227.67	0.017	0.001	1263.43	154.88
WTS37060	wbo641	28.6097	101.6801	2.5-5	PRIME	KNSTD	0.095	0.004	0.904	33	3506	622	580.32	199.54	0.086	0.004	330.66	37.11
WTS37061	wbo642	28.9339	101.5374	50-100	PRIME	KNSTD	0.100	0.004	0.904	64	4055	400	492.16	183.45	0.091	0.003	411.68	46.41
WTS37062	wbo643	29.5094	101.4341	50-100	PRIME	KNSTD	0.205	0.007	0.904	27	4361	372	528.57	180.08	0.185	0.007	237.65	26.32
WTS37063	wbo644	29.7238	101.5188	50-100	PRIME	KNSTD	0.756	0.022	0.904	18	4258	258	433.40	183.17	0.684	0.020	60.78	6.36
WTS37064	wbo645	29.9301	101.3889	50-100	PRIME	KNSTD	1.419	0.025	0.904	47	4151	204	269.94	163.32	1.283	0.022	30.46	3.27
WTS37065	wbo647	29.6866	102.2007	2.5-5	PRIME	KNSTD	0.031	0.002	0.904	14	2400	548	743.98	262.46	0.028	0.001	541.32	64.73
WTS37066	wbo651	31.2938	102.0493	2.5-5	PRIME	KNSTD	0.268	0.008	0.904	33	3500	513	540.81	172.27	0.242	0.007	123.87	13.77
WTS37067	wbo653	31.0279	101.8686	2.5-5	PRIME	KNSTD	0.099	0.005	0.904	63	3747	622	604.02	279.67	0.090	0.004	382.72	44.75
Yumu Shan & Longshou Shan, NE Tibet, China (Palumbo et al., 2010b)																		
WTS45001	06C3-(Y1)	39.2046	99.6106	20-200	ETH	S555	0.188	0.014	0.912	4	2162	103	226.09	95.50	0.172	0.012	96.94	12.02
WTS45002	07C8-(Y2)	39.2098	99.6164	20-200	ETH	S555	0.102	0.008	0.912	1	2112	68	188.24	73.52	0.093	0.007	174.22	22.72
WTS45003	07C9-(Y2)	39.2098	99.6164	2-7.1	ETH	S555	0.134	0.009	0.912	1	2112	68	188.24	73.52	0.122	0.008	132.30	16.51
WTS45004	06C2-(Y3)	39.2218	99.6213	20-200	ETH	S555	0.159	0.011	0.912	13	2360	212	306.59	128.05	0.145	0.010	131.52	16.94

Continued on next page

Sample ID	**Sample ID published**[b]	**Drainage point**[a] LAT [°N]	LON [°E]	**Grain-size** [μm*10^2]	**AMS**	**Standard**	**^{10}Be conc. published**[b] [at. g^{-1}*10^6]	1σ	**CF**[c]	**Area** [km^2]	**Mean basin elevation** [m a.s.l.]	1σ	**Mean basin slope** [m km^{-1}]	1σ	**^{10}Be conc. recalculated** [at. g^{-1}*10^6]	1σ	**Denudation rate** [mm kyr^{-1}]	1σ
WTS45005	06C6-(Y4)	39.1994	99.7431	20-200	ETH	S555	0.098	0.008	0.912	9	2505	221	321.62	123.11	0.089	0.007	236.34	31.68
WTS45006	06C4-(Y5)	39.1948	99.7566	20-200	ETH	S555	0.098	0.009	0.912	11	2585	233	292.43	109.32	0.089	0.008	247.84	33.42
WTS45007	06C7-(Y6)	39.1597	99.8637	20-200	ETH	S555	0.089	0.008	0.912	4	2456	216	399.19	137.15	0.081	0.007	246.85	34.68
WTS45008	06C8-(Y7)	39.1490	99.8895	20-200	ETH	S555	0.112	0.008	0.912	3	2390	238	409.84	124.07	0.102	0.007	190.97	24.14
WTS45009	06C13-(Y8)	39.1199	99.8796	2-7.1	ETH	S555	0.087	0.007	0.912	9	2774	152	384.23	182.64	0.079	0.006	314.30	41.73
WTS45010	06C14-(Y9)	39.1173	99.9256	2-7.1	ETH	S555	0.039	0.008	0.912	31	2594	282	388.56	186.17	0.036	0.007	629.48	148.68
WTS45011	07C1-(Y10)	39.0477	100.0235	2-7.1	ETH	S555	0.070	0.008	0.912	3	2062	193	313.36	95.39	0.064	0.007	243.53	37.91
WTS45012	07C2-(Y10)	39.0477	100.0235	20-200	ETH	S555	0.035	0.006	0.912	3	2062	193	313.36	95.39	0.032	0.005	488.49	103.47
WTS45013	06C1-(Y11)	39.0274	100.0366	2-7.1	ETH	S555	0.091	0.008	0.912	3	1874	61	169.57	94.39	0.083	0.007	164.81	22.76
WTS45014	06C15-(Y12)	39.0190	100.0576	2-7.1	ETH	S555	0.041	0.004	0.912	1	1911	75	297.68	121.74	0.037	0.004	377.76	58.00
WTS45015	07C7-(Y13)	38.9758	100.1134	2-7.1	ETH	S555	0.025	0.007	0.912	0	1756	33	188.06	44.72	0.023	0.006	558.99	173.70
WTS45016	06C25-(L1)	39.1952	100.3657	2-7.1	ETH	S555	0.267	0.015	0.912	4	1639	50	112.59	44.31	0.244	0.013	47.62	5.56
WTS45017	07C30-(L2)	39.1846	100.3819	2-7.1	ETH	S555	0.371	0.022	0.912	8	1758	86	132.71	59.79	0.339	0.020	36.99	4.47
WTS45018	06C24-(L3)	39.1619	100.4045	2-7.1	ETH	S555	0.096	0.007	0.912	1	1719	68	221.72	94.88	0.088	0.006	143.82	18.14
WTS45019	07C31-(L4)	39.1205	100.4881	2-7.1	ETH	S555	0.029	0.007	0.912	1	1784	63	245.37	71.26	0.026	0.006	501.75	128.67
WTS45020	06C30-(L5)	39.0974	100.5385	2-7.1	ETH	S555	0.022	0.004	0.912	2	1699	66	154.08	79.60	0.020	0.004	608.65	127.96
WTS45021	06C18-(L6)	39.0534	100.6344	2-7.1	ETH	S555	0.076	0.009	0.912	6	2107	170	330.80	192.58	0.069	0.008	232.44	37.76
WTS45022	06C19-(L7)	39.0458	100.6486	2-7.1	ETH	S555	0.108	0.009	0.912	1	2190	196	516.76	211.40	0.099	0.008	179.58	23.72
WTS45023	06C20-(L7)	39.0458	100.6486	20-200	ETH	S555	0.070	0.008	0.912	1	2190	196	516.76	211.40	0.064	0.007	277.75	42.84
WTS45024	06C17-(L8)	39.0554	100.7092	2-7.1	ETH	S555	0.178	0.010	0.912	26	2748	428	275.52	180.37	0.162	0.009	155.25	19.13
WTS45025	06C23-(L9)	38.9575	100.8055	2-7.1	ETH	S555	0.125	0.008	0.912	16	2963	284	399.79	135.51	0.114	0.007	245.99	30.62
WTS45026	06C21-(L10)	38.9457	100.8416	2-7.1	ETH	S555	0.174	0.012	0.912	8	2860	215	362.07	129.10	0.159	0.011	165.55	20.35
WTS45027	06C22-(L10)	38.9457	100.8416	20-200	ETH	S555	0.208	0.013	0.912	8	2860	215	362.07	129.10	0.190	0.012	138.32	16.91
Qilian Shan, NE Tibet, China (Palumbo et al., 2010a)																		
WTS51001	07C44-(Q1)	39.7164	97.2273	2.5-7.1	ETH	S2007	0.449	0.019	0.912	347	3493	324	270.70	145.90	0.410	0.017	97.95	10.89
WTS51002	07C41-(Q2)	39.6799	97.5126	2.5-7.1	ETH	S2007	1.104	0.035	0.912	538	3872	429	323.30	197.40	1.007	0.032	50.03	5.53
WTS51003	07C42-(Q3)	39.6430	97.6603	2.5-7.1	ETH	S2007	0.393	0.019	0.912	663	3746	426	340.70	186.60	0.359	0.017	131.38	15.33
WTS51004	07C43-(Q4)	39.4031	97.6953	2.5-7.1	ETH	S2007	0.337	0.018	0.912	5	4327	239	515.50	155.20	0.307	0.016	209.16	25.12
WTS51005	07C45-(Q5)	39.4007	97.6283	2.5-7.1	ETH	S2007	1.064	0.044	0.912	66	4232	270	423.10	160.70	0.971	0.040	62.83	6.95
WTS51006	07C46-(Q6)	39.3390	98.8149	2.5-7.1	ETH	S2007	0.048	0.004	0.912	567	3789	561	508.00	200.50	0.043	0.004	1119.58	145.60
WTS51007	07C19-(Q7)	39.2507	99.0530	2.5-7.1	ETH	S2007	0.078	0.005	0.912	41	3295	444	556.10	164.30	0.071	0.005	507.56	63.90
WTS51008	07C13-(Q8)	39.1620	99.1695	2.5-7.1	ETH	S2007	0.092	0.006	0.912	558	3767	516	510.60	186.50	0.084	0.006	564.90	70.21
WTS51009	07C12-(Q9)	39.0750	99.2463	2.5-7.1	ETH	S2007	0.071	0.006	0.912	53	3621	433	537.40	165.20	0.065	0.005	661.74	85.83
WTS51010	07C20-(Q10)	39.0273	99.2867	2.5-7.1	ETH	S2007	0.036	0.005	0.912	38	3835	402	560.50	166.20	0.033	0.005	1482.18	256.90
WTS51011	07C23-(Q11)	38.8562	99.5290	2.5-7.1	ETH	S555	0.353	0.018	0.912	56	3649	470	528.30	172.30	0.322	0.016	135.42	15.79
WTS51012	06C16-(Q12)	38.7944	99.5552	2.5-7.1	ETH	S555	0.220	0.012	0.912	813	3787	478	434.50	182.20	0.201	0.011	236.07	28.88
WTS51015	06C34-(L12)	39.0373	100.9516	2.5-7.1	ETH	S555	1.272	0.050	0.912	5	2680	221	199.80	67.60	1.161	0.046	19.50	2.16
WTS51016	06C10-(H1)	39.8247	99.4561	2.5-7.1	ETH	S555	0.378	0.019	0.912	0	1421	47	182.10	96.10	0.345	0.017	28.69	3.31
WTS51017	06C12-(H3)	39.6493	100.0728	2.5-7.1	ETH	S555	0.137	0.021	0.912	2	1897	55	146.30	62.10	0.125	0.019	112.77	21.64

Continued on next page

Sample ID	**Sample ID published**[b]	**Drainage point**[a] LAT [°N]	LON [°E]	**Grain-size** [μm*10^2]	**AMS**	**Standard**	**^{10}Be conc. published**[b] [at. g^{-1}*10^6]	1σ	**CF**[c]	**Area** [km^2]	**Mean basin elevation** [m a.s.l.]	1σ	**Mean basin slope** [m km^{-1}]	1σ	**^{10}Be conc. recalculated** [at. g^{-1}*10^6]	1σ	**Denudation rate** [mm kyr^{-1}]	1σ
Longmen Shan, E Tibet, China (Godard et al., 2010)																		
WTS65006	SC004	30.7608	103.4691	2.5-10	Gif-sur-Y.	NIST‡	0.062	0.016	1	342	1899.8	623.2	517.30	226.00	0.062	0.016	193.55	53.79
WTS65007	SC016	31.2367	103.7924	2.5-10	Gif-sur-Y.	NIST‡	0.078	0.035	1	338	2490.6	809.7	681.90	288.70	0.078	0.035	227.32	107.91
WTS65008	SC031	31.4599	104.0007	2.5-10	Gif-sur-Y.	NIST‡	0.029	0.007	1	316	2948.9	785.6	699.40	279.20	0.029	0.007	807.33	226.43
WTS65009	SC033	31.3175	103.9958	2.5-10	Gif-sur-Y.	NIST‡	0.039	0.011	1	59	1421.3	295.0	400.50	153.50	0.039	0.011	220.46	66.55
WTS65011	SC059	31.0658	103.4933	2.5-10	Gif-sur-Y.	NIST‡	0.026	0.006	1	5	1503.9	250.5	564.50	154.80	0.026	0.006	343.66	88.08
WTS65012	SC071	31.5159	104.1132	2.5-10	Gif-sur-Y.	NIST‡	0.057	0.013	1	318	2272.8	758.1	600.10	233.40	0.057	0.013	277.77	70.96
Three Rivers Region, China (Henck et al., 2011)																		
WTS69002	11a-SAL	27.2360	98.8920	4.25-8.5	PRIME	07KNSTD	0.161	0.007	1	2	2007	284	597.42	168.76	0.161	0.007	68.26	7.40
WTS69012	18-YANG	31.6879	98.6529	1.8-4.25	PRIME	07KNSTD	0.361	0.026	1	140	4432	351	393.59	180.57	0.361	0.026	138.19	17.22
WTS69018	22-YANG	31.3206	97.9745	1.8-4.25	PRIME	07KNSTD	0.783	0.033	1	360	4319	171	248.73	126.65	0.783	0.033	58.53	6.78
WTS69019	24-YANG	31.4011	97.8806	1.8-4.25	PRIME	07KNSTD	0.881	0.039	1	429	4571	210	311.60	141.85	0.881	0.039	59.15	6.81
WTS69029	33-SAL	29.8568	97.7030	1.8-4.25	PRIME	07KNSTD	1.554	0.050	1	244	4808	268	362.91	158.84	1.554	0.050	35.45	3.81
WTS69031	35-SAL	29.6806	97.8370	1.8-4.25	PRIME	07KNSTD	1.238	0.051	1	131	4661	319	378.38	147.04	1.238	0.051	41.37	4.61
WTS69034	39-MEK	29.6598	98.3676	1.8-4.25	PRIME	07KNSTD	0.345	0.015	1	167	4030	388	411.88	183.58	0.345	0.015	108.69	12.40
WTS69035	4-MEK	28.5561	98.8087	1.8-4.25	PRIME	07KNSTD	0.070	0.005	1	466	4092	600	507.55	187.73	0.070	0.005	548.64	70.79
WTS69038	43-MEK	29.5490	98.2122	4.25-8.5	PRIME	07KNSTD	2.768	0.068	1	324	4901	305	416.43	184.52	2.768	0.068	20.38	2.20
WTS69039	46-SAL	30.0743	97.2794	1.8-4.25	PRIME	07KNSTD	0.367	0.016	1	66	4189	482	544.00	221.15	0.367	0.016	112.96	12.89
WTS69042	50-SAL	30.0394	97.1578	1.8-4.25	PRIME	07KNSTD	0.106	0.006	1	868	4930	610	467.54	205.26	0.106	0.006	574.78	68.33
WTS69043	52-SAL	29.7038	96.7977	1.8-4.25	PRIME	07KNSTD	0.277	0.015	1	197	5192	226	441.73	229.23	0.277	0.015	240.35	28.96
WTS69044	53-SAL	29.7723	96.7087	1.8-4.25	PRIME	07KNSTD	0.112	0.007	1	360	5068	317	423.96	215.45	0.112	0.007	566.16	70.22

Table head: [a] Coordinates in WGS84 decimal degrees from 90-m SRTM data of the basin outlets as identified on the SRTM DEMs after performing all hydrological analyses.
[b] Data or value from previous publication. [c] Correction factor to re-normalise published Be data to KNSTD07 standard.

Table body: PRIME = Purdue PRIME lab; LLNL = LLNL-CAMS; Gif-sur-Y. = Gif-sur-Yvette; NIST‡ = NIST_27900, NIST† = NIST Certified; KNSTD* = KNSTD assumed.

TABLE C.5: Candidate predictors. Area-weighted means and standard deviations for n = 297 >1000 km^2-basins draining the Himalaya-Tibet orogen. For further information related to predictors see C.1. Information on cluster generation can be found in the *Statistical analysis* section.

ID	Cluster	STRAIN	d_STRAIN	PGA	d_PGA	K_S	d_K_S	HEP	d_HEP	LWAV	d_LWAV	AI	d_AI
			1 σ	[m s^{-2}]	1 σ	[$m^{0.9}$]	1 σ		1 σ	[m km^{-1}]	1 σ		1 σ
Nam Co, Tibetan Plateau, China (Strobl et al., 2012)													
WTS10301	3	8.31	2.22	4465	1506	40	49	2060	1774	5180	948	0.48	0.01
WTS10302	3	10.30	1.00	3015	3557	44	27	1961	1098	4586	973	0.48	0.02
WTS10303	3	13.00	4.36	6893	1409	43	32	2813	1559	4520	1372	0.46	0.01
WTS10304	3	11.00	0	4530	5643	43	32	2536	1481	3594	1267	0.46	0.01
WTS10305	3	11.00	0	8520	0	46	21	2595	1183	4731	1561	0.46	0
WTS10306	3	15.00	0	9890	0	41	3	3443	1357	3114	815	0.46	0.01
WTS10307	3	18.00	0	4650	0	52	18	3195	1473	1624	1433	0.45	0.01
WTS10308	3	15.00	0	9890	0	42	13	3561	1451	3094	813	0.46	0.01
WTS10309	3	9.56	1.18	7380	1240	44	50	1937	1288	3640	853	0.47	0.02
WTS10310	3	9.42	0.35	4170	1923	36	43	1922	1692	3489	1081	0.47	0.01
WTS10311	3	9.12	0.41	3717	1570	52	34	2258	1898	3580	1121	0.47	0.02
WTS10312	3	19.00	0	9380	0	43	19	2737	1149	2274	1171	0.46	0.01
WTS10313	3	16.50	2.38	6047	2899	38	22	2669	1397	1551	1444	0.47	0.01
WTS10314	3	29.67	0.58	3057	1719	22	12	1690	976	4654	1626	0.47	0.01
Ladakh Batholith, Transhimalaya, India (Dortch et al., 2011c)													
WTS10701	1	60.00	2.00	5230	2291	93	26	2139	803	17045	2045	0.18	0.03
WTS10702	1	24.75	8.68	5187	1419	96	32	1957	829	9298	3592	0.17	0.03
WTS10703	1	24.69	7.09	4795	1468	100	37	1955	831	9027	3996	0.16	0.03
WTS10704	1	42.50	20.41	4446	2089	117	68	2143	770	14269	1685	0.14	0.02
WTS10705	1	48.00	13.48	5091	2781	114	34	2244	797	10860	4231	0.17	0.04
WTS10706	1	44.00	15.94	5547	4055	92	30	1941	790	13797	2453	0.16	0.03
WTS10707	1	23.80	5.89	4740	2265	116	100	2048	848	10084	4395	0.16	0.03
WTS10708	1	57.75	3.86	4937	2917	84	20	2057	817	15243	3846	0.18	0.03
WTS10709	1	49.74	16.70	5455	3099	105	80	2075	836	13081	4109	0.16	0.04
WTS10710	1	45.25	16.13	5023	4473	82	14	1906	752	13151	2053	0.17	0.03
WTS10711	1	58.50	7.78	6980	4130	116	68	2214	718	6688	2400	0.16	0.02
WTS10712	1	66.21	17.12	5731	2042	97	63	2334	934	14988	2735	0.16	0.03
WTS10713	1	33.00	8.57	4646	1158	105	35	1911	629	14409	1612	0.15	0.02
WTS10714	1	33.33	8.62	4570	1177	80	14	1862	671	15613	1613	0.16	0.03
Ladakh Batholith, Transhimalaya, India (Dietsch et al.)													
WTS10801	1	78.50	28.99	5920	2305	69	7	2909	910	8974	1492	0.14	0
WTS10802	1	58.00	0	7550	0	93	15	2668	789	12517	2185	0.14	0.01
WTS10803	1	58.00	0	7550	0	93	7	2354	571	13675	2149	0.14	0.01
WTS10804	1	53.00	0	4060	0	56	9	2384	814	5617	1671	0.12	0.01
WTS10805	1	53.00	0	4060	0	100	0	2439	575	5591	1967	0.13	0
WTS10806	1	53.00	0	4060	0	96	0	2143	389	9863	2849	0.14	0

Continued on next page

ID	Cluster	STRAIN	d_STRAIN	PGA	d_PGA	K_S	d_K_S	HEP	d_HEP	LWAV	d_LWAV	AI	d_AI
			1 σ	[m s^{-2}]	1 σ	[m$^{0.9}$]	1 σ		1 σ	[m km^{-1}]	1 σ		1 σ
WTS10807	1	90.00	0	8170	0	113	24	3086	943	9456	2191	0.12	0
WTS10808	1	90.00	0	8170	0	100	24	2808	843	9694	1330	0.12	0.01
WTS10809	1	63.00	38.18	4590	5063	83	11	2295	617	8155	2611	0.13	0.01
WTS10810	1	99.00	0	4290	0	68	14	2874	912	8411	2744	0.14	0.01
WTS10811	1	99.00	0	4290	0	98	9	2917	602	13255	3714	0.13	0.01
WTS10812	1	85.33	23.67	5920	2305	124	28	2818	674	13418	2237	0.14	0.01
Zoulang Nan Shan, NE Tibetan Plateau, China (Hetzel, 2013)													
WTS11901	3	18.20	1.30	2117	1095	118	30	8221	3009	12063	2299	0.66	0.20
WTS11902	3	17.47	0.74	5833	2807	87	27	6856	3189	8131	3095	0.76	0.15
WTS11903	3	17.50	0.58	7600	2164	111	39	8679	2726	11298	1079	0.77	0.15
WTS11904	3	17.67	0.52	8110	1767	108	33	7988	3281	11706	1230	0.70	0.18
WTS11905	3	17.65	0.88	5069	2903	107	30	7411	3122	13331	5013	0.73	0.19
WTS11906	3	17.00	0	6070	0	86	25	8568	3565	9738	1265	0.78	0.11
WTS11907	3	17.33	0.58	7630	2206	63	6	5749	2441	3104	1343	0.77	0.10
WTS11908	3	17.50	0.55	7380	3473	76	5	6771	2216	9230	1361	0.79	0.07
WTS11910	3	18.00	0	9190	0	61	7	5928	3030	2625	1425	0.77	0.12
Anyemaquen Shan, E Tibet, China (Kirby and Harkins, 2013)													
WTS12401	3	11.00	0	8760	0	38	4	6022	2542	7825	2062	0.65	0.02
WTS12402	3	11.00	0	4895	3486	34	3	7001	2590	390	994	0.79	0.01
WTS12403	3	11.00	0	5370	0	55	16	8689	2863	2938	855	0.67	0.03
WTS12404	3	11.00	0	5370	0	82	27	9527	3116	2992	1294	0.70	0.07
WTS12405	3	15.00	0	2500	1032	99	32	10341	2686	11680	1880	0.79	0.11
WTS12406	3	16.50	0.71	9660	255	76	16	9772	2975	2858	979	0.82	0.05
WTS12407	3	18.00	0	9260	0	79	20	14202	4699	5518	1456	0.87	0.07
WTS12408	3	10.10	0.72	4204	3339	38	13	7454	3268	3449	1505	0.81	0.05
WTS12409	3	16.75	0.50	4645	4158	67	23	12047	4365	3226	1345	0.97	0.10
WTS12410	3	17.00	1.07	4555	3658	60	27	11399	4850	3781	1901	1.00	0.10
WTS12411	3	16.33	0.58	2760	2499	57	15	8468	3531	2764	925	0.98	0.09
WTS12412	3	17.00	0.82	5227	2461	87	26	10674	3571	7203	1555	0.87	0.11
WTS12413	3	13.00	0	5400	42	83	39	9427	3708	2562	1261	0.72	0.14
Himalaya, Nepal (Wobus et al., 2005)													
WTS12501	5	73.00	0	1830	0	162	93	60187	19096	36306	7050	1.58	0.05
WTS12502	5	74.11	0.76	1910	85	188	112	55200	23340	34725	5500	1.35	0.29
WTS12503	5	74.60	0.55	1967	58	135	58	54233	18125	30883	5647	1.55	0.09
WTS12504	5	75.00	0	2000	0	86	15	51899	19310	26009	4446	1.59	0.08
WTS12505	5	80.17	3.71	283	1128	85	21	41592	12408	23858	5424	1.50	0
WTS12506	5	67.30	5.25	6895	2260	74	23	42134	14330	7947	1328	1.55	0.08
WTS12507	5	62.75	1.39	5860	1697	85	27	40771	13073	7345	1519	1.50	0.07
WTS12508	5	65.00	0	7060	0	90	29	39175	12699	5485	1306	1.48	0.08
Marsyandi Basin, Himalaya, Nepal (Godard et al., 2012)													

Continued on next page

ID	Cluster	STRAIN	d_STRAIN	PGA	d_PGA	K$_S$	d_K_S	HEP	d_HEP	LWAV	d_LWAV	AI	d_AI
			1 σ	[m s^{-2}]	1 σ	[m$^{0.9}$]	1 σ		1 σ	[m km^{-1}]	1 σ		1 σ
WTS12601	5	70.70	5.79	4195	3080	112	93	40870	20024	26210	13507	1.39	0.38
WTS12603	5	70.33	13.20	5243	2860	55	30	40482	19267	10023	3279	1.75	0.11
WTS12605	5	78.10	6.77	4961	2593	122	84	38781	20946	39644	10290	1.44	0.49
WTS12606	5	90.50	8.85	3038	1886	67	33	49858	22437	23918	4940	1.95	0.07
WTS12608	4	71.80	9.24	5360	3227	196	144	25685	21885	43269	7568	0.98	0.57
WTS12610	4	55.31	5.48	4249	3196	141	125	11434	5010	16465	7431	0.85	0.19
WTS12612	4	70.57	6.70	3881	2622	154	62	12828	5761	23648	10058	0.92	0.45
WTS12613	4	71.33	7.28	3768	2808	142	105	12161	5637	19779	8122	0.91	0.37
WTS12615	5	78.43	5.74	6570	2858	170	108	37644	30610	45462	3799	1.19	0.64
WTS12620	4	54.90	5.30	5631	2764	175	131	13303	7288	23374	4681	0.79	0.40
WTS12623	4	61.25	7.63	5606	2845	180	162	14847	8471	34603	3516	0.94	0.61
WTS12625	5	70.70	5.79	4195	3080	108	59	40870	20024	26210	13507	1.39	0.38
WTS12626	4	77.25	11.94	3533	2434	177	133	37022	26186	46226	6835	1.17	0.61
Zanskar & Ladakh, Transhimalaya, India (Munack et al., 2014)													
WTS12701	1	12.00	1.15	6068	3828	135	90	2568	1474	16442	2748	0.15	0.03
WTS12702	1	55.00	11.31	7585	2227	163	69	3000	1097	8849	1702	0.14	0.01
WTS12703	1	22.75	0.96	4300	3344	109	85	3361	1354	4858	2005	0.31	0.06
WTS12704	1	22.33	1.53	4190	2548	86	90	2661	1386	3336	1952	0.28	0.06
WTS12705	1	17.13	3.98	3736	3006	110	87	1974	1193	16690	2460	0.14	0.03
WTS12706	1	35.75	8.62	5580	3756	157	78	2971	1132	5408	2401	0.14	0.02
WTS12707	1	9.68	1.64	4000	2730	124	96	2195	1276	10566	4509	0.15	0.02
WTS12708	1	71.33	31.47	6733	2209	114	39	2210	672	12457	1136	0.13	0.01
WTS12709	1	59.20	19.82	5494	2851	109	56	2570	846	12901	2618	0.17	0.04
WTS12710	1	23.20	1.30	5448	3714	107	98	3203	1355	7724	3626	0.29	0.05
WTS12711	1	41.00	8.49	5415	5296	158	96	2688	1160	7483	2140	0.15	0.02
WTS12712	1	13.50	0.71	7915	1096	142	63	3710	1464	8098	2552	0.18	0.03
WTS12713	1	32.38	7.35	4285	2735	122	86	3005	1100	9181	3653	0.24	0.05
WTS12714	1	89.33	25.91	5707	2524	120	56	2974	1011	13720	3153	0.19	0.03
WTS12715	1	131.67	21.37	4507	2864	113	58	2500	1013	14860	5076	0.18	0.04
WTS12716	1	79.67	17.49	5618	1381	127	52	2488	709	15761	2708	0.15	0.02
WTS12717	1	37.75	8.14	4894	2984	83	54	3139	1603	3847	2022	0.35	0.12
WTS12718	1	63.75	29.84	5958	2379	123	34	2311	789	13136	1775	0.14	0.02
WTS12719	1	68.80	28.20	6334	2226	126	71	2303	812	13090	1781	0.14	0.02
WTS12720	1	23.17	7.83	5442	3138	92	71	2977	1283	7099	2103	0.31	0.06
WTS12721	1	25.43	5.47	4722	3477	115	84	1955	986	15748	2359	0.14	0.02
WTS12722	1	13.49	7.09	4652	2948	97	67	3149	1201	9666	3306	0.30	0.06
WTS12723	1	50.50	31.53	4787	3277	108	65	2028	686	10424	1781	0.15	0.02
WTS12724	1	37.20	6.30	4713	3092	107	82	1871	792	12990	2538	0.14	0.02
WTS12725	1	24.00	0	4637	3228	111	87	3227	1215	5967	1762	0.35	0.09
WTS12726	1	13.20	1.48	3436	2864	125	93	2223	1277	15745	3078	0.14	0.03
WTS12727	1	72.00	11.31	7680	3140	144	61	2488	642	9620	2932	0.16	0.03

Continued on next page

ID	Cluster	STRAIN	d_STRAIN	PGA	d_PGA	K$_S$	d_K_S	HEP	d_HEP	LWAV	d_LWAV	AI	d_AI
			1 σ	[m s^{-2}]	1 σ	[m$^{0.9}$]	1 σ		1 σ	[m km^{-1}]	1 σ		1 σ
WTS12728	1	133.33	28.87	3407	2296	112	31	2409	900	9834	5080	0.18	0.05
WTS12729	1	125.00	35.36	4063	2288	115	63	2442	909	9504	5053	0.17	0.05
WTS12730	1	38.50	5.45	3713	1579	139	86	3445	1087	9061	3680	0.23	0.06
WTS12731	1	47.00	38.43	6177	1990	130	47	2185	596	11289	1172	0.14	0.01
WTS12732	1	29.00	3.54	6286	2421	107	92	2894	1203	7249	2514	0.26	0.04
WTS12733	1	132.50	17.08	4835	3483	136	64	2733	910	5537	3446	0.16	0.03
Zanskar & Ladakh, Transhimalaya, India this study													
WTS13201	1	48.83	16.93	5543	3042	218	92	2082	834	13076	4103	0.16	0.04
WTS13202	1	18.00	2.45	5725	2541	164	126	2292	854	3907	2211	0.13	0.03
WTS13203	1	53.50	10.66	3493	1644	152	72	3399	1199	11001	2309	0.16	0.02
WTS13204	1	23.80	5.89	4646	2240	144	111	2049	846	10040	4358	0.16	0.03
WTS13205	1	12.87	6.54	8612	1084	123	89	2132	866	7019	3999	0.15	0.04
WTS13206	1	32.50	23.38	3356	2739	96	61	1918	726	7926	2535	0.16	0.02
WTS13207	1	17.60	8.88	6085	2009	93	62	1943	788	5274	2508	0.16	0.02
WTS13209	1	26.42	4.01	4258	3209	122	106	2009	873	8846	3013	0.16	0.03
WTS13210	1	46.50	11.74	3907	3099	148	74	2680	1020	6208	2950	0.14	0.02
Himalaya, Nepal (Andermann, 2011)													
WTS13307	4	54.00	11.33	6339	2800	172	129	16561	9518	25859	2577	0.71	0.22
WTS13308	4	78.67	18.90	5980	3204	150	68	28027	13566	35666	4043	0.88	0.25
WTS13309	4	73.00	1.41	3290	2616	218	149	21976	12759	30184	1990	0.79	0.27
WTS13310	4	73.00	1.41	3290	2616	214	72	21976	12759	30184	1990	0.79	0.27
WTS13312	5	129.22	28.26	3598	2699	123	76	41688	17953	24744	9114	1.41	0.39
WTS13314	5	74.67	0.52	1950	71	132	25	54986	18492	32382	2731	1.54	0.10
WTS13316	5	108.25	15.97	3540	1558	106	37	44514	14872	21337	3415	1.44	0.17
WTS13318	5	110.17	17.46	4655	3185	153	86	41567	15913	31706	3637	1.24	0.32
WTS13319	4	100.33	8.50	5190	3968	161	128	20976	12742	39836	1582	0.86	0.25
WTS13323	5	89.40	17.76	5838	3513	50	31	21972	14061	3928	1527	1.14	0.29
WTS13324	5	90.50	11.15	5180	495	96	50	37094	13360	19160	2575	1.80	0.21
Bayan Har this study													
WTS13401n	3	9.13	0.78	9013	920	60	13	6242	2826	14178	1753	0.75	0.11
WTS13403n	3	22.56	1.98	8466	138	16	6	2128	1503	1362	1468	0.70	0.03
WTS13405n	3	12.33	1.15	10013	1049	51	10	5419	2108	3969	1374	0.70	0.06
WTS13406n	3	13.33	0.82	9945	983	28	6	3174	1556	3130	1357	0.74	0.04
WTS13407n	3	22.23	1.09	6346	290	20	11	2678	2752	3690	1297	0.71	0.04
WTS13408n	3	18.54	0.78	15538	466	21	7	3378	2113	3696	1361	0.81	0.05
WTS13409n	3	18.15	3.30	13933	993	28	10	4790	2863	3407	1508	0.82	0.04
WTS13410n	3	32.86	1.35	10147	218	40	11	6657	2979	1168	1432	0.68	0.03
WTS13411n	3	33.00	0	10310	0	35	5	5547	2227	2159	1352	0.71	0.03
WTS13412n	3	33.00	0	10415	148	63	9	7926	2757	1729	1475	0.69	0.02
WTS13413n	3	33.55	0.69	10345	206	85	15	10035	3260	2922	2024	0.69	0.05

Continued on next page

ID	Cluster	STRAIN	d_STRAIN	PGA	d_PGA	K_S	d_K_S	HEP	d_HEP	LWAV	d_LWAV	AI	d_AI
			1 σ	[m s^{-2}]	1 σ	[m$^{0.9}$]	1 σ		1 σ	[m km^{-1}]	1 σ		1 σ
WTS13414n	3	25.27	1.33	7467	450	19	10	2330	2336	2210	1616	0.77	0.05
WTS13415n	3	7.18	0.09	14868	802	30	8	2796	1191	3323	970	0.63	0.04
WTS13417n	3	20.67	1.86	7732	253	14	5	1615	1304	1845	1389	0.66	0.03
WTS13418n	3	20.57	1.16	8291	177	39	11	5055	2567	5389	2224	0.72	0.05
WTS13419n	3	21.71	0.49	8614	87	47	18	5812	2906	1553	1495	0.71	0.04
WTS13420n	3	20.00	0.89	8502	30	26	6	3857	2415	2406	1185	0.72	0.03
Kunlun Shan and Central Tibet, China (Li et al., 2014)													
WTS13501n	3	11.86	0.38	17342	216	26	14	1402	1116	2369	1334	0.41	0.03
WTS13502n	3	11.25	0.75	13376	834	13	6	926	831	1745	1474	0.41	0.01
WTS13503n	3	22.60	0.55	6364	68	58	16	4750	2851	8771	1693	0.78	0.14
WTS13506n	3	12.73	1.67	7268	219	82	27	3816	2157	12933	3489	0.32	0.14
WTS13508n	3	21.30	0.48	7045	200	81	26	3567	1927	5331	3095	0.32	0.10
WTS13510n	3	22.84	1.26	6285	151	49	27	2695	2166	7651	1956	0.43	0.12
WTS13512n	3	32.81	4.84	11529	2145	18	9	1419	1198	2643	1435	0.51	0.04
WTS13513n	3	36.67	3.11	12373	1787	28	8	2498	1492	1806	1422	0.57	0.03
WTS13516n	3	57.25	11.33	14733	703	21	10	2404	1780	2787	1148	0.60	0.02
Namche Barwa-Gyala Peri Massif, Tibet, China (Finnegan et al., 2008)													
WTS33002	4	29.50	9.19	4025	4872	182	92	19080	5902	13016	1641	0.72	0.05
WTS33003	4	24.50	6.36	7055	1973	178	92	19069	6078	15628	1353	0.69	0.02
WTS33004	4	9.40	1.38	9655	474	208	111	20950	6816	18759	1992	0.71	0.07
WTS33007	4	10.07	2.54	6970	3323	188	113	20486	6989	19190	2966	0.70	0.04
WTS33008	4	27.73	11.26	4104	2918	110	83	11948	5602	8956	4713	0.63	0.04
WTS33010	4	13.79	4.86	5277	2842	208	107	20389	5717	21022	2599	0.72	0.05
WTS33013	4	24.50	6.36	5660	0	177	90	19799	5874	14954	1490	0.73	0.08
E Tibet, China (Ouimet et al., 2009)													
WTS37001	3	65.50	25.09	2753	1815	30	50	5066	2705	2936	1478	1.13	0.06
WTS37002	3	22.50	9.19	6945	2510	23	81	3829	2715	2304	1274	1.26	0.05
WTS37003	4	16.50	0.71	5270	156	140	128	22302	8836	8875	1901	1.19	0.27
WTS37004	4	9.38	-1.00	172	0	181	75	33644	8251	18069	3393	1.20	0.16
WTS37005	4	16.00	0	4013	3141	133	106	22867	8604	11801	2887	1.37	0.26
WTS37006	4	47.67	4.16	4363	4357	140	76	26893	8106	15526	2577	0.90	0.16
WTS37007	4	58.50	3.54	1760	764	181	59	28519	9075	19320	2882	0.87	0.12
WTS37008	4	71.20	4.82	3602	3455	190	100	32777	10487	22083	4140	1.30	0.45
WTS37009	4	64.00	0	142	0	195	107	29420	6484	5691	2667	1.14	0.26
WTS37010	4	9.27	0.67	7960	806	210	83	33990	8721	7894	2612	1.00	0.15
WTS37011	4	16.50	1.29	5155	3067	134	67	23605	6668	3054	2330	1.38	0.26
WTS37012	4	31.00	1.41	5975	3528	148	72	19663	5685	7520	1809	0.85	0.16
WTS37013	3	49.00	5.72	6805	3596	116	49	17547	5725	2526	1283	0.95	0.12
WTS37014	3	35.75	2.63	3715	1160	82	58	13091	6243	4525	1448	0.92	0.08
WTS37015	3	69.40	6.70	4141	2924	36	24	8681	5297	3018	1653	0.83	0.07

Continued on next page

ID	Cluster	STRAIN	d_STRAIN	PGA	d_PGA	K_S	d_K_S	HEP	d_HEP	LWAV	d_LWAV	AI	d_AI
			1 σ	[m s^{-2}]	1 σ	[m$^{0.9}$]	1 σ		1 σ	[m km^{-1}]	1 σ		1 σ
WTS37016	3	49.50	0.71	4240	1683	116	57	17319	6281	1929	1453	0.95	0.16
WTS37017	4	51.50	4.04	2623	785	142	68	17589	6225	2653	1586	0.87	0.15
WTS37018	4	38.50	2.12	6765	233	161	113	20999	6936	3114	1202	0.93	0.22
WTS37019	4	27.50	2.12	3510	4950	169	104	21436	6274	2046	1665	0.84	0.19
WTS37020	4	29.00	2.83	1845	2029	162	58	19645	5676	2237	1714	0.74	0.13
WTS37021	4	60.00	5.57	6403	911	175	71	24024	5847	12264	2858	0.85	0.22
WTS37022	4	30.00	1.73	2520	0	160	75	24026	6273	2331	1203	0.94	0.21
WTS37023	4	93.80	15.58	5292	3667	98	17	19559	7906	7154	2445	1.15	0.15
WTS37024	4	79.00	0	7190	0	180	38	27790	7311	13031	3071	1.09	0.26
WTS37025	4	53.67	4.16	6173	1411	185	107	26198	6913	11135	2623	1.02	0.31
WTS37026	4	64.50	7.72	3510	2150	203	107	30161	8806	14050	2840	1.01	0.23
WTS37027	4	68.50	7.78	950	495	208	119	34552	7956	12797	2748	1.21	0.23
WTS37028	4	74.50	0.71	1330	1032	219	129	34538	8552	20844	3726	1.43	0.57
WTS37029	4	16.33	0.82	5588	2200	138	54	20275	5457	6367	3655	0.86	0.16
WTS37030	4	17.00	2.65	5110	3649	128	50	20799	6697	10423	2174	1.10	0.16
WTS37031	4	56.33	20.74	3517	2159	64	29	18982	7734	4863	1711	1.16	0.16
WTS37032	3	42.00	18.38	6215	4405	35	15	12391	5119	1305	1436	1.00	0.04
WTS37033	4	64.60	4.98	2428	2403	192	180	30116	12406	34940	5953	1.89	1.14
WTS37034	4	64.75	5.56	2725	2435	195	100	32070	8317	29481	4112	0.99	0.20
WTS37035	4	47.00	0	1275	1237	162	88	28523	9149	23736	4110	0.99	0.25
WTS37036	4	12.50	1.00	6118	2879	167	77	26936	7267	7783	2633	1.00	0.21
WTS37037	4	17.25	0.96	4448	4792	149	78	23231	6175	10845	2457	0.93	0.18
WTS37038	3	20.00	0	6770	0	74	20	16471	5822	4755	1116	1.04	0.13
WTS37039	3	29.00	2.83	4430	2305	97	40	15626	5428	6589	1474	0.94	0.10
WTS37040	3	26.25	2.63	3898	4359	82	23	14798	4693	6467	1336	0.92	0.08
WTS37041	3	26.25	2.63	3898	4359	79	11	14798	4693	6467	1336	0.92	0.08
WTS37042	3	45.00	5.66	2115	2638	59	18	10603	3866	3679	1019	0.90	0.07
WTS37043	3	23.00	1.41	4515	2553	128	64	18101	6013	3862	1360	0.95	0.15
WTS37044	3	24.00	0	5100	0	117	51	15880	4625	3012	1066	0.85	0.11
WTS37045	3	27.25	1.26	5723	4405	69	21	12635	5017	2313	1614	0.84	0.08
WTS37046	3	32.67	2.08	5920	71	65	19	13495	4866	6771	1366	0.88	0.07
WTS37047	4	81.25	3.95	5993	2533	120	37	16969	5455	1798	1533	0.83	0.11
WTS37048	4	69.00	8.05	7538	3251	115	47	17111	5954	6161	1962	0.94	0.19
WTS37049	3	25.00	4.00	6377	4706	30	22	5909	3702	2839	1710	1.15	0.05
WTS37050	3	29.00	0	9330	0	33	19	7449	3585	2304	1302	1.13	0.05
WTS37051	4	37.50	2.12	5405	1492	68	22	17657	5607	3202	1249	0.98	0.07
WTS37052	4	16.75	0.50	7003	3201	136	31	21614	6556	4980	2073	0.96	0.20
WTS37053	4	16.75	0.50	7003	3201	145	83	21614	6556	4980	2073	0.96	0.20
WTS37054	4	10.00	0	2220	0	97	35	17644	6626	3195	1282	1.15	0.10
WTS37055	3	16.00	0	8640	0	16	5	8187	4104	672	1201	1.18	0.05
WTS37056	4	63.50	7.78	3000	1556	234	130	35846	10718	34433	4290	1.56	0.55

Continued on next page

ID	Cluster	STRAIN	d_STRAIN	PGA	d_PGA	K_S	d_K_S	HEP	d_HEP	LWAV	d_LWAV	AI	d_AI
			1 σ	[m s^{-2}]	1 σ	[$m^{0.9}$]	1 σ		1 σ	[m km^{-1}]	1 σ		1 σ
WTS37057	4	45.00	0	5220	0	89	45	22275	8963	11170	2204	1.05	0.16
WTS37058	4	22.00	0	6840	2008	211	100	34879	7347	9815	1687	1.01	0.18
WTS37059	4	24.25	1.71	6308	2495	152	82	31479	9576	14933	2467	1.01	0.29
WTS37060	4	18.00	1.73	3040	1287	176	103	28531	7919	18849	2880	1.08	0.24
WTS37061	4	16.50	3.00	3123	3405	139	84	24099	7879	6258	2025	1.19	0.21
WTS37062	4	21.75	2.22	5923	3213	142	77	25271	7824	2441	1222	1.34	0.18
WTS37063	4	25.00	0	9450	0	120	76	20856	8132	2953	1597	1.26	0.17
WTS37064	3	13.50	2.65	5108	4457	67	43	12507	7094	3986	1383	1.11	0.09
WTS37065	4	56.00	0	9070	0	186	69	33485	9746	16842	3857	1.09	0.21
WTS37066	4	33.33	0.58	8297	582	160	75	22007	5846	7074	2058	0.88	0.20
WTS37067	4	51.67	3.06	5830	4810	179	113	23467	6514	12889	3211	1.00	0.29
Yumu Shan & Longshou Shan, NE Tibet, China (Palumbo et al., 2010b)													
WTS45001	2	15.00	0	6880	0	43	9	2184	940	14792	2962	0.18	0.01
WTS45002	2	15.00	0	6880	0	38	12	1695	657	15260	1724	0.17	0.02
WTS45003	2	15.00	0	6880	0	48	5	1695	657	15260	1724	0.17	0.02
WTS45004	2	15.00	0	4520	3338	64	19	3093	1230	15033	2251	0.20	0.04
WTS45005	2	15.00	0	2160	0	74	22	3670	1550	13616	2155	0.24	0.05
WTS45006	2	15.50	0.71	2540	537	71	24	3523	1445	13392	2204	0.26	0.06
WTS45007	2	15.00	0	3875	35	93	30	4466	1552	12501	2553	0.22	0.06
WTS45008	2	15.00	0	6625	3924	99	28	4406	1510	12782	2179	0.24	0.05
WTS45009	2	15.00	0	3850	0	70	28	4786	1892	13500	2222	0.28	0.05
WTS45010	2	15.00	0	5700	3204	97	41	4625	2227	14385	2346	0.26	0.06
WTS45011	2	15.00	0	4630	0	75	27	2911	1000	15454	3982	0.17	0.04
WTS45012	2	15.00	0	4630	0	69	13	2911	1000	15454	3982	0.17	0.04
WTS45013	2	15.00	0	4630	0	22	7	1525	902	16285	3077	0.16	0.01
WTS45014	2	15.00	0	4630	0	45	1	2744	1199	12786	4598	0.14	0.01
WTS45015	2	14.00	0	4630	0	17	3	1630	471	12543	5997	0.14	0
WTS45016	2	8.37	0.89	4520	5713	24	9	775	323	3585	1164	0.12	0.01
WTS45017	2	8.37	0.89	4520	5713	32	14	1020	477	3785	1457	0.14	0.01
WTS45018	2	7.75	0	8560	0	48	13	1501	669	3909	1443	0.14	0
WTS45019	2	9.00	0	3760	0	41	7	1774	591	4779	2463	0.14	0.01
WTS45020	2	9.00	0	3760	0	31	10	1284	630	7497	2382	0.13	0.01
WTS45021	2	9.03	0.04	7120	0	91	63	2940	1461	9976	2069	0.18	0.04
WTS45022	2	9.03	0.04	6470	919	103	27	4233	1814	8687	2290	0.21	0.04
WTS45023	2	9.03	0.04	6470	919	86	13	4233	1814	8687	2290	0.21	0.04
WTS45024	2	8.60	0.79	4350	1808	79	52	3943	2675	10149	1924	0.32	0.11
WTS45025	2	9.06	0	4240	0	99	43	5892	2024	7877	1861	0.38	0.11
WTS45026	2	9.53	0.67	3155	1534	88	45	5186	1661	6773	1497	0.34	0.06
WTS45027	2	9.53	0.67	3155	1534	82	18	5186	1661	6773	1497	0.34	0.06
Qilian Shan, NE Tibet, China (Palumbo et al., 2010a)													

Continued on next page

ID	Cluster	STRAIN	d_STRAIN	PGA	d_PGA	K$_S$	d_K_S	HEP	d_HEP	LWAV	d_LWAV	AI	d_AI
			1 σ	[m s^{-2}]	1 σ	[m$^{0.9}$]	1 σ		1 σ	[m km^{-1}]	1 σ		1 σ
WTS51001	2	12.78	1.20	3872	3319	58	30	2899	1672	16498	2436	0.32	0.07
WTS51002	3	13.40	1.40	5073	2818	68	54	4003	2385	13691	6506	0.45	0.13
WTS51003	3	14.37	0.76	6034	3055	72	42	4365	2463	17009	7620	0.46	0.14
WTS51004	3	14.50	0.71	5030	4031	108	10	7122	2140	5470	991	0.60	0.06
WTS51005	3	14.50	0.58	4670	3559	87	15	5954	2124	5171	1629	0.59	0.09
WTS51006	3	16.19	0.83	3522	2463	124	76	7720	2857	24986	9547	0.62	0.21
WTS51007	2	12.50	0.71	7640	113	138	47	7274	2474	36195	3544	0.42	0.13
WTS51008	3	17.00	1.47	5531	2547	127	73	8047	2751	24023	9406	0.67	0.20
WTS51009	3	16.60	0.55	5005	3392	130	52	8218	2568	29949	2829	0.60	0.17
WTS51010	3	17.29	0.49	6023	2260	138	50	9101	2501	26983	3380	0.74	0.19
WTS51011	3	18.33	1.21	5430	3270	123	57	8404	2649	23281	3252	0.62	0.20
WTS51012	3	18.02	1.26	4855	3068	107	61	7465	3058	13693	4426	0.69	0.19
WTS51015	2	7.42	0	3680	0	66	31	2709	978	1025	1426	0.30	0.08
WTS51016	2	3.46	0	8800	0	42	0	879	494	418	1025	0.08	0.01
WTS51017	2	4.63	0.23	2730	2178	26	8	1068	459	787	1180	0.14	0
Longmen Shan, E Tibet, China (Godard et al., 2010)													
WTS65006	4	11.33	0.78	5787	2843	122	66	28183	10312	31066	4771	1.15	0.10
WTS65007	4	8.64	0.67	6829	2087	178	101	35496	13239	26187	7610	1.27	0.28
WTS65008	4	8.20	0.82	4517	3425	177	95	36097	11884	22430	4636	1.43	0.34
WTS65009	4	6.42	1.21	5430	1372	95	35	21300	7545	38170	3702	0.98	0.02
WTS65011	4	9.59	0	1490	0	132	40	29797	7624	22665	4355	1.00	0
WTS65012	4	7.01	0.73	4485	2577	156	90	29624	9789	25173	5007	1.12	0.21
Three Rivers Region, China (Henck et al., 2011)													
WTS69002	5	9.74	0.36	3780	976	160	46	41874	10969	3648	1032	1.25	0.06
WTS69012	3	18.20	2.28	2882	2210	112	89	11736	4978	5675	3162	0.74	0.09
WTS69018	3	20.92	0.79	5418	2957	47	26	7089	3471	5306	2411	0.64	0.04
WTS69019	3	21.53	0.64	2719	2139	62	28	8812	3787	4010	2229	0.71	0.06
WTS69029	3	15.00	2.00	5686	3028	79	49	10699	4381	4944	3209	0.81	0.08
WTS69031	3	12.37	4.20	3102	3404	88	47	11127	4028	5681	3628	0.79	0.08
WTS69034	4	17.38	2.00	4167	3690	102	67	11576	4808	3331	2026	0.64	0.08
WTS69035	4	14.25	2.82	4817	3378	148	104	17252	5790	5500	3008	0.91	0.12
WTS69038	3	7.80	2.35	4695	4044	92	78	12565	5106	11023	4025	0.87	0.11
WTS69039	4	14.67	1.53	6487	2384	155	88	14981	5124	6752	2082	0.69	0.09
WTS69042	3	14.67	12.10	4659	3527	111	59	13782	5529	15322	6204	0.89	0.16
WTS69043	3	30.89	12.06	4479	2934	70	26	12822	6007	6453	2449	0.94	0.06
WTS69044	3	34.92	12.40	4715	2983	85	33	12438	5732	6388	2399	0.90	0.08

Table C.6: BIOCLIM temperature derivates. Area-weighted means and standard deviations for n = 297 >1000 km^2-basins draining the Himalaya-Tibet orogen. *Note that temperature data are presented in $^\circ C * 10$.* For further information related to BIOCLIM predictors see C.3.

ID	Bio1	d_01 1 σ	Bio2	d_2 1 σ	Bio3	d_3 1 σ	Bio4	d_4 1 σ	Bio5	d_5 1 σ	Bio6	d_6 1 σ	Bio7	d_7 1 σ	Bio8	d_8 1 σ	Bio9	d_9 1 σ	Bio10	d_10 1 σ	Bio11	d_11 1 σ
Nam Co, Tibetan Plateau, China (Strobl et al., 2012)																						
WTS10301	-40.80	6.20	135	5	38.90	0.32	7500	0	120.00	6.67	-223.00	8.23	340	0	48.60	5.87	-123.00	8.23	53.10	6.17	-137	4.83
WTS10302	-37.00	8.68	138	5	39.00	0	7500	0	125.00	5.77	-220.00	11.55	340	0	52.50	8.10	-122.50	9.57	57.00	8.68	-135	5.77
WTS10303	-33.36	8.41	130	0	38.27	0.47	7500	0	127.27	9.05	-213.64	10.27	340	0	56.36	8.23	-120.00	6.32	60.91	8.09	-131	7.51
WTS10304	-26.00	7.62	130	0	38.50	0.58	7500	0	135.00	5.77	-205.00	5.77	340	0	63.00	7.62	-112.50	9.57	67.50	7.05	-122	9.57
WTS10305	-34.67	7.23	130	0	38.00	0	7500	0	126.67	5.77	-216.67	11.55	340	0	55.33	7.23	-123.33	5.77	59.33	7.23	-133	5.77
WTS10306	-23.00	0	140	0	40.00	0	7400	0	140.00	0	-210.00	0	350	0	70.00	0	-110.00	0	70.00	0	-120	0
WTS10307	-19.00	7.07	140	0	40.00	0	7400	0	145.00	7.07	-205.00	7.07	350	0	73.50	6.36	-102.50	10.61	73.50	6.36	115	7.07
WTS10308	-26.00	5.20	140	0	40.00	0	7400	0	136.67	5.77	-213.33	5.77	350	0	67.00	5.20	-110.00	0	67.00	5.20	-123	5.77
WTS10309	-37.86	7.03	130	0	38.14	0.38	7486	38	122.86	9.51	-218.57	10.69	340	0	51.71	6.60	-121.43	6.90	56.29	6.42	-134	7.87
WTS10310	-43.11	5.04	132	4	38.78	0.44	7489	33	116.67	7.07	-226.67	5.00	340	0	46.33	4.61	-126.67	5.00	50.89	5.04	-136	5.00
WTS10311	-40.18	5.13	132	4	38.55	0.52	7491	30	120.91	7.01	-224.55	5.22	340	0	49.09	5.01	-124.55	5.22	53.82	5.13	-134	5.22
WTS10312	-25.75	9.25	140	0	40.00	0	7425	50	135.00	12.91	-215.00	12.91	350	0	67.00	8.83	-108.75	10.31	67.00	8.83	-122	9.57
WTS10313	-25.75	8.66	140	0	40.00	0	7400	0	135.00	11.95	-213.75	10.61	350	0	66.88	8.41	-110.00	10.35	66.88	8.41	-121	8.35
WTS10314	-25.25	7.25	146	5	40.75	0.46	7400	0	132.50	7.07	-220.00	7.56	350	0	66.50	6.91	-106.63	8.23	66.50	6.91	-122	8.86
Ladakh Batholith, Transhimalaya, India (Dortch et al., 2011c)																						
WTS10701	-43.29	31.32	123	5	31.57	0.79	8957	79	150.00	33.17	-234.29	28.20	384	5.35	68.14	30.93	-109.00	53.78	69.86	30.37	-161	32.37
WTS10702	-64.27	13.62	115	5	29.14	0.35	9218	50	131.36	15.52	-255.91	12.60	385	5.12	49.82	13.76	-160.32	24.54	51.05	13.84	-185	12.60
WTS10703	-60.51	17.71	115	6	29.15	0.54	9238	63	135.64	19.97	-252.82	15.89	385	5.55	53.85	18.31	-153.03	32.70	55.03	18.30	-182	17.16
WTS10704	-30.58	32.49	118	5	29.95	0.91	9195	23	165.79	34.05	-222.63	31.42	387	4.52	70.26	41.99	-93.89	54.51	84.00	31.71	-152	32.12
WTS10705	-54.78	25.62	123	4	31.17	0.83	9065	49	141.74	26.57	-247.39	24.54	388	3.88	57.96	25.09	-122.17	47.45	59.57	24.76	-173	25.69
WTS10706	-41.00	29.91	123	5	30.94	1.12	9088	34	153.13	32.60	-235.00	27.33	388	3.42	70.94	28.66	-103.94	47.38	72.94	28.97	-160	28.28
WTS10707	-54.85	27.72	116	6	29.34	0.79	9263	79	141.77	30.06	-247.90	25.03	387	6.63	59.58	27.96	-143.06	49.28	60.94	28.24	-177	26.36
WTS10708	-62.88	14.58	121	4	30.88	0.64	9038	52	132.50	16.69	-253.75	15.06	385	5.35	49.63	13.81	-132.13	36.79	51.50	13.94	-181	14.58
WTS10709	-41.05	33.40	124	6	31.34	1.15	9064	48	154.64	34.80	-234.82	31.04	388	4.54	70.86	32.05	-101.82	49.58	72.98	32.65	-159	32.62
WTS10710	-54.43	19.97	121	4	30.43	0.79	9100	0	138.57	21.16	-247.14	17.99	388	3.78	58.29	19.55	-123.00	41.45	60.00	19.67	-172	17.99
WTS10711	-33.25	34.69	124	5	31.25	1.39	9025	104	161.25	34.82	-226.25	32.04	388	3.54	78.25	33.67	-85.50	45.92	80.75	34.23	-152	34.12
WTS10712	-17.00	40.83	126	5	32.52	1.35	8836	152	175.15	39.54	-209.09	39.48	382	4.35	92.15	38.75	-71.67	54.09	94.73	39.09	-133	41.67
WTS10713	-46.75	22.15	116	5	29.50	0.67	9200	0	149.17	23.92	-238.33	21.67	385	5.15	66.50	21.08	-121.00	47.46	68.25	22.49	-168	21.67
WTS10714	-59.40	13.13	114	5	29.20	0.45	9200	0	136.00	15.17	-250.00	12.25	384	5.48	54.40	13.30	-144.60	35.15	55.40	13.30	-180	12.25
Ladakh Batholith, Transhimalaya, India (Dietsch et al.)																						
WTS10801	31.00	8.98	130	0	34.25	0.50	8650	100	220.00	8.16	-162.50	9.57	380	0	137.50	9.57	-15.50	8.50	140.00	8.16	-84	9.43
WTS10802	32.00	0	130	0	34.00	0	8700	0	220.00	0	-160.00	0	380	0	140.00	0	-15.00	0	140.00	0	-84	0
WTS10803	7.00	0	130	0	33.00	0	8800	0	200.00	0	-190.00	0	390	0	120.00	0	-39.00	0	120.00	0	-110	0
WTS10804	23.00	25.70	130	0	33.25	0.96	8875	96	215.00	25.17	-175.00	25.17	390	0	132.00	23.15	-23.50	24.77	135.00	25.17	-95	25.17
WTS10805	-13.00	0	130	0	32.00	0	9000	0	180.00	0	-210.00	0	390	0	98.00	0	-58.00	0	100.00	0	-130	0
WTS10806	-47.00	0	120	0	31.00	0	9100	0	150.00	0	-240.00	0	390	0	66.00	0	-92.00	0	67.00	0	-170	0

Continued on next page

ID	Bio1	d_01	Bio2	d_2	Bio3	d_3	Bio4	d_4	Bio5	d_5	Bio6	d_6	Bio7	d_7	Bio8	d_8	Bio9	d_9	Bio10	d_10	Bio11	d_11
		1 σ		1 σ		1 σ		1 σ		1 σ		1 σ		1 σ		1 σ		1 σ		1 σ		1 σ
WTS10807	39.00	0	130	0	33.00	0	8900	0	230.00	0	-160.00	0	390	0	150.00	0	-7.00	0	150.00	0	-81	0
WTS10808	39.00	0	130	0	33.00	0	8900	0	230.00	0	-160.00	0	390	0	150.00	0	-7.00	0	150.00	0	-81	0
WTS10809	-10.00	11.31	125	7	31.50	0.71	9100	0	185.00	7.07	-205.00	7.07	390	0	101.50	12.02	-55.00	11.31	102.50	10.61	-130	14.14
WTS10810	35.00	21.02	130	0	34.25	0.96	8650	129	225.00	19.15	-157.50	20.62	382	5.00	88.75	90.03	-11.50	20.49	145.00	19.15	-81	22.58
WTS10811	9.00	0	130	0	33.00	0	8800	0	200.00	0	-180.00	0	390	0	120.00	0	-37.00	0	120.00	0	-110	0
WTS10812	8.33	1.15	130	0	33.00	0	8800	0	200.00	0	-183.33	5.77	390	0	120.00	0	-37.67	1.15	120.00	0	-110	0
Zoulang Nan Shan, NE Tibetan Plateau, China (Hetzel, 2013)																						
WTS11901	-40.44	26.89	131	3	32.78	0.44	9100	278	142.22	33.08	-250.00	21.79	391	12.69	71.11	29.01	-150.00	21.79	71.11	29.01	-161	20.28
WTS11902	-62.23	17.61	129	3	32.40	0.50	9011	198	116.40	21.42	-267.43	13.79	384	6.98	49.20	18.96	-170.00	14.75	49.20	18.96	-181	14.45
WTS11903	-55.00	23.43	130	0	33.00	0	9020	286	122.00	28.64	-258.00	16.43	384	8.94	56.40	25.50	-166.00	20.74	56.40	25.50	-176	20.74
WTS11904	-51.09	22.41	130	0	33.00	0	9073	265	127.27	26.49	-256.36	15.67	385	9.34	60.55	24.42	-161.82	18.88	60.55	24.42	-171	18.88
WTS11905	-56.09	21.59	129	4	32.52	0.50	9028	230	123.25	26.14	-261.54	16.48	385	9.70	55.35	23.29	-164.62	17.93	55.35	23.29	-175	18.02
WTS11906	-62.00	17.32	130	0	32.67	0.58	8933	231	113.33	23.09	-263.33	11.55	383	5.77	49.00	19.05	-170.00	17.32	49.00	19.05	-183	11.55
WTS11907	-63.60	4.93	130	0	32.00	0	8980	84	116.00	5.48	-268.00	4.47	382	4.47	47.20	5.76	-174.00	5.48	47.20	5.76	-184	5.48
WTS11908	-66.20	1.10	130	0	33.00	0	8900	0	110.00	0	-270.00	0	380	0	43.80	1.10	-170.00	0	43.80	1.10	-180	0
WTS11910	-63.40	15.01	126	5	32.20	0.45	8980	217	114.00	16.73	-268.00	13.04	384	5.48	48.00	16.67	-172.00	13.04	48.00	16.67	-182	13.04
Anyemaquen Shan, E Tibet, China (Kirby and Harkins, 2013)																						
WTS12401	-7.50	4.95	155	7	39.00	0	7950	71	155.00	7.07	-230.00	0	390	0	86.50	4.95	-115.00	7.07	86.50	4.95	-115	7.07
WTS12402	-17.00	0	150	0	39.00	0	7700	0	150.00	0	-240.00	0	380	0	75.00	0	-120.00	0	75.00	0	-120	0
WTS12403	3.00	0	160	0	40.00	0	7900	0	170.00	0	-220.00	0	390	0	96.00	0	-110.00	0	96.00	0	-110	0
WTS12404	3.00	0	160	0	40.00	0	7900	0	170.00	0	-220.00	0	390	0	96.00	0	-110.00	0	96.00	0	-110	0
WTS12405	-34.33	4.04	140	0	37.00	0	8067	58	133.33	5.77	-246.67	5.77	376	5.77	62.00	4.58	-146.67	5.77	62.00	4.58	-146	5.77
WTS12406	-23.75	4.79	150	0	38.75	0.50	7850	58	137.50	5.00	-240.00	0	377	5.00	69.00	5.60	-127.50	5.00	69.00	5.60	-132	5.00
WTS12407	1.75	10.21	158	5	41.50	0.58	7200	0	160.00	14.14	-217.50	9.57	370	0	86.00	10.46	-89.50	14.18	86.00	10.46	-97	9.50
WTS12408	-4.57	8.62	151	4	40.14	0.36	7486	36	155.00	10.19	-222.14	8.93	377	4.69	84.14	8.36	-106.57	8.88	84.14	8.36	-106	8.88
WTS12409	-11.90	10.47	152	4	40.90	0.32	7220	42	144.00	10.75	-225.00	8.50	369	3.16	73.80	10.14	-106.50	7.47	73.80	10.14	-112	11.37
WTS12410	-16.96	11.82	152	4	40.56	0.51	7200	29	138.40	13.44	-230.40	10.98	368	4.73	68.44	11.81	-107.56	11.29	68.44	11.81	-116	11.49
WTS12411	-52.67	5.51	140	0	37.00	0	7833	58	106.67	5.77	-256.67	5.77	363	5.77	42.00	5.57	-146.67	5.77	42.00	5.57	-156	5.77
WTS12412	-37.50	8.70	140	0	37.25	0.50	7900	82	125.00	12.91	-245.00	5.77	367	5.00	56.50	9.47	-137.50	5.00	56.50	9.47	-147	9.57
WTS12413	-7.83	21.76	153	5	39.33	0.52	7967	186	158.33	24.83	-230.00	17.89	388	11.69	85.33	22.41	-117.00	17.89	85.33	22.41	-118	19.71
Himalaya, Nepal (Wobus et al., 2005)																						
WTS12501	170.00	0	110	0	47.00	0	4350	71	265.00	7.07	42.00	5.66	230	0	215.00	7.07	115.00	7.07	215.00	7.07	105	7.07
WTS12502	156.15	34.53	110	0	47.23	1.01	4338	51	256.92	35.68	27.46	34.91	223	5.06	196.92	35.68	98.77	34.17	196.92	35.68	91	33.52
WTS12503	210.00	10.54	110	0	45.70	0.48	4450	53	315.00	12.69	81.40	10.49	233	4.83	255.00	12.69	152.00	9.19	255.00	12.69	145	12.69
WTS12504	220.00	0	110	0	45.25	0.50	4500	0	327.50	5.00	92.00	4.00	237	5.00	267.50	5.00	160.00	0	267.50	5.00	157	5.00
WTS12505	205.00	5.77	110	0	45.50	0.58	4450	58	310.00	11.55	76.50	9.81	235	5.77	250.00	11.55	150.00	11.55	250.00	11.55	140	11.55
WTS12506	215.71	7.87	110	0	45.00	0	4514	38	324.29	7.87	83.71	6.32	240	0	255.71	7.87	155.71	7.87	262.86	4.88	145	7.87
WTS12507	208.33	11.15	110	0	45.00	0	4517	39	313.33	15.57	76.83	8.65	235	5.22	248.33	11.15	148.33	11.15	256.67	7.78	143	7.78
WTS12508	210.00	10.69	110	0	45.00	0	4525	46	315.00	14.14	77.00	9.26	237	4.63	253.75	11.88	150.00	10.69	256.25	9.16	146	9.16
Marsyandi Basin, Himalaya, Nepal (Godard et al., 2012)																						

Continued on next page

ID	Bio1	d_01	Bio2	d_2	Bio3	d_3	Bio4	d_4	Bio5	d_5	Bio6	d_6	Bio7	d_7	Bio8	d_8	Bio9	d_9	Bio10	d_10	Bio11	d_11
		1 σ		1 σ		1 σ		1 σ		1 σ		1 σ		1 σ		1 σ		1 σ		1 σ		1 σ
WTS12601	168.40	65.36	111	4	46.09	1.22	4469	160	271.40	65.18	37.15	67.11	233	9.42	211.85	62.44	109.88	63.98	214.05	62.35	102	64.34
WTS12603	217.33	7.99	110	0	46.13	0.35	4573	80	320.00	11.95	81.80	5.87	238	4.14	260.67	7.99	156.67	7.24	260.67	7.99	148	6.76
WTS12605	162.18	56.55	109	5	46.46	0.92	4400	119	263.57	55.59	33.25	56.89	228	7.37	206.50	53.11	104.93	54.55	207.18	52.67	97	54.98
WTS12606	203.33	11.18	110	0	46.67	0.50	4422	67	301.11	11.67	73.11	8.21	230	5.00	245.56	8.82	145.56	8.82	245.56	8.82	137	9.72
WTS12608	43.00	86.11	115	5	46.71	0.86	4657	314	149.71	79.26	-91.40	93.17	240	15.05	93.60	80.06	-10.23	83.64	96.29	78.31	-20	87.29
WTS12610	-50.74	32.44	120	1	45.36	0.48	5154	169	68.05	30.91	-192.46	35.60	260	6.28	9.35	28.98	-81.93	32.73	13.85	29.23	-117	33.74
WTS12612	-28.09	40.23	118	4	45.65	0.57	4900	129	86.58	40.34	-164.51	42.76	250	4.82	27.38	36.88	-58.26	40.02	32.31	37.65	-91	39.53
WTS12613	-30.59	38.11	117	5	45.53	0.59	4915	134	84.37	38.15	-166.60	40.90	250	5.39	25.16	34.79	-60.85	37.90	30.12	35.59	-94	37.59
WTS12615	119.14	52.97	111	3	47.29	0.64	4395	143	219.05	47.53	-9.29	54.16	228	10.14	162.86	49.96	65.43	46.41	164.38	47.91	54	51.93
WTS12620	-29.39	53.18	119	3	45.98	0.55	5058	252	87.81	49.97	-169.60	57.08	257	9.87	28.30	47.87	-62.89	50.65	33.05	48.05	-96	55.26
WTS12623	-8.65	53.93	118	4	46.26	0.45	4904	225	106.39	51.34	-147.43	59.58	253	9.26	46.83	49.60	-47.65	49.32	50.74	48.42	-74	55.32
WTS12625	168.40	65.36	111	4	46.09	1.22	4469	160	271.40	65.18	37.15	67.11	233	9.42	211.85	62.44	109.88	63.98	214.05	62.35	102	64.34
WTS12626	73.88	96.02	114	5	46.71	0.77	4585	311	178.27	88.70	-59.58	102.83	236	15.46	122.46	89.36	18.21	93.98	124.58	87.46	9	96.60
Zanskar & Ladakh, Transhimalaya, India (Munack et al., 2014)																						
WTS12701	-17.09	44.09	108	4	27.00	0	9718	218	180.00	47.75	-211.82	38.68	390	10.44	11.73	83.19	-62.27	82.09	101.82	46.13	-148	39.32
WTS12702	5.00	32.83	117	5	30.14	0.69	9143	53	195.71	33.59	-188.57	29.11	382	4.88	52.00	78.78	-38.86	31.28	117.43	31.85	-118	32.69
WTS12703	-65.53	24.66	125	5	32.65	0.70	8618	88	125.06	23.77	-251.76	24.04	377	4.37	42.71	22.78	-110.94	23.81	45.29	24.25	-175	25.77
WTS12704	-41.13	26.34	126	5	33.13	0.64	8475	46	143.75	26.69	-227.50	24.35	370	0	63.50	23.51	-86.88	25.72	68.13	26.76	-150	25.63
WTS12705	-41.00	37.43	110	0	27.73	0.46	9468	194	152.73	39.54	-233.18	35.10	385	6.71	31.55	63.76	-114.50	68.42	76.27	39.47	-166	33.80
WTS12706	-24.00	28.50	113	5	28.75	0.75	9217	72	167.50	29.27	-215.83	25.03	382	4.52	50.83	65.24	-65.83	27.37	89.08	28.06	-146	26.39
WTS12707	-42.76	30.02	105	5	26.48	0.51	9666	190	152.76	32.17	-235.52	25.01	388	8.33	32.79	68.98	-105.38	57.89	76.55	32.09	-172	26.86
WTS12708	-18.80	28.56	122	4	30.60	0.89	9160	55	176.00	30.50	-210.00	25.50	388	4.47	93.20	27.14	-74.20	46.98	95.80	29.35	-140	25.50
WTS12709	-23.71	42.24	125	5	32.47	1.37	8782	147	167.65	39.77	-213.53	42.12	380	0	59.82	51.04	-72.53	47.11	87.06	39.78	-139	42.55
WTS12710	-70.17	17.42	121	2	32.11	0.32	8667	49	118.89	19.37	-256.11	16.50	377	4.61	38.67	16.36	-117.56	22.94	40.83	16.66	-182	17.42
WTS12711	-6.00	37.07	115	5	29.67	0.82	9200	89	185.00	36.19	-198.33	31.25	383	5.16	31.00	80.83	-49.17	35.58	106.00	35.69	-130	35.79
WTS12712	-2.43	33.88	106	5	27.00	0	9729	214	191.43	34.85	-195.71	27.60	388	9.00	-22.86	100.80	-35.14	54.06	117.29	37.88	-133	29.82
WTS12713	-57.52	26.37	123	4	31.91	0.85	8761	72	134.78	26.26	-246.96	25.84	380	0	51.96	25.40	-107.09	32.18	53.96	25.38	-170	26.27
WTS12714	-12.40	36.25	124	5	32.10	1.52	8705	128	176.00	35.89	-200.50	36.20	378	3.66	63.40	56.93	-56.25	34.16	96.05	33.71	-128	36.48
WTS12715	-26.92	33.01	120	6	31.31	1.25	8831	95	162.31	33.20	-216.15	31.76	378	3.76	81.38	30.85	-70.31	31.68	83.31	32.14	-143	32.22
WTS12716	-27.20	32.65	124	5	31.90	0.99	8920	103	166.00	31.69	-219.00	31.43	386	5.16	84.20	32.54	-77.00	40.40	85.40	31.57	-145	31.71
WTS12717	-49.95	29.43	127	5	33.68	0.95	8382	50	136.91	32.28	-234.55	27.03	369	5.26	55.09	29.11	-95.50	27.60	57.95	29.57	-157	27.59
WTS12718	-16.00	45.93	122	8	30.73	1.56	9127	101	179.09	46.14	-208.18	43.55	387	4.67	75.18	56.21	-79.36	67.47	96.91	43.35	-137	45.00
WTS12719	-4.64	46.90	124	7	31.14	1.61	9100	111	190.71	47.31	-197.14	44.80	387	4.26	74.64	65.26	-64.29	66.84	107.57	43.93	-125	46.02
WTS12720	-61.55	31.54	128	4	33.45	0.82	8564	67	128.18	32.81	-248.18	31.25	380	0	46.27	29.41	-107.36	30.02	49.36	31.27	-171	32.81
WTS12721	-25.91	44.45	113	5	28.50	0.80	9405	113	168.18	46.56	-219.55	40.29	385	5.10	25.77	69.87	-93.91	68.18	90.14	45.00	-150	40.87
WTS12722	-49.92	36.61	131	3	33.77	1.01	8554	78	140.77	36.85	-238.46	36.02	379	2.77	56.92	33.44	-97.85	35.14	60.77	35.66	-159	36.71
WTS12723	-22.29	39.11	123	6	31.00	1.41	9086	110	172.14	38.86	-215.00	36.11	387	4.69	88.64	36.91	-85.64	61.20	90.93	37.56	-142	38.97
WTS12724	-33.36	41.36	114	5	29.09	1.04	9255	52	161.82	42.15	-226.36	40.07	385	5.22	59.73	52.55	-100.09	63.75	81.91	41.51	-156	39.88
WTS12725	-54.22	31.79	123	5	32.78	0.83	8478	44	131.00	32.73	-240.00	30.41	368	3.33	51.11	29.60	-99.78	31.28	54.44	31.51	-163	29.58
WTS12726	-32.27	36.18	109	3	27.07	0.26	9587	196	162.67	37.31	-226.00	32.03	387	7.04	21.00	79.16	-92.07	69.78	86.33	38.79	-159	33.76
WTS12727	-47.88	23.97	121	4	30.88	0.99	9013	64	146.25	23.26	-238.75	24.16	386	5.18	63.88	22.99	-105.75	41.62	65.50	22.56	-166	23.26

Continued on next page

ID	Bio1	d_01	Bio2	d_2	Bio3	d_3	Bio4	d_4	Bio5	d_5	Bio6	d_6	Bio7	d_7	Bio8	d_8	Bio9	d_9	Bio10	d_10	Bio11	d_11
		1 σ		1 σ		1 σ		1 σ		1 σ		1 σ		1 σ		1 σ		1 σ		1 σ		1 σ
WTS12728	-31.13	29.91	120	5	31.00	1.07	8888	35	160.00	32.51	-220.00	27.77	378	3.54	78.25	29.64	-74.63	29.15	80.50	30.50	-147	29.39
WTS12729	-18.73	33.67	122	6	31.45	1.21	8873	47	172.73	35.52	-208.18	32.19	379	3.02	90.55	33.84	-62.64	32.76	93.09	34.10	-135	33.03
WTS12730	-26.50	36.59	125	5	32.50	1.05	8633	82	160.00	36.33	-213.33	34.45	376	5.16	46.00	62.59	-71.50	35.42	81.67	33.80	-139	37.45
WTS12731	-24.83	23.42	122	4	30.67	0.82	9150	55	168.33	24.83	-216.67	19.66	388	4.08	88.00	23.66	-78.50	39.59	88.83	23.25	-145	21.68
WTS12732	-44.76	17.57	121	4	32.24	0.77	8576	44	141.90	18.61	-230.00	15.17	370	2.18	61.62	16.35	-88.29	16.63	64.14	17.31	-156	18.57
WTS12733	-21.08	31.85	120	6	30.92	1.12	8938	51	170.00	33.17	-209.23	29.85	379	2.77	88.85	31.31	-68.38	40.49	90.54	31.51	-139	30.55
Zanskar & Ladakh, Transhimalaya, India this study																						
WTS13201	-39.65	34.75	124	6	31.39	1.19	9063	49	156.14	36.29	-233.51	32.32	389	4.74	72.25	33.45	-100.23	50.58	74.33	33.92	-158	33.93
WTS13202	-21.75	44.55	114	5	28.50	0.76	9650	185	178.75	46.12	-220.00	38.54	398	8.35	37.25	78.04	-65.63	70.59	98.13	46.64	-150	40.47
WTS13203	18.67	21.50	118	4	30.83	0.75	9017	41	206.67	22.51	-175.00	21.68	380	0	-17.50	92.87	-24.33	20.62	127.67	20.61	-103	22.49
WTS13204	-53.46	29.64	117	6	29.38	0.85	9265	81	143.17	31.82	-246.67	26.70	387	6.76	61.02	29.98	-141.05	51.44	62.35	30.18	-176	28.20
WTS13205	-34.07	44.96	122	9	30.73	1.49	9220	56	164.00	45.64	-228.67	42.24	392	7.04	65.40	48.39	-112.53	71.32	81.53	44.64	-156	44.37
WTS13206	-53.15	12.15	120	0	30.31	0.48	9146	52	143.08	14.94	-246.92	11.09	390	0	60.00	12.27	-122.15	35.94	61.54	12.06	-173	12.61
WTS13207	-51.93	18.32	120	4	30.14	0.77	9179	43	145.00	18.71	-244.29	17.85	388	5.35	61.71	18.92	-130.14	41.27	63.14	18.70	-173	18.65
WTS13209	-58.66	25.47	113	5	28.63	0.66	9338	118	138.13	27.88	-252.50	22.14	386	6.53	56.59	26.09	-139.22	47.43	57.47	25.94	-182	24.06
WTS13210	-12.74	29.80	114	5	29.63	1.12	9089	66	176.84	31.28	-203.16	27.70	379	2.29	51.95	69.34	-54.95	28.54	99.58	29.27	-134	29.24
Himalaya, Nepal (Andermann, 2011)																						
WTS13307	28.96	56.31	121	8	47.35	0.93	4835	334	139.52	47.84	-111.91	63.28	254	16.74	83.22	51.49	-28.13	57.13	86.22	49.51	-36	58.02
WTS13308	108.33	34.40	110	0	48.33	0.52	4350	84	205.00	32.09	-22.50	36.35	230	6.32	155.00	32.09	51.83	32.69	155.00	32.09	44	33.16
WTS13309	36.67	31.89	122	8	47.83	0.75	4800	268	146.67	24.22	-106.17	39.94	251	17.22	91.50	29.36	-19.67	32.66	93.67	27.24	-28	33.87
WTS13310	36.67	31.89	122	8	47.83	0.75	4800	268	146.67	24.22	-106.17	39.94	251	17.22	91.50	29.36	-19.67	32.66	93.67	27.24	-28	33.87
WTS13312	152.14	50.70	111	3	47.31	0.83	4446	163	249.69	52.44	18.14	51.08	230	9.47	197.75	49.34	94.14	49.18	198.15	48.99	85	48.63
WTS13314	210.00	10.54	110	0	45.70	0.48	4450	53	315.00	12.69	81.40	10.49	233	4.83	255.00	12.69	152.00	9.19	255.00	12.69	145	12.69
WTS13316	203.33	24.49	110	0	46.33	0.50	4556	73	306.67	30.00	69.78	23.48	236	5.00	247.78	23.33	142.22	23.33	248.89	24.72	134	23.04
WTS13318	139.22	61.32	111	3	47.78	0.88	4450	154	237.78	61.51	5.67	60.76	231	10.23	185.17	58.19	81.39	58.36	185.39	57.75	73	58.24
WTS13319	67.33	37.02	114	5	48.22	0.67	4500	212	168.89	29.77	-68.22	42.26	235	15.09	116.44	32.92	12.00	37.05	117.78	31.25	4	37.85
WTS13323	189.23	12.56	110	0	46.62	0.51	4585	38	289.23	19.35	53.08	13.67	236	4.80	236.15	12.61	131.54	12.14	236.15	12.61	123	14.46
WTS13324	150.00	21.79	104	5	47.22	0.44	4400	50	237.78	24.38	16.56	20.88	222	4.41	196.67	20.62	94.44	21.86	196.67	20.62	85	21.16
Bayan Har this study																						
WTS13401n	-53.96	11.99	133	5	35.78	0.42	8226	110	112.70	14.66	-257.83	8.50	371	6.50	45.78	12.87	-155.22	11.23	45.78	12.87	-164	11.63
WTS13403n	-34.04	5.58	140	0	38.75	0.44	7706	50	130.38	5.93	-231.70	6.12	360	0	60.02	5.10	-128.11	6.22	60.02	5.10	-136	6.38
WTS13405n	-48.67	6.86	140	0	36.00	0	8217	75	118.33	9.83	-255.00	5.48	373	5.16	50.33	7.34	-150.00	8.94	50.33	7.34	-160	8.94
WTS13406n	-50.00	4.95	139	3	36.00	0	8223	60	115.38	6.60	-256.15	5.06	370	2.77	49.08	5.07	-151.54	5.55	49.08	5.07	-160	4.94
WTS13407n	-43.29	5.56	140	0	37.83	0.38	7859	68	120.69	7.04	-242.41	5.77	361	3.51	52.55	6.09	-139.31	5.93	52.55	6.09	-147	4.91
WTS13408n	-33.65	3.97	140	0	37.25	0.44	7838	71	126.67	6.37	-236.25	4.95	362	4.64	60.38	4.95	-129.58	3.59	60.38	4.95	-139	3.59
WTS13409n	-27.59	7.26	140	0	37.85	0.36	7750	50	131.94	8.46	-230.48	7.77	360	2.16	64.53	7.29	-122.42	8.03	64.53	7.29	-133	8.12
WTS13410n	-16.75	5.85	146	5	40.75	0.46	7288	35	140.00	7.56	-210.00	7.56	350	0	72.13	5.87	-104.50	5.93	72.13	5.87	-113	5.18
WTS13411n	-20.00	0	145	7	41.00	0	7250	71	145.00	7.07	-210.00	0	350	0	72.50	6.36	-105.00	7.07	72.50	6.36	-115	7.07
WTS13412n	-10.60	7.92	148	4	41.00	0	7240	55	148.00	8.37	-204.00	8.94	350	0	77.40	7.64	-98.60	8.05	77.40	7.64	-107	9.44
WTS13413n	-12.37	9.39	146	5	41.00	0.32	7230	47	145.50	9.99	-205.50	10.50	350	0	75.20	9.06	-101.10	9.59	75.20	9.06	-109	10.43

Continued on next page

ID	Bio1	d_01 1 σ	Bio2	d_2 1 σ	Bio3	d_3 1 σ	Bio4	d_4 1 σ	Bio5	d_5 1 σ	Bio6	d_6 1 σ	Bio7	d_7 1 σ	Bio8	d_8 1 σ	Bio9	d_9 1 σ	Bio10	d_10 1 σ	Bio11	d_11 1 σ
WTS13414n	-45.18	6.21	140	0	38.06	0.23	7714	35	117.22	7.01	-241.94	6.68	360	0	48.97	5.85	-140.00	7.17	48.97	5.85	-148	6.55
WTS13415n	-39.80	7.12	140	0	36.00	0	8240	55	132.00	8.37	-242.00	8.37	370	0	61.20	7.12	-140.00	10.00	61.20	7.12	-148	8.37
WTS13417n	-49.00	3.39	140	0	37.00	0	8136	50	120.71	4.75	-251.43	3.63	370	0	51.14	3.66	-148.57	3.63	51.14	3.66	-156	4.97
WTS13418n	-47.64	5.56	140	0	37.92	0.28	8040	65	120.80	7.02	-247.20	4.58	369	2.77	50.88	5.93	-145.60	5.07	50.88	5.93	-153	6.38
WTS13419n	-28.65	6.35	140	0	39.00	0	7635	49	135.29	6.24	-224.71	6.24	360	0	64.53	6.40	-123.53	6.06	64.53	6.40	-130	6.59
WTS13420n	-32.67	4.01	140	0	39.00	0	7583	39	129.17	5.15	-228.33	3.89	360	0	59.75	4.11	-126.67	4.92	59.75	4.11	-134	5.15
Kunlun Shan and Central Tibet, China (Li et al., 2014)																						
WTS13501n	-62.56	9.29	140	0	37.94	0.24	7976	44	110.76	9.93	-248.24	9.51	360	0	39.53	9.35	-151.76	8.83	39.53	9.35	-162	9.03
WTS13502n	-47.03	4.12	140	0	38.00	0	7900	0	124.41	5.61	-231.47	5.00	359	2.39	53.21	4.18	-138.82	4.09	53.21	4.18	-148	4.09
WTS13503n	-88.75	12.28	140	0	37.00	0	8075	96	81.75	14.20	-282.50	9.57	365	5.77	13.50	12.71	-182.50	9.57	13.50	12.71	-192	9.57
WTS13506n	-31.47	28.27	143	4	36.00	0	8758	295	152.26	33.24	-239.68	23.02	390	10.80	78.10	31.01	-141.94	18.87	78.10	31.01	-146	22.86
WTS13508n	-44.95	20.09	141	3	36.22	0.42	8574	198	135.65	23.13	-249.57	16.65	383	7.83	61.96	20.85	-146.96	14.90	61.96	20.85	-156	15.79
WTS13510n	-61.28	16.65	140	0	37.00	0	8276	161	113.19	19.31	-259.76	12.97	372	6.36	42.29	18.04	-159.29	13.69	42.29	18.04	-169	14.45
WTS13512n	-54.96	6.87	147	4	39.00	0	8102	38	118.76	7.96	-250.36	7.72	370	0	46.72	7.00	-149.04	7.43	46.72	7.00	-159	7.55
WTS13513n	-58.71	4.35	146	5	39.00	0	8078	52	113.91	5.83	-254.35	5.90	368	3.44	43.09	5.74	-152.17	5.18	43.09	5.74	-162	5.41
WTS13516n	-43.13	5.30	150	0	39.41	0.50	7986	35	125.80	6.09	-246.80	6.21	370	0	55.86	5.13	-133.80	6.02	55.86	5.13	-147	6.57
Namche Barwa-Gyala Peri Massif, Tibet, China (Finnegan et al., 2008)																						
WTS33002	61.00	34.32	130	0	44.00	0	5800	115	192.50	33.04	-99.00	37.29	295	5.77	132.25	33.37	-7.25	34.55	132.25	33.37	-16	34.90
WTS33003	35.60	24.46	130	0	43.40	0.55	5900	100	168.00	23.87	-128.00	28.64	298	4.47	108.60	23.02	-36.80	28.88	108.60	23.02	-42	24.46
WTS33004	57.14	42.91	130	0	43.43	0.53	5914	186	190.00	41.23	-105.00	46.00	297	4.88	128.86	40.30	-13.14	42.89	128.86	40.30	-22	43.78
WTS33007	50.86	34.92	130	0	43.29	0.49	5929	150	184.29	33.59	-111.43	38.33	297	4.88	123.14	33.12	-18.86	35.33	123.14	33.12	-28	36.06
WTS33008	30.48	22.58	130	0	43.79	0.41	5886	124	164.09	21.41	-134.27	26.20	297	5.49	102.56	21.22	-46.94	23.97	102.56	21.22	-47	23.10
WTS33010	58.67	38.08	130	0	43.33	0.58	5867	153	193.33	35.12	-101.67	43.11	296	5.77	129.67	36.47	-13.00	44.31	129.67	36.47	-19	40.26
WTS33013	54.75	36.33	130	0	43.50	0.58	5850	129	187.50	35.00	-107.25	40.71	295	5.77	127.50	35.00	-16.25	39.96	127.50	35.00	-23	36.72
E Tibet, China (Ouimet et al., 2009)																						
WTS37001	20.86	6.23	130	0	43.00	0	5900	0	150.00	8.16	-152.86	7.56	301	3.78	91.57	5.86	-59.29	6.13	91.57	5.86	-59	6.13
WTS37002	26.60	16.82	130	0	43.80	0.45	5780	45	152.00	16.43	-148.00	21.68	298	4.47	95.40	16.88	-52.20	16.86	95.40	16.88	-52	16.86
WTS37003	22.50	31.61	135	5	45.25	0.89	5650	53	145.00	34.64	-152.50	31.96	300	0	90.25	30.60	-54.38	31.79	90.25	30.60	-54	31.79
WTS37004	64.41	15.11	109	2	37.53	0.80	6012	49	198.82	15.76	-94.18	20.14	289	2.43	138.82	15.76	-17.88	14.62	138.82	15.76	-17	14.62
WTS37005	-3.17	24.86	133	5	44.58	0.79	5608	29	115.83	27.33	-179.17	24.66	293	4.92	64.42	24.35	-78.50	23.87	64.42	24.35	-78	23.87
WTS37006	125.20	22.03	96	0	36.80	0.45	5680	84	244.00	24.08	-15.00	21.64	260	0	192.00	21.68	45.40	20.29	194.00	24.08	45	20.29
WTS37007	130.00	30.00	96	1	36.67	0.58	5767	115	250.00	30.00	-7.33	27.01	260	0	200.00	30.00	51.67	26.54	200.00	30.00	51	26.54
WTS37008	62.92	54.83	104	12	37.67	2.90	5817	127	186.08	56.51	-86.17	66.24	272	11.38	132.33	55.21	-16.58	51.86	133.17	56.38	-16	51.86
WTS37009	77.20	46.89	103	12	36.80	2.95	5960	134	204.00	50.30	-71.40	59.01	278	8.37	149.60	49.10	-4.00	45.07	149.60	49.10	-4	45.07
WTS37010	85.83	25.25	115	5	38.17	1.17	6100	110	220.00	25.30	-75.33	28.93	295	5.48	158.33	25.63	0.50	21.93	158.33	25.63	0	21.93
WTS37011	16.00	22.77	138	5	42.25	0.96	6050	58	157.50	22.17	-165.00	23.80	320	0	88.50	20.82	-66.00	22.77	88.50	20.82	-66	22.77
WTS37012	37.00	24.87	158	4	44.80	0.84	6480	45	186.00	26.08	-166.00	25.10	350	0	114.00	25.11	-49.00	28.57	114.00	25.11	-52	25.13
WTS37013	5.00	16.11	153	5	43.14	0.69	6729	49	154.29	17.18	-200.00	15.28	350	0	85.14	15.88	-76.86	15.44	85.14	15.88	-87	16.41
WTS37014	8.27	14.64	156	5	43.27	0.47	6782	40	157.27	15.55	-200.00	12.65	356	5.05	88.18	14.67	-74.36	13.74	88.18	14.67	-84	14.10
WTS37015	22.16	8.61	153	5	44.03	0.31	6548	51	169.35	9.98	-176.13	8.44	345	5.06	99.77	8.90	-57.97	8.26	99.77	8.90	-67	8.59

Continued on next page

ID	Bio1	d_01 1 σ	Bio2	d_2 1 σ	Bio3	d_3 1 σ	Bio4	d_4 1 σ	Bio5	d_5 1 σ	Bio6	d_6 1 σ	Bio7	d_7 1 σ	Bio8	d_8 1 σ	Bio9	d_9 1 σ	Bio10	d_10 1 σ	Bio11	d_11 1 σ
WTS37016	17.25	19.07	155	6	43.75	0.50	6600	0	165.00	19.15	-185.00	19.15	347	5.00	95.75	18.55	-63.00	18.11	95.75	18.55	-73	18.81
WTS37017	28.67	17.21	157	6	44.67	0.58	6500	0	173.33	20.82	-170.00	17.32	346	5.77	105.67	16.92	-51.33	16.29	105.67	16.92	-60	16.86
WTS37018	30.00	28.37	155	5	44.33	0.82	6433	52	176.67	30.77	-168.33	27.87	341	4.08	107.67	29.57	-49.17	27.46	107.67	29.57	-58	28.52
WTS37019	57.17	35.40	150	0	44.33	0.82	6150	55	201.67	37.64	-131.00	40.53	330	0	129.67	35.67	-26.17	34.71	129.67	35.67	-27	35.91
WTS37020	98.25	15.63	135	6	42.75	0.96	6050	58	240.00	14.14	-74.75	18.39	312	5.00	165.00	10.00	13.75	15.00	170.00	14.14	13	15.00
WTS37021	54.00	29.22	138	5	42.75	0.50	6100	0	192.50	33.04	-123.00	32.19	315	5.77	125.25	28.46	-29.25	28.36	125.25	28.46	-29	28.36
WTS37022	63.33	27.91	121	9	39.89	1.27	6000	0	198.89	28.48	-100.67	34.55	296	5.00	132.22	22.24	-19.56	26.99	135.56	26.51	-19	26.99
WTS37023	12.80	11.95	132	4	43.00	0	6000	0	146.00	11.74	-164.00	11.74	310	0	84.40	11.18	-68.50	11.70	84.40	11.18	-68	11.70
WTS37024	34.00	26.37	130	0	42.17	0.41	6000	0	168.33	29.27	-143.33	32.04	308	4.08	105.33	26.62	-48.33	26.01	105.33	26.62	-48	26.01
WTS37025	57.25	36.71	123	7	39.88	1.73	5988	64	191.25	39.07	-105.63	44.67	295	9.26	131.13	39.05	-25.13	35.87	131.13	39.05	-25	35.87
WTS37026	71.83	31.49	106	11	37.50	2.07	5967	82	196.67	30.77	-81.33	40.47	280	8.94	144.33	31.38	-10.83	29.23	144.33	31.38	-10	29.23
WTS37027	50.67	15.04	107	6	38.33	1.15	5833	58	176.67	11.55	-102.33	22.50	276	5.77	120.00	17.32	-29.33	14.15	120.00	17.32	-29	14.15
WTS37028	47.00	45.88	108	11	38.25	2.50	5825	126	172.50	50.58	-105.75	60.37	275	12.91	117.75	45.32	-32.25	44.18	117.75	45.32	-32	44.18
WTS37029	50.55	24.74	140	0	45.18	0.40	5918	40	182.73	25.73	-129.91	27.72	310	0	121.55	24.56	-30.00	25.16	121.55	24.56	-30	24.65
WTS37030	17.63	14.93	140	0	44.14	0.38	5900	0	143.75	15.06	-160.00	16.90	306	5.18	87.00	13.67	-62.50	14.44	87.00	13.67	-62	14.44
WTS37031	19.63	13.32	130	0	43.00	0	5800	0	145.00	15.12	-152.50	14.88	300	0	89.00	13.32	-59.25	13.18	89.00	13.32	-59	13.18
WTS37032	31.80	2.68	134	5	43.00	0	5900	0	162.00	4.47	-144.00	5.48	310	0	102.00	4.47	-49.20	2.68	102.00	4.47	-49	2.68
WTS37033	38.91	73.89	111	10	39.82	2.32	5618	117	159.18	77.83	-115.18	85.98	273	10.27	107.27	75.20	-37.82	71.31	107.27	75.20	-37	71.31
WTS37034	113.00	32.73	99	2	37.75	0.96	5700	115	232.50	33.04	-28.75	34.54	262	5.00	180.00	29.44	34.00	30.14	182.50	33.04	34	30.14
WTS37035	121.10	42.66	103	8	38.30	2.16	5620	175	243.00	45.96	-22.00	48.65	263	4.83	187.00	45.23	44.20	41.08	188.00	45.90	44	41.08
WTS37036	53.43	25.27	140	0	42.86	0.77	6029	47	198.57	27.42	-126.64	28.69	322	4.26	128.64	25.62	-29.36	24.87	128.64	25.62	-29	24.87
WTS37037	53.50	14.29	150	0	44.50	0.58	6075	50	200.00	16.33	-132.50	12.58	337	5.00	127.50	12.58	-30.25	14.31	127.50	12.58	-30	14.31
WTS37038	7.00	6.16	150	0	43.00	0	6300	0	152.50	5.00	-187.50	5.00	340	0	82.50	5.80	-79.00	6.16	82.50	5.80	-79	6.16
WTS37039	3.75	12.19	156	5	42.63	0.52	7000	0	155.00	15.12	-206.25	13.02	361	3.54	86.00	11.21	-81.63	11.54	86.00	11.21	-91	12.00
WTS37040	1.50	12.32	157	5	42.33	0.52	7100	0	156.67	16.33	-210.00	12.65	365	5.48	85.00	10.99	-84.83	11.16	85.00	10.99	-96	12.77
WTS37041	1.50	12.32	157	5	42.33	0.52	7100	0	156.67	16.33	-210.00	12.65	365	5.48	85.00	10.99	-84.83	11.16	85.00	10.99	-96	12.77
WTS37042	-2.56	8.60	154	5	42.22	0.44	7067	71	151.11	9.28	-211.11	7.82	361	3.33	81.00	8.86	-88.22	7.60	81.00	8.86	-98	8.19
WTS37043	11.50	19.52	158	5	43.00	0.76	6900	0	165.00	19.27	-196.25	18.47	362	4.63	93.88	20.24	-73.25	18.59	93.88	20.24	-83	20.05
WTS37044	13.60	13.37	160	0	43.00	0.71	6980	45	168.00	13.04	-196.00	11.40	364	5.48	96.40	14.29	-72.00	12.88	96.40	14.29	-82	13.03
WTS37045	17.46	13.81	160	0	43.46	0.52	6923	44	172.31	14.81	-193.08	14.37	361	3.76	98.92	13.63	-67.69	13.22	98.92	13.63	-77	13.75
WTS37046	14.14	12.71	159	4	43.71	0.49	6771	49	164.29	15.12	-192.86	11.13	358	3.78	95.29	13.52	-68.71	12.15	95.29	13.52	-78	12.68
WTS37047	20.67	17.47	152	4	44.00	0.63	6467	52	165.00	18.71	-173.33	16.33	340	0	97.00	16.30	-58.17	16.39	97.00	16.30	-67	16.75
WTS37048	15.92	25.24	143	5	43.67	0.89	6208	29	154.17	28.11	-174.17	24.66	329	2.89	90.17	25.02	-60.08	25.03	90.17	25.02	-68	24.84
WTS37049	12.10	5.95	140	0	43.70	0.48	5910	32	142.00	6.32	-168.00	6.32	310	0	83.20	5.88	-68.80	6.01	83.20	5.88	-68	6.01
WTS37050	15.50	2.12	140	0	43.00	0	5900	0	145.00	7.07	-165.00	7.07	310	0	86.50	2.12	-65.50	2.12	86.50	2.12	-65	2.12
WTS37051	38.75	1.71	130	0	43.50	0.58	5850	58	170.00	0	-137.50	5.00	300	0	110.00	0	-41.25	1.71	110.00	0	-41	1.71
WTS37052	34.30	27.55	140	0	45.20	0.63	5790	32	160.00	30.18	-142.40	28.83	302	4.22	102.80	27.75	-44.90	27.63	102.80	27.75	-44	27.63
WTS37053	34.30	27.55	140	0	45.20	0.63	5790	32	160.00	30.18	-142.40	28.83	302	4.22	102.80	27.75	-44.90	27.63	102.80	27.75	-44	27.63
WTS37054	4.50	2.12	135	7	44.00	0	5850	71	130.00	0	-175.00	7.07	300	0	74.50	2.12	-75.00	1.41	74.50	2.12	-75	1.41
WTS37055	14.00	8.49	140	0	44.00	0	5900	0	145.00	7.07	-165.00	7.07	305	7.07	84.00	8.49	-66.00	8.49	84.00	8.49	-66	8.49
WTS37056	12.00	52.33	115	7	41.50	0.71	5600	0	131.00	55.15	-150.00	56.57	280	0	81.50	54.45	-63.50	51.62	81.50	54.45	-63	51.62

Continued on next page

ID	Bio1	d_01	Bio2	d_2	Bio3	d_3	Bio4	d_4	Bio5	d_5	Bio6	d_6	Bio7	d_7	Bio8	d_8	Bio9	d_9	Bio10	d_10	Bio11	d_11
		1 σ		1 σ		1 σ		1 σ		1 σ		1 σ		1 σ		1 σ		1 σ		1 σ		1 σ
WTS37057	98.00	20.78	110	0	42.33	0.58	5200	0	213.33	20.82	-50.00	24.76	263	5.77	163.33	20.82	26.00	20.22	163.33	20.82	26	20.22
WTS37058	108.00	33.11	120	0	46.00	0	4925	50	215.00	31.09	-46.25	36.12	262	5.00	165.00	31.09	38.00	31.97	165.00	31.09	38	31.97
WTS37059	101.89	39.96	123	7	45.11	0.93	5089	60	215.56	42.46	-50.78	46.56	265	7.26	162.56	38.94	32.78	40.71	162.56	38.94	32	40.71
WTS37060	70.00	43.67	128	4	46.33	0.82	5067	82	181.67	43.55	-91.67	46.55	273	8.16	132.67	41.89	-0.50	42.81	132.67	41.89	0	42.81
WTS37061	37.50	29.06	135	5	46.20	1.23	5340	143	153.00	29.83	-134.20	30.56	289	3.16	100.90	26.37	-34.90	30.40	100.90	26.37	-34	30.40
WTS37062	12.75	18.30	131	4	44.38	0.52	5638	52	132.50	18.32	-160.00	19.27	296	5.18	81.13	18.61	-63.63	18.07	81.13	18.61	-63	18.07
WTS37063	19.80	17.71	130	0	44.00	0	5700	0	144.00	16.73	-154.00	20.74	298	4.47	89.40	19.35	-57.40	17.33	89.40	19.35	-57	17.33
WTS37064	23.10	10.34	135	5	44.00	0	5820	42	149.00	9.94	-154.00	11.74	300	0	92.70	10.22	-56.60	10.10	92.70	10.22	-56	10.10
WTS37065	96.75	33.08	96	4	36.00	1.15	5775	96	215.00	35.12	-44.50	35.71	262	5.00	165.00	35.12	16.25	30.14	165.00	35.12	16	30.14
WTS37066	54.00	36.38	136	5	42.38	0.74	6063	52	192.50	38.45	-122.38	42.53	316	5.18	124.63	35.21	-29.38	36.02	125.88	37.17	-29	36.02
WTS37067	49.13	41.53	135	8	42.25	1.16	6075	46	187.50	43.67	-126.88	49.60	312	8.86	120.50	40.51	-34.38	40.74	120.50	40.51	-34	40.74
Yumu Shan & Longshou Shan, NE Tibet, China (Palumbo et al., 2010b)																						
WTS45001	36.00	0	140	0	32.00	0	10000	0	240.00	0	-190.00	0	430	0	160.00	0	-87.00	0	160.00	0	-100	0
WTS45002	36.00	0	140	0	32.00	0	10000	0	240.00	0	-190.00	0	430	0	160.00	0	-87.00	0	160.00	0	-100	0
WTS45003	36.00	0	140	0	32.00	0	10000	0	240.00	0	-190.00	0	430	0	160.00	0	-87.00	0	160.00	0	-100	0
WTS45004	36.60	12.90	140	0	32.00	0	9960	55	236.00	16.73	-192.00	8.37	428	8.37	160.00	12.25	-89.00	5.79	160.00	12.25	-100	10.04
WTS45005	22.75	15.39	140	0	32.00	0	9875	150	220.00	18.26	-202.50	9.57	420	8.16	145.00	19.15	-98.75	13.74	145.00	19.15	-111	10.90
WTS45006	20.67	18.58	140	0	32.00	0	9800	173	216.67	20.82	-203.33	11.55	416	11.55	143.33	23.09	-100.67	16.17	143.33	23.09	-112	13.28
WTS45007	27.00	18.29	143	5	32.50	0.58	9850	129	225.00	25.17	-197.50	12.58	422	12.58	147.50	22.17	-97.25	9.22	147.50	22.17	-107	13.52
WTS45008	38.00	19.80	145	7	33.00	0	9900	141	240.00	28.28	-190.00	14.14	430	14.14	160.00	28.28	-91.50	4.95	160.00	28.28	-99	15.56
WTS45009	18.67	9.24	140	0	32.33	0.58	9800	100	213.33	11.55	-203.33	5.77	416	5.77	136.67	5.77	-100.33	8.39	136.67	5.77	-113	5.77
WTS45010	23.25	12.27	140	0	32.63	0.52	9825	104	220.00	16.04	-200.00	9.26	418	6.41	142.50	12.82	-98.13	7.55	142.50	12.82	-110	8.65
WTS45011	60.50	6.36	150	0	33.00	0	10000	0	265.00	7.07	-175.00	7.07	440	0	185.00	7.07	-80.50	4.95	185.00	7.07	-80	4.95
WTS45012	60.50	6.36	150	0	33.00	0	10000	0	265.00	7.07	-175.00	7.07	440	0	185.00	7.07	-80.50	4.95	185.00	7.07	-80	4.95
WTS45013	62.00	5.20	150	0	33.00	0	10000	0	266.67	5.77	-173.33	5.77	443	5.77	186.67	5.77	-79.00	4.36	186.67	5.77	-79	4.36
WTS45014	65.00	0	150	0	33.00	0	10000	0	270.00	0	-170.00	0	445	7.07	190.00	0	-76.50	0.71	190.00	0	-76	0.71
WTS45015	69.00	2.83	150	0	33.00	0	10000	0	280.00	0	-170.00	0	450	0	195.00	7.07	-73.50	2.12	195.00	7.07	-73	2.12
WTS45016	62.00	5.66	150	0	33.00	0	10000	0	275.00	7.07	-175.00	7.07	450	0	185.00	7.07	-81.00	4.24	185.00	7.07	-81	4.24
WTS45017	63.67	4.93	150	0	33.00	0	10000	0	276.67	5.77	-173.33	5.77	450	0	186.67	5.77	-79.67	3.79	186.67	5.77	-79	3.79
WTS45018	67.00	0	150	0	33.00	0	10000	0	280.00	0	-170.00	0	450	0	190.00	0	-77.00	0	190.00	0	-77	0
WTS45019	68.00	0	150	0	33.00	0	10000	0	280.00	0	-170.00	0	450	0	190.00	0	-76.00	0	190.00	0	-76	0
WTS45020	67.00	1.41	150	0	33.00	0	10000	0	280.00	0	-170.00	0	450	0	190.00	0	-76.50	0.71	190.00	0	-76	0.71
WTS45021	50.67	15.95	143	6	32.67	0.58	10000	0	256.67	20.82	-183.33	11.55	436	11.55	176.67	20.82	-83.33	9.71	176.67	20.82	-88	11.93
WTS45022	49.25	13.33	143	5	32.75	0.50	10000	0	255.00	17.32	-185.00	10.00	435	10.00	175.00	17.32	-85.75	9.29	175.00	17.32	-89	9.98
WTS45023	49.25	13.33	143	5	32.75	0.50	10000	0	255.00	17.32	-185.00	10.00	435	10.00	175.00	17.32	-85.75	9.29	175.00	17.32	-89	9.98
WTS45024	7.75	17.26	134	5	32.13	0.35	9550	278	200.00	23.90	-207.50	11.65	408	13.56	125.75	20.74	-120.00	13.09	125.75	20.74	-120	13.09
WTS45025	14.40	22.66	134	5	32.40	0.55	9580	335	210.00	30.82	-206.00	13.42	410	15.81	134.00	26.08	-114.60	17.20	134.00	26.08	-114	17.20
WTS45026	7.75	18.32	135	6	32.25	0.50	9475	275	200.00	24.49	-210.00	11.55	405	12.91	127.50	20.62	-117.50	15.00	127.50	20.62	-117	15.00
WTS45027	7.75	18.32	135	6	32.25	0.50	9475	275	200.00	24.49	-210.00	11.55	405	12.91	127.50	20.62	-117.50	15.00	127.50	20.62	-117	15.00
Qilian Shan, NE Tibet, China (Palumbo et al., 2010a)																						

Continued on next page

ID	Bio1	d_01	Bio2	d_2	Bio3	d_3	Bio4	d_4	Bio5	d_5	Bio6	d_6	Bio7	d_7	Bio8	d_8	Bio9	d_9	Bio10	d_10	Bio11	d_11
		1 σ		1 σ		1 σ		1 σ		1 σ		1 σ		1 σ		1 σ		1 σ		1 σ		1 σ
WTS51001	-29.85	15.20	135	5	32.61	0.50	9709	174	164.85	18.89	-244.24	12.75	409	6.37	91.12	17.24	-145.76	13.47	91.12	17.24	-158	12.53
WTS51002	-49.20	21.61	131	3	32.61	0.49	9504	264	141.39	25.87	-260.78	17.76	401	8.64	69.27	23.82	-162.55	17.76	69.27	23.82	-174	16.89
WTS51003	-49.52	21.92	130	0	32.33	0.47	9523	265	140.88	26.73	-260.72	18.18	401	9.00	69.04	24.22	-162.90	17.67	69.04	24.22	-175	16.51
WTS51004	-62.00	5.29	130	0	32.67	0.58	9367	58	126.67	5.77	-273.33	5.77	396	5.77	55.00	6.24	-173.33	5.77	55.00	6.24	-183	5.77
WTS51005	-68.30	9.02	130	0	32.80	0.42	9270	125	117.50	11.37	-276.00	6.99	393	6.75	48.10	9.68	-177.00	6.75	48.10	9.68	-188	6.32
WTS51006	-54.56	26.04	130	3	32.02	0.13	9351	304	131.00	31.55	-263.45	21.19	394	11.80	61.02	28.94	-167.27	21.38	61.02	28.94	-180	21.04
WTS51007	-18.43	19.34	131	4	32.00	0	9671	180	172.86	21.38	-234.29	17.18	408	6.90	99.00	21.38	-134.29	17.18	99.00	21.38	-148	14.64
WTS51008	-56.28	26.14	129	4	32.10	0.31	9209	316	126.32	32.15	-263.97	20.08	389	12.46	57.50	28.85	-166.76	21.47	57.50	28.85	-178	20.97
WTS51009	-43.30	24.81	130	0	32.00	0	9290	281	142.00	30.48	-252.00	19.89	393	13.37	70.60	26.57	-155.00	20.14	70.60	26.57	-165	20.14
WTS51010	-58.75	20.87	128	4	32.33	0.49	9058	275	121.67	27.91	-263.33	14.97	385	11.68	53.25	23.04	-168.33	18.01	53.25	23.04	-178	18.01
WTS51011	-32.09	24.00	131	3	32.36	0.50	9218	256	152.73	28.67	-242.73	17.37	393	9.24	80.45	25.99	-144.55	21.62	80.45	25.99	-156	18.59
WTS51012	-51.57	23.59	129	4	32.58	0.50	9049	241	128.60	28.62	-257.79	18.33	386	10.31	59.93	25.27	-160.44	19.92	59.93	25.27	-172	19.57
WTS51015	25.33	16.50	137	6	32.00	0	9767	252	223.33	25.17	-200.00	10.00	420	10.00	150.00	20.00	-108.33	12.58	150.00	20.00	-108	12.58
WTS51016	82.00	0	150	0	31.00	0	11000	0	300.00	0	-160.00	0	460	0	220.00	0	-68.00	0	220.00	0	-68	0
WTS51017	54.50	0.71	140	0	32.00	0	11000	0	265.00	7.07	-180.00	0	450	0	180.00	0	-90.00	0	180.00	0	-90	0
Longmen Shan, E Tibet, China (Godard et al., 2010)																						
WTS65006	114.14	28.64	86	6	31.25	2.13	6342	244	243.33	31.26	-27.50	32.49	270	2.80	188.06	28.87	27.11	25.20	193.06	31.70	27	25.20
WTS65007	60.80	43.84	104	9	36.00	2.71	6102	248	193.56	43.34	-95.96	51.35	288	6.61	134.16	43.81	-22.73	40.07	136.38	46.71	-22	40.07
WTS65008	42.30	36.79	113	10	37.28	2.00	6048	169	175.74	37.35	-117.91	42.39	295	7.45	115.78	36.93	-39.98	34.23	117.26	39.59	-39	34.23
WTS65009	133.00	14.18	86	5	30.40	1.51	6610	173	265.00	14.34	-11.60	15.26	280	0	209.00	16.63	42.00	11.48	214.00	15.06	42	11.48
WTS65011	130.00	0	86	0	31.00	0	6600	0	270.00	0	-9.00	0	280	0	210.00	0	44.00	0	210.00	0	44	0
WTS65012	89.33	34.34	103	12	35.10	2.92	6285	235	225.00	34.89	-63.96	40.31	288	7.81	163.67	35.86	3.69	31.27	168.25	37.76	3	31.27
Three Rivers Region, China (Henck et al., 2011)																						
WTS69002	160.00	0	110	0	45.00	0	4600	0	260.00	0	20.00	0	240	0	210.00	0	110.00	0	210.00	0	95	0
WTS69012	6.38	17.08	148	4	43.63	0.62	6525	58	154.38	17.50	-178.75	19.28	330	0	85.38	16.69	-71.94	16.87	85.38	16.69	-80	17.40
WTS69018	15.30	8.59	150	0	44.15	0.36	6460	50	165.00	9.87	-168.75	9.11	330	2.21	94.00	8.47	-62.18	8.47	94.00	8.47	-70	8.74
WTS69019	0.37	10.34	145	5	43.73	0.45	6443	50	148.82	11.77	-181.96	10.40	329	1.96	79.29	9.99	-75.80	9.94	79.29	9.99	-84	10.12
WTS69029	-5.46	14.37	130	0	44.00	0.28	5846	51	125.00	15.56	-168.85	15.05	296	4.96	67.04	14.55	-71.69	14.15	67.04	14.55	-81	14.20
WTS69031	3.88	16.31	130	0	44.06	0.25	5788	34	133.13	15.80	-159.38	16.92	290	2.50	74.88	15.08	-61.69	16.15	74.88	15.08	-71	16.30
WTS69034	32.52	22.30	131	3	44.83	0.65	5783	39	163.91	21.90	-130.52	23.57	290	0	103.48	22.08	-33.96	21.77	103.48	22.08	-43	22.58
WTS69035	15.93	30.38	116	6	43.07	0.68	5409	74	133.30	29.70	-130.02	35.73	263	8.05	81.89	29.67	-42.86	30.52	81.89	29.67	-54	30.56
WTS69038	-7.67	17.06	130	0	44.03	0.18	5740	50	119.67	17.71	-168.00	17.30	289	2.54	62.87	16.36	-71.93	16.50	62.87	16.36	-82	16.77
WTS69039	20.90	22.49	136	5	44.30	0.48	5960	52	157.00	24.06	-147.00	22.63	303	4.83	94.00	21.45	-47.70	21.74	94.00	21.45	-57	22.10
WTS69042	-13.52	31.22	131	3	43.62	0.60	5827	57	117.62	34.08	-176.55	29.70	293	4.69	58.80	31.02	-79.14	29.83	58.80	31.02	-89	30.44
WTS69043	-26.81	7.00	130	0	43.38	0.50	5786	36	101.90	8.21	-188.10	8.73	290	0	45.10	6.74	-90.76	6.59	45.10	6.74	-100	7.06
WTS69044	-20.63	12.69	130	0	43.43	0.50	5785	36	108.60	13.95	-182.25	13.68	290	0	51.18	12.45	-84.83	12.22	51.18	12.45	-94	12.24

Table head: Predictor abbreviations used in the text have been truncated following the scheme Bio1 = BIO01, and d_1 = Bio1 standard deviation etc.

TABLE C.7: BIOCLIM precipitation derivates. Area-weighted means and standard deviations for n = 297 >1000 km^2-basins draining the Himalaya-Tibet orogen. *Note that the unit for precipitation data is mm.* For further information related to BIOCLIM predictors see C.3.

ID	Bio12	d_12 1 σ	Bio13	d_13 1 σ	Bio14	d_14 1 σ	Bio15	d_15 1 σ	Bio16	d_16 1 σ	Bio17	d_17 1 σ	Bio18	d_18 1 σ	B_19	dBio19 1 σ
Nam Co, Tibetan Plateau, China (Strobl et al., 2012)																
WTS10301	273.75	7.44	78.50	1.35	1.00	0	120.00	0	201.00	3.16	3.30	0.48	197.00	6.75	3.30	0.48
WTS10302	280.00	11.55	79.50	1.73	1.00	0	120.00	0	205.00	5.77	3.50	0.58	202.50	9.57	3.50	0.58
WTS10303	280.91	11.36	79.09	1.58	1.00	0	120.00	0	200.91	5.39	4.00	0	198.18	7.51	4.00	0
WTS10304	287.50	9.57	80.75	2.06	1.00	0	120.00	0	205.00	5.77	4.00	0	205.00	5.77	4.00	0
WTS10305	276.67	5.77	78.67	1.53	1.00	0	120.00	0	200.00	0	4.00	0	196.67	5.77	4.00	0
WTS10306	300.00	0	84.00	0	1.00	0	120.00	0	220.00	0	3.00	0	220.00	0	3.00	0
WTS10307	303.33	5.77	86.00	1.41	1.00	0	125.00	7.07	225.00	7.07	3.00	0	225.00	7.07	3.00	0
WTS10308	296.67	5.77	83.67	0.58	1.00	0	120.00	0	216.67	5.77	3.00	0	216.67	5.77	3.00	0
WTS10309	271.67	4.08	78.29	1.38	1.00	0	121.43	3.78	200.00	5.77	4.00	0	194.29	5.35	4.00	0
WTS10310	271.43	3.78	77.78	0.97	1.00	0	120.00	0	200.00	0	3.22	0.44	194.44	5.27	3.22	0.44
WTS10311	272.86	4.88	78.18	0.98	1.00	0	120.00	0	200.00	0	3.55	0.52	196.36	5.05	3.55	0.52
WTS10312	300.00	7.07	84.00	2.16	1.00	0	122.50	5.00	217.50	9.57	3.00	0	217.50	9.57	3.00	0
WTS10313	298.89	7.82	84.13	2.10	1.00	0	125.00	5.35	217.50	8.86	3.00	0	217.50	8.86	3.00	0
WTS10314	307.14	7.56	85.38	1.69	1.00	0	120.00	0	223.75	5.18	3.00	0	223.75	5.18	4.00	0
Ladakh Batholith, Transhimalaya, India (Dortch et al., 2011c)																
WTS10701	97.33	6.65	20.71	2.06	3.00	0	56.00	10.20	43.71	1.70	13.29	0.49	39.71	2.75	17.86	3.98
WTS10702	80.50	2.93	17.86	1.25	2.45	0.51	55.68	4.37	35.82	2.20	11.48	0.51	33.73	2.25	13.95	0.79
WTS10703	80.12	3.69	17.28	1.28	2.38	0.49	53.79	4.48	35.05	2.44	11.45	0.50	32.95	2.46	14.15	1.06
WTS10704	86.63	12.56	15.63	1.21	2.42	0.51	45.89	5.95	35.63	3.24	12.53	1.22	31.37	1.46	18.53	5.88
WTS10705	91.24	2.98	21.43	1.62	2.61	0.50	61.87	4.61	43.26	1.89	12.35	0.83	40.96	2.57	15.22	1.54
WTS10706	87.64	2.74	19.56	0.89	2.44	0.51	55.94	1.84	40.50	1.10	11.94	0.93	37.75	1.24	15.88	1.96
WTS10707	81.58	5.02	17.35	1.55	2.32	0.47	53.97	5.51	35.87	2.63	11.42	0.53	33.69	2.65	14.60	2.36
WTS10708	92.33	1.97	21.75	1.28	2.88	0.35	62.00	3.82	43.50	1.51	12.88	0.35	41.13	1.81	15.25	0.71
WTS10709	89.78	3.47	20.27	1.77	2.50	0.50	58.21	5.30	41.84	1.97	12.09	0.92	38.98	2.81	16.09	2.42
WTS10710	86.75	1.96	19.86	0.69	2.57	0.53	56.29	1.80	40.14	1.07	12.14	0.90	38.00	1.00	15.00	1.00
WTS10711	91.44	5.36	19.00	1.31	3.00	0	51.00	5.95	40.75	1.39	13.13	0.64	37.00	1.51	18.00	3.66
WTS10712	107.37	13.57	19.94	2.24	3.24	0.44	50.00	10.25	44.64	1.97	14.06	1.12	38.88	3.33	22.73	6.90
WTS10713	81.25	6.34	16.17	1.11	2.33	0.49	48.83	5.13	34.58	2.11	12.00	0.95	31.50	1.38	15.83	2.66
WTS10714	78.60	2.19	16.80	1.30	2.40	0.55	52.20	4.49	34.40	1.82	11.60	0.55	31.60	1.52	14.40	0.89
Ladakh Batholith, Transhimalaya, India (Dietsch et al.)																
WTS10801	125.00	10.00	18.00	0	3.75	0.50	41.00	2.45	45.25	0.50	15.25	1.26	36.00	0	31.50	3.70
WTS10802	120.00	0	18.00	0	4.00	0	39.00	0	45.00	0	15.00	0	36.00	0	30.00	0
WTS10803	110.00	0	18.00	0	3.00	0	40.00	0	43.00	0	14.00	0	37.00	0	25.00	0
WTS10804	101.50	5.97	17.00	0.82	3.00	0	44.25	1.71	42.00	0.82	12.75	0.96	35.00	0.82	25.00	4.55
WTS10805	96.00	0	18.00	0	3.00	0	44.00	0	41.00	0	14.00	0	36.00	0	20.00	0
WTS10806	87.00	0	19.00	0	3.00	0	53.00	0	39.00	0	13.00	0	37.00	0	15.00	0

Continued on next page

ID	Bio12	d_12	Bio13	d_13	Bio14	d_14	Bio15	d_15	Bio16	d_16	Bio17	d_17	Bio18	d_18	B_19	dBio19
		1 σ		1 σ		1 σ		1 σ		1 σ		1 σ		1 σ		1 σ
WTS10807	110.00	0	15.00	0	3.00	0	39.00	0	40.00	0	14.00	0	33.00	0	30.00	0
WTS10808	110.00	0	15.00	0	3.00	0	39.00	0	40.00	0	14.00	0	33.00	0	30.00	0
WTS10809	95.00	3.46	17.00	0	3.00	0	43.50	2.12	40.00	1.41	14.00	0	35.00	1.41	21.00	1.41
WTS10810	128.33	11.69	17.50	0.58	3.50	0.58	41.50	1.91	45.50	2.52	15.00	1.41	35.75	0.96	32.50	6.45
WTS10811	110.00	0	18.00	0	3.00	0	40.00	0	43.00	0	14.00	0	37.00	0	25.00	0
WTS10812	110.00	0	18.00	0	3.00	0	40.00	0	43.00	0	14.00	0	37.00	0	25.00	0
Zoulang Nan Shan, NE Tibetan Plateau, China (Hetzel, 2013)																
WTS11901	328.33	41.96	80.00	12.31	1.00	0	104.44	5.27	212.22	29.91	4.89	1.05	212.22	29.91	4.89	1.05
WTS11902	346.67	26.98	88.00	7.03	0.97	0.17	106.86	4.71	228.86	17.28	5.17	0.98	228.86	17.28	5.43	0.88
WTS11903	342.00	41.47	86.00	10.37	1.00	0	110.00	0	224.00	25.10	4.80	1.10	224.00	25.10	5.20	0.84
WTS11904	335.45	38.82	84.36	9.89	1.00	0	108.18	4.05	220.91	24.68	4.73	1.01	220.91	24.68	5.09	0.83
WTS11905	340.36	33.15	86.17	9.15	0.98	0.13	106.15	4.89	225.73	22.56	5.06	0.99	225.73	22.56	5.28	0.90
WTS11906	353.33	28.87	88.67	7.51	1.00	0	110.00	0	230.00	17.32	5.33	1.15	230.00	17.32	5.33	1.15
WTS11907	352.00	8.37	89.20	2.05	1.00	0	102.00	4.47	234.00	5.48	5.20	0.84	234.00	5.48	5.80	0.45
WTS11908	360.00	0	91.00	0	1.00	0	100.00	0	240.00	0	6.00	0	240.00	0	6.00	0
WTS11910	348.00	26.83	88.40	5.98	0.80	0.45	110.00	0	230.00	14.14	4.80	1.30	230.00	14.14	5.20	1.30
Anyemaquen Shan, E Tibet, China (Kirby and Harkins, 2013)																
WTS12401	485.00	7.07	100.00	0	2.00	0	92.00	1.41	280.00	0	9.00	0	280.00	0	9.00	0
WTS12402	530.00	0	110.00	0	2.00	0	91.00	0	300.00	0	9.00	0	300.00	0	9.00	0
WTS12403	520.00	0	110.00	0	2.00	0	92.00	0	290.00	0	9.00	0	290.00	0	9.00	0
WTS12404	520.00	0	110.00	0	2.00	0	92.00	0	290.00	0	9.00	0	290.00	0	9.00	0
WTS12405	457.50	5.00	97.67	1.15	2.00	0	92.00	1.00	270.00	0	10.00	0	270.00	0	10.00	0
WTS12406	532.50	9.57	110.00	0	2.00	0	92.50	0.58	305.00	5.77	10.50	0.58	305.00	5.77	10.50	0.58
WTS12407	667.50	9.57	132.50	5.00	3.00	0	88.75	0.50	365.00	5.77	15.00	0	365.00	5.77	15.00	0
WTS12408	583.13	4.79	120.00	0	2.00	0	91.00	0.78	330.00	0	10.14	0.36	330.00	0	10.14	0.36
WTS12409	657.69	8.32	135.00	5.27	3.00	0	89.60	0.52	367.00	6.75	14.50	0.53	367.00	6.75	14.50	0.53
WTS12410	663.75	7.11	137.20	4.58	3.00	0	89.46	0.66	370.40	7.35	14.84	0.37	370.40	7.35	14.84	0.37
WTS12411	480.00	0	103.33	5.77	3.00	0	92.33	0.58	283.33	5.77	12.00	0	283.33	5.77	12.00	0
WTS12412	497.50	9.57	105.00	5.77	3.00	0	92.00	0	287.50	9.57	11.75	0.50	287.50	9.57	11.75	0.50
WTS12413	516.25	17.68	106.67	5.16	2.00	0	91.80	0.45	293.33	13.66	9.50	1.22	293.33	13.66	9.50	1.22
Himalaya, Nepal (Wobus et al., 2005)																
WTS12501	1900.00	0	470.00	0	7.00	1.41	110.00	0	1300.00	0	28.00	4.24	1300.00	0	35.00	5.66
WTS12502	1700.00	395.81	432.31	82.28	6.62	3.45	107.69	4.39	1143.08	229.32	29.38	11.09	1012.31	61.39	38.08	13.34
WTS12503	2290.00	144.91	566.00	44.77	11.80	0.92	105.00	5.27	1510.00	137.03	47.50	4.03	1130.00	48.30	61.80	6.94
WTS12504	2425.00	150.00	607.50	45.00	12.75	0.50	107.50	5.00	1625.00	150.00	51.50	1.00	1175.00	50.00	68.75	2.50
WTS12505	2100.00	0	510.00	11.55	11.50	0.58	105.00	5.77	1350.00	57.74	47.00	2.31	1000.00	0	59.50	4.04
WTS12506	2200.00	129.10	558.57	39.76	11.43	0.53	102.86	4.88	1457.14	78.68	49.86	0.90	1142.86	53.45	65.43	1.13
WTS12507	2091.67	131.14	524.17	46.80	11.17	0.39	101.67	3.89	1383.33	111.46	50.08	1.31	1066.67	77.85	63.58	1.24
WTS12508	2120.00	113.53	522.50	38.45	11.38	0.52	102.50	4.63	1362.50	118.77	49.13	1.73	1075.00	70.71	61.63	1.51
Marsyandi Basin, Himalaya, Nepal (Godard et al., 2012)																

Continued on next page

ID	Bio12	d_12 1 σ	Bio13	d_13 1 σ	Bio14	d_14 1 σ	Bio15	d_15 1 σ	Bio16	d_16 1 σ	Bio17	d_17 1 σ	Bio18	d_18 1 σ	B_19	dBio19 1 σ
WTS12601	1817.65	622.08	453.67	157.78	8.33	3.69	102.48	6.98	1181.98	416.17	39.50	12.14	1004.79	321.31	51.69	14.71
WTS12603	2500.00	111.80	626.00	28.98	9.13	0.74	104.67	5.16	1640.00	91.03	40.73	2.71	1360.00	135.22	53.67	4.12
WTS12605	1885.59	685.80	475.36	178.31	7.64	3.20	101.79	6.84	1241.07	471.15	36.32	10.03	1104.64	392.72	47.82	12.39
WTS12606	2677.78	44.10	664.44	17.40	9.56	1.13	102.22	4.41	1755.56	72.65	42.11	1.96	1666.67	165.83	56.56	3.17
WTS12608	847.25	592.51	209.03	162.05	3.83	1.04	95.03	9.45	532.57	425.39	31.09	4.64	524.57	430.79	43.80	7.11
WTS12610	404.46	14.33	96.70	4.18	3.11	0.31	85.55	5.34	232.82	8.94	37.24	1.89	215.84	8.71	57.59	5.53
WTS12612	452.39	22.56	103.60	10.83	3.82	0.38	80.38	5.47	252.09	20.63	42.49	2.09	232.75	19.78	67.46	4.79
WTS12613	456.10	22.59	104.26	10.72	3.85	0.36	79.97	5.38	253.24	20.26	43.00	2.02	233.68	19.62	68.96	4.46
WTS12615	1525.24	934.83	385.19	243.05	5.05	1.24	99.38	12.88	995.71	642.82	31.95	4.88	992.38	646.87	44.00	9.09
WTS12620	410.82	77.94	99.19	21.28	3.12	0.33	86.49	5.80	239.82	53.64	35.44	2.07	224.74	56.48	52.26	4.08
WTS12623	426.33	62.56	104.87	18.01	3.22	0.42	87.26	4.71	253.91	44.39	35.30	2.62	240.43	49.03	50.91	3.78
WTS12625	1817.65	622.08	453.67	157.78	8.33	3.69	102.48	6.98	1181.98	416.17	39.50	12.14	1004.79	321.31	51.69	14.71
WTS12626	1359.48	899.69	298.60	219.97	4.75	2.29	97.77	8.74	770.63	576.79	32.15	6.32	747.08	563.17	44.27	8.41
Zanskar & Ladakh, Transhimalaya, India (Munack et al., 2014)																
WTS12701	100.54	48.16	17.91	11.85	2.64	0.92	44.55	8.99	44.18	26.71	14.00	4.92	22.82	3.40	29.64	21.50
WTS12702	111.00	28.38	15.71	5.50	3.29	0.49	38.00	5.23	42.14	14.25	15.29	3.04	28.43	1.81	30.71	13.24
WTS12703	141.76	7.28	32.41	3.50	4.06	0.24	62.59	9.68	68.65	5.48	18.41	0.80	62.94	6.50	24.59	4.65
WTS12704	156.25	5.18	31.00	4.54	4.38	0.52	52.13	8.85	68.75	7.48	20.50	0.76	61.00	8.55	31.63	4.66
WTS12705	79.89	32.50	14.14	6.96	2.59	0.80	41.86	5.58	33.00	17.16	12.05	3.57	23.19	2.64	20.09	14.81
WTS12706	98.40	25.39	13.17	2.98	3.08	0.29	34.67	3.45	33.00	8.32	14.58	1.44	24.58	3.53	22.83	8.41
WTS12707	79.73	24.26	12.69	5.60	2.28	0.53	41.17	4.64	32.34	12.27	11.76	2.43	22.34	2.00	19.24	11.13
WTS12708	94.50	8.26	16.20	1.10	2.60	0.55	45.60	7.02	37.40	2.61	13.00	1.00	33.00	1.22	19.20	4.44
WTS12709	110.53	15.71	21.18	2.70	3.24	0.44	50.41	10.28	47.29	3.41	14.94	1.64	40.88	4.68	23.88	8.34
WTS12710	135.26	5.13	31.06	2.62	3.89	0.32	62.44	6.88	65.00	4.41	17.61	0.78	59.94	5.01	22.72	2.72
WTS12711	111.00	33.93	15.67	5.09	3.33	0.52	37.67	4.46	40.17	13.99	15.33	2.94	27.00	3.16	28.33	13.69
WTS12712	127.29	45.16	20.57	10.52	2.86	0.90	46.86	6.91	50.43	24.24	16.14	4.26	25.71	4.07	35.86	19.36
WTS12713	120.97	8.70	26.22	3.23	3.22	0.42	58.00	8.68	55.00	4.68	15.78	1.13	50.17	5.73	21.30	3.83
WTS12714	123.33	12.78	19.65	1.79	3.75	0.44	41.80	4.53	46.85	2.35	16.70	0.92	38.85	2.50	28.30	6.97
WTS12715	111.07	10.28	19.15	1.95	3.23	0.44	44.38	4.23	43.69	2.29	15.31	0.63	37.69	2.66	23.31	4.23
WTS12716	97.22	7.74	19.60	1.58	3.00	0	51.40	9.30	42.90	0.57	13.40	0.52	38.50	1.65	19.40	4.60
WTS12717	183.08	17.15	37.59	7.18	4.91	0.29	57.45	9.55	83.50	14.60	22.73	1.49	74.41	14.44	34.05	3.02
WTS12718	98.64	15.81	16.45	1.86	2.82	0.60	46.73	8.28	38.45	4.84	13.18	1.66	32.73	1.19	21.82	9.27
WTS12719	101.79	16.35	16.36	1.95	2.93	0.62	45.07	7.99	39.57	5.57	13.57	1.79	32.71	1.20	24.21	10.00
WTS12720	148.18	6.03	33.82	4.90	4.09	0.30	63.82	11.59	72.00	7.87	18.36	0.92	66.09	9.27	25.64	5.01
WTS12721	90.58	35.01	15.05	5.38	2.68	0.72	42.18	4.07	36.27	14.74	12.91	3.44	25.45	3.10	23.32	14.49
WTS12722	148.57	8.64	32.15	5.76	4.15	0.38	61.15	14.04	69.38	8.94	18.77	1.69	62.85	10.80	27.46	7.43
WTS12723	93.19	8.90	17.43	1.22	2.93	0.27	49.64	8.17	38.93	1.98	12.86	1.03	34.50	1.09	19.21	5.22
WTS12724	88.13	22.02	14.82	1.83	2.73	0.47	42.18	4.47	34.18	6.48	12.55	1.69	28.27	1.90	19.36	8.82
WTS12725	161.00	9.94	33.33	5.83	4.67	0.50	54.56	9.63	73.22	10.35	21.00	1.12	65.44	11.46	30.78	4.29
WTS12726	100.40	37.02	13.87	6.21	2.60	0.63	41.20	4.87	34.33	14.85	12.73	3.47	22.87	3.04	22.27	13.43
WTS12727	92.30	4.45	20.25	1.28	3.00	0	56.13	5.36	41.88	1.13	13.13	0.35	38.88	1.46	16.38	2.45

Continued on next page

ID	Bio12	d_12	Bio13	d_13	Bio14	d_14	Bio15	d_15	Bio16	d_16	Bio17	d_17	Bio18	d_18	B_19	dBio19
		1 σ		1 σ		1 σ		1 σ		1 σ		1 σ		1 σ		1 σ
WTS12728	101.07	7.71	18.63	2.07	3.13	0.35	44.13	4.16	42.25	3.01	15.00	0.93	36.75	3.24	22.00	3.21
WTS12729	103.11	8.66	18.09	1.97	3.09	0.30	43.36	3.75	42.55	2.66	14.73	0.90	36.55	2.77	23.55	4.03
WTS12730	133.33	10.33	23.50	3.83	4.17	0.41	45.83	9.37	53.17	4.88	18.00	1.10	46.17	6.31	28.50	6.69
WTS12731	89.75	8.19	16.83	0.75	2.67	0.52	47.67	6.47	37.67	2.73	13.00	1.10	33.50	1.64	18.17	3.60
WTS12732	141.79	5.48	27.33	2.46	4.05	0.22	48.86	4.78	60.33	3.98	19.14	0.65	53.24	4.50	28.57	2.38
WTS12733	99.21	7.69	16.92	1.98	3.00	0	42.15	4.85	39.92	1.98	14.54	0.52	34.08	2.33	23.08	4.97
Zanskar & Ladakh, Transhimalaya, India this study																
WTS13201	89.90	3.58	20.19	1.85	2.51	0.50	57.91	5.73	41.77	2.02	12.09	0.91	38.86	2.94	16.23	2.62
WTS13202	77.82	11.73	13.50	1.77	2.00	0	45.50	4.81	32.38	4.31	10.88	1.13	25.63	2.83	18.38	8.14
WTS13203	134.83	22.00	17.83	3.66	3.83	0.41	37.83	3.06	49.17	9.20	17.83	1.72	32.50	2.51	38.83	8.75
WTS13204	81.78	5.27	17.29	1.63	2.32	0.47	53.70	5.87	35.84	2.62	11.43	0.53	33.62	2.69	14.78	2.75
WTS13205	86.35	6.37	18.07	1.83	2.27	0.46	55.40	6.32	38.33	1.88	11.27	0.70	35.53	3.02	15.87	4.39
WTS13206	84.60	1.84	19.31	0.48	2.38	0.51	57.46	3.28	39.15	0.80	11.77	0.73	37.08	0.95	14.38	0.87
WTS13207	83.82	2.93	18.71	0.61	2.36	0.50	57.57	3.37	38.21	1.48	11.57	0.51	35.93	1.44	14.50	1.02
WTS13209	75.95	4.96	15.69	1.45	2.38	0.49	49.50	4.48	32.88	2.04	11.13	0.66	30.50	2.18	14.06	2.35
WTS13210	101.63	25.05	14.11	2.94	3.21	0.42	36.21	3.22	36.95	9.28	15.11	1.79	27.42	4.36	26.63	9.53
Himalaya, Nepal (Andermann, 2011)																
WTS13307	581.56	280.20	154.70	85.17	2.35	0.49	102.17	6.14	386.96	221.84	22.87	3.99	377.83	227.52	33.96	5.21
WTS13308	997.50	340.79	296.67	94.59	2.50	0.55	110.00	8.94	758.33	265.21	17.50	3.45	758.33	265.21	26.50	6.53
WTS13309	595.00	162.66	155.00	38.34	2.67	0.52	105.00	5.48	385.00	100.35	21.83	0.75	380.00	105.26	33.00	0.89
WTS13310	595.00	162.66	155.00	38.34	2.67	0.52	105.00	5.48	385.00	100.35	21.83	0.75	380.00	105.26	33.00	0.89
WTS13312	1766.10	442.13	487.54	133.63	5.47	3.04	115.38	5.33	1246.92	334.50	26.51	7.47	1207.38	352.96	34.80	9.49
WTS13314	2290.00	144.91	566.00	44.77	11.80	0.92	105.00	5.27	1510.00	137.03	47.50	4.03	1130.00	48.30	61.80	6.94
WTS13316	1927.27	78.62	491.11	26.67	9.44	2.07	111.11	3.33	1266.67	70.71	37.89	7.62	1042.22	197.47	47.78	10.59
WTS13318	1575.00	445.60	395.56	128.16	5.00	3.36	112.78	5.75	1016.67	337.83	25.56	9.34	977.22	329.02	34.44	11.79
WTS13319	864.44	316.39	232.22	92.44	2.67	0.50	108.89	7.82	584.44	234.10	21.00	2.18	581.11	237.93	31.56	3.84
WTS13323	1507.69	213.94	389.23	55.15	7.23	0.60	102.46	5.35	970.00	173.21	34.54	1.33	958.46	191.00	45.00	1.00
WTS13324	1966.67	100.00	534.44	27.89	7.44	3.13	111.11	3.33	1333.33	70.71	33.78	5.21	1333.33	70.71	39.56	6.86
Bayan Har this study																
WTS13401n	380.43	17.96	85.78	4.18	2.00	0	94.65	0.98	232.17	12.04	8.78	0.60	232.17	12.04	8.83	0.58
WTS13403n	422.83	6.01	95.72	1.15	2.92	0.27	96.66	0.96	259.25	3.85	9.92	0.27	259.25	3.85	10.92	0.27
WTS13405n	386.67	10.33	86.00	2.37	2.00	0	93.33	1.21	233.33	8.16	9.00	0	233.33	8.16	9.00	0
WTS13406n	382.31	8.32	85.00	1.87	2.00	0	93.23	1.09	230.77	4.94	9.00	0	230.77	4.94	9.00	0
WTS13407n	403.45	12.61	89.97	2.82	3.00	0	94.90	1.11	243.79	7.75	11.00	0	243.79	7.75	12.00	0
WTS13408n	477.92	11.41	103.08	5.04	3.00	0	92.38	0.71	281.25	7.97	12.00	0	281.25	7.97	12.00	0
WTS13409n	508.55	12.52	109.84	1.27	3.00	0	92.31	0.86	296.94	6.67	12.61	0.49	296.94	6.67	12.61	0.49
WTS13410n	473.75	5.18	106.25	5.18	2.00	0	96.63	0.52	286.25	5.18	10.00	0	286.25	5.18	10.63	0.52
WTS13411n	475.00	7.07	110.00	0	2.00	0	97.50	0.71	290.00	0	10.00	0	290.00	0	10.50	0.71
WTS13412n	474.00	5.48	110.00	0	2.00	0	97.20	0.45	290.00	0	10.00	0	290.00	0	10.40	0.55
WTS13413n	477.00	4.70	110.00	0	2.00	0	97.30	0.66	290.00	0	10.00	0	290.00	0	10.55	0.51

Continued on next page

ID	Bio12	d_12 1 σ	Bio13	d_13 1 σ	Bio14	d_14 1 σ	Bio15	d_15 1 σ	Bio16	d_16 1 σ	Bio17	d_17 1 σ	Bio18	d_18 1 σ	B_19	dBio19 1 σ
WTS13414n	422.22	4.22	94.89	1.06	3.00	0	95.14	0.80	256.11	4.94	11.00	0	256.11	4.94	11.97	0.17
WTS13415n	344.00	5.48	78.00	1.00	3.00	0	93.80	0.84	210.00	0	10.00	0	210.00	0	12.00	0
WTS13417n	364.29	8.52	85.21	1.72	3.00	0	98.00	0.96	225.00	5.19	9.00	0	225.00	5.19	10.00	0
WTS13418n	397.20	7.37	93.52	1.29	3.00	0	98.52	1.08	245.20	5.10	9.12	0.33	245.20	5.10	10.00	0.50
WTS13419n	435.88	5.07	98.29	0.77	2.82	0.39	96.88	0.86	266.47	4.93	9.82	0.39	266.47	4.93	10.82	0.39
WTS13420n	441.67	3.89	99.17	0.72	2.92	0.29	96.75	0.87	270.00	0	10.17	0.58	270.00	0	11.00	0.43
Kunlun Shan and Central Tibet, China (Li et al., 2014)																
WTS13501n	204.71	5.14	61.29	0.47	1.00	0	120.00	0	150.00	0	4.25	0.45	150.00	0	5.24	0.44
WTS13502n	229.71	1.71	68.18	0.76	1.00	0	120.00	0	167.35	4.48	3.97	0.17	167.35	4.48	4.97	0.17
WTS13503n	267.50	15.00	68.75	3.95	1.75	0.50	105.00	5.77	172.50	9.57	5.75	0.50	172.50	9.57	6.25	0.96
WTS13506n	168.29	48.96	41.45	12.23	1.19	0.65	98.68	2.24	108.55	30.98	3.74	1.95	108.55	30.98	3.81	2.04
WTS13508n	172.61	29.88	44.22	7.61	1.00	0	103.83	5.08	114.70	19.79	3.39	0.50	114.70	19.79	3.39	0.50
WTS13510n	219.29	27.35	57.19	7.15	1.10	0.30	106.43	4.85	146.43	17.92	3.48	0.94	146.43	17.92	4.00	0.96
WTS13512n	272.65	9.51	78.61	2.28	0.84	0.37	114.70	5.02	191.45	5.87	2.91	0.48	191.45	5.87	4.07	0.26
WTS13513n	292.17	6.71	83.17	0.65	0.96	0.21	111.74	3.88	201.30	3.44	3.65	0.65	201.30	3.44	4.70	0.56
WTS13516n	350.20	7.95	94.38	1.46	2.00	0	111.00	3.03	241.00	5.05	6.00	0	241.00	5.05	6.00	0
Namche Barwa-Gyala Peri Massif, Tibet, China (Finnegan et al., 2008)																
WTS33002	710.00	136.38	152.50	26.30	3.25	0.50	91.25	0.50	420.00	82.87	14.00	1.41	420.00	82.87	15.00	2.45
WTS33003	594.29	59.96	130.00	12.25	2.60	0.55	92.20	0.45	360.00	37.42	12.20	1.10	360.00	37.42	12.40	1.34
WTS33004	674.29	163.79	144.29	32.07	2.57	0.53	93.29	0.76	402.86	94.47	12.43	1.81	402.86	94.47	13.43	3.21
WTS33007	647.14	134.75	137.14	25.63	2.57	0.53	93.00	0.82	385.71	77.00	12.29	1.60	385.71	77.00	13.00	2.65
WTS33008	529.06	54.00	114.55	8.63	2.00	0	93.45	1.46	311.52	28.13	9.30	0.84	311.52	28.13	9.30	0.84
WTS33010	690.00	160.93	146.67	30.55	2.67	0.58	92.67	1.15	406.67	92.92	13.00	2.00	406.67	92.92	14.00	3.61
WTS33013	675.00	135.03	145.00	26.46	2.75	0.50	91.75	0.50	400.00	77.03	13.00	1.63	400.00	77.03	13.75	2.50
E Tibet, China (Ouimet et al., 2009)																
WTS37001	886.67	11.18	184.29	5.35	4.00	0	93.14	0.69	521.43	12.15	16.71	0.49	521.43	12.15	16.71	0.49
WTS37002	893.33	25.82	188.00	13.04	3.80	0.45	94.80	1.30	532.00	29.50	15.40	1.14	532.00	29.50	15.40	1.14
WTS37003	875.33	42.74	203.75	18.47	3.25	0.89	99.25	1.16	541.25	36.43	13.13	2.70	541.25	36.43	13.13	2.70
WTS37004	1022.94	52.17	187.65	4.37	7.24	0.56	78.12	0.49	517.06	16.11	28.88	1.69	516.47	16.56	28.88	1.69
WTS37005	906.47	40.92	220.00	13.48	3.92	0.90	99.92	0.29	578.33	28.23	15.08	2.47	578.33	28.23	15.08	2.47
WTS37006	982.00	72.94	190.00	7.07	5.80	0.84	84.00	1.00	526.00	29.66	22.00	2.74	526.00	29.66	22.00	2.74
WTS37007	930.00	24.49	183.33	5.77	5.00	1.00	84.00	2.65	500.00	10.00	20.33	3.06	496.67	11.55	20.33	3.06
WTS37008	966.67	74.39	187.50	26.33	5.83	0.58	84.42	4.64	526.67	70.50	23.58	1.51	526.67	70.50	23.58	1.51
WTS37009	894.29	53.18	170.00	18.71	5.60	0.55	82.60	3.71	482.00	54.04	22.40	0.89	482.00	54.04	22.40	0.89
WTS37010	936.67	36.74	175.00	5.48	5.83	0.75	78.83	1.72	471.67	14.72	24.50	2.51	471.67	14.72	24.50	2.51
WTS37011	922.50	43.49	167.50	9.57	5.75	0.96	81.25	0.96	482.50	29.86	24.00	2.45	482.50	29.86	24.00	2.45
WTS37012	744.00	26.08	144.00	5.48	3.60	0.55	88.00	0.71	400.00	21.21	15.60	1.52	400.00	21.21	15.60	1.52
WTS37013	720.00	18.03	148.57	6.90	4.00	0	92.86	0.38	411.43	13.45	15.57	0.79	411.43	13.45	16.14	0.90
WTS37014	722.86	15.90	148.18	6.03	4.00	0	91.36	0.67	409.09	13.75	16.55	0.69	409.09	13.75	16.82	0.60
WTS37015	713.75	12.12	145.48	5.06	4.00	0	92.74	0.73	409.68	10.48	14.87	0.34	409.68	10.48	15.06	0.25

Continued on next page

ID	Bio12	d_12	Bio13	d_13	Bio14	d_14	Bio15	d_15	Bio16	d_16	Bio17	d_17	Bio18	d_18	B_19	dBio19
		1 σ		1 σ		1 σ		1 σ		1 σ		1 σ		1 σ		1 σ
WTS37016	721.67	24.83	147.50	9.57	4.00	0	92.25	0.50	415.00	19.15	15.50	1.00	415.00	19.15	15.75	0.96
WTS37017	716.67	20.82	143.33	5.77	4.00	0	91.00	1.00	403.33	15.28	15.33	0.58	403.33	15.28	15.33	0.58
WTS37018	741.67	39.71	148.33	7.53	3.83	0.75	90.00	0.89	411.67	29.27	16.00	2.00	411.67	29.27	16.00	2.00
WTS37019	760.00	37.95	153.33	8.16	3.67	0.82	86.67	0.52	401.67	37.64	15.17	2.99	401.67	37.64	15.17	2.99
WTS37020	697.50	23.63	142.50	5.00	3.00	0	85.25	0.50	352.50	18.93	12.25	0.50	352.50	18.93	12.25	0.50
WTS37021	760.00	62.72	155.00	12.91	4.00	0.82	88.00	1.63	415.00	50.00	15.25	2.87	415.00	50.00	15.25	2.87
WTS37022	819.00	83.99	158.89	12.69	4.22	0.83	83.00	1.50	420.00	60.21	17.78	2.22	420.00	60.21	17.78	2.22
WTS37023	870.00	23.57	179.00	8.76	4.30	0.48	92.20	1.03	506.00	16.47	17.50	1.18	506.00	16.47	17.50	1.18
WTS37024	811.25	63.79	170.00	12.65	4.33	0.52	89.17	1.72	466.67	51.64	17.33	1.97	466.67	51.64	17.33	1.97
WTS37025	810.91	77.39	163.75	15.98	4.38	0.92	84.88	2.85	436.25	68.65	18.00	2.27	436.25	68.65	18.00	2.27
WTS37026	853.33	56.10	161.67	11.69	5.17	0.41	82.17	3.13	445.00	50.10	20.67	0.82	445.00	50.10	20.67	0.82
WTS37027	926.67	49.33	176.67	5.77	6.00	0	83.67	2.31	496.67	40.41	23.00	0	496.67	40.41	23.00	0
WTS37028	957.50	113.25	182.50	29.86	5.75	0.50	84.75	5.06	515.00	88.13	23.00	0.82	515.00	88.13	23.00	0.82
WTS37029	738.33	37.86	165.45	14.40	2.09	0.30	98.73	1.68	454.55	38.57	9.91	0.83	454.55	38.57	9.91	0.83
WTS37030	847.86	31.67	188.75	11.26	3.38	0.52	98.38	0.92	521.25	26.42	14.00	1.07	521.25	26.42	14.00	1.07
WTS37031	916.67	40.62	193.75	10.61	4.50	0.53	93.25	0.71	547.50	27.65	17.75	1.39	547.50	27.65	17.75	1.39
WTS37032	835.00	5.48	170.00	0	4.00	0	93.20	0.84	488.00	4.47	15.20	0.45	488.00	4.47	15.20	0.45
WTS37033	1016.15	87.04	205.45	36.43	6.00	0.77	87.91	5.34	570.91	88.60	23.18	2.52	570.91	88.60	23.18	2.52
WTS37034	930.00	35.59	177.50	5.00	5.50	0.58	83.50	1.00	495.00	19.15	21.25	2.06	495.00	19.15	21.25	2.06
WTS37035	949.17	63.45	192.00	12.29	5.20	0.79	86.50	2.37	531.00	43.83	19.70	3.02	528.00	46.14	19.70	3.02
WTS37036	861.74	47.45	151.43	11.67	5.07	0.92	77.21	1.12	427.86	30.68	22.57	2.71	427.86	30.68	22.57	2.71
WTS37037	815.00	20.82	142.50	5.00	4.25	0.50	79.00	0.82	400.00	16.33	19.50	1.00	400.00	16.33	19.50	1.00
WTS37038	847.50	12.58	157.50	5.00	5.00	0	82.25	0.50	442.50	9.57	21.75	0.50	442.50	9.57	21.75	0.50
WTS37039	695.00	7.07	145.00	5.35	4.00	0	92.50	0.53	393.75	7.44	16.00	0	393.75	7.44	16.50	0.53
WTS37040	683.33	8.16	145.00	5.48	4.00	0	92.67	0.52	393.33	8.16	16.00	0	393.33	8.16	16.50	0.55
WTS37041	683.33	8.16	145.00	5.48	4.00	0	92.67	0.52	393.33	8.16	16.00	0	393.33	8.16	16.50	0.55
WTS37042	676.00	9.66	147.78	4.41	4.00	0	94.56	0.53	395.56	7.26	15.56	0.53	395.56	7.26	15.56	0.53
WTS37043	718.00	13.17	143.75	5.18	3.88	0.35	89.88	0.64	395.00	13.09	16.38	0.74	395.00	13.09	16.63	0.74
WTS37044	704.00	13.42	144.00	5.48	4.00	0	91.40	0.55	392.00	13.04	16.20	0.45	392.00	13.04	16.60	0.55
WTS37045	701.33	10.60	144.62	5.19	4.00	0	91.23	1.09	393.08	11.09	16.08	0.28	393.08	11.09	16.46	0.52
WTS37046	726.00	12.65	144.29	5.35	4.00	0	90.29	0.49	401.43	10.69	16.71	0.49	401.43	10.69	17.00	0
WTS37047	703.75	28.75	148.33	7.53	3.67	0.52	94.00	0.63	413.33	21.60	14.33	1.03	413.33	21.60	14.67	1.03
WTS37048	771.67	54.08	161.67	11.15	3.67	0.49	93.58	0.51	449.17	36.55	15.00	2.17	449.17	36.55	15.00	2.17
WTS37049	859.00	9.94	186.00	5.16	3.90	0.32	96.10	0.74	519.00	8.76	15.60	0.70	519.00	8.76	15.60	0.70
WTS37050	865.00	7.07	185.00	7.07	4.00	0	95.00	0	515.00	7.07	16.00	0	515.00	7.07	16.00	0
WTS37051	842.50	5.00	170.00	0	4.00	0	92.75	0.50	490.00	0	15.00	0	490.00	0	15.00	0
WTS37052	829.23	51.88	185.00	19.58	2.60	0.52	99.10	1.45	506.00	43.51	11.90	1.79	506.00	43.51	11.90	1.79
WTS37053	829.23	51.88	185.00	19.58	2.60	0.52	99.10	1.45	506.00	43.51	11.90	1.79	506.00	43.51	11.90	1.79
WTS37054	885.00	7.07	200.00	0	4.00	0	97.50	0.71	545.00	7.07	15.50	0.71	545.00	7.07	15.50	0.71
WTS37055	870.00	14.14	195.00	7.07	4.00	0	97.00	0	530.00	14.14	15.50	0.71	530.00	14.14	15.50	0.71
WTS37056	1066.67	57.74	220.00	28.28	6.50	0.71	91.00	4.24	610.00	70.71	23.50	2.12	610.00	70.71	23.50	2.12

Continued on next page

ID	Bio12	d_12	Bio13	d_13	Bio14	d_14	Bio15	d_15	Bio16	d_16	Bio17	d_17	Bio18	d_18	B_19	dBio19
		1 σ		1 σ		1 σ		1 σ		1 σ		1 σ		1 σ		1 σ
WTS37057	1075.00	50.00	216.67	11.55	5.33	0.58	89.00	1.00	603.33	32.15	20.67	1.15	603.33	32.15	20.67	1.15
WTS37058	1017.50	55.60	220.00	14.14	4.25	0.50	94.25	0.50	600.00	35.59	16.50	1.00	600.00	35.59	16.50	1.00
WTS37059	997.27	56.05	208.89	17.64	4.22	0.44	93.00	2.12	576.67	42.13	15.78	1.30	576.67	42.13	15.78	1.30
WTS37060	981.67	31.25	223.33	21.60	3.83	0.75	96.83	2.04	595.00	38.34	14.67	1.86	595.00	38.34	14.67	1.86
WTS37061	948.33	19.46	219.00	15.24	3.70	0.48	98.30	2.11	584.00	27.57	13.90	1.20	584.00	27.57	13.90	1.20
WTS37062	937.00	28.30	211.25	8.35	4.00	0.76	97.75	0.71	575.00	22.68	15.75	1.83	575.00	22.68	15.75	1.83
WTS37063	922.00	38.34	202.00	13.04	3.80	0.45	96.00	1.22	558.00	29.50	16.20	1.30	558.00	29.50	16.20	1.30
WTS37064	866.67	14.97	189.00	5.68	3.60	0.52	96.40	0.52	524.00	14.30	14.70	0.67	524.00	14.30	14.70	0.67
WTS37065	950.00	38.99	180.00	11.55	6.25	0.96	82.25	0.96	517.50	43.49	24.50	3.00	517.50	43.49	24.50	3.00
WTS37066	795.00	83.32	157.50	11.65	4.25	1.16	85.25	0.71	420.00	56.32	16.75	3.88	420.00	56.32	16.75	3.88
WTS37067	802.00	85.87	157.50	14.88	4.25	0.89	87.38	2.39	428.75	66.64	16.13	3.04	428.75	66.64	16.13	3.04
Yumu Shan & Longshou Shan, NE Tibet, China (Palumbo et al., 2010b)																
WTS45001	170.00	0	41.00	0	1.00	0	100.00	0	110.00	0	4.00	0	110.00	0	4.00	0
WTS45002	170.00	0	41.00	0	1.00	0	100.00	0	110.00	0	4.00	0	110.00	0	4.00	0
WTS45003	170.00	0	41.00	0	1.00	0	100.00	0	110.00	0	4.00	0	110.00	0	4.00	0
WTS45004	176.00	25.10	41.40	5.90	1.00	0	98.60	2.07	114.00	16.73	4.20	0.45	114.00	16.73	4.20	0.45
WTS45005	203.33	23.38	48.25	7.72	1.00	0	98.75	2.50	130.00	18.26	4.00	0	130.00	18.26	4.00	0
WTS45006	206.67	32.15	49.67	9.29	1.00	0	98.33	2.89	136.67	23.09	4.00	0	136.67	23.09	4.00	0
WTS45007	200.00	29.44	47.75	8.22	1.00	0	99.75	0.50	127.25	21.06	4.00	0	127.25	21.06	4.00	0
WTS45008	185.00	35.36	43.00	8.49	1.00	0	99.50	0.71	114.50	21.92	4.00	0	114.50	21.92	4.00	0
WTS45009	213.33	15.28	51.33	4.93	1.00	0	99.67	0.58	136.67	11.55	4.00	0	136.67	11.55	4.00	0
WTS45010	207.50	19.09	49.50	5.76	1.00	0	99.75	0.46	133.75	13.02	4.00	0	133.75	13.02	4.00	0
WTS45011	150.00	14.14	35.50	2.12	1.00	0	95.00	5.66	94.00	5.66	4.50	0.71	94.00	5.66	4.50	0.71
WTS45012	150.00	14.14	35.50	2.12	1.00	0	95.00	5.66	94.00	5.66	4.50	0.71	94.00	5.66	4.50	0.71
WTS45013	150.00	14.14	35.00	1.73	1.00	0	93.67	4.62	92.67	4.62	4.67	0.58	92.67	4.62	4.67	0.58
WTS45014	140.00	0	34.00	0	1.00	0	91.00	0	90.00	0	5.00	0	90.00	0	5.00	0
WTS45015	140.00	0	33.00	1.41	1.00	0	93.50	4.95	86.00	4.24	5.00	0	86.00	4.24	5.00	0
WTS45016	140.00	14.14	34.50	2.12	1.00	0	94.50	2.12	89.00	7.07	4.00	0	89.00	7.07	4.00	0
WTS45017	140.00	10.00	34.00	1.73	1.00	0	94.00	1.73	87.67	5.51	4.00	0	87.67	5.51	4.00	0
WTS45018	140.00	0	33.00	0	1.00	0	93.00	0	85.00	0	4.00	0	85.00	0	4.00	0
WTS45019	140.00	0	33.00	0	1.00	0	92.00	0	84.00	0	4.00	0	84.00	0	4.00	0
WTS45020	140.00	0	33.50	0.71	1.00	0	94.00	2.83	85.50	2.12	4.00	0	85.50	2.12	4.00	0
WTS45021	170.00	26.46	41.33	6.43	1.00	0	96.33	0.58	109.00	19.05	3.67	0.58	109.00	19.05	3.67	0.58
WTS45022	172.50	22.17	42.00	5.42	1.00	0	96.50	0.58	111.75	16.50	3.50	0.58	111.75	16.50	3.50	0.58
WTS45023	172.50	22.17	42.00	5.42	1.00	0	96.50	0.58	111.75	16.50	3.50	0.58	111.75	16.50	3.50	0.58
WTS45024	262.22	40.24	62.75	9.71	1.00	0	98.88	1.55	170.00	26.73	4.00	0	170.00	26.73	4.00	0
WTS45025	272.86	43.86	60.80	11.39	1.00	0	97.80	2.17	162.00	33.47	4.00	0	162.00	33.47	4.00	0
WTS45026	275.00	36.97	64.50	9.04	1.00	0	98.25	1.71	172.50	27.54	4.00	0	172.50	27.54	4.00	0
WTS45027	275.00	36.97	64.50	9.04	1.00	0	98.25	1.71	172.50	27.54	4.00	0	172.50	27.54	4.00	0
Qilian Shan, NE Tibet, China (Palumbo et al., 2010a)																

Continued on next page

ID	Bio12	d_12	Bio13	d_13	Bio14	d_14	Bio15	d_15	Bio16	d_16	Bio17	d_17	Bio18	d_18	B_19	dBio19
		1 σ		1 σ		1 σ		1 σ		1 σ		1 σ		1 σ		1 σ
WTS51001	185.88	24.51	50.18	6.55	1.00	0	100.36	2.56	127.79	17.07	4.97	0.17	127.79	17.07	5.97	0.17
WTS51002	232.42	33.93	60.80	8.68	1.00	0	103.14	4.69	155.49	21.94	4.96	0.20	155.49	21.94	5.96	0.20
WTS51003	241.48	30.95	63.96	8.99	1.00	0	105.46	5.07	163.04	23.66	4.88	0.32	163.04	23.66	5.88	0.32
WTS51004	263.33	5.77	70.00	1.73	1.00	0	110.00	0	180.00	0	5.00	0	180.00	0	6.00	0
WTS51005	268.00	11.35	70.70	3.06	1.00	0	107.00	4.83	181.00	8.76	5.00	0	181.00	8.76	6.00	0
WTS51006	304.03	42.71	80.91	11.25	0.64	0.49	109.27	2.62	208.55	28.89	4.20	0.99	208.55	28.89	4.89	1.29
WTS51007	252.22	33.83	66.29	9.66	0.29	0.49	107.14	4.88	174.29	25.07	3.29	0.49	174.29	25.07	3.43	0.53
WTS51008	327.16	42.84	83.74	11.64	0.71	0.46	107.94	4.07	217.50	29.24	4.57	1.23	217.50	29.24	4.97	1.25
WTS51009	308.33	40.19	79.60	11.47	1.00	0	106.00	5.16	207.00	27.10	4.40	0.70	207.00	27.10	4.90	0.88
WTS51010	340.00	26.56	87.08	9.34	1.00	0	104.17	5.15	225.83	24.29	4.83	0.94	225.83	24.29	5.33	0.78
WTS51011	305.38	38.86	76.82	11.48	1.00	0	107.18	4.83	204.55	29.79	4.36	0.81	204.55	29.79	4.55	0.82
WTS51012	333.59	36.24	84.53	10.06	0.99	0.12	105.44	5.00	222.13	24.48	4.96	0.98	222.13	24.48	5.15	0.92
WTS51015	233.33	35.12	54.33	8.50	1.00	0	97.33	2.52	146.67	25.17	4.00	0	146.67	25.17	4.00	0
WTS51016	87.00	0	20.00	0	1.00	0	87.00	0	54.00	0	3.00	0	54.00	0	3.00	0
WTS51017	130.00	0	31.00	1.41	1.00	0	95.50	2.12	83.00	2.83	3.00	0	83.00	2.83	3.00	0
Longmen Shan, E Tibet, China (Godard et al., 2010)																
WTS65006	1082.61	76.90	226.94	33.28	8.23	1.09	84.25	4.75	602.22	68.16	31.97	3.61	591.94	57.76	31.97	3.61
WTS65007	1061.76	57.64	204.44	10.35	8.13	0.94	80.04	4.02	556.00	21.04	31.20	3.40	552.00	20.74	31.20	3.40
WTS65008	1060.58	56.77	197.41	7.32	8.15	0.94	78.35	3.00	545.37	19.78	31.98	3.39	542.59	21.30	31.98	3.39
WTS65009	990.91	5.39	222.00	7.89	6.90	0.32	89.70	3.83	578.00	20.98	26.40	0.70	557.00	14.18	26.40	0.70
WTS65011	1000.00	0	230.00	0	8.00	0	87.00	0	600.00	0	30.00	0	580.00	0	30.00	0
WTS65012	983.46	52.43	196.04	13.64	6.75	0.86	81.69	5.34	520.63	25.38	26.73	3.09	512.29	20.65	26.73	3.09
Three Rivers Region, China (Henck et al., 2011)																
WTS69002	1500.00	0	290.00	0	14.00	0	77.00	0	810.00	0	56.00	0	810.00	0	76.00	0
WTS69012	569.13	4.17	126.88	4.79	2.75	0.45	97.50	0.63	343.75	5.00	10.31	1.01	343.75	5.00	10.56	0.89
WTS69018	519.32	4.52	118.25	3.85	2.13	0.33	97.80	0.72	318.25	3.85	9.10	0.59	318.25	3.85	9.68	0.80
WTS69019	523.85	7.22	119.22	2.72	2.45	0.50	97.75	0.80	317.45	4.40	10.00	0.92	317.45	4.40	10.43	0.54
WTS69029	551.94	6.01	126.15	4.96	2.96	0.20	93.23	0.71	332.69	4.52	12.54	0.71	332.69	4.52	13.58	0.58
WTS69031	553.13	4.79	126.25	5.00	3.00	0	92.81	0.98	332.50	4.47	12.44	0.51	332.50	4.47	13.50	0.52
WTS69034	533.87	13.83	121.74	4.91	2.00	0	94.48	0.85	324.35	9.45	9.17	0.83	324.35	9.45	10.65	0.65
WTS69035	654.92	38.25	151.05	9.39	5.57	0.74	88.12	5.12	382.63	23.03	22.19	3.14	382.63	23.03	23.72	3.86
WTS69038	564.52	11.21	129.00	3.05	3.00	0	93.03	0.76	340.33	8.09	13.00	0.96	340.33	8.09	14.33	0.92
WTS69039	551.00	17.29	123.00	4.83	2.60	0.52	93.40	0.70	331.00	12.87	11.80	1.03	331.00	12.87	12.90	0.88
WTS69042	566.71	16.33	129.85	3.28	3.00	0	92.58	0.72	338.79	9.85	14.02	0.71	338.79	9.85	14.82	0.43
WTS69043	560.67	2.58	130.00	0	3.00	0	92.38	0.80	335.24	5.12	14.62	0.50	335.24	5.12	15.00	0
WTS69044	563.75	5.86	130.00	0	3.00	0	91.98	0.89	335.00	5.06	14.68	0.47	335.00	5.06	15.00	0

Table head: Standard deviations are denoted following the scheme d_12 = Bio12 standard deviation etc.

Bibliography

Aalto, R. E., Dunne, T., and Guyot, J. L. (2006). Geomorphic controls on Andean denudation rates. *The Journal of Geology*, 114(1):85–99.

Abramowski, U., Bergau, A., Seebach, D., Zech, R., Glaser, B., Sosin, P., Kubik, P. W., and Zech, W. (2006). Pleistocene glaciations of Central Asia: results from ^{10}Be surface exposure ages of erratic boulders from the Pamir (Tajikistan), and the Alay-Turkestan range (Kyrgyzstan). *Quaternary Science Reviews*, 25(9-10):1080–1096.

Achenbach, H. (2010). New findings concerning the Pleistocene Glaciation of the Leh Basin, Ladakh (34 °03 N/77 °38 E). *Journal of Mountain Science*, 7(4):367–374.

Ahnert, F. (1970). Functional relationships between denudation, relief, and uplift in large, mid-latitude drainage basins. *American Journal of Science*, 268(3):243.

Ali, K. F. and de Boer, D. H. (2007). Spatial patterns and variation of suspended sediment yield in the upper Indus River basin, northern Pakistan. *Journal of Hydrology*, 334(3-4):368–387.

Ali, K. F. and de Boer, D. H. (2010). Spatially distributed erosion and sediment yield modeling in the upper Indus River basin. *Water Resources Research*, 46(8):W08504.

Altenberger, U., Prosser, G., Grande, A., Günter, C., and Langone, A. (2013). A seismogenic zone in the deep crust indicated by pseudotachylytes and ultramylonites in granulite-facies rocks of Calabria (Southern Italy). *Contributions to Mineralogy and Petrology*, 166(4):975–994.

Altenberger, U., Prosser, G., and Ruggiero, M. (2011). Garnet-bearing pseudotachylytes of Calabria – a petrological link to lower crustal hypocenters. *Geological Society, London, Special Publications*, 369:153–169.

Andermann, C. (2011). *Climate, topography and erosion in the Nepal Himalayas.* PhD thesis, Université Rennes 1, Rennes.

Anderson, R. S. and Anderson, S. P. (2010). *Geomorphology - The Mechanics and Chemistry of Landscapes.* Cambridge University Press Cambridge, Cambridge.

Andó, S., Morton, A., and Garzanti, E. (2013). Metamorphic grade of source rocks revealed by chemical fingerprints of detrital amphibole and garnet. In Scott, R., Smyth, H., Morton, A., and Richardson, N., editors, *Sediment provenance studies in hydrocarbon exploration and production.* Geological Society of London.

Augustin, L., Barbante, C., Barnes, P. R., Barnola, J. M., Bigler, M., Castellano, E., Cattani, O., Chappellaz, J., Dahl-Jensen, D., and Delmonte, B. (2004). Eight glacial cycles from an Antarctic ice core. *Nature*, 429(6992):623–628.

Balco, G., Stone, J. O., Lifton, N. A., and Dunai, T. J. (2008). A complete and easily accessible means of calculating surface exposure ages or erosion rates from ^{10}Be and ^{26}Al measurements. *Quaternary Geochronology*, 3(3):174–195.

Ballantyne, C. K. (2002). Paraglacial geomorphology. *Quaternary Science Reviews*, 21(18):1935–2017.

Barnard, P. L., Owen, L. A., Sharma, M. C., and Finkel, R. C. (2001). Natural and human-induced landsliding in the Garhwal Himalaya of northern India. *Geomorphology*, 40(1):21–35.

Barry, R. G. (2008). *Mountain Weather and Climate*. Cambridge Univ Press, 3 edition.

Barry, R. G. and Chorley, R. J. (2003). *Atmosphere, weather and climate*. Routledge, 8 edition.

Beaumont, C., Kooi, H., and Willett, S. D. (2000). Coupled tectonic-surface process models with applications to rifted margins and collisional orogens. In Summerfield, M. A., editor, *Geomorphology and Global Tectonics*, pages 29–55. John Wiley & Sons.

Bendick, R. and Bilham, R. (2001). How perfect is the Himalayan arc? *Geology*, 29(9):791.

Benn, D. and Owen, L. A. (1998). The role of the Indian summer monsoon and the mid-latitude westerlies in Himalayan glaciation: review and speculative discussion. *Journal of the Geological Society*, 155(2):353–363.

Berger, A. and Loutre, M. F. (1991). Insolation values for the climate of the last 10 million years. *Quaternary Science Reviews*.

Berthelsen, A. (1953). On the geology of the Rupshu District, NW Himalaya; a contribution to the problem of central gneisses. *Meddelelser fra Dansk Geologisk Forening*, 12:351–414.

Bierman, P. R., Reuter, J. M., Pavich, M., Gellis, A. C., Caffee, M. W., and Larsen, J. (2005). Using cosmogenic nuclides to contrast rates of erosion and sediment yield in a semi-arid, arroyo-dominated landscape, Rio Puerco Basin, New Mexico. *Earth Surface Processes and Landforms*, 30(8):935–953.

Bierman, P. R. and Steig, E. J. (1996). Estimating rates of denudation using cosmogenic isotope abundances in sediment. *Earth Surface Processes and Landforms*, 21(2):125–139.

Billi, A. (2005). Grain size distribution and thickness of breccia and gouge zones from thin (<1 m) strike-slip fault cores in limestone. *Journal of Structural Geology*, 27(10):1823–1837.

Billi, A. and Storti, F. (2004). Fractal distribution of particle size in carbonate cataclastic rocks from the core of a regional strike-slip fault zone. *Tectonophysics*, 384(1-4):115–128.

Blöthe, J. H. and Korup, O. (2013). Millennial lag times in the Himalayan sediment routing system. *Earth and Planetary Science Letters*, 382:38–46.

Blöthe, J. H., Munack, H., Korup, O., Fülling, A., Garzanti, E., Resentini, A., and Kubik, P. W. (2014). Late Quaternary valley infill and dissection in the Indus River, western Tibetan Plateau margin. *Quaternary Science Reviews*, 94(C):102–119.

Bookhagen, B. and Burbank, D. W. (2010). Toward a complete Himalayan hydrological budget: Spatiotemporal distribution of snowmelt and rainfall and their impact on river discharge. *Journal of Geophysical Research*, 115(F3):F03019.

Bookhagen, B., Thiede, R. C., and Strecker, M. R. (2005a). Abnormal monsoon years and their control on erosion and sediment flux in the high, arid northwest Himalaya. *Earth and Planetary Science Letters*, 231(1-2):131–146.

Bookhagen, B., Thiede, R. C., and Strecker, M. R. (2005b). Late Quaternary intensified monsoon phases control landscape evolution in the northwest Himalaya. *Geology*, 33(2):149.

Brardinoni, F., Slaymaker, O., and Hassan, M. A. (2003). Landslide inventory in a rugged forested watershed: a comparison between air-photo and field survey data. *Geomorphology*, 54(3-4):179–196.

Braucher, R., Bourlés, D. L., Colin, F., and Brown, E. T. (1998). Brazilian laterite dynamics using in situ-produced ^{10}Be. *Earth and Planetary Science Letters*, 163:197–205.

Brookfield, M. E. (1983). Reconnaissance Geology of the Area between Leh and the Markha Valley, Ladakh. In Gupta, V. J., editor, *Contributions to Himalayan Geology 2. Stratigraphy and structure of Kashmir and Ladakh Himalaya.*, pages 173–179. Hindustan Publishing Corporation, New Delhi.

Brown, E. T., Stallard, R. F., Larsen, M. C., Bourlès, D. L., Raisbeck, G. M., and Yiou, F. (1998). Determination of predevelopment denudation rates of an agricultural watershed (Cayaguas River, Puerto Rico) using in-situ-produced ^{10}Be in river-borne quartz. *Earth and Planetary Science Letters*, 160(3):723–728.

Brown, E. T., Stallard, R. F., Larsen, M. C., Raisbeck, G. M., and Yiou, F. (1995). Denudation rates determined from the accumulation of in situ-produced ^{10}Be in the Luquillo experimental forest, Puerto Rico. *Earth and Planetary Science Letters*, 129(1):193–202.

Brückl, E., Brückl, J., and Heuberger, H. (2001). Present structure and prefailure topography of the giant rockslide of Köfels. *Zeitschrift für Gletscherkunde und Glazialgeologie*, 37(1):49–79.

Burbank, D. W., Blythe, A., Putkonen, J., Pratt-Sitaula, B., Gabet, E. J., Oskin, M., Barros, A., and Ojha, T. (2003). Decoupling of erosion and precipitation in the Himalayas. *Nature*, 426(6967):652–655.

Burbank, D. W. and Fort, M. B. (1985). Bedrock control on glacial limits: Examples from the Ladakh and Zanskar ranges, north-western Himalaya, India. *Journal of Glaciology*, 31(108):143–149.

Burbank, D. W., Leland, J., Fielding, E., Anderson, R. S., Brozovic, N., Reid, M., and Duncan, C. (1996). Bedrock incision, rock uplift and threshold hillslopes in the northwestern Himalayas. *Nature*, 379(6565):505–510.

Cade, B. S. and Noon, B. R. (2003). A gentle introduction to quantile regression for ecologists. *Frontiers in Ecology and the Environment*, 1(8):412–420.

Cheng, H., Zhang, P. Z., Spötl, C., Edwards, R. L., Cai, Y. J., Zhang, D. Z., Sang, W. C., Tan, M., and An, Z. S. (2012). The climatic cyclicity in semiarid-arid central Asia over the past 500,000 years. *Geophysical Research Letters*, 39(1):L01705.

Chmeleff, J., von Blanckenburg, F., Kossert, K., and Jakob, D. (2010). Determination of the ^{10}Be half-life by multicollector ICP-MS and liquid scintillation counting. *Nuclear Inst. and Methods in Physics Research, B*, 268(2):192–199.

Christl, M., Vockenhuber, C., Kubik, P. W., Wacker, L., Lachner, J., Alfimov, V., and Synal, H. A. (2013). The ETH Zurich AMS facilities: Performance parameters and reference materials. *Nuclear Instruments and Methods in Physics Research Section B: Beam Interactions with Materials and Atoms*, 294:29–38.

Clift, P. D. (2002). A brief history of the Indus River. *Geological Society, London, Special Publications*, 195(1):237–258.

Clift, P. D. and Giosan, L. (2013). Sediment Fluxes and Buffering in the PostGlacial Indus Basin. *Basin Research*, 25:1–18.

Clift, P. D. and Plumb, R. A. (2008). *The Asian Monsoon - Causes, History and Effects*. Cambridge University Press Cambridge.

Clift, P. D., Shimizu, N., Layne, G. D., and Blusztajn, J. (2001). Tracing patterns of erosion and drainage in the Paleogene Himalaya through ion probe Pb isotope analysis of detrital K-feldspars in the Indus Molasse, India. *Earth and Planetary Science Letters*, 188(3):475–491.

Cockburn, H. A. P. and Summerfield, M. A. (2004). Geomorphological applications of cosmogenic isotope analysis. *Progress in Physical Geography*, 28(1):1–42.

Codilean, A. T. (2006). Calculation of the cosmogenic nuclide production topographic shielding scaling factor for large areas using DEMs. *Earth Surface Processes and Landforms*, 31(6):785–794.

Craddock, J. P., Malone, D. H., Magloughlin, J., Cook, A. L., Rieser, M. E., and Doyle, J. R. (2009). Dynamics of the emplacement of the Heart Mountain allochthon at White Mountain: Constraints from calcite twinning strains, anisotropy of magnetic susceptibility, and thermodynamic calculations. *Geological Society of America Bulletin*, 121(5-6):919–938.

Crosta, G. B., Frattini, P., and Fusi, N. (2007). Fragmentation in the Val Pola rock avalanche, Italian Alps. *Journal of Geophysical Research*, 112(F1):F01006.

Cunningham, A. (1854). *Ladák, physical, statistical, and historical; with notices of the surrounding countries*. H. Allen and Co.

Cyr, A. J., Granger, D. E., Olivetti, V., and Molin, P. (2010). Quantifying rock uplift rates using channel steepness and cosmogenic nuclide-determined erosion rates: Examples from northern and southern Italy. *Lithosphere*, 2(3):188–198.

Damm, B. (2006). Late Quaternary glacier advances in the upper catchment area of the Indus River (Ladakh and Western Tibet). *Quaternary International*, 154-155:87–99.

Davies, T. R. and Korup, O. (2007). Persistent alluvial fanhead trenching resulting from large, infrequent sediment inputs. *Earth Surface Processes and Landforms*, 32(5):725–742.

Davies, T. R. and McSaveney, M. J. (2009). The role of rock fragmentation in the motion of large landslides. *Engineering Geology*, 109(1-2):67–79.

Davies, T. R. and McSaveney, M. J. (2011). Rock-avalanche size and runout–implications for landslide dams. In Evans, S. G., Hermanns, R. L., Strom, A. L., and Scarascia-Mugnozza, G., editors, *Natural and Artificial Rockslide Dams - Lecture Notes in Earth Sciences*, pages 441–462. Springer.

Davis, L. L. and West, L. R. (1973). Observed effects of topography on ground motion. *Bulletin of the Seismological Society of America*, 63:283–298.

De Blasio, F. V. and Elverhøi, A. (2008). A model for frictional melt production beneath large rock avalanches. *Journal of Geophysical Research*, 113(F2):F02014.

de Sigoyer, J., Guillot, S., and Dick, P. (2004). Exhumation of the ultrahigh-pressure Tso Morari unit in eastern Ladakh (NW Himalaya): A case study. *Tectonics*, 23(3):TC3003.

Decelles, P. G., Quade, J., Kapp, P., Fan, M., Dettman, D. L., and Ding, L. (2007). High and dry in central Tibet during the Late Oligocene. *Earth and Planetary Science Letters*, 253(3):389–401.

Deline, P. (2009). Interactions between rock avalanches and glaciers in the Mont Blanc massif during the late Holocene. *Quaternary Science Reviews*, 28(11-12):1070–1083.

Densmore, A. L. and Hovius, N. (2000). Topographic fingerprints of bedrock landslides. *Geology*, 28(4):371.

Desilets, D., Zreda, M., and Prabu, T. (2006). Extended scaling factors for in situ cosmogenic nuclides: New measurements at low latitude. *Earth and Planetary Science Letters*, 246(3-4):265–276.

Dietrich, W. E. and Perron, J. T. (2006). The search for a topographic signature of life. *Nature*, 439(7075):411–418.

Dietsch, C., Dortch, J. M., Reynhout, S. A., Owen, L. A., and Caffee, M. W. Very slow erosion rates and landscape preservation across the southwestern Ladakh Range, India. *Earth Surface Processes and Landforms*.

Ding, L., Kapp, P., and Wan, X. (2005). Paleocene-Eocene record of ophiolite obduction and initial India-Asia collision, south central Tibet. *Tectonics*, 24(3):TC3001.

DiPietro, J. A. and Pogue, K. R. (2004). Tectonostratigraphic subdivisions of the Himalaya: A view from the west. *Tectonics*, 23(5):TC5001.

Dortch, J. M., Dietsch, C., Owen, L. A., Caffee, M. W., and Ruppert, K. (2011a). Episodic fluvial incision of rivers and rock uplift in the Himalaya and Transhimalaya. *Journal of the Geological Society*, 168(3):783–804.

Dortch, J. M., Owen, L. A., and Caffee, M. W. (2010). Quaternary glaciation in the Nubra and Shyok valley confluence, northernmost Ladakh, India. *Quaternary Research*, 74(1):132–144.

Dortch, J. M., Owen, L. A., and Caffee, M. W. (2013). Timing and climatic drivers for glaciation across semi-arid western Himalayan-Tibetan orogen. *Quaternary Science Reviews*, 78(C):188–208.

Dortch, J. M., Owen, L. A., Haneberg, W. C., Caffee, M. W., Dietsch, C., and Kamp, U. (2011b). Nature and timing of large landslides in the Himalaya and Transhimalaya of northern India. *Quaternary Science Reviews*, 28(11-12):1037–1054.

Dortch, J. M., Owen, L. A., Schoenbohm, L. M., and Caffee, M. W. (2011c). Asymmetrical erosion and morphological development of the central Ladakh Range, northern India. *Geomorphology*, 135(1-2):167–180.

Draper, N. and Smith, H. (1981). *Applied regression analysis.* Wiley Series in Probability and Mathematical Statistics. John Wiley & Sons, New York, 2nd edition.

Drew, F. (1873). Alluvial and lacustrine deposits and glacial records of the Upper-Indus Basin. *Quarterly Journal of the Geological Society*, 29(1-2):441–471.

Dunai, T. J. (2000). Scaling factors for production rates of in situ produced cosmogenic nuclides: a critical reevaluation. *Earth and Planetary Science Letters*, 176(1):157–169.

Dunai, T. J. (2001). Influence of secular variation of the geomagnetic field on production rates of in situ produced cosmogenic nuclides. *Earth and Planetary Science Letters*, 193(1):197–212.

Dunai, T. J. (2010). *Cosmogenic Nuclides: Principles, concepts and applications in the Earth surface sciences.* Cambridge University Press Cambridge.

Dunning, S. A. and Armitage, P. J. (2011). The grain-size distribution of rock-avalanche deposits: implications for natural dam stability. In Evans, S. G., Strom, A. L., and Scarascia-Mugnozza, G., editors, *Natural and Artificial Rockslide Dams*, pages 479–498. Springer.

Dunning, S. A., Mitchell, W. A., Rosser, N. J., and Petley, D. N. (2007). The Hattian Bala rock avalanche and associated landslides triggered by the Kashmir Earthquake of 8 October 2005. *Engineering Geology*, 93(3-4):130–144.

Dunning, S. A., Petley, D. N., and Strom, A. L. (2005). The morphologies and sedimentology of valley confined rock-avalanche deposits and their effect on potential dam hazard. In Hungr, O., Couture, R., and Eberhardt, E., editors, *Landslide Risk Management*, pages 691–704. A.T. Balkema, Amsterdam.

Dunning, S. A., Rosser, N. J., Petley, D. N., and Massey, C. R. (2006). Formation and failure of the Tsatichhu landslide dam, Bhutan. *Landslides*, 3(2):107–113.

Elsner, J. B., Kossin, J. P., and Jagger, T. H. (2008). The increasing intensity of the strongest tropical cyclones. *Nature*, 455(7209):92–95.

Erismann, T. H. and Abele, G. (2001). *Dynamics of rockslides and rockfalls*. Springer, Heidelberg.

Erismann, T. H., Heuberger, H., and Preuss, E. (1977). Der Bimsstein von Köfels (Tirol), ein Bergsturz-"Friktionit". *Tschermaks mineralogische und petrographische Mitteilungen*, 24(1-2):67–119.

Fabel, D., Stroeven, A. P., Harbor, J., Kleman, J., Elmore, D., and Fink, D. (2002). Landscape preservation under Fennoscandian ice sheets determined from in situ produced ^{10}Be and ^{26}Al. *Earth and Planetary Science Letters*, 201(2):397–406.

Fielding, E., Isacks, B., Barazangi, M., and Duncan, C. (1994). How flat is Tibet? *Geology*, 22:163–167.

Finnegan, N. J., Hallet, B., Montgomery, D. R., Zeitler, P. K., Stone, J. O., Anders, A. M., and Yuping, L. (2008). Coupling of rock uplift and river incision in the Namche Barwa-Gyala Peri massif, Tibet. *Geological Society of America Bulletin*, 120(1-2):142–155.

Finnegan, N. J., Schumer, R., and Finnegan, S. (2014). A signature of transience in bedrock river incision rates over timescales of 10^4-10^7 years. *Nature*, 505(7483):391–394.

Flint, J. J. (1974). Stream gradient as a function of order, magnitude, and discharge. *Water Resources Research*, 10(5):969–973.

Flohn, H. (1958). Beiträge zur Klimakunde von Hochasien (Contributions towards a Climatology of High Asia). *Erdkunde*, 12(4):294–308.

Fort, M. B. (1983). Geomorphological Observations in the Ladakh Area (Himalayas): Quaternary Evolution and Present Dynamics. In Gupta, V. J., editor, *Contributions to Himalayan Geology 2. Stratigraphy and Structure of Kashmir and Ladakh Himalaya.*, pages 39–58. Hindustan Publishing Corporation.

Friedrich, R. J. (1982). In defense of multiplicative terms in multiple regression equations. *American Journal of Political Science*, 26(4):797–833.

Friele, P. A. and Clague, J. J. (2004). Large Holocene landslides from Pylon Peak, southwestern British Columbia - Canadian Journal of Earth Sciences. *Canadian Journal of Earth Sciences*, 41(2):165–182.

Fuchs, G. (1981). Outline of the Geology of the Himalaya. *Mittl Österr Geol Ges*, 74/75:101–107.

Fuchs, G. (1986). The Geology of the Markha-Khurnak Region in Ladakh (India). *Jahrbuch der Geologischen Bundesanstalt*, 128(3+4):403–437.

Fuchs, G. and Linner, M. (1996). On the geology of the suture zone and Tso Morari dome in eastern Ladakh (Himalaya). *Jahrbuch der Geologischen Bundesanstalt*, 139(2):191–207.

Gaetani, M. and Garzanti, E. (1991). Multicyclic History of the Northern India Continental Margin (Northwestern Himalaya) (1). *AAPG Bulletin*, 75(9):1427–1446.

Galehouse, J. S. (1971). Point counting . In Carver, R. E., editor, *Procedures in Sedimentary Petrology*, pages 385–407. Wiley-Interscience New York, New York.

Gansser, A. (1964). *Geology of the Himalayas*. Interscience Publishers (London and New York).

Gardner, T. W., Jorgensen, D. W., Shuman, C., and Lemieux, C. R. (1987). Geomorphic and tectonic process rates: Effects of measured time interval. *Geology*, 15(3):259.

Garzanti, E. and Andó, S. (2007). Heavy Mineral Concentration in Modern Sands: Implications for Provenance Interpretation. *Developments in Sedimentology*, 58:517–545.

Garzanti, E., Resentini, A., Vezzoli, G., Andó, S., Malusà, M., and Padoan, M. (2012). Forward compositional modelling of Alpine orogenic sediments. *Sedimentary Geology*, 280:149–164.

Garzanti, E., Resentini, A., Vezzoli, G., Andó, S., Malusà, M. G., Padoan, M., and Paparella, P. (2010). Detrital Fingerprints of Fossil Continental-Subduction Zones (Axial Belt Provenance, European Alps). *The Journal of Geology*, 118(4):341–362.

Garzanti, E. and van Haver, T. (1988). The Indus clastics: forearc basin sedimentation in the Ladakh Himalaya (India). *Sedimentary Geology*, 59:237–249.

Garzanti, E. and Vezzoli, G. (2003). A Classification of Metamorphic Grains in Sands Based on their Composition and Grade: Research Methods Papers. *Journal of Sedimentary Research*, 73(5):830–837.

Garzanti, E., Vezzoli, G., Andņ, S., Paparella, P., and Clift, P. D. (2005). Petrology of Indus River sands: a key to interpret erosion history of the Western Himalayan Syntaxis. *Earth and Planetary Science Letters*, 229(3-4):287–302.

Giardini, D., Grünthal, G., Shedlock, K. M., and Zhang, P. (1999). The GSHAP global seismic hazard map. *Annals of Geophysics*, 42(6).

Gillespie, A. R. and Molnar, P. (1995). Asynchronous maximum advances of mountain and continental glaciers. *Reviews of Geophysics*, 33(3):311–364.

Godard, V., Bourlés, D. L., Spinabella, F., Burbank, D. W., Bookhagen, B., Fisher, G. B., Moulin, A., and Leanni, L. (2014). Dominance of tectonics over climate in Himalayan denudation. *Geology*, 42(3):243–246.

Godard, V., Burbank, D. W., Bourlés, D. L., Bookhagen, B., Braucher, R., and Fisher, G. B. (2012). Impact of glacial erosion on ^{10}Be concentrations in fluvial sediments of the Marsyandi catchment, central Nepal. *Journal of Geophysical Research*, 117(F3):F03013.

Godard, V., Lavé, J., Carcaillet, J., Cattin, R., Bourlès, D., and Zhu, J. (2010). Spatial distribution of denudation in Eastern Tibet and regressive erosion of plateau margins. *Tectonophysics*, 491(1-4):253–274.

Gosse, J. C. and Stone, J. O. (2006). Terrestrial cosmogenic nuclide methods passing milestones toward paleo-altimetry. *Eos, Transactions American Geophysical Union*, 82(7):82–89.

Granger, D. E., Fabel, D., and Palmer, A. N. (2001). Pliocene-Pleistocene incision of the Green River, Kentucky, determined from radioactive decay of cosmogenic ^{26}Al and ^{10}Be in Mammoth Cave sediments. *Geological Society of America Bulletin*, 113(7):825–836.

Granger, D. E., Kirchner, J. W., and Finkel, R. (1996). Spatially averaged long-term erosion rates measured from in situ-produced cosmogenic nuclides in alluvial sediment. *The Journal of Geology*, 104:249–257.

Guillot, S., de Sigoyer, J., Lardeaux, J. M., and Mascle, G. (1997). Eclogitic metasediments from the Tso Morari area (Ladakh, Himalaya): Evidence for continental subduction during India-Asia convergence. *Contributions to Mineralogy and Petrology*, 128(2):197–212.

Hartigan, J. A. and Wong, M. A. (1979). Algorithm AS 136: A K-Means Clustering Algorithm. *Applied Statistics*, 28(1):100.

Harvey, A. M. (2011). The coupling status of alluvial fans and debris cones: a review and synthesis. *Earth Surface Processes and Landforms*, 37(1):64–76.

Hedrick, K. A., Seong, Y. B., Owen, L. A., Caffee, M. W., and Dietsch, C. (2011). Towards defining the transition in style and timing of Quaternary glaciation between the monsoon-influenced Greater Himalaya and the semi-arid Transhimalaya of Northern India. *Quaternary International*, 236(1-2):21–33.

Heimsath, A. M., Chappell, J., Dietrich, W. E., Nishiizumi, K., and Finkel, R. C. (2000). Soil production on a retreating escarpment in southeastern Australia. *Geology*, 28(9):787–790.

Heimsath, A. M., Dietrich, W. E., Nishiizumi, K., and Finkel, R. (1997). The soil production function and landscape equilibrium. *Nature*, 388(6640):358–361.

Henck, A. C., Huntington, K. W., Stone, J. O., Montgomery, D. R., and Hallet, B. (2011). Spatial controls on erosion in the Three Rivers Region, southeastern Tibet and southwestern China. *Earth and Planetary Science Letters*, 303(1-2):71–83.

Henderson, A. L., Najman, Y., Parrish, R., BouDagher-Fadel, M., Barford, D., Garzanti, E., and Andó, S. (2010). Geology of the Cenozoic Indus Basin sedimentary rocks: Paleoenvironmental interpretation of sedimentation from the western Himalaya during the early phases of India-Eurasia collision. *Tectonics*, 29(6).

Hermanns, R. L., Blikra, L. H., Naumann, M., Nilsen, B., Panthi, K. K., Stromeyer, D., and Longva, O. (2006). Examples of multiple rock-slope collapses from Köfels (Ötz valley, Austria) and western Norway. *Engineering Geology*, 83(1-3):94–108.

Hetzel, R. (2013). Active faulting, mountain growth, and erosion at the margins of the Tibetan Plateau constrained by in situ-produced cosmogenic nuclides. *Tectonophysics*, 582(C):1–24.

Hetzel, R., Altenberger, U., and Strecker, M. R. (1996). Structural and chemical evolution of pseudotachylytes during seismic events. *Mineralogy and Petrology*, 58(1-2):33–50.

Heuberger, H., Masch, L., Preuss, E., and Schröcker, A. (1984). Quaternary landslides and rock fusion in Central Nepal and in the Tyrolean Alps. *Mountain Research and Development*, pages 345–362.

Hewawasam, T., von Blanckenburg, F., Schaller, M., and Kubik, P. W. (2003). Increase of human over natural erosion rates in tropical highlands constrained by cosmogenic nuclides. *Geology*, 31(7):597–600.

Hewitt, K. (1988). Catastrophic landslide deposits in the Karakoram Himalaya. *Science*, 242(4875):64–67.

Hewitt, K. (1998). Catastrophic landslides and their effects on the Upper Indus streams, Karakoram Himalaya, northern Pakistan. *Geomorphology*, 26(1-3):47–80.

Hewitt, K. (1999). Quaternary Moraines vs Catastrophic Rock Avalanches in the Karakoram Himalaya, Northern Pakistan. *Quaternary Research*, 51:220–237.

Hewitt, K. (2002). Postglacial Landform and Sediment Associations in a Landslide-Fragmented River System: The Transhimalayan Indus Streams, Central Asia. In *Landscapes of Transition*, pages 63–91. Springer Netherlands, Dordrecht.

Hewitt, K., Gosse, J., and Clague, J. J. (2011). Rock avalanches and the pace of late Quaternary development of river valleys in the Karakoram Himalaya. *Geological Society of America Bulletin*, 123(9-10):1836–1850.

Heyman, J. (2014). Paleoglaciation of the Tibetan Plateau and surrounding mountains based on exposure ages and ELA depression estimates. *Quaternary Science Reviews*, 91:30–41.

Heyman, J., Stroeven, A. P., Harbor, J. M., and Caffee, M. W. (2011). Too young or too old: Evaluating cosmogenic exposure dating based on an analysis of compiled boulder exposure ages. *Earth and Planetary Science Letters*, 302(1-2):71–80.

Hijmans, R. J., Cameron, S. E., Parra, J. L., Jones, P. G., and Jarvis, A. (2005). Very high resolution interpolated climate surfaces for global land areas. *International Journal of Climatology*, 25(15):1965–1978.

Hirschi, M., Seneviratne, S. I., Alexandrov, V., Boberg, F., Boroneant, C., Christensen, O. B., Formayer, H., Orlowsky, B., and Stepanek, P. (2010). Observational evidence for soil-moisture impact on hot extremes in southeastern Europe. *Nature Geoscience*, 4(1):17–21.

Hobley, D. E. J., Sinclair, H., and Cowie, P. A. (2010). Processes, rates, and time scales of fluvial response in an ancient postglacial landscape of the northwest Indian Himalaya. *Geological Society of America Bulletin*, 122(9-10):1569–1584.

Hobley, D. E. J., Sinclair, H. D., and Mudd, S. M. (2012). Reconstruction of a major storm event from its geomorphic signature: The Ladakh floods, 6 August 2010. *Geology*, 40(6):483–486.

Hodges, K. V., Wobus, C. W., Ruhl, K., Schildgen, T., and Whipple, K. X. (2004). Quaternary deformation, river steepening, and heavy precipitation at the front of the Higher Himalayan ranges. *Earth and Planetary Science Letters*, 220(3-4):379–389.

Horn, B. K. (1981). Hill shading and the reflectance map. *Proceedings of the IEEE*, 69(1):14–47.

Hovius, N., Stark, C., and Allen, P. (1997). Sediment flux from a mountain belt derived by landslide mapping. *Geology*, 25(3):231.

Howard, A. D., Dietrich, W. E., and Seidl, M. A. (1994). Modeling fluvial erosion on regional to continental scales. *Journal of Geophysical Research*, 99(B7):13971.

Ingersoll, R. V., Fullard, T. F., Ford, R. L., Grimm, J. P., Pickle, J. D., and Sares, S. W. (1984). The effect of grain size on detrital modes; a test of the Gazzi-Dickinson point-counting method. *Journal of Sedimentary Research*, 54(1):103–116.

Jade, S., Raghavendra Rao, H. J., Vijayan, M. S. M., Gaur, V. K., Bhatt, B. C., Kumar, K., Jaganathan, S., Ananda, M. B., and Dileep Kumar, P. (2010). GPS-derived deformation rates in northwestern Himalaya and Ladakh. *International Journal of Earth Sciences*, 100(6):1293–1301.

Jamieson, S., Sinclair, H., Kirstein, L., and Purves, R. (2004). Tectonic forcing of longitudinal valleys in the Himalaya: morphological analysis of the Ladakh Batholith, North India. *Geomorphology*, 58(1-4):49–65.

Juyal, N. (2010). Cloud burst-triggered debris flows around Leh. *Current science*, 99(9):1166–1167.

Kaiser, H. F. (1958). The varimax criterion for analytic rotation in factor analysis. *Psychometrika*, 23(3):187–200.

Keefer, D. K. (2002). Investigating Landslides Caused by Earthquakes – A Historical Review - Springer. *Surveys in Geophysics*, 23:473–510.

Keigler, R., Thouret, J.-C., Hodgson, K. A., Neall, V. E., Lecointre, J. A., Procter, J. N., and Cronin, S. J. (2011). The Whangaehu Formation: Debris-avalanche and lahar deposits from ancestral Ruapehu volcano, New Zealand. *Geomorphology*, 133(1-2):57–79.

Kennedy, G. C., Wasserburg, G. J., Heard, H. C., and Newton, R. C. (1962). The upper three-phase region in the system SiO_2-H_2O. *American Journal of Science*, 260(7):501–521.

Kirby, E. and Harkins, N. W. (2013). Distributed deformation around the eastern tip of the Kunlun fault. *International Journal of Earth Sciences*, 102(7):1759–1772.

Kirchner, J. W., Finkel, R., Riebe, C. S., Granger, D. E., Clayton, J., King, J., and Megahan, W. (2001). Mountain erosion over 10 yr, 10 k.y., and 10 m.y. time scales. *Geology*, 29(7):591.

Kirstein, L. (2011). Thermal evolution and exhumation of the Ladakh Batholith, northwest Himalaya, India. *Tectonophysics*, 503(3-4):222–233.

Kober, F., Hippe, K., Salcher, B., Ivy-Ochs, S., Kubik, P. W., Wacker, L., and Hählen, N. (2012). Debris-flow–dependent variation of cosmogenically derived catchment-wide denudation rates. *Geology*, 40(10):935–938.

Koenker, R. (2005). *Quantile Regression*. Econometric Society Monographs. Cambridge University Press Cambridge.

Koenker, R. and Bassett, Jr, G. (1978). Regression quantiles. *Econometrica: journal of the Econometric Society*, pages 33–50.

Kohl, C. and Nishiizumi, K. (1992). Chemical isolation of quartz for measurement of in-situ-produced cosmogenic nuclides. *Geochimica et Cosmochimica Acta*, 56(9):3583–3587.

Kong, P., Na, C., Fink, D., Ding, L., and Huang, F. (2006). Erosion in northwest Tibet from in-situ-produced cosmogenic ^{10}Be and ^{26}Al in bedrock. *Earth Surface Processes and Landforms*, 32(1):116–125.

Koons, P. O. (1989). The topographic evolution of collisional mountain belts; a numerical look at the Southern Alps, New Zealand. *American Journal of Science*, 289:1041–1069.

Korschinek, G., Bergmaier, A., Faestermann, T., Gerstmann, U. C., Knie, K., Rugel, G., Wallner, A., Dillmann, I., Dollinger, G., von Gostomski, C. L., Kossert, K., Maiti, M., Poutivtsev, M., and Remmert, A. (2010). A new value for the half-life of ^{10}Be by Heavy-Ion Elastic Recoil Detection and liquid scintillation counting. *Nuclear Instruments and Methods in Physics Research Section B: Beam Interactions with Materials and Atoms*, 268(2):187–191.

Korup, O. (2006). Rock-slope failure and the river long profile. *Geology*, 34(1):45.

Korup, O. (2012). Earth's portfolio of extreme sediment transport events. *Earth Science Reviews*, 112(3-4):115–125.

Korup, O. and Clague, J. J. (2009). Natural hazards, extreme events, and mountain topography. *Quaternary Science Reviews*, 28(11-12):977–990.

Korup, O., Clague, J. J., Hermanns, R. L., Hewitt, K., Strom, A. L., and Weidinger, J. T. (2007). Giant landslides, topography, and erosion. *Earth and Planetary Science Letters*, 261(3-4):578–589.

Korup, O., Densmore, A. L., and Schlunegger, F. (2010a). The role of landslides in mountain range evolution. *Geomorphology*, 120(1-2):77–90.

Korup, O., McSaveney, M. J., and Davies, T. R. (2004). Sediment generation and delivery from large historic landslides in the Southern Alps, New Zealand. *Geomorphology*, 61(1-2):189–207.

Korup, O. and Montgomery, D. R. (2008). Tibetan plateau river incision inhibited by glacial stabilization of the Tsangpo gorge. *Nature*, 455(7214):786–789.

Korup, O., Montgomery, D. R., and Hewitt, K. (2010b). Glacier and landslide feedbacks to topographic relief in the Himalayan syntaxes. *Proceedings of the National Academy of Sciences*, 107(12):5317.

Korup, O., Strom, A. L., and Weidinger, J. T. (2006). Fluvial response to large rock-slope failures: Examples from the Himalayas, the Tien Shan, and the Southern Alps in New Zealand. *Geomorphology*, 78(1-2):3–21.

Korup, O. and Weidinger, J. T. (2011). Rock type, precipitation, and the steepness of Himalayan threshold hillslopes. *Geological Society, London, Special Publications*, 353(1):235–249.

Kreemer, C., Holt, W. E., and Haines, A. J. (2003). An integrated global model of presentday plate motions and plate boundary deformation. *Geophysical Journal International*, 154(1):8–34.

Kumar, R., Lal, N., Singh, S., and Jain, A. K. (2007). Cooling and exhumation of the Trans-Himalayan Ladakh batholith as constrained by fission track apatite and zircon ages. *Current science*, 92(4):490.

Lal, D. (1991). Cosmic ray labeling of erosion surfaces: in situ nuclide production rates and erosion models. *Earth and Planetary Science Letters*, 104(2-4):424–439.

Lal, D., Harris, N. B. W., Sharma, K. K., Gu, Z., Ding, L., Liu, T., Dong, W., Caffee, M. W., and Jull, A. J. T. (2004). Erosion history of the Tibetan Plateau since the last interglacial: constraints from the first studies of cosmogenic ^{10}Be from Tibetan bedrock. *Earth and Planetary Science Letters*, 217(1-2):33–42.

Lamb, S. and Davis, P. (2003). Cenozoic climate change as a possible cause for the rise of the Andes. *Nature*, 425(6960):792–797.

Larsen, I. J. and Montgomery, D. R. (2012). Landslide erosion coupled to tectonics and river incision. *Nature Geoscience*, 5(7):468–473.

Larsen, I. J., Montgomery, D. R., and Greenberg, H. M. (2014). The contribution of mountains to global denudation. *Geology*, 42(6):527–530.

Lavé, J. and Avouac, J. P. (2001). Fluvial incision and tectonic uplift across the Himalayas of central Nepal. *Journal of Geophysical Research: Solid Earth (1978–2012)*, 106(B11):26561–26591.

Legros, F., Cantagrel, J. M., and Devouard, B. (2000). Pseudotachylyte (Frictionite) at the Base of the Arequipa Volcanic Landslide Deposit (Peru): Implications for Emplacement Mechanisms. *The Journal of Geology*, 108(5):601–611.

Li, Y., Li, D., Liu, G., Harbor, J., Caffee, M. W., and Stroeven, A. P. (2014). Patterns of landscape evolution on the central and northern Tibetan Plateau investigated using in-situ produced ^{10}Be concentrations from river sediments. *Earth and Planetary Science Letters*, pages 1–13.

Lifton, N. A., Bieber, J. W., Clem, J. M., Duldig, M. L., Evenson, P., Humble, J. E., and Pyle, R. (2005). Addressing solar modulation and long-term uncertainties in scaling secondary cosmic rays for in situ cosmogenic nuclide applications. *Earth and Planetary Science Letters*, 239(1-2):140–161.

Lin, A. (2008). *Fossil Earthquakes: The Formation and Preservation of Pseudotachylytes*, volume 111 of *Lecture Notes in Earth Sciences*. Springer Berlin Heidelberg, Berlin, Heidelberg.

Lin, A., Chen, A., Liau, C. F., Lee, C. T., Lin, C. C., Lin, P. S., Wen, S. C., and Ouchi, T. (2001). Frictional fusion due to coseismic landsliding during the 1999 ChiChi (Taiwan) ML 7.3 Earthquake. *Geophysical Research Letters*, 28(20):4011–4014.

Lottermoser, W., Kaliba, P., Forcher, K., and Amthauer, G. (1993). *MOESALZ: a computer program for the evaluation of Mössbauer data*. University of Salzburg.

Maddock, R. H. (1986). Frictional melting in landslide-generated frictionites (hyalomylonites) and fault-generated pseudotachylytes-discussion. *Tectonophysics*, 128(1):151–153.

Mahéo, G., Fayoux, X., Guillot, S., Garzanti, E., Capiez, P., and Mascle, G. (2006). Relicts of an intra-oceanic arc in the Sapi-Shergol mélange zone (Ladakh, NW Himalaya, India): implications for the closure of the Neo-Tethys Ocean. *Journal of Asian Earth Sciences*, 26(6):695–707.

Malamud, B. D., Turcotte, D. L., Guzzetti, F., and Reichenbach, P. (2004). Landslide inventories and their statistical properties. *Earth Surface Processes and Landforms*, 29(6):687–711.

Marti, K. and Craig, H. (1987). Cosmic-ray-produced neon and helium in the summit lavas of Maui. *Nature*, 325:335–337.

Masch, L. and Preuss, E. (1977). The occurrence of the hyalomylonite of Langtang, Himalaya (Nepal). *Neues Jahrbuch für Mineralogie - Abhandlungen*, 129:292–311.

Masch, L., Wenk, H. R., and Preuss, E. (1985). Electron microscopy study of hyalomylonites—evidence for frictional melting in landslides. *Tectonophysics*, 115:131–160.

McColl, S. T. and Davies, T. R. (2012). Large ice-contact slope movements: glacial buttressing, deformation and erosion. *Earth Surface Processes and Landforms*, 38(10):1102–1115.

McSaveney, M. J. (2002). Recent rockfalls and rock avalanches in Mt. Cook National Park, New Zealand. *Engineering Geology*, 15:35–69.

Mitchell, S. G. and Montgomery, D. R. (2006). Influence of a glacial buzzsaw on the height and morphology of the Cascade Range in central Washington State, USA. *Quaternary Research*, 65(1):96–107.

Mitchell, W. A., McSaveney, M. J., Zondervan, A., Kim, K., Dunning, S. A., and Taylor, P. J. (2007). The Keylong Serai rock avalanche, NW Indian Himalaya: geomorphology and palaeoseismic implications. *Landslides*, 4(3):245–254.

Mitchell, W. A., Taylor, P., and Osmaston, H. (1999). Quaternary geology in Zanskar, NW Indian Himalaya: evidence for restricted glaciation and preglacial topography. *Journal of Asian Earth Sciences*, 17(3):307–318.

Molnar, P. (2003). Geomorphology: Nature, nurture and landscape. *Nature*, 426(6967):612–614.

Molnar, P. and England, P. (1990). Late Cenozoic uplift of mountain ranges and global climate change: chicken or egg? *Nature*, 346(6279):29–34.

Montgomery, D. R., Balco, G., and Willett, S. D. (2001). Climate, tectonics, and the morphology of the Andes. *Geology*, 29(7):579–582.

Montgomery, D. R. and Brandon, M. T. (2002). Topographic controls on erosion rates in tectonically active mountain ranges. *Earth and Planetary Science Letters*, 201(3-4):481–489.

Moon, S., Chamberlain, C. P., Blisniuk, K., Levine, N., Rood, D. H., and Hilley, G. E. (2011). Climatic control of denudation in the deglaciated landscape of the Washington Cascades. *Nature Geoscience*, 4(7):469–473.

Morris, T. H. and Herbertson, G. F. (1996). Large-Rock Avalanche Deposits, Eastern Basin and Range, Utah: Emplacement, Diagenesis, and Economic Potential. *AAPG Bulletin*, 80(7):1135–1149.

Müller, M. J., Baltes, K., Werle, D., Lutz, E., and Renschler, C. (1996). *Handbuch ausgewählter Klimastationen der Erde*. Universität Trier, Trier.

Munack, H., Korup, O., Resentini, A., Limonta, M., Garzanti, E., Blöthe, J. H., Scherler, D., Wittmann, H., and Kubik, P. W. (2014). Postglacial denudation of western Tibetan Plateau margin outpaced by long-term exhumation. *Geological Society of America Bulletin*.

Niemi, N. A., Oskin, M., Burbank, D. W., Heimsath, A. M., and Gabet, E. J. (2005). Effects of bedrock landslides on cosmogenically determined erosion rates. *Earth and Planetary Science Letters*, 237(3-4):480–498.

Nishiizumi, K., Klein, J., Middleton, R., and Craig, H. (1990). Cosmogenic ^{10}Be, ^{26}Al, and ^{3}He in olivine from Maui lavas. *Earth and Planetary Science Letters*, 98(3):263–266.

Nishiizumi, K., Winterer, E. L., Kohl, C. P., Klein, J., Middleton, R., Lal, D., and Arnold, J. R. (1989). Cosmic ray production rates of ^{10}Be and ^{26}Al in quartz from glacially polished rocks. *Journal of Geophysical Research*, 94(B12):17907.

Norris, R. J. and Cooper, A. F. (1997). Erosional control on the structural evolution of a transpressional thrust complex on the Alpine fault, New Zealand. *Journal of Structural Geology*, 10:1323–1342.

O'Hara, K. D. and Huggins, F. E. (2004). A Mössbauer study of pseudotachylytes: redox conditions during seismogenic faulting. *Contributions to Mineralogy and Petrology*, 148(5):602–614.

Osmaston, H. (1994). Geomorphology and Quaternary History of Zanskar. In Crook, J. and Osmaston, H., editors, *Himalayan Buddhist Villages*, pages 1–36. Jainendra prakach jain at shri jainendra press, Delhi.

Ouimet, W. B. (2011). The hills came tumbling down. *Nature Geoscience*, 4:424–425.

Ouimet, W. B., Whipple, K. X., and Granger, D. E. (2009). Beyond threshold hillslopes: Channel adjustment to base-level fall in tectonically active mountain ranges. *Geology*, 37(7):579–582.

Ouimet, W. B., Whipple, K. X., Royden, L. H., Sun, Z., and Chen, Z. (2007). The influence of large landslides on river incision in a transient landscape: Eastern margin of the Tibetan Plateau (Sichuan, China). *Geological Society of America Bulletin*, 119(11-12):1462–1476.

Overpeck, J., Anderson, D., Trumbore, S., and Prell, W. (1996). The southwest Indian Monsoon over the last 18 000 years - Springer. *Climate Dynamics*.

Owen, L. A. (2009). Latest Pleistocene and Holocene glacier fluctuations in the Himalaya and Tibet. *Quaternary Science Reviews*, 28(21-22):2150–2164.

Owen, L. A., Caffee, M. W., Bovard, K. R., Finkel, R., and Sharma, M. (2006). Terrestrial cosmogenic nuclide surface exposure dating of the oldest glacial successions in the Himalayan orogen: Ladakh Range, northern India. *Geological Society of America Bulletin*, 118(3-4):383–392.

Owen, L. A., Caffee, M. W., Finkel, R. C., and Seong, Y. B. (2008). Quaternary glaciation of the Himalayan-Tibetan orogen. *Journal of Quaternary Science*, 23(6-7):513–531.

Owen, L. A., Finkel, R. C., Barnard, P. L., Haizhou, M., Asahi, K., Caffee, M. W., and Derbyshire, E. (2005). Climatic and topographic controls on the style and timing of Late Quaternary glaciation throughout Tibet and the Himalaya defined by ^{10}Be cosmogenic radionuclide surface exposure dating. *Quaternary Science Reviews*, 24(12-13):1391–1411.

Palumbo, L., Hetzel, R., Tao, M., and Li, X. (2010a). Catchment-wide denudation rates at the margin of NE Tibet from in situ-produced cosmogenic ^{10}Be. *Terra Nova*, 23(1):42–48.

Palumbo, L., Hetzel, R., Tao, M., and Li, X. (2010b). Topographic and lithologic control on catchment-wide denudation rates derived from cosmogenic ^{10}Be in two mountain ranges at the margin of NE Tibet. *Geomorphology*, 117(1-2):130–142.

Pant, R. K., Phadtare, N. R., Chamyal, L. S., and Juyal, N. (2005). Quaternary deposits in Ladakh and Karakoram Himalaya: A treasure trove of the palaeoclimate records. *Current science*, 88(11):1789–1798.

Parker, R. N., Densmore, A. L., Rosser, N. J., de Michele, M., Li, Y., Huang, R., Whadcoat, S., and Petley, D. N. (2011). Mass wasting triggered by the 2008 Wenchuan earthquake is greater than orogenic growth. *Nature Geoscience*, 4(7):449–452.

Passchier, C. W. and Trouw, R. A. J. (2005). *Microtectonics*. Springer-Verlag, Berlin/Heidelberg.

Patzelt, G. (2012). Die Bergstürze vom Tschirgant und von Haiming, Oberinntal, Tirol Begleitworte zur Kartenbeilage. *Jahrbuch der Geologischen Bundesanstalt*, 152(1-4):13–24.

Pavlis, T. L., Hamburger, M. W., and Pavlis, G. L. (1997). Erosional processes as a control on the structural evolution of an actively deforming fold and thrust belt: An example from the Pamir-Tien Shan region, central Asia. *Tectonics*, 16(5):810–822.

Petzold, A. and Hinz, W. (1976). *Silikatchemie: Einführung in die Grundlagen*. Deutscher Verlag für Grundstoffindustrie.

Phillips, F. M., Leavy, B. D., Jannik, N. O., Elmore, D., and Kubik, P. W. (1986). The accumulation of cosmogenic chlorine-36 in rocks: A method for surface exposure dating. *Science*, 231(4733):41–43.

Phillips, F. M., Zreda, M. G., Smith, S. S., Elmore, D., Kubik, P. W., and Sharma, P. (1990a). Cosmogenic chlorine-36 chronology for glacial deposits at Bloody Canyon, eastern Sierra Nevada. *Science*, 248(4962):1529–1532.

Phillips, F. M., Zreda, M. G., Smith, S. S., Elmore, D., Kubik, P. W., and Sharma, P. (1990b). Cosmogenic chlorine-36 chronology for glacial deposits at Bloody Canyon, eastern Sierra Nevada. *Science*, 248(4962):1529–1532.

Pickup, G. and Marshall, A. (2009). Geomorphology, hydrology, and climate of the Fly River system. In Bolton, B., editor, *The Fly River, Papua New Guinea: Environmental studies in an impacted tropical river system*, pages 3–49. Elsevier.

Pinet, P. and Souriau, M. (1988). Continental erosion and largescale relief. *Tectonics*, 7(3):563–582.

Pognante, U. and Lombardo, B. (1989). Metamorphic evolution of the High Himalayan crystallines in SE Zanskar, India. *Journal of Metamorphic Geology*, 7(1):9–17.

Pollet, N. and Schneider, J. L. M. (2004). Dynamic disintegration processes accompanying transport of the Holocene Flims sturzstrom (Swiss Alps). *Earth and Planetary Science Letters*, 221(1-4):433–448.

Portenga, E. W. and Bierman, P. R. (2011). Understanding Earth's eroding surface with ^{10}Be. *GSA Today*, 21(8):4–10.

Prager, C., Zangerl, C., Brandner, R., and Patzelt, G. (2007). Increased rockslide activity in the Middle Holocene? New evidences from the Tyrolean Alps (Austria). *Landslides and climate change, Challenges and Solutions*, pages 25–34.

Putkonen, J. K. (2004). Continuous snow and rain data at 500 to 4400 m altitude near Annapurna, Nepal, 1999-2001. *Arctic, Antarctic, and Alpine Research*, 36(2):244–248.

Raymo, M. and Ruddiman, W. (1992). Tectonic forcing of late Cenozoic climate. *Nature*, 359(6391):117–122.

Reiners, P. W., Ehlers, T. A., Mitchell, S. G., and Montgomery, D. R. (2003). Coupled spatial variations in precipitation and long-term erosion rates across the Washington Cascades. *Nature*, 426(6967):645–647.

Reinhardt, L., Jerolmack, D., Cardinale, B. J., Vanacker, V., and Wright, J. (2010). Dynamic interactions of life and its landscape: feedbacks at the interface of geomorphology and ecology. *Earth Surface Processes and Landforms*, 35(1):78–101.

Reneau, S. L., Dietrich, W. E., Rubin, M., Donahue, D. J., and Jull, A. T. (1989). Analysis of hillslope erosion using dated colluvial deposits. *Journal of Geology;(USA)*, 97(1).

Reznichenko, N. V., Davies, T. R., Shulmeister, J., and Larsen, S. H. (2012). A new technique for identifying rock avalanche–sourced sediment in moraines and some paleoclimatic implications. *Geology*, 40(4):319–322.

Riebe, C. S., Kirchner, J. W., Granger, D. E., and Finkel, R. C. (2001). Minimal climatic control on erosion rates in the Sierra Nevada, California. *Geology*, 29(5):447.

Robertson, A. and Degnan, P. (1994). The Dras arc Complex: lithofacies and reconstruction of a Late Cretaceous oceanic volcanic arc in the Indus Suture Zone, Ladakh Himalaya. *Sedimentary Geology*, 92(1):117–145.

Roe, G. H., Whipple, K. X., and Fletcher, J. K. (2008). Feedbacks among climate, erosion, and tectonics in a critical wedge orogen. *American Journal of Science*, 308(7):815–842.

Roering, J., Perron, J. T., and Kirchner, J. W. (2007). Functional relationships between denudation and hillslope form and relief. *Earth and Planetary Science Letters*, 264(1-2):245–258.

Roering, J. J. and Gerber, M. (2005). Fire and the evolution of steep, soil-mantled landscapes. *Geology*, 33(5):349.

Rohrmann, A., Heermance, R., Kapp, P., and Cai, F. (2013). Wind as the primary driver of erosion in the Qaidam Basin, China. *Earth and Planetary Science Letters*, 374:1–10.

Rowley, D. B. (1996). Age of initiation of collision between India and Asia: A review of stratigraphic data. *Earth and Planetary Science Letters*, 145(1):1–13.

Rowley, D. B. and Currie, B. S. (2006). Palaeo-altimetry of the late Eocene to Miocene Lunpola basin, central Tibet. *Nature*, 439(7077):677–681.

Russell, R. D. (1937). Mineral composition of Mississippi River sands. *Geological Society of America Bulletin*, 48:1307–1348.

Ruxton, B. P. and McDougall, I. (1967). Denudation rates in northeast Papua from potassium-argon dating of lavas. *American Journal of Science*, 265(7):545–561.

Sadler, P. M. (1981). Sediment accumulation rates and the completeness of stratigraphic sections. *The Journal of Geology*, pages 569–584.

Sadler, P. M. and Jerolmack, D. J. (2014). Scaling laws for aggradation, denudation and progradation rates: the case for time-scale invariance at sediment sources and sinks. In Smith, D. G., Bailey, R. J., Burgess, P. M., and Fraser, A. J., editors, *Strata and Time: Probing the Gaps in Our Understanding*. Geological Society, London, Special Publications, London.

Sanhueza-Pino, K., Korup, O., Hetzel, R., Munack, H., Weidinger, J. T., Dunning, S. A., Ormukov, C., and Kubik, P. W. (2011). Glacial advances constrained by ^{10}Be exposure dating of bedrock landslides, Kyrgyz Tien Shan. *Quaternary Research*, 76(3):295–304.

Santamaria Tovar, D., Shulmeister, J., and Davies, T. R. (2008). Evidence for a landslide origin of New Zealand's Waiho Loop moraine. *Nature Geoscience*, 1(8):524–526.

Saunders, I. and Young, A. (1983). Rates of surface processes on slopes, slope retreat and denudation. *Earth Surface Processes and Landforms*, 8(5):473–501.

Scherler, D., Bookhagen, B., and Strecker, M. R. (2013). Tectonic control on ^{10}Be-derived erosion rates in the Garhwal Himalaya, India. *Journal of Geophysical Research: Earth Surface*, 119(2):83–105.

Scherler, D., Munack, H., Mey, J., Eugster, P., Wittmann, H., Codilean, A. T., Kubik, P. W., and Strecker, M. R. (2014). Ice dams, outburst floods, and glacial incision at the western margin of the Tibetan Plateau: A >100 ky chronology from the Shyok Valley, Karakoram. *Geological Society of America Bulletin*, 126(5-6):738–758.

Schildgen, T., Phillips, W., and Purves, R. S. (2005). Simulation of snow shielding corrections for cosmogenic nuclide surface exposure studies. *Geomorphology*, 64(1-2):67–85.

Schlup, M., Carter, A., Cosca, M., and Steck, A. (2003). Exhumation history of eastern Ladakh revealed by ^{40}Ar/^{39}Ar and fission-track ages: the Indus River-Tso Morari transect, NW Himalaya. *Journal of the Geological Society*, 160(3):385–399.

Schmidt, K. M. and Montgomery, D. R. (1995). Limits to Relief. *Science*, 270:617–620.

Schramm, J.-M. and Weidinger, J. T. (1998). Petrologic and structural controls on geomorphology of prehistoric Tsergo Ri slope failure, Langtang Himal, Nepal. *Geomorphology*, 26(1-3):107–121.

Schumer, R. and Jerolmack, D. J. (2009). Real and apparent changes in sediment deposition rates through time. *Journal of Geophysical Research*, 114:F00A06.

Searle, M. P., Pickering, K., and Cooper, D. (1990). Restoration and evolution of the intermontane Indus molasse basin, Ladakh Himalaya, India. *Tectonophysics*, 174(3-4):301–314.

Searle, M. P., Weinberg, R. F., and Dunlap, W. J. (1998). Transpressional tectonics along the Karakoram fault zone, northern Ladakh: constraints on Tibetan extrusion. *Geological Society, London, Special Publications*, 135(1):307–326.

Shea, T. and van Wyk de Vries, B. (2008). Structural analysis and analogue modeling of the kinematics and dynamics of rockslide avalanches. *Geosphere*, 4(4):657.

Shroder, Jr, J. F. (1998). Slope failure and denudation in the western Himalaya. *Geomorphology*, 26(1):81–105.

Sibson, R. H. (1975). Generation of pseudotachylyte by ancient seismic faulting. *Geophysical Journal International*, 43(3):775–794.

Sinclair, H. and Jaffey, N. (2001). Sedimentology of the Indus Group, Ladakh, northern India: implications for the timing of initiation of the palaeo-Indus River. *Journal of the Geological Society*, 158:151–162.

Small, E. E., Anderson, R. S., and Hancock, G. S. (1999). Estimates of the rate of regolith production using and from an alpine hillslope. *Geomorphology*, 27(1-2):131–150.

Sobel, E. R. (2003). Formation of internally drained contractional basins by aridity-limited bedrock incision. *Journal of Geophysical Research*, 108(B7).

Spate, O., Learmonth, A., and Farmer, B. H. (1967). *India, Pakistan and Ceylon: The Regions*. Methuen.

Spray, J. G. (1992). A physical basis for the frictional melting of some rock-forming minerals. *Tectonophysics*, 204:205–221.

Spray, J. G. (2010). Frictional Melting Processes in Planetary Materials: From Hypervelocity Impact to Earthquakes. *Annual Review of Earth and Planetary Sciences*, 38(1):221–254.

Steck, A. (2003). Geology of the NW Indian Himalaya. *Eclogae Geologicae Helvetiae*, 96(2):147–196.

Steck, A., Spring, L., Vannay, J. C., and Masson, H. (1993). Geological transect across the northwestern Himalaya in eastern Ladakh and Lahul (a model for the continental collision of India and Asia). *Eclogae Geologicae Helvetiae*, 86(1):219–263.

Stone, J. O. (2000). Air pressure and cosmogenic isotope production. *Journal of Geophysical Research*, 105(B10):23753–23759.

Stone, J. O., Ballantyne, C. K., and Keith Fifield, L. (1998). Exposure dating and validation of periglacial weathering limits, northwest Scotland. *Geology*, 26(7):587.

Storti, F. and Balsamo, F. (2010). Impact of ephemeral cataclastic fabrics on laser diffraction particle size distribution analysis in loose carbonate fault breccia. *Journal of Structural Geology*, 32(4):507–522.

Strobl, M., Hetzel, R., Niedermann, S., Ding, L., and Zhang, L. (2012). Landscape evolution of a bedrock peneplain on the southern Tibetan Plateau revealed by in situ-produced cosmogenic ^{10}Be and ^{21}Ne. *Geomorphology*, 153-154(C):192–204.

Strom, A. L. and Abdrakhmatov, K. (2004a). Rock Avalanches and Rockslide Dams of the Northern Kyrgyzstan. *Nato Advanced Research Workshop (Security of Natural and Artificial Rockslide Dams), Post-Workshop Field Trip Guidebook, Moscow- Bishkek*, pages 12–15.

Strom, A. L. and Abdrakhmatov, K. (2004b). Rockslides and Rock Avalanches of the Kokomeren River Basin and Karakudjur Rockslide. *Nato Advanced Research Workshop (Security of Natural and Artificial Rockslide Dams), Post-Workshop Field Trip Guidebook, Moscow- Bishkek*, pages 11–14.

Summerfield, M. A. (2005). A tale of two scales, or the two geomorphologies. *Transactions of the Institute of British Geographers*, 30(4):402–415.

Summerfield, M. A. and Hulton, N. J. (1994). Natural controls of fluvial denudation rates in major world drainage basins. *Journal of Geophysical Research: Solid Earth (1978–2012)*, 99(B7):13871–13883.

Takagi, H., Arita, K., Danhara, T., and Iwano, H. (2007). Timing of the Tsergo Ri landslide, Langtang Himal, determined by fission-track dating of pseudotachylyte. *Journal of Asian Earth Sciences*, 29(2-3):466–472.

Taylor, P. (2000). The Quaternary glacial history of the Zanskar Range, north-west Indian Himalaya. *Quaternary International*, pages 1–19.

Thayyen, R. J., Dimri, A. P., Kumar, P., and Agnihotri, G. (2012). Study of cloudburst and flash floods around Leh, India, during August 4–6, 2010. *Natural Hazards*, 65(3):2175–2204.

Thiede, R. C. and Ehlers, T. A. (2013). Large spatial and temporal variations in Himalayan denudation. *Earth and Planetary Science Letters*, 371-372(C):278–293.

Thompson, L. G., Yao, T., Davis, M. E., Henderson, K. A., Mosley-Thompson, E., Lin, P.-N., Beer, J., Synal, H. A., Cole-Dai, J., and Bolzan, J. F. (1997). Tropical climate instability: The last glacial cycle from a Qinghai-Tibetan ice core. *Science*, 276(5320):1821–1825.

Tomkins, K. M., Humphreys, G. S., Wilkinson, M. T., Fink, D., Hesse, P. P., Doerr, S. H., Shakesby, R. A., Wallbrink, P. J., and Blake, W. H. (2007). Contemporary versus long-term denudation along a passive plate margin: the role of extreme events. *Earth Surface Processes and Landforms*, 32(7):1013–1031.

Torres Acosta, V., Schildgen, T., Clarke, B., Scherler, D., Bookhagen, B., Wittmann, H., von Blanckenburg, F., and Strecker, M. R. (2014). Effects of vegetation cover on landscape denudation rates. *Geophysical Research Abstracts*, 16.

Turnbull, J. M. and Davies, T. R. (2006). A mass movement origin for cirques. *Earth Surface Processes and Landforms*, 31(9):1129–1148.

van der Beek, P., Melle, J. V., Guillot, S., Pêcher, A., Reiners, P. W., Nicolescu, S., and Latif, M. (2009). Eocene Tibetan plateau remnants preserved in the northwest Himalaya. *Nature Geoscience*, 2(5):364–368.

van Husen, D., Ivy-Ochs, S., and Alfimov, V. (2007). Mechanism and age of late glacial landslides in the Calcareous Alps; the Almtal, Upper Austria. *Austrian Journal of Earth Sciences*, 100:114–126.

Vanacker, V., von Blanckenburg, F., Govers, G., Molina, A., Poesen, J., Deckers, J., and Kubik, P. W. (2007a). Restoring dense vegetation can slow mountain erosion to near natural benchmark levels. *Geology*, 35(4):303.

Vanacker, V., von Blanckenburg, F., Hewawasam, T., and Kubik, P. W. (2007b). Constraining landscape development of the Sri Lankan escarpment with cosmogenic nuclides in river sediment. *Earth and Planetary Science Letters*, 253(3):402–414.

von Blanckenburg, F. (2005). The control mechanisms of erosion and weathering at basin scale from cosmogenic nuclides in river sediment. *Earth and Planetary Science Letters*, 242:224–239.

von Blanckenburg, F., Belshaw, N. S., and O'Nions, R. K. (1996). Separation of ^{9}Be and cosmogenic ^{10}Be from environmental materials and SIMS isotope dilution analysis. *Chemical Geology*, 129(1):93–99.

von Blanckenburg, F. and Kubik, P. W. (2004). Cosmogenic nuclide evidence for low weathering and denudation in the wet, tropical highlands of Sri Lanka. *Journal of Geophysical Research*, 109(F3).

Walker, M. (2005). *Quaternary dating methods*. John Wiley & Sons.

Walsh, L. S., Martin, A. J., Ojha, T. P., and Fedenczuk, T. (2012). Correlations of fluvial knickzones with landslide dams, lithologic contacts, and faults in the southwestern Annapurna Range, central Nepalese Himalaya. *Journal of Geophysical Research*, 117(F1):F01012.

Wang, C., Zhao, X., Liu, Z., Lippert, P. C., Graham, S. A., Coe, R. S., Yi, H., Zhu, L., Liu, S., and Li, Y. (2008). Constraints on the early uplift history of the Tibetan Plateau. *Proceedings of the National Academy of Sciences*, 105(13):4987–4992.

Wang, Y. J. (2001). A High-Resolution Absolute-Dated Late Pleistocene Monsoon Record from Hulu Cave, China. *Science*, 294(5550):2345–2348.

Ward, Jr, J. H. (1963). Hierarchical grouping to optimize an objective function. *Journal of the American statistical association*, 58(301):236–244.

Warrick, J. A., Milliman, J. D., Walling, D. E., Wasson, R. J., Syvitski, J. P. M., and Aalto, R. E. (2013). Earth is (mostly) flat: Apportionment of the flux of continental sediment over millennial time scales: COMMENT. *Geology*, 42(1):e316–e316.

Wassmer, P., Schneider, J.-L., Pollet, N., and Schmitter-Voirin, C. (2004). Effects of the internal structure of a rock–avalanche dam on the drainage mechanism of its impoundment, Flims sturzstrom and Ilanz paleo-lake, Swiss Alps. *Geomorphology*, 61(1-2):3–17.

Weidinger, J. T. (2006). Predesign, failure and displacement mechanisms of large rockslides in the Annapurna Himalayas, Nepal. *Engineering Geology*, 83(1-3):201–216.

Weidinger, J. T. (2010). Stability and Life Span of Landslide Dams in the Himalayas (India, Nepal) and the Qin Ling Mountains (China). In Evans, S. G., Hermanns, R. L., Strom, A. L., and Scarascia-Mugnozza, G., editors, *Natural and Artificial Rockslide Dams*, pages 243–277. Springer Berlin Heidelberg, Berlin, Heidelberg.

Weidinger, J. T. and Korup, O. (2009). Frictionite as evidence for a large Late Quaternary rockslide near Kanchenjunga, Sikkim Himalayas, India — Implications for extreme events in mountain relief destruction. *Geomorphology*, 103(1):57–65.

Weidinger, J. T., Korup, O., Munack, H., Altenberger, U., Dunning, S. A., Tippelt, G., and Lottermoser, W. (2014). Giant rockslides from the inside. *Earth and Planetary Science Letters*, 389:62–73.

Weidinger, J. T., Schramm, J.-M., and Nuschej, F. (2002). Ore mineralization causing slope failure in a high-altitude mountain crest—on the collapse of an 8000m peak in Nepal. *Journal of Asian Earth Sciences*, 21(3):295–306.

Weidinger, J. T., Schramm, J.-M., and Surenian, R. (1996). On preparatory causal factors, initiating the prehistoric Tsergo Ri landslide (Langthang Himal, Nepal). *Tectonophysics*, 260(1):95–107.

Weinberg, R. F. and Dunlap, W. (2000). Growth and deformation of the Ladakh Batholith, Northwest Himalayas: implications for timing of continental collision and origin of calc-alkaline batholiths. *The Journal of Geology*, 108(3):303–320.

Weltje, G. J. (1997). End-member modeling of compositional data: numerical-statistical algorithms for solving the explicit mixing problem. *Mathematical Geology*, 29(4):503–549.

West, A. J., Hetzel, R., Li, G., Jin, Z., Zhang, F., Hilton, R. G., and Densmore, A. L. (2014). Dilution of ^{10}Be in detrital quartz by earthquake-induced landslides: Implications for determining denudation rates and potential to provide insights into landslide sediment dynamics. *Earth and Planetary Science Letters*, 396(C):143–153.

Whipple, K. X. (2009). The influence of climate on the tectonic evolution of mountain belts. *Nature Geoscience*, 2(2):97–104.

Whipple, K. X. and Tucker, G. (1999). Dynamics of the stream-power river incision model: Implications for height limits of mountain ranges, landscape response timescales, and research needs. *Journal of Geophysical Research*, 104(B8):17661.

Willenbring, J. K., Codilean, A. T., and McElroy, B. (2013). Earth is (mostly) flat: Apportionment of the flux of continental sediment over millennial time scales. *Geology*, 41(3):343–346.

Willenbring, J. K. and von Blanckenburg, F. (2010). Long-term stability of global erosion rates and weathering during late-Cenozoic cooling. *Nature*, 465(7295):211–214.

Willett, S. D. (1999). Orogeny and orography: The effects of erosion on the structure of mountain belts. *Journal of Geophysical Research*, 104(B12):28957.

Williams, M., Dunkerley, D., de Dekker, P., Kershaw, P., and Chappell, J. (1998). *Quaternary Environments*. Arnold, London, 2 edition.

Winograd, I. J., Coplen, T. B., Landwehr, J. M., Riggs, A. C., Ludwig, K. R., Szabo, B. J., Kolesar, P. T., and Revesz, K. M. (1992). Continuous 500,000-year climate record from vein calcite in Devils Hole, Nevada. *Science*, 258(5080):255–260.

Wittmann, H., von Blanckenburg, F., Kruesmann, T., Norton, K. P., and Kubik, P. W. (2007). Relation between rock uplift and denudation from cosmogenic nuclides in river sediment in the Central Alps of Switzerland. *Journal of Geophysical Research*, 112(F4).

Wobus, C. W., Heimsath, A. M., Whipple, K. X., and Hodges, K. V. (2005). Active out-of-sequence thrust faulting in the central Nepalese Himalaya. *Nature*, 434(7036):1008–1011.

Wobus, C. W., Hodges, K. V., and Whipple, K. X. (2003). Has focused denudation sustained active thrusting at the Himalayan topographic front? *Geology*, 31(10):861.

Wohl, E. (2000). *Mountain Rivers*, volume 14 of *Water Resources Monograph*. American Geophysical Union, Washington, D. C.

Xu, C., Xu, X., Gorum, T., van Westen, C. J., and Fan, X. (2014). Did the 2008 Wenchuan Earthquake Lead to a Net Volume Loss? In Sassa, K., editor, *World Landslide Forum 3*, pages 191–196, Beijing. Springer International Publishing.

Yanites, B. J., Tucker, G. E., and Anderson, R. S. (2009). Numerical and analytical models of cosmogenic radionuclide dynamics in landslide-dominated drainage basins. *Journal of Geophysical Research*, 114(F1):F01007.

Yin, A. (2006). Cenozoic tectonic evolution of the Himalayan orogen as constrained by along-strike variation of structural geometry, exhumation history, and foreland sedimentation. *Earth Science Reviews*, 76(1-2):1–131.

Zeitler, P. K. (1985). Cooling history of the NW Himalaya, Pakistan. *Tectonics*, 4(1):127–151.

Zeitler, P. K., Meltzer, A., Koons, P. O., Craw, D., Hallet, B., Chamberlain, C., Kidd, W., Park, S., Seeber, L., and Bishop, M. (2001). Erosion, Himalayan geodynamics, and the geomorphology of metamorphism. *GSA Today*, 11(1):4–9.

Zomer, R. J., Trabucco, A., Straaten, O. v., and Bossio, D. A. (2006). Carbon, land and water: a global analysis of the hydrologic dimensions of climate change mitigation through afforestation/reforestation. *Research Report - International Water Management Institute*, 101:44.